Enabling multimodal whole-brain investigation for drug discovery

Perens, Johanna

Publication date:
2021

Document Version
Publisher's PDF, also known as Version of record

PhD thesis

Enabling multimodal whole-brain investigation for drug discovery

Johanna Perens

Technical University Denmark

November 30, 2021

Johanna Perens

Enabling multimodal whole-brain investigation for drug discovery

Academic supervisors: Anders Bjorholm Dahl, Tim Dyrby
Industrial supervisors: Jacob Hecksher-Sørensen, Casper Gravesen Salinas

November 30, 2021

Technical University Denmark
Department of Applied Mathematics and Computer Science
Section for Visual Computing
Richard Petersens Plads, building 324
2800 Kongens Lyngby, Denmark
compute.dtu.dk

"The brain is a world consisting of a number of unexplored continents and great stretches of unknown territory."

Santiago Ramón y Cajal

Preface

The project "Enabling multimodal whole-brain investigation for drug discovery" was conducted from December 2018 to December 2021 at the Section for Visual Computing, Department of Applied Mathematics and Computer Science, Technical University of Denmark (DTU) in collaboration with the Department of Computational Biology, Gubra ApS and the Danish Research Centre for Magnetic Resonance (DRCMR), Centre for Functional and Diagnostic Imaging and Research, Copenhagen University Hospital Amager and Hvidovre. The project was performed in fulfillment of the requirements for obtaining a Doctor of Philosophy (PhD) within the topic of biomedical image analysis. The project was supervised by Professor Anders Bjorholm Dahl (main supervisor, DTU), Jacob Hecksher-Sørensen (main supervisor, Gubra ApS), Associate Professor Tim B. Dyrby (co-supervisor, DTU and DRCMR) and Casper Gravesen Salinas (co-supervisor, Gubra ApS). The work presented in this thesis was financed by Innovation Fund Denmark and Gubra ApS. The experimental part of the project was carried out at Gubra ApS, DRCMR, and The 3D Imaging Centre, DTU while image processing was conducted at Gubra ApS and DTU. An external research stay was conducted in a form of digital collaboration with BrainGlobe initative.

Summary

3D imaging modalities enable preclinical rodent brain imaging for investigating disease mechanisms and developing effective therapies. One of the major challenges in the neuroimaging field has been the integration of data from *in vivo* magnetic resonance imaging (MRI) and *ex vivo* light sheet fluorescence microscopy (LSFM). And although several computational tools are available for processing LSFM datasets, there is still room for improvement to enable automated, unbiased, and accurate analysis of LSFM-imaged whole brain volumes. This PhD project addressed these issues by developing a multimodal mouse brain atlas, a LSFM-based rat brain atlas and a voxel-wise statistical analysis pipeline to facilitate analysis and bridging of whole rodent brain datasets. The multimodal mouse brain atlas bridges MRI, LSFM and Allen Institute's Common Coordinate Framework version 3. Additionally, it includes a skull-derived stereotaxic coordinate system, which connects every voxel in atlas templates to spatial positions in living mouse brains. The applicational value of established atlas resources and the analysis pipeline was demonstrated by characterizing and comparing LSFM-imaged brain activity patterns induced by six different body weight-lowering drugs. The screening study identified a set of brain regions, which may play a key role in appetite and body weight regulation by investigating shared and distinct features of drug-induced activation patterns. Outcomes of this PhD project allow high-throughput, unbiased investigation of complex processes as well as drug effects in whole rodent brains, and support anti-obesity drug discovery programs by identification of activity signatures in response to body weight-lowering drugs.

Resumé

3D- imaging modaliteter muliggør præklinisk rekonstruktion af hjerner fra mus og rotter med henblik på undersøgelse af sygdomsmekanismer og udvikling af effektiv behandling. En af de største udfordringer inden for neuroimagingområdet har været at integrere data fra in vivo magnetisk resonansbilleddannelse (MRI) og ex vivo light sheet fluorescensmikroskopi (LSFM). På trods af at flere beregningsværktøjer er tilgængelige til behandling af LSFM-datasæt, er der stadig plads til forbedringer for at muliggøre automatiseret, unbiased og nøjagtig analyse af LSFM-afbildede hjernevolumener. Dette ph.d.-projekt adresserede disse spørgsmål ved at udvikle et multimodalt musehjerneatlas, et LSFM-baseret rottehjerneatlas og en voxel baseret statistisk analysepipeline for at lette analyse af og skabe bro mellem datasæt af hjerner fra gnavere. Det multimodale musehjerneatlas bygger bro mellem MRI, LSFM og Allen Institutes Common Coordinate Framework version 3. Derudover inkluderer det et kranie-deriveret stereotaksisk koordinatsystem, som forbinder hver voxel i atlas templates til rumlige positioner i levende musehjerner. Værdien af de etablerede atlas og tilhørende analysepipeline er demonstreret ved at karakterisere og sammenligne LSFM-afbildede mønstre i hjerneaktivitet induceret af seks forskellige lægemidler som reducerer kropsvægt. Screenings studiet identificerede et sæt hjerneregioner, som kan spille en nøglerolle i regulering af appetit og kropsvægt ved at undersøge fælles og unikke træk ved lægemiddel-inducerede aktiveringsmønstre. Resultaterne af dette ph.d.-projekt giver mulighed for high throughput, objektiv undersøgelse af komplekse processer såvel som effekter af lægemidler i hele hjerner af gnavere og understøtter programmer til at identificere fedmereducerende signaturer for hjerneaktivering som bliver aktiveret når kropsvægten reduceres.

Acknowledgements

I would like to express my sincere gratitude to my supervisors Anders Bjorholm Dahl, Jacob Hecksher-Sørensen, Tim Dyrby and Casper Gravesen Salinas for their valuable guidance and encouragement throughout the project. I would also like to thank Jacob Jelsing and Niels Vrang for enabling me to conduct such an interesting PhD project at Gubra, but also generally for establishing an industrial PhD program for young scientist at Gubra. Thanks to the BrainGlobe initiative for giving me the opportunity to collaborate in the project and I hope this collaboration will continue in the future. A special thanks to Jacob Lercke Skytte and Urmas Roostalu, who were also tightly involved in this PhD project, for inspiring scientific discussions and constructive feedback. And of course, big thanks also to all the others involved in Gubra's imaging team who have been supporting me during this journey, both professionally and personally: Grethe Skovbjerg, Hanne Duus Lautsen, Franziska Wichern, and Chen Zhang. I would also like to acknowledge Henrik Björk Hansen for sharing his expertise in manuscript writing, Pernille Barkholt for the scientific input in brain space, and Martin Mikkelsen for looking out for me. A great thanks to all the previous and current PhD students at Gubra who shared this hilly journey with me, it wouldn't have been so fun and enjoyable without you: Mette Simone Madsen, Frederikke Emilie Sembach, Helene Ægidius, Flora Alexopoulou, Louise Steen Thisted, Christoffer Andersen Hagemann, Malte Hasle Nielsen, Mathias Bonde Møllerhøj, Sarah Torp Sørensen, and Joakim Holck Andersen. I would also like to thank all members of the Computational Biology department for the support and input on my PhD project. Acknowledgements go also to my former and current colleagues at the Section for Visual Computing, DTU, and at the Microstructure and Plasticity group, DRCMR. It has been a pleasure to carry out my PhD project having so many intelligent, caring, and inspiring people around me.

Finally, I am deeply grateful for all the support I have received from my family as well as friends in Estonia and Germany.

Aitäh teile, ema ja isa, et te mind alati julgustanud olete oma rada käia ja julgeid eesmärke seada. Olen ääretult tänulik, et te mind kõigis minu ettevõtmistes toetanud olete ning alati minu jaoks olemas olete olnud. Samuti soovin tänada oma vanavanemaid ning onusid peredega suure toetuse ja kaasaelamise eest. Aitäh minu lähimatele sõpradele, kes te minuga läbi ja tule ja vee tulete: Ann Lakspere, Siret Leoke, Silvia Juhansoo, Helina Tammeleht, Kriss-Elin Rokk ja Sten Rõngelep.

Zusätzlich würde ich mich gerne bei meinen Kommilitonen Barbara Schweißhelm, Anisa Dashi und Lukas Beddrich bedanken, mit denen ich meine wunderschönen Studienjahre in München verbracht habe. Tief verbunden und dankbar bin ich meinem Lebensgefährten Andreas Pöschl und seiner Familie für die liebevolle Fürsorge und Unterstützung während meines Studiums.

Yours sincerely,
Johanna Perens

Abbreviations

AIBS	Allen Institute of Brain Science
CCFv3	Common Coordinate Framework version 3
CMI	cluster mass inference
CSI	cluster size inference
CT	computed tomography
FDR	false discovery rate
FP MBSC	Franklin and Paxinos' Mouse Brain in Stereotaxic Coordinates
FWER	family-wise error rate
GLM	generalized linear model
iDISCO	immunolabeling-enabled 3D imaging of solvent-cleared organs
LSFM	light sheet fluorescence microscopy
MRI	magnetic resonance imaging
NBF	neutral buffered formalin
PB	parabrachial nucleus
PBS	phosphate buffered saline
PET	positron emission tomography
PMA	Princeton Mouse Brain Atlas
pTFCE	probabilistic threshold-free cluster enhancement
SN	substantia nigra
SNR	signal-to-noise ratio
STPT	serial two-photon tomography
TFCE	threshold-free cluster enhancement
WHS	Waxholm space

Contents

Preface v

Summary vii

Resumé ix

Acknowledgements xi

Abbreviations xiii

1 Introduction 1

1.1 Motivation . . . 1
1.2 Scientific aims . . . 3
1.3 Contributions . . . 3
1.3.1 Publications . . . 3
1.3.2 Conferences . . . 4
1.4 Thesis outline . . . 4

2 Investigating the brain 7

2.1 Gross anatomy . . . 7
2.2 Experimental methods in neuroscience . . . 9
2.2.1 Micro-computed tomography . . . 10
2.2.2 Magnetic resonance imaging . . . 12
2.2.3 Light sheet fluorescence microscopy . . . 15
2.3 Role of imaging in drug development . . . 17
2.4 Brain atlases . . . 19
2.5 Image processing . . . 22
2.5.1 Image registration . . . 23
2.5.2 Detection of activated neurons . . . 25
2.5.3 Statistical analysis . . . 27

3 Generation of digital rodent brain atlases for analyzing LSFM-imaged brains **31**
3.1 LSFM-based mouse brain atlas (Publication A) 32
3.2 LSFM-based rat brain atlas 34
3.3 Discussion and future directions 36

4 Bridging *in vivo* and *ex vivo* neuroimaging modalities **39**
4.1 Multimodal mouse brain atlas framework (Manuscript B) 39
4.2 *In vivo* validation of the stereotaxic coordinate system 41
4.3 Discussion and future directions 44

5 Evaluation of brain activity in response to drug therapy **49**
5.1 Voxel-wise statistics for LSFM whole-brain samples (Publication C) . 50
5.2 Effect of anti-obesity drugs on brain activity (Publication D) 51
5.3 Discussion and future directions 54

6 Conclusion and outlook **57**

Appendices **61**

Bibliography **137**

Introduction

1.1 Motivation

Neurological disorders are considered a major cause of disabilities and reduced life expectancy in the world today. Such diseases affecting the central and peripheral nervous system include brain cancers, neurodegenerative diseases, multiple sclerosis, stroke, brain and spinal cord injuries, epilepsy, migraine, and infections attacking the nervous system. It has been suggested to add obesity to the list of brain diseases as there is a growing evidence for interplay between neural and metabolic systems [Bri+10; Cha+11; Ern+09; Jol+12; SMS13]. According to the Global Burden of Disease Study 2019, neurological disorders are the second leading cause of deaths (circa 12 million per year globally including obesity related deaths [GBD19; Wor21]) after cardiovascular diseases. Due to their chronic course and in majority of cases increasing severity, neurological disorders pose considerable burden to patients, their families as well as society.

Despite extensive research on neurological disease mechanisms, to date no cure exist for many of them (e.g., Parkinson's disease [AO20], Alzheimer's disease [VS20], stroke [PC21]). One reason for this is the extreme complexity of the brain, which structural and functional relationship is far from understood. Even though modern neuroimaging techniques have greatly expanded our knowledge on basic aspects of neuronal specialization and network architecture, it is still a challenge to unfold the dynamic processes of the brain due to inherent limitations of the modalities. Non-invasive imaging modalities such as magnetic resonance imaging (MRI) and positron emission tomography (PET) enable *ex vivo* and longitudinal *in vivo* measurements of human and animal brains. However, biological information in their image volumes is encoded in indirect measures and resolution does not provide cellular resolution [Sym+04; Dav+20; Wan+20a; Wei+16]. In contrast to MRI and

PET, histology enables visualization of molecular markers in micrometre scales. Histological techniques enable cellular resolution but their invasive character and tissue processing protocol make them unsuitable for *in vivo* whole-brain imaging, but also induce changes in tissue morphology complicating spatial localisation of signals [Man+20; Ert+12; Per+21a]. Lack of information in either spatial or temporal domains can, however, be overcome by integrating neuroimaging datasets across scales and modalities. Currently, very few frameworks are available for studying or combining multimodal information [Mac+04; Gou+19; Sto+18; Pat18]. Development of standardized frameworks is fundamental for revealing the function of the brain and accelerate the translation of findings from preclinical research to clinical setups by enabling validation of MRI and PET measures against molecular markers.

Studies of brain activation in response to different challenges or administration of substances, is a common practice in preclinical pharmaceutical research for identifying key areas of the brain involved in biological mechanisms. Histology-based activation studies rely on the detection of single cells expressing the transcription marker c-Fos (i.e., a rapidly expressed protein upon stimulation activating downstream processes in the cell), counting of activated cells in their respective brain regions and performing statistical testing between control and treatment groups at regional level [Asi+95; Sor+07; Tót+18]. The 3D histology technique, light sheet fluorescence microscopy (LSFM) of optically cleared and fluorescently labelled tissue, enables researchers to image a whole brain at once [Ued+20]. Compared to 2D histology, LSFM benefits from optical sectioning that preserves tissue integrity and enables high-throughput data collection. Application of LSFM for activation studies has been previously demonstrated in regional manner [Ren+16]. However, existing digital atlases [Wan+20b] are based on different imaging modalities, and using these modalities for regional parcellations leads to inaccuracies in LSFM-imaged brains. Additionally, a region-wise approach does not provide access to detailed characteristics of activation signals inside regional delineations. To enable accurate analysis of neuronal activation at a whole-brain and local level, it is essential to improve existing analysis pipelines with LSFM-based atlases and voxel-wise statistical analysis techniques.

The work done in the present PhD project addressed the issues related to the lack of integration between multimodal datasets and analysis of whole-brain activation profiles in response to stimuli by creating dedicated tools for automated computational analysis of whole-brain datasets. Developed tools were implemented in image analysis pipelines for investigating the role of brain in appetite and body-weight reg-

ulation, thereby supporting Gubra's efforts in drug discovery for treating obesity.

1.2 Scientific aims

The PhD project had the following three objectives:

1. Creation of a multimodal atlas tool for enabling integration of *in vivo*/*ex vivo* MRI- and *ex vivo* LSFM-imaged rodent whole-brain datasets. The atlas tool should allow to overlay MRI- and LSFM-imaged brain volumes in the same template space, include detailed region delineations for quantitative analysis of extracted signals and provide stereotaxic coordinates for linking every voxel in an imaged brain volume to spatial positions in living mouse brains.

2. Expansion of the standard image analysis pipeline used to quantify brain activity in LSFM-imaged brain samples by voxel-wise statistical analysis approach for complementing existing region-wise approaches.

3. Application of the developed atlas resources and improved image analysis pipeline for identifying whole-brain networks involved in appetite and body-weight regulation. The experiment involved screening of activation signatures induced by pharmaceutical compounds with documented clinical effect on body-weight reduction.

1.3 Contributions

The outcome of the PhD project is documented in three peer-reviewed and published articles and one manuscript in preparation. The results have also been presented at two international conferences listed below.

1.3.1 Publications

Publication A

Johanna Perens, Casper Gravesen Salinas, Jacob Lercke Skytte, Urmas Roostalu, Anders Bjorholm dahl, Tim B. Dyrby, Franziska Wichern, Pernille Barkholt, Niels Vrang, Jacob Jelsing, Jacob Hecksher-Sørensen. *An Optimized Mouse Brain Atlas for Automated Mapping and Quantification of Neuronal Activity Using iDISCO+ and Light Sheet Fluorescence Microscopy.* Neuroinformatics 19, pp. 433-446, 2021.

Manuscript B
Johanna Perens, Casper Gravesen Salinas, Urmas Roostalu, Jacob Lercke Skytte, Carsten Gundlach, Jacob Jelsing, Niels Vrang, Jacob Hecksher-Sørensen, Anders Bjorholm Dahl, Tim B. Dyrby. *Multimodal 3D mouse brain atlas framework with skull-derived coordinate system.* In preparation, 2021.

Publication C
Johanna Perens, Jacob Lercke Skytte, Casper Gravesen Salinas, Jacob Hecksher-Sørensen, Tim B. Dyrby, Anders Bjorholm Dahl. *Comparative study of voxel-based statistical analysis methods for fluorescently labelled and light-sheet imaged whole-brain samples.* 2021 IEEE 18th International Symposium on Biomedical Imaging (ISBI), peer reviewed proceedings, pp. 1433-1437, 2021.

Publication D
Henrik H. Hansen, Johanna Perens, Urmas Roostalu, Jacob Lercke Skytte, Casper Gravesen Salinas, Pernille Barkholt, Ditte Dencker Thorbek, Kristoffer T. G. Rigbolt, Niels Vrang, Jacob Jelsing. *Whole-brain activation signatures of weight-lowering drugs.* Molecular Metabolism 47, 101171, 2021.

1.3.2 Conferences

INCF Neuroinformatics 2019
Johanna Perens, Casper Gravesen Salinas, Jacob Lercke Skytte, Urmas Roostalu, Anders Bjorholm dahl, Tim B. Dyrby, Pernille Barkholt, Katrine Fabricius, Jacob Jelsing, Jacob Hecksher-Sørensen. *A Dedicated Light Sheet Fluorescence Microscopy Atlas for Mapping Neuronal Activity and Genetic Markers in the Mouse Brain.* Poster presentation, University of Warsaw, Poland, 2019.

1.4 Thesis outline

This thesis consists of six chapters. Publications A, C, D and manuscript B can be found in appendix with publications. The current chapter introduced the problematic and formulated scientific objectives of the project. The second chapter gives an overview of the brain anatomy, neuroimaging modalities and image processing techniques. Chapters three to five describe how image processing was implemented for integrating and analyzing neuroimaging datasets through computational tools

developed during the PhD project. The fifth chapter demonstrates applicability of the developed tools. Limitations of the tools and future work is described at the end of chapters three, four and five. The sixth and last chapter concludes the thesis by summarizing the outcomes of the PhD project and discussing the potential impact of the work.

Investigating the brain

2.1 Gross anatomy

The brain together with spinal cord forms the central nervous system of an organism. An average human brain consists of 86 billion neuronal and 85 billion non-neuronal cells whereas an average mouse brain has 71 million neuronal and 38 million non-neuronal cells [HML06; Her09]. Brain tissue can be divided into two classes - grey matter and white matter. Grey matter areas consist of neuronal cell bodies, unmyelinated neuronal projections and dendrites. In contrast to grey matter, white matter is rich in myelinated axons and contains relatively few cell bodies. Non-neuronal cells of the brain are glial cells (astrocytes, oligodendrocytes, microglia, polydendrocytes and ependymal cells), which regulate neuronal metabolism, insulate projections, provide protection and regeneration, and secrete cerebrospinal fluid [WKP10a]. While processing of the information, received either from a peripheral sensory input or other neurons in the brain, takes place in grey matter, white matter tracts facilitate long-range communication between grey matter neurons. Segregation of the brain tissue into grey and white matter has been shown to be the optimal configuration for the brain to benefit from high synaptic density and shortest delays in information transport [WC05].

Mammalian brains are divided into two topologically almost symmetric hemispheres, which communicate via the corpus callosum, the largest axonal bundle in the brain. The brain is highly organized allowing parcellation of the tissue into regions based on the cellular and functional characteristics (Figure 2.1). Major regions of the brain include cerebrum, cerebellum, and brain stem. The cerebral cortex is organized in layered and columnar arrangements, responsible for sensory information processing, bodily movements, communication, memory, and emotions [JMP18]. The cerebral nuclei coordinate behaviour based on associations, decisions, emotions, and reward

[BB19; Smi+09; MT91; BC12]. The cerebellum is a lobural brain structure shown to be indirectly involved in processes governed by other brain regions by monitoring and fine-tuning executed actions to match expectation (e.g., planning, execution and learning of movements, and communication through language) [DAn18]. The brain stem consists of the interbrain, the midbrain, and the hindbrain. The interbrain's thalamic area is responsible for transmission of sensorymotor signals and cognitive control [HK17] while the hypothalamic area regulates hormonal processes and circadian rhythm. [XD17]. The midbrain accommodates dopaminergic system of the brain which plays a role in motivating behaviour, learning through associations and reward, memory processing, and regulation of emotions [BR16]. The hindbrain connects to and exchanges information with the spinal cord and regulates autonomic functions of the body including respiration, energy homeostasis and cardiovascular physiology [SG09].

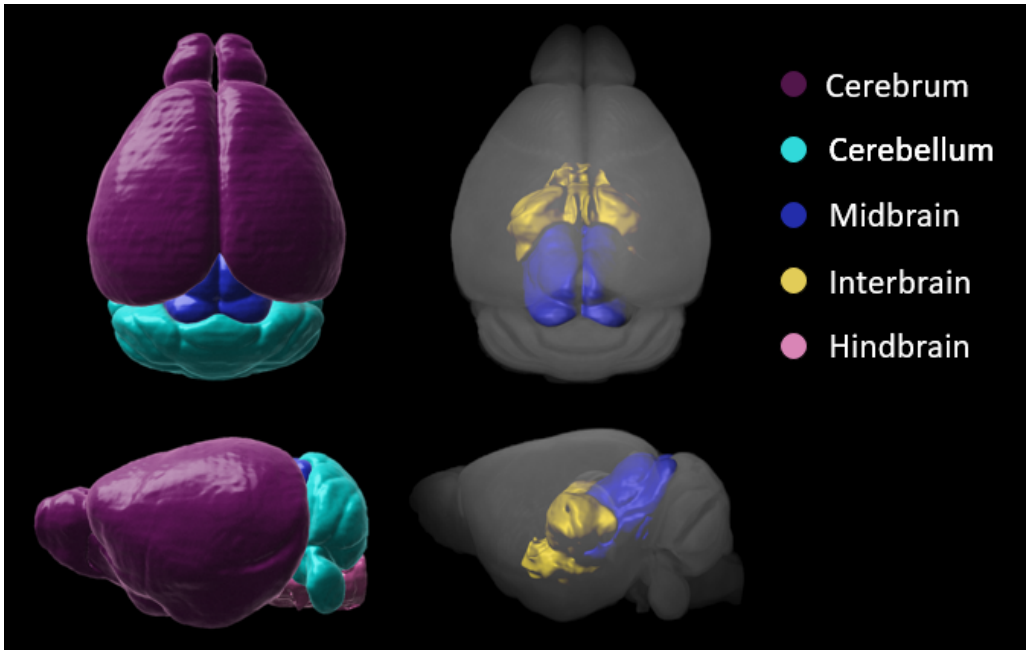

Figure 2.1: Mouse brain parcellated into five main regions. Regions are surface rendered and visualized on an average MRI brain template in top and sagittal view. Region parcellations were obtained from Mouse Brain CCFv3 developed by Allen Institute of Brain Science [Wan+20b; Don08]

2.2 Experimental methods in neuroscience

Various methods have been developed for studying cellular distribution, processes, architecture, and functional aspects of cellular populations in the brain. Experimental techniques for probing the brain can largely be divided into invasive and non-invasive techniques. Invasive techniques involve extraction of brain tissue from the skull or manipulation of neuronal populations within the skull *in vivo*, whereas non-invasive neuroimaging techniques allow repeated measurements of the brain without opening or introducing instruments inside the skull.

Many invasive methods involve preparation of extracted tissue for optical imaging with different light and fluorescence microscopy techniques [WKP10b]. Histochemical and immunohistochemical staining of sectioned or intact tissue is used to study cellular distribution utilizing antibodies, in situ hybridization or chemical dyes. Hodology focuses on revealing structural connections between neurons via tract tracing with dyes, microbeads, and viruses. Cell and tissue cultures isolated from their natural environment are used to characterize cells, their interactions with other cells and response to experimental conditions in detail. Further techniques from molecular genetics include introduction (knock-in) or disabling (knock-out) of genes for studying their role biological role, optogenetics for manipulating neuronal activity with light, and DREADDS (designer receptor exclusively activated by designer drugs) for manipulating neuronal activity with special ligands.

Non-invasive neuroimaging techniques probe different physical characteristics of the tissue and therefore, provide images with unique contrast mechanisms. X-ray computed tomography (CT) collects x-ray absorption profile of the head from different angles and thus, measures tissue density [KLG16]. In contrast to CT, magnetic resonance imaging (MRI) does not use ionizing radiation but magnetic fields in combination with radiofrequency pulses to exparencite certain types of atoms in the tissue for acquiring an image volume [YDP18]. The tissue contrast in MRI images is an indirect measure related to density and relaxation time of exparencited atoms. In addition to structural information, MRI allows also functional measurements of brain activity, perfusion, magnetic susceptibility and diffusion characteristics. Further functional imaging techniques include single-photon emission CT (SPECT), positron emission tomography (PET) and a relatively new technique called photoacustic tomography (PAT). SPECT and PET both utilize radiolabelled molecules for investigating blood flow, neuronal activity, metabolism as well as distribution of radioactively labelled drugs [NGS20]. PAT operates through detection of acustic

waves in optically exparencited tissue and is sensitive to hemodynamic changes related to brain activity [Zha+18].

Electrophysiology includes a collection of techniques which can be performed either in a non-invasive or invasive manner. These techniques are applied for investigating neural processing and communication by recording neuronal activity in the resting state or in response to an external stimulus. Signal propagation inside the neurons is taking place through voltage changes in cell membrane which induce measurable currents and magnetic fields. Invasive electrophysiology techniques record neuronal firing via electrodes inserted (e.g., patch clamp method) into or attached to isolated neurons *in situ* [LL11]. Non-invasive electroencephalography (EEG) and magnetoencephalography (MEG), are neuroimaging methods used to record activity of neuronal clusters via electrodes mounted on the scalp [Bai17; FT19].

The following sections explain the neuroimaging methods used in this PhD project in more detail.

2.2.1 Micro-computed tomography

Computed tomography (CT) is a X-ray imaging technique suitable for visualizing mineralized tissue in 3-dimensions. CT measures attenuation of X-rays - electromagnetic waves with wavelengths in range of 10 pm to 10 nm - upon passing a specimen from several angles. Attenuation occurs through the photoelectric effect, coherent scattering, and incoherent scattering when X-rays interact with the tissue [Cie11b]. The photoelectric effect involves absorption of X-ray photons by atomic electron shells resulting in release of electrons and secondary X-ray photons emitted by electrons occupying the empty vacancies in lower shells. Secondary X-ray photons can be differentiated from the illuminating X-rays by their distinctive wavelengths. Scattering takes place when X-ray photons are deflected from their original path, and in case of incoherent scattering lose energy, due to interactions with electrons. The total attenuation of the incident X-rays, which is a combination of the three effects, is dependent on density and thickness of the substance. Because of low and relatively homogeneous absorption of X-rays by soft tissue, radio-opaque contrast agents need to be used to investigate microstructure of soft tissue, for example the brain [Cre+08].

X-rays were first reported by Wilhelm Conrad Röntgen in 1895 and triggered a rapid adoption of 2D X-ray imaging in the medical field [Cie11a]. However, lim-

itations of 2D imaging could not be solved before the development of computers, although several attempts for receiving volumetric information of the tissue were made. Reconstruction of 3-dimensional CT volumes became possible in 1960s when Allan MacLeod Cormack and Godfrey Newbold Hounsfield through theoretical calculations, experimental setup, and help from first computers realized the concept of computed tomography. Following the first CT-scan of a patient in 1971, fast progress was made in improving the setup in terms of scan time and resolution. Today, clinical CT scanners generate volumetric images with voxel sizes in millimetre-range while micro-CT system for high-resolution imaging of tissue specimen or small animals achieve voxel sizes in the micrometre-range [Rit04].

Components of the micro-CT setup include an X-ray source, a metal filter, a rotating sample holder, and a X-ray detector [AWB15]. X-rays are generated by accelerating electrons towards an anode by applying a high voltage to the X-ray source. Upon collision with the anode, electrons produce X-ray radiation in different wavelengths. The radiation spectrum is filtered to fit the X-ray energies to the substance of interest for creating optimal contrast. In order to obtain a magnified image of the specimen, a cone-shaped beam, optical magnification or Bragg diffraction can be used for illuminating the sample [Rit04]. Attenuated X-ray profiles are acquired and converted into visible light by fluorescent crystal plates, fluorescent granule screens or fluorescence-doped fiber optics. Finally, the light is converted into electrons by a charged-coupled device (CCD) array detector to form an image. Specimens are radiated under multiple angles and for every angle an attenuation profile is acquired. For every 2D slice of the volume, attenuation profiles are summarized in form of a sinogram which is a linear transform of the original volume [AWB15]. 2D slice of the specimen can then be reconstructed from attenuation profiles by inverse Radon transform obtained via filtered back projection.

In the current PhD work, a micro-CT scanner ZEISS XRadia Versa XRM-410 was used for collecting image volumes of mouse skulls in order to create stereotaxic coordinate system for the multimodal atlas. ZEISS XRadia Versa XRM-410 setup is composed of a cone beam for illuminating and magnifying the sample, a scintillator for converting X-rays to light, a secondary optical magnification system and a CCD detector. Skull volumes were obtained from mouse heads perfusion fixated with neutral buffered formalin (NBF), post-fixed in NBF for 4 days and washed in phosphate buffered saline (PBS) for 3 weeks. Image volumes were acquired from 1601 projections of PBS immersed specimens, with voltage of X-ray source set to 50 kpV (Figure 2.2).

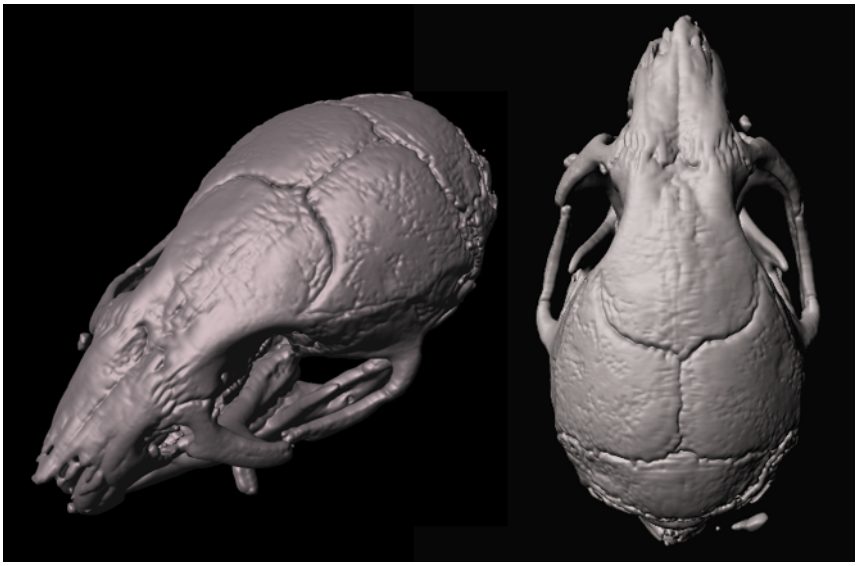

Figure 2.2: A raw mouse skull volume obtained with micro-CT shown in side and top view. The skull volume has an isotropic voxel size of $(22\ \mu\text{m})^3$. The image volume was acquired at The 3D Imaging Center (3DIM), Technical University Denmark.

2.2.2 Magnetic resonance imaging

3D magnetic resonance imaging (MRI) is widely used in the clinic due to its non-invasive character and ability to provide high contrast images of soft tissue, including the brain. The method utilizes nuclear magnetic resonance (NMR) to induce a signal in the tissue [Dra57]. NMR can only be induced in atomic nuclei with non-zero spin (implying also non-zero magnetic dipole moment), i.e., nuclei with odd number of neutrons and/or protons. As hydrogen atoms (protons) have non-zero spin and water molecules are highly abundant in soft tissue, they are commonly stimulated to induce NMR in soft tissue. For inducing NMR, an unidirectional, homogeneous magnetic field is applied resulting in splitting of nuclear energy niveaus (Zeeman splitting) and precession of nuclear magnetic dipole moment about the direction of the magnetic field (Larmor precession). Nuclear resonance can be observed by radiating atoms with energy matching the energy difference of the splitted niveaus (radiofrequency range for 1-10 tesla magnetic fields) resulting in magnetic dipole moments to move out of alignment with the magnetic field and synchronize their precession phases. Exparencited nuclei return to their ground state as a result of relaxation processes by emitting detectable electromagnetic waves.

The NMR phenomenon was discovered by Isidor Rabi in 1938 and the first NMR spectrometer was built in 1950s after Felix Bloch and Edward Mills Purcell demonstrated the effect in different solids and liquids [Rab+38; Bec+12; Blo46; PTP46].

However, for producing 2D and even 3D images of tissue, a system for spatial encoding of the signal needed to be developed. The problem of spatial encoding was solved in 1973 by Peter Mansfield and Paul Lauterbur, who introduced spatial variation in the main magnetic field in form of additional magnetic fields [Lau73]. The secondary magnetic fields produce gradual change in the main magnetic field, which alters the local resonance frequency and phase enabling to encode information on spatial location. Introduction of gradient systems paved the way for rapid development of clinical, high-field MRI scanners in 70s and 80s [Bec+12]. Today, in addition to clinical applications, MRI is also widely used in preclinical research with ultra-high field strengths necessary for high-resolution imaging of small animals. Furthermore, MRI scans have become an essential part of PET measurements for allowing anatomical localisation of signals from radiolabelled molecules.

Contrast in MRI images originates from several mechanisms - density of protons, spin-lattice (thermal) relaxation and spin-spin (inter-nuclear) relaxation [NR99]. Both relaxation types are exponential processes and can be described by relaxation times T1 and T2, respectively. Although intensity in MRI images is always a combination of proton density and relaxation processes, contrasts can be suppressed by choosing scan parameters according to certain rules. Unsuppressed contrast is said to provide the most "weight" to the image. As composition of molecules varies in organs, local differences occur in hydrogen density and T1/T2 relaxation times inducing contrast between tissue structures. Exception is bony tissue which appears dark in MRI images due to its low content of hydrogen atoms.

In addition to structural proton density-, T1- and T2-weighted images, MRI allows to measure diffusion characteristics of the tissue. As diffusion of molecules in extracellular and intracellular compartments of the tissue is restricted by cell components and membranes, its directionality can be used to reveal microstructural features of the tissue. Especially white matter tracts exhibit highly asymmetric shapes forcing molecules to diffuse in restricted, anisotropic manner. In diffusion MRI, random movement (Brownian motion) of hydrogen atoms is measured. For producing diffusion-weighted images, diffusion-sensitizing gradients with opposing polarity are applied [CP19]. Diffusion-sensitizing gradients do not affect stationary molecules, but cause magnetic dipole moments of hydrogen atoms to dephase as diffusing molecules experience different magnetic fields during their movement. The vector sum of all magnetic dipole moments is the final measured signal and phase dispersion due to varying diffusion trajectories results in rapid signal decay. Diffusion-sensitzing gradients measure the extent of diffusion in the applied direction. For col-

lecting 3-dimensional information on diffusion characteristics, diffusion-sensitizing gradients need to be applied in several directions. From diffusion-weigthed images, a tensor describing the direction and magnitude of diffusion can be derived. The diffusion tensor can further be used to calculate fractional anisotropy, radial, axial and mean diffusivity (also called apparent diffusion coefficient), but also to reconstruct a map of white tracts in the brain.

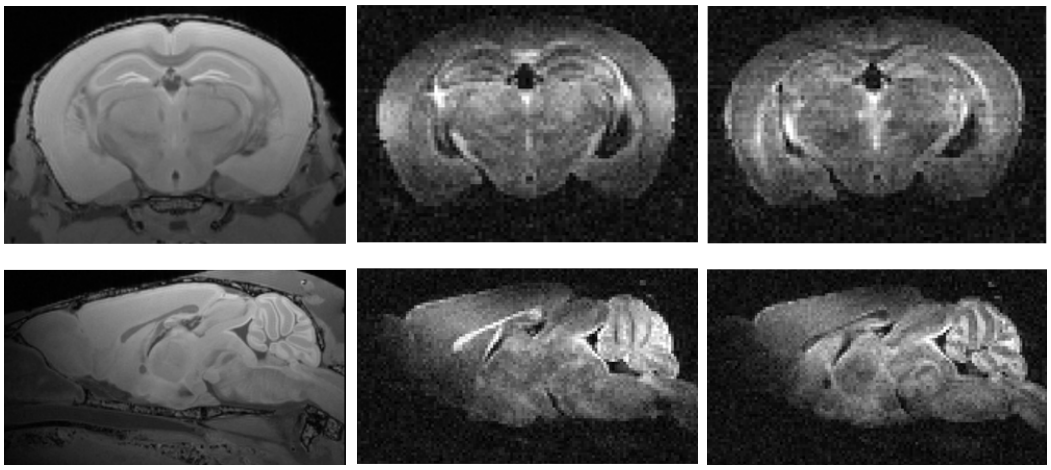

(a) T2-weighted (b) Diffusion encoding dir. 1 (c) Diffusion encoding dir. 2

Figure 2.3: Raw brain volumes obtained with MRI. Representative slices from raw volumes are shown in coronal (upper panel) and sagittal (lower panel) view. a) Structural T2-weighted image with isotropic voxel size of (78 μm)^3, b-c) Diffusion-weighted images with isotropic voxel size of (125 μm)^3 obtained at different diffusion-sensitizing gradient directions. The image volumes were acquired at Danish Research Centre for Magnetic Resonance (DRCMR), Copenhagen University Hospital Amager and Hvidovre.

A MRI scanner consist of a superconducting coil for generating a strong main magnetic field, gradient coils for spatial encoding of the signal, a transmit coil for electromagnetic stimulation, a receiver coil for signal detection, shim coils for realizing a homogeneous main magnetic field, and a controller software [YDP18]. Field strengths of the main magnetic field used for human imaging range from 1.5 to 7 tesla, while field strengths used for preclinical imaging range from 7 to 21 tesla [Dum+18; Wan+20a]. Magnetic fields produced by gradient coils have usually strengths in millitesla range. Transmitter and receiver coils come in different designs. Their design is chosen based on the brain size, as smaller coils achieve higher signal-to-noise (SNR) ratios.

The mouse brain images acquired in this PhD project were collected with a preclinical Bruker BioSpec 7 tesla scanner equipped with a cryogenic dual transmit/receive

surface coil CryoProbe from Bruker and Paravision controller software. Cryogenic coils reduce temperature-related noise in acquired images and improve thereby SNR about 2.5 times compared to normal room temperature coils. Preparation of brain samples was performed according to [Dyr+11] and included perfusion fixation with NBF, extraction of the skull with brain, immersion-fixation in NBF for four days and washing of specimen from excess fixative 2-4 weeks in PBS. Brain samples were washed from excess fixative and imaged in skulls to minimize susceptibility artifacts. The specimen were placed in a PBS-filled tube for imaging. MRI imaging was carried out on brains in skull and involved acquisition of T2-weighted structural and diffusion-weighted scans using gradient echo and spin echo radiofrequency pulse sequences, respectively (Figure 2.3).

2.2.3 Light sheet fluorescence microscopy

Light sheet fluorescence microscopy (LSFM) is a high-speed, high-resolution microscopy technique enabling detection of chemically labelled molecular markers or pharmaceutical compounds in 3D. It relies on fluorescence for signal detection. Fluorescent molecules become exparencited from ground state to energetically higher state by absorbing photons with energy equal to the energy difference of the states. Molecules fall back to their ground state on a time scale between 0.5 to 20 ns and release energy in form of light. As a small part of the energy is also transferred to molecules nearby nonradiatively, also as heat, the released energy is smaller (i.e., the wavelength is longer) than then absorbed energy (i.e., photons with shorter wavelength). LSFM can be performed both *in vivo* and *ex vivo*, but in order to image fluorescence deep in the specimen, tissue needs to have a low content of pigment naturally or made transparent through clearing [Ert+12; Ren+14; Sus+14; Chu+13; Bec+12]. *Ex vivo* LSFM can be considered a histological method as molecular markers or labelled tracers are visualized according to same principles as in 2D histology with the difference that treatment is applied on intact samples. In addition to fluorescent molecules, LSFM enables imaging of tissue structure in certain wavelengths (optimal excitation wavelengths between approx. 480 and 630 nm) due to naturally occurring fluorescent components of the tissue (e.g., collagen, elastin) [Mon05].

The first known concept of light sheet microscopy was published in year 1902 where gold particles were visualized by light passing through a slit aperture [SZ02]. The same method was also used in photomacrography in the 1960s for studying superficial features of objects [McL64]. However, decades passed by before the light sheet microscopy found application again in 1993. Inspired by photomacrography, Voie

and colleagues developed a technique called orthogonal-plane fluorescence optical sectioning (OPFOS) which setup resembles today's LSFM system [VBS93]. They applied OPFOS for exploring fluorescently labelled and cleared intact cochlear samples and layed thereby the foundation for 3D histology.

LSFM operates by collecting a stack of optically sectioned 2D images from a specimen [CGD19]. Optical sectioning is realized by illuminating a thin plane in the specimen with a sheet-shaped light beam and capturing emitted light from the section with a camera orthogonal to the illuminating beam. Optical sectioning enables imaging of intact specimens while minimizing photobleaching and background noise. Sheet-shaped light beams can be produced in different ways, for example by sending light through cylindrical lens or scanning a laser beam horizontally through the specimen. Light used for excitation is either generated by a diode laser or by band-pass filtering a white light laser in order to adjust its spectral range to the excitation spectra of the fluorophore. Emitted light is filtered through a band-pass before reaching the camera to remove non-specific signal.

Axial resolution (z-dimension) of the image volume is defined by the light sheet thickness. However, light sheets are not perfectly planar but exhibit hyperbolic shape with Gaussian profile [Fan+21]. The thickness of the light sheet's waist depends on the numerical aperture while the range of approximately planar beam waist is proportional to the squared sheet thickness. This implies that a suitable balance between the light sheet thickness and its planar range must be found depending on the size of the specimen and necessary resolution to resolve features of interest. To achieve approximately homogeneous axial resolution for large specimen, image volumes are acquired by moving the beam waist in discrete steps or continuous sweep mode horizontally through the sample.

LSFM images used in this PhD project were acquired with LaVision Ultramicroscope II (Milteny Biotec, Bergisch Gladbach, Germany). The setup included a white light laser, a dual-sided light sheet system, cylindrical lenses, filter cubes, objective lenses, a chamber with sample holder, and a sCMOS camera. The dual-sided light sheet system had three light sheets at each side for reducing shadowing artifacts. Cylindrical lenses were used for light beam shaping and filter cubes for band-pass filtering of excitation and emission light. The samples were imaged in dibenzyl ether (DBE). Imspector software was used to set up the scan and define the acquisition parameters. Preparation of mouse and rat brain samples involved perfusion fixation with NBF, immunohistochemical staining against neuronal activation marker c-Fos

in case of pharmacological studies and clearing according to the iDISCO protocol [Ren+14]. Brain volumes were acquired in the channel specific to tissue autofluorescence (excitation 560 ± 20 nm, emission 650 ± 25 nm) and in case of pharmacological studies, also in the c-Fos specific channel (excitation 630 ± 15 nm, emission 680 ± 15 nm) (Figure 2.4).

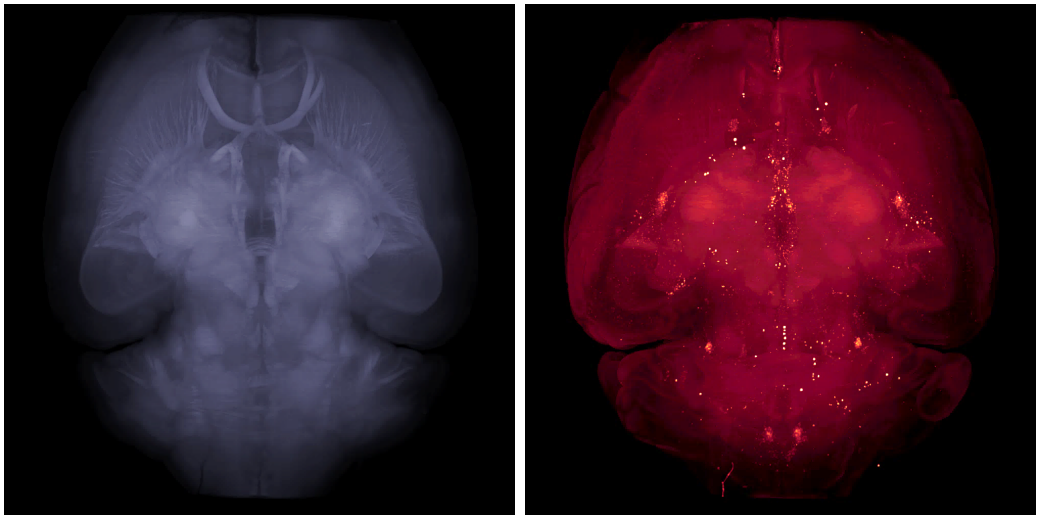

(a) Autofluorescence (b) c-Fos

Figure 2.4: Raw brain volumes obtained with LSFM. a) Fluorescence emitted by endogenous molecules, b) fluorescence emitted by cells expressing transcription factor c-Fos in response to drug administration. Brain volumes show maximum projection of the signal in horizontal view. Data was collected with the in plane voxel dimensions 4.8 μm x 4.8 μm, axial voxel dimension of 3 μm, and 10 μm step size in z. The image volumes were acquired at Gubra ApS.

2.3 Role of imaging in drug development

Drug development is a long process which takes approximately 10 years from target identification until approval by regulatory authorities [GR17]. The process involves several phases: target discovery, drug discovery and screening to identify most potent compounds, testing of compounds in preclinical animal experiments, three phases of clinical trials in humans and finally post-approval surveillance studies. As the cost of the experiments increases with each phase, it is beneficial to identify the compound with the most suitable characteristics early on and cancel further experiments with less prospective candidates. Neuroimaging modalities provide an opportunity to characterize, screen, and optimize pharmaceutical drugs effectively, which is why they are widely used in both preclinical and clinical studies.

As described in chapter 2.2, neuroimaging methods provide information in different means, scales and temporal resolution. Due to its invasive character, LSFM is most suitable for *ex vivo* preclinical studies. Nevertheless, LSFM supports drug discovery efforts at several levels. A way to identify brain access and distribution of a compound, is to measure the intensity of a fluorophore-labelled compound in different brain regions post administration [Gab+20; Sec+14]. For identifying brain regions stimulated by the drug, changes in brain activation can be detected by fluorescently labelling neurons expressing c-Fos protein and comparing c-Fos+ neuron counts between the compound-treated and control groups (showing baseline activity) [Kja+19; Sal+18; Sko+21; Han+21]. The protein product of the c-Fos gene triggers down-stream processes in nervous system and is detectable between 20 and 90 minutes post stimulation [Per+16]. Detection of protein or gene expression via fluorescently labelled antibodies can be further applied to visualize distribution of certain neuronal cell types or receptor populations [Roo+19; Gab+20; Guo+19]. Through co-localization analysis of compounds, brain activity, cell types and receptor distribution it is possible to gain detailed insight into exposure, target engagement and efficacy of a given drug.

Furthermore, the high resolution of LSFM can be used to investigate changes in vasculature, neuronal projections or pathologies in disease and therapy. Vascular labelling can be used to study vascularization of tumor bearing brains and response of vascular branching to different treatments [Bre+16]. Labelling of neuronal processes provides an opportunity to compare structural connectivities of a healthy brain to a brain affected by stroke or a neurodegenerative disease [Gou+19]. Effect of a drug to Alzheimer's or Parkinson's disease can be revealed by detecting and counting pathological formations in the brain such as beta-amyloid plaques or α-synuclein accumulations before and after treatment [Lie+16; Hob+20].

Contrary to LSFM, MRI and PET enable non-invasive imaging *in vivo*, and are therefore applicable for both preclinical as well as clinical studies. Biodistribution studies with PET involve labelling of the compound with a positron-emitting radiotracer and measuring its concentration-time course in brain tissue. Biodistribution studies allow assessment of blood-brain-barrier penetrance, accumulation in desired and undesired brain areas, amount of free (available for target binding), and non-specificly bound entities of the drug [GR17]. PET studies of target occupancy require development of target-binding radioligands which are then engaged in competition experiments with the unlabelled drug. Target occupation experiments conducted over a range of different drug doses provide evidence on biodistribution,

affinity of the drug to the target, and potential drug dose for maximizing efficacy [MJ04]. Furthermore, PET allows visualization of pharmacodynamic processes in response to drug administration such as brain activity, metabolism, neurotransmission, neuroinflammation (i.e., microglial activation), and pathologic protein depositions (e.g., beta-amyloid plaques and tau) via variety of radioligands [GR17; MJ04].

However, PET comes with certain limitations related to radioactive load, image resolution, uni-channel approach (only one tracer can be imaged at once), lack of structural information, and shortage of radioligands due to difficult production process [LJ00]. Several of these limitations can be compensated with MRI. Combination of PET and structural MRI enables identification of brain areas in which radiotracer signal is observed. Furthermore, structural MRI biomarkers reflecting pathology of a disease, can be used as a measure of drug efficacy. Simultaneous imaging of biodistribution and brain activity via PET and functional MRI, respectively, allows to reveal dynamic relationship between drug-target interactions and stimulated processes in the brain [MJ04]. Functional MRI measurements in combination with drug administrations have been termed pharmacological MRI and can also be carried out independently of PET [LJ00]. Pharmacological MRI relies on longitudinal measurements of brain activity upon pharmacological stimulus and may involve different competition studies as well as cognitive tasks [Jen12]).

In this PhD project, LSFM-imaging in combination with fluorescent labelling of c-Fos expressing cells was applied to reveal commonalities and discrepancies in neuronal activity patterns of different body weight-lowering compounds.

2.4 Brain atlases

Brain atlases are essential tools in neuroscience and are used to localize signals measured in imaging experiments and for navigating the brain during surgeries. Main components of an atlas include a brain template, region delineations and a coordinate system. Brain templates are based on modality-specific structural images of an individual or population-averaged brain. Population-averaged brain templates represent the mean morphology of the species more precisely than a template based on an individual brain, as the chosen animal may be an outlier [Kov+05]. Region delineations parcellate the brain into subvolumes derived from the cellular, biochemical or physical information of the tissue. Region delineations are drawn manually by experts and collected into one annotation map. While region delineations allow

coarse navigation through the brain, subregional accuracy can be achieved with fine-gridded coordinate systems. Surgical, so-called stereotaxic coordinate systems are cartesian coordinate spaces with an origin either on the brain or skull surface [FP97; Xia07; Cha+07]. Reference points, one for origin and at least one for determining the angle of the brain, are derived based on structural landmarks, which show consistent locations across individuals of the same species. Stereotaxic coordinate systems rely on skull landmarks called bregma and lambda, as they are visually detectable on top of the skull and do not require removal of the skull plate or imaging for identification.

Many mouse brain atlases exist, for both 2D and 3D imaging modalities, however only few of them contain brain templates from several modalities [Joh+10; Mac+04; Pat18]. This is because atlases are commonly used to interpret data collected with the same modality as the atlas template. In order to provide sufficient structural information for navigation, atlases may contain multiple templates based on different staining, molecular labelling or signal induction techniques available for the imaging modality. For example, templates of 2D histological atlases visualize cytoarchitecture by cresyl violet (Nissl) or acetylcholinesterase staining and myeloarchitecture by myelin basic protein immunolabelling [FP97; Don08]. MRI atlases include brain templates exhibiting different signal weightings and parameters derived from diffusion measurements as they distinguish between topological characteristics of the brain tissue in different manner [Joh+10; Agg+09; Chu+11]. Brain templates of fluorescence microscopy atlases rely solely on tissue autofluorescence collected in red wavelengths [Wan+20b].

Region boundaries of the atlases are derived from inter-tissue contrast visible in brain templates. Histological atlas templates exhibit cellular resolution and allow better divisions of the brain than MRI templates. Fine-scale structural differences in the brain tissue can be incorporated to region delineations by collecting additional information from transgenic mouse models, immunohistochemical labelling, viral tracing and in situ hybridization experiments [Wan+20b]. As region delineations are derived from modality specific-information and the definition of the borders is relatively subjective, boundaries of brain regions can vary between different brain atlases [Cho+19].

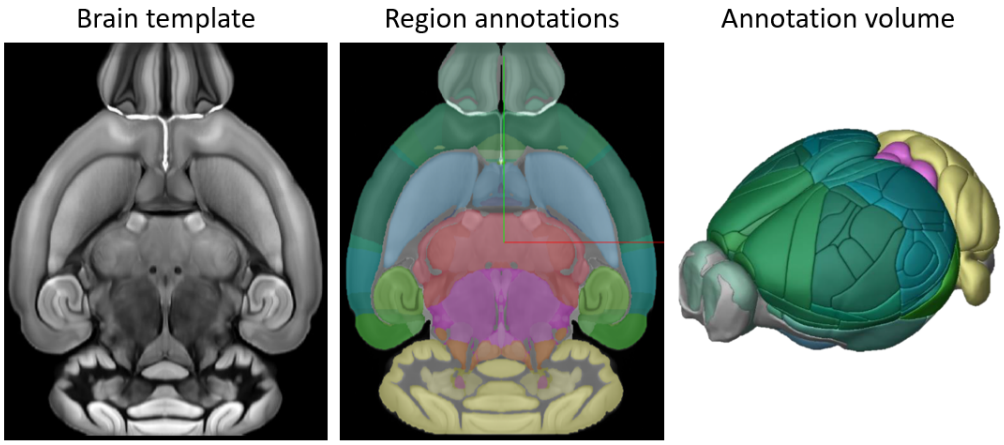

Figure 2.5: Brain template and annotation volume of AIBS CCFv3. Brain template (left) is based on tissue autofluorescence and shown in horizontal slice view. Region delineations are shown both in horizontal view (middle) and in volumetric format (right). Adapted from [All17].

The most well known and used histological atlases for mice include the Mouse Brain in Stereotaxic Coordinates by Franklin and Paxinos (FP MBSC)[FP97], and the Mouse Brain Common Coordinate Framework by Allen Institute of Brain Science (AIBS CCF) [Wan+20b; Don08]. Both the FP MBSC and AIBS CCF version 1 are based on 2D histological sections of one representative mouse brain and provide users with a stereotaxic coordinate system. Coordinate systems of both atlases are derived from bregma and lambda landmarks which are extrapolated from positions of needles inserted through the skull before extracting the brains for sectioning. In contrast to the AIBS CCF version 1 and FP MBSC, the latest AIBS CCF, version 3 (AIBS CCFv3), relies on population-average 3D mouse brain volume constructed from serial two-photon tomography (STPT) imaged mouse brains (Figure 2.5) [Wan+20b]. They have become standard atlases in the histological field due to their detailed region delineations - AIBS CCFv3 includes over 600 and FP MBSC over 800 brain regions. The AIBS CCFv3 is especially valued for its high-resolution (isotropic 10 μm and 25 μm) volumetric template, which allows mapping of datasets acquired with different 3D imaging modalities and connection to comprehensive AIBS' databases such as gene expression [Lei+07] and tract tracing experiments [Kua+15; Oh+14].

Also several MRI atlases have been established for mouse brains [Agg+09; BAJ07; Cha+07; Chu+11; Kov+05; Ma+05; Ma+08; Dor+08]. Resolution of brain templates provided by the MRI atlases range from 21.5 μm to 100 μm and number of region delineations from 9 to 62 structures, showing that the AIBS CCFv3 is clearly superior to MRI atlases in terms of resolution and number of delineated brain re-

gions. However, MRI atlas templates are almost exclusively generated from *in situ* (i.e., in-skull) imaged brains mimicking *in vivo* situation more closely than brain templates of histological atlases based on extracted mouse brains. Furthermore, CT-imaging of the same skulls enables identification of reference landmarks and generation of a stereotaxic coordinate system for MRI atlases [Agg+09; Cha+07; Xia07].

Until now, the AIBS CCFv3 template has been used as a standard brain for aligning and analyzing LSFM-imaged brain samples [Ren+16; Gou+19; Für+18]. However, LSFM-imaged samples differ morphologically from the AIBS CCFv3 template as well as *in vivo*/*in situ* brains due to the sample processing protocol causing the tissue to deform inhomogeneously depending on the used tissue clearing technique (e.g., iDISCO shrinks whereas CLARITY and CUBIC expand the tissue [Wan+18; TYL21]). Therefore, accurate definition of regional borders has been erroneous for some brain regions and identification of spatial locations in *in vivo* brain difficult for signals observed in LSFM-imaged brains. In order to mediate precise mapping of LSFM-imaged brains, deformations need to be unfolded by finding an optimal alignment strategy to the AIBS CCFv3 and establishing a link to *in vivo* coordinates through a skull-derived stereotaxic coordinate system. Murakami and colleagues have already shown that dedicated alignment strategies with the AIBS CCFv3 allow creation of atlases with an LSFM-based template and accurate region delineations for mapping LSFM-imaged CUBIC-X processed brains [Mur+18].

2.5 Image processing

3D imaging modalities may generate hundreds of gigabytes of data per study and require therefore computational algorithms to process, analyze, and integrate information in image volumes. The current chapter introduces image processing concepts relevant for multimodal atlas creation and analysis of neuronal activity datasets collected with LSFM. The first section focuses on alignment of intra- and inter-modal 3D image volumes. The second section describes detection of activated neurons. And the final, third section visits statistical analysis strategies used to evaluate registration accuracy and compare LSFM-imaged activity patterns of control and drug-treated groups.

2.5.1 Image registration

Acquisition of images takes place in specimen's native space $\Sigma \subset \mathbb{R}^3$ - every specimen is oriented in a certain direction in 3-dimensional space and exhibit unique morphology. Image registration is a procedure for aligning images of two specimen (or of the same specimen acquired under different circumstances) into one common space by matching orientations and structural features of the images voxel-by-voxel. During registration, the reference image $\mathcal{F}(\mathbf{x})$ is kept fixed and the moving image $\mathcal{M}(x)$ is transformed into the space of the reference image ($\mathbf{x}$ denotes voxel coordinates of an image). Formally, voxels are displaced by $\mathbf{d(x)}$ during transformation $\mathbf{T(x)} = \mathbf{x} + \mathbf{d(x)}$ yielding the spatial mapping of two images $\mathbf{T} : \Sigma_{\mathcal{F}} \subset \mathbb{R}^3 \rightarrow \Sigma_{\mathcal{M}} \subset \mathbb{R}^3$ (note that mathematically transformation is defined from fixed to moving image to ensure that all voxels in a fixed imaged will be mapped to and holes will not occur in the final registered image).

Mapping of one image to another can be seen as an optimization problem where a cost function is to be minimized [Kle+10]. The optimization algorithm requires a number of components for performing registration such as a geometrical transformation, a similarity metric, an optimization model, and a regularization parameter. The geometrical transformation defines the type of displacement applied to voxels, the similarity metric quantifies the alignment quality, and the optimization model describes the iterative strategy for minimizing differences between the two images. A regularization parameter determines the extent of deformation allowed to be applied to the moving image.

There exist several types of geometrical transformations including rigid, affine and B-spline (i.e., basic spline) transformations [Wu+16]. A rigid transformation involves only translation and rotation, but an affine transformation combines anisotropic scaling and skewing with a rigid transformation. While rigid and affine transformations perform global, linear displacements of voxels, a B-spline transformations introduce local, non-linear deformations to the image. For B-spline transformations, a regular grid, with defined number of control points and spacing between the points, is superimposed on the fixed image. During registration process, the grid is deformed via local displacements of control points based on a multi-dimensional cubic B-spline polynomial while the control points act as parameters in the B-spline model. Generally, the rigid transformation is used to align images of the same specimen collected with the same imaging modality, the affine transformation to align images of the same specimen acquired with different modalities, and the affine to-

gether with B-spline transformation to align images of different specimen.

For evaluating registration accuracy, a suitable similarity measure needs be chosen depending on the modality and protocol used to acquire the moving and fixed image. Similarity metrics which perform sufficiently well for images showing similar intensity distributions (i.e., obtained with exactly the same modality and protocol) are mean squared difference and normalized correlation coefficient. However, for aligning moving and fixed images acquired with different imaging modalities, a more sophisticated measure needs to be applied. In this case, the mutual information metric can be used which quantifies how well intensities in one image have been matched with the intensities in the other image (in other words intensity correspondence) [KMG12]. Mathematically, the mutual information measures entropy (i.e., dispersion) of the 2D joint histogram describing probability distribution functions of the image pair.

The optimization algorithm aims to minimize a cost function containing a dissimilarity (negative similarity) measure and a regularization term. Both dissimilarity and regularization terms are accompanied by coefficients describing the weight of dissimilarity against regularity. The regularization term is usually penalizing large deformations, gradients or curvature, and is therefore often based on first or second order spatial derivatives of the transformation. Minimization of the cost function is performed in an iterative manner by applying initial transformation parameters, calculating a cost function, and updating the optimization model to receive new transformation parameters. The process will be repeated until an optimum of cost function or another stopping criterion (e.g., decrease in cost function, change of parameter vector, number of iterations) is reached [Kle+10].

In this PhD project, the mutual information metric was used for both intra- and inter-modality registrations. Generally, multi-resolution affine and B-spline registrations were performed at four increasing resolution levels. An exception was the mapping of CT-imaged skulls with MRI-imaged brains of the same animals which was performed via uni-resolution rigid and multi-resolution affine transformations. A standard gradient descent approach was utilized as an optimization strategy and further registration parameters (e.g. a gain factor controlling the step size) were chosen based on the extent of deformation needed for alignment. Registrations were performed with Elastix software [Kle+10; Sha+14].

2.5.2 Detection of activated neurons

LSFM provides high-resolution 3D image volumes of c-Fos expressing cells (proxy for neuronal activity). The c-Fos protein is a transcription factor located in the cell nuclei and the fluorescent labelling is therefore confined into spherical shapes, enabling relatively simple algorithms to identify single activated cells. In case of cytoplasmic labelling, it is a lot more challenging distinguishing individual neurons due to their inter-connected, irregular shapes. In this PhD project, an adapted ClearMap cell detection algorithm was used [Ren+16] to compare neuronal activation between drug-treated animal groups and control animal groups.

The cell detection algorithm is visualized in Figure 2.6. The first step of the algorithm involves 2D slice-by-slice affine registration of autofluorescence and c-Fos specific channels. This is necessary due to possible channel shifts occurring during scanning, which can affect atlas registration and filtering of non-specific signals. After channel alignment, both channels undergo slice-wise background filtering by morphological opening with a disk element and subsequent intensity thresholding. The background filtered c-Fos signal is then divided by the background filtered autofluorescence to suppress the signal appearing in both channels. This signal is believed to be related to lipofuscin deposits in the tissue, and not neuronal activation [Di 15]. Next, local intensity peaks are identified in the corrected c-Fos specifc volume via a sliding maximum filter cube, and considered to be cell candidates. Cell candidates are used as input for seeded watershed segmentation, from which the final true cells can be found by filtering away too small or large cell candidates.

The parameters of the filter cube need to be adapted to the voxel size of the LSFM scan to resolve single nuclei in an optimal way. Also, parameters related to the background thresholding of autofluorescence and c-Fos specific volumes need to be fine-tuned for individual studies due to signal variance related to laser calibrations, animal batches, chemicals or slight changes in sample treatment. Parameters used for watershed segmentation depend on the size as well as density of the identifiable objects and may need to be adjusted for other marker types. The final cell segmentation volume is a binary volume where every detected cell centre (one voxel) exhibits a unit value.

There are different strategies to evaluate the detected c-Fos+ cells and compare the activation between different study groups (described in section 2.5.3), but they all involve alignment of individual specimen volumes with an atlas. In the frame-

work of this PhD project, a LSFM-based atlas with AIBS CCFv3 annotations was generated for facilitating accurate and reproducible mapping of LSFM volumes. For comparing the control and treatment group in regional level, the LSFM atlas is registered to individual cell segmentation volumes. As cell segmentation volumes do not contain structural information, autofluorescence volume of the same animal is used as a reference volume. Prior to registration, autofluorescence volumes need to be pre-processed by bias field correction, enhancing contrast, and normalizing intensity distributions. Post registration, segmented cell centres are counted within every region delineation in the atlas annotation volume. Finally, region-wise statistical analysis is conducted to reveal the effect of the treatment.

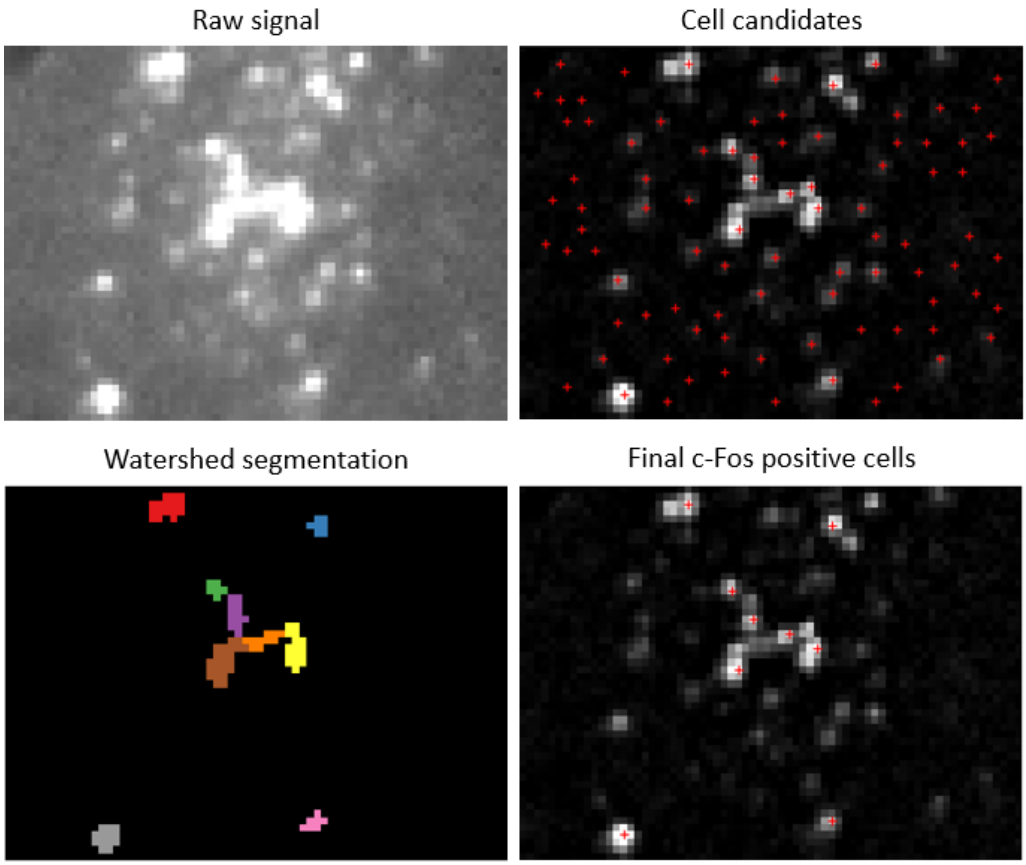

Figure 2.6: Different steps of cell detection algorithm. Left image in the upper panel shows raw signal of c-Fos specific channel. Right image in the upper panel visualizes potential c-Fos+ cell candidates (red crosses) overlaid on a background corrected c-Fos channel. Left image in the lower panel depicts watershed segmentations of true c-Fos+ cells and right image in the lower panel shows the final detected c-Fos+ cells (red crosses) on a background corrected c-Fos channel.

Another strategy allows to reveal the local, voxel-level effects of a treatment com-

pared to the control conditions. It involves mapping of individual cell segmentation volumes to the LSFM atlas via pre-processed autofluorescence volumes. To visualized increases and/or decreases in activation in response to treatment, group average heatmaps can be generated. This can be done by creating spheres of uniform value centered on detected c-Fos+ cells, while summing the values of overlapping spheres in individual heatmaps and averaging heatmaps of the animals in the same study group. By subtracting group average heatmaps from one another, up- and downregulation of c-Fos expression can be determined at voxel-level. Furthermore, heatmaps can also be utilized for conducting voxel-wise statistical analysis. In that case, atlas registered cell segmentation volumes will be smoothed by a Gaussian kernel, where an optimal kernel size can be found using a bootstrap approach [Van+18], yielding a density estimate of the activated cells.

2.5.3 Statistical analysis

During this PhD project, different statistical analysis methods were applied for comparing registration of LSFM-imaged samples with existing and developed atlases, but also for revealing the effect of pharmacological treatment on neuronal activity patterns. The current section introduces the fundamentals of hypothesis testing with Normally as well as not Normally distributed data, and multiple comparison corrections.

In statistical analysis, hypothesis testing is used to determine the likelihood of difference between populations based on a certain parameter [JT05]. It involves postulation of two statements, a so called null hypothesis and an alternate hypothesis. Null hypothesis (H_0) states that the population parameters are equal, whereas the alternate hypothesis (H_a) states that the population parameters are different. In this PhD project, the parameter which was used to compare populations was the group mean value of the measured metric and the alternate hypothesis was two-sided (i.e., mean of one population can be lower or higher than the mean of the other population). Next, an appropriate test statistic and significance level α are chosen to decide if the null hypothesis should be rejected or retained. Significance level describes probability of rejecting the null hypothesis in case it is true (type I error). It is common to choose $\alpha = 0.05$ allowing 5% possibility that difference between population parameters is found even though the opposite is true. The decision whether to reject or retain H_0 is made based on the value computed by test statistic. The value of test statistic is connected to a probability (p-value) of receiving a population mean different to another population mean, if H_0 is true. If the

probability is lower than the significance level, the null hypothesis can be rejected due to evidence for H_a. It is important to keep in mind that there is a certain probability to accept H_0 in case it is false (type II error). Type II errors can be reduced by expanding the sample size or increasing the significance level.

When multiple statistical tests are conducted simultaneously, it becomes more likely to incorrectly reject H_0. Consequently, it becomes necessary to reduce the error rate for obtaining more trustworthy results. Common methods for reducing type I error is to control either the family-wise error rate (FWER) or the false discovery rate (FDR). The Bonferroni method, which controls the FWER and does not allow any type I errors at all, creates a more stringent significance value by dividing α by the number of conducted statistical tests [Dun61]. In contrast to FWER, FDR does allow type I errors, but reduces their proportion relative to true positives. FDR can be controlled via the Benjamini-Hochberg method, which implements an adjusted p-value, called a q-value, for every test [BH95]. q-values are calculated by multiplying the rank of the p-value (when ordered in increasing order) with a percentage of allowed type I errors within H_0-rejected results and dividing by total number of tests. All conducted tests with smaller p-value than q-value are considered significant.

To compare the means of two populations, the Student's t-test can be used, while for three or more populations, analysis of variance (ANOVA) can be applied. Both approaches assume that the data follows a continuous or ordinal scale, is Normally distributed, and exhibits equal variance. However, count data, such as number of c-Fos expressing cells, is typically left-skewed and includes positive integer datapoints. For count data it is more appropriate to assume it follows a negative binomial distribution. This can be carried out using generalized linear models [MT10]. In order to model count data according to a negative binomial and compare number of activated cells per brain region between the control and drug-treated groups, generalized linear models (GLMs) were used. GLM is a generalized form of linear regression. It has three elements: a linear predictor, a probability distribution and a link. The linear predictor is a linear combination of a variable $\mathbf{x}$ and parameter b, the probability distribution describes randomness in the observable variable $\mathbf{y}$ and the link is a function connecting predictor with the probability distribution. Appropriate link function for the negative binomial distribution is the logit function and the model is called logistic regression. Both Student's t-tests and ANOVA hypothesis testing can be performed in GLM models via likelihood ratio tests, which determines how much variance in the overall dataset is described by e.g. a drug treatment effect.

However, the likelihood ratio test does not reveal the treatment groups which are the drivers of a potential significant treatment effect.

To identify the groups giving rise to the overall treatment effect, a post-hoc statistical test, Dunnett's test, needs to be performed [Dun55]. This involves calculation of Dunnett's critical value (based on the significance level, number of samples per group, and in a GLM setting, the output from the likelihood ratio test), computation of differences in means between the control and treatment groups and comparing the Dunnett's critical value to the group mean differences. In case group mean difference exceeds the Dunnett's critical value, the drug effect of the treatment group is declared significant.

Generation of digital rodent brain atlases for analyzing LSFM-imaged brains

Digital brain atlases allow mapping of brain samples into a common reference space for direct comparison and localization of measured signals. The AIBS CCFv3, a histology-based mouse brain atlas, has been the preferred reference space for aligning LSFM-imaged mouse brain samples due to its volumetric brain template, detailed brain region delineations and resources provided by AIBS [Wan+20b]. For rat brains, no volumetric histology-based atlases are available to date. Alignment of LSFM-based rat brain samples have been possible only through MRI-based atlases such as Waxholm Space (WHS) Sprague Dawley Rat Atlas [Pap+14; Ose+19; Kjo+15]. However, brain templates generated from either STPT or MRI images differ from LSFM-imaged samples not only in terms of contrast, but also morphology due to inhomogeneous deformations induced by tissue clearing media. Consequently, accuracy of mapping LSFM-imaged samples to reference space are impacted, yielding erroneous overlap of structural features of co-registered brains and region delineations in brain volumes.

Different clearing methods cause the tissue to deform in a various ways - some of them shrink (e.g. iDISCO) while others expand the tissue (e.g. CLARITY, CUBIC) [TYL21]. In recent years, registration pipelines have been developed for CLARITY-, CUBIC-, and UClear-processed LSFM-imaged mouse brains [Gou+19; Mur+18; Uma+19]. They adopt different strategies for obtaining annotations from the AIBS CCFv3 - Goubran and colleagues aligned CLARITY samples directly with the AIBS CCFv3 template, whereas Murakami and colleagues developed CUBIC-based template with annotations from the AIBS CCFv3, and Venkataraju with the

group created a brain template of UClear-cleared brains directly in the AIBS CCFv3 space. In order to facilitate analysis of iDISCO-processed rodent brain samples, this PhD project aimed to develop a framework for fast and precise co-registration and delineation of iDISCO-processed, LSFM-imaged rodent brain samples using existing volumetric brain atlases.

3.1 LSFM-based mouse brain atlas (Publication A)

The idea to create a mouse brain atlas based on a LSFM brain template emerged from the observation that direct registration of whole mouse brain volumes with the AIBS CCFv3 template worked well for some low-level brain regions (e.g., cerebrum and cerebellum), but resulted in inaccurate structural overlap for others (e.g., hindbrain and interbrain). This indicated variable effect of iDISCO treatment on brain regions and the necessity to facilitate mapping of low-level brain regions individually. The region-wise mapping strategy allowed to apply different degrees of anisotropic scaling to individual areas via affine transformation for correcting the regional shrinkage. Furthermore, a separate set of B-spline registration parameters for every area enabled to optimize the extent of non-linear deformation to fine-tune the structural overlap on a local level. By following the strategy for registering LSFM-imaged brains to the AIBS CCFv3 it became clear that the method, although accurate, is relatively laborious to use on newly acquired datasets. It required manual annotation of low-level regions in all newly imaged iDISCO-processed brains. A solution to the problem was found in a LSFM-based mouse brain atlas, which includes a brain template exhibiting an average morphology of iDISCO-processed brains and region delineations transferred from the AIBS CCFv3 via accurate region-wise mapping.

The paper "An Optimized Mouse Brain Atlas for Automated Mapping and Quantification of Neuronal Activity Using iDISCO+ and Light Sheet Fluorescence Microscopy" published in 2021 in Neuroinformatics journal (Publication A) describes the creation of a LSFM-based mouse brain atlas, demonstrates improved mapping capabilities, and exemplifies its use for whole-brain LSFM c-Fos studies. The LSFM atlas (Figure 3.1) is based on 139 C57Bl/6J iDISCO-processed mouse brain volumes of tissue autofluorescence and region delineations from the AIBS CCFv3. The atlas is symmetric and has an isotropic voxel size of $(20\ \mu\text{m})^3$. The brain template was created by applying dedicated pre-processing algorithms for normalizing

signal intensities in autofluorescence volumes followed by iterative registration and averaging scheme for generating the template of average morphology. Region delineations were transferred from the AIBS CCFv3 by registering low-level brain areas of the LSFM and AIBS CCFv3 atlas templates separately, applying obtained transformation matrices to high-level region annotations and merging annotations in the LSFM template space. The final annotation volume included 666 brain regions. The LSFM-based atlas achieved more accurate whole-brain mapping of newly acquired iDISCO-processed, LSFM-imaged brain samples than the AIBS CCFv3. The improvement in mapping was evaluated by comparing registration of LSFM-imaged samples with the LSFM and AIBS CCFv3 atlases via intensity variance, landmark distance and mapping of c-Fos expressing cells. Finally, applicational value of the atlas was exemplified in a pharmacological study where response of lean and diet-induced obese mice to body weight-lowering drug semaglutide was compared in terms of neuronal activity.

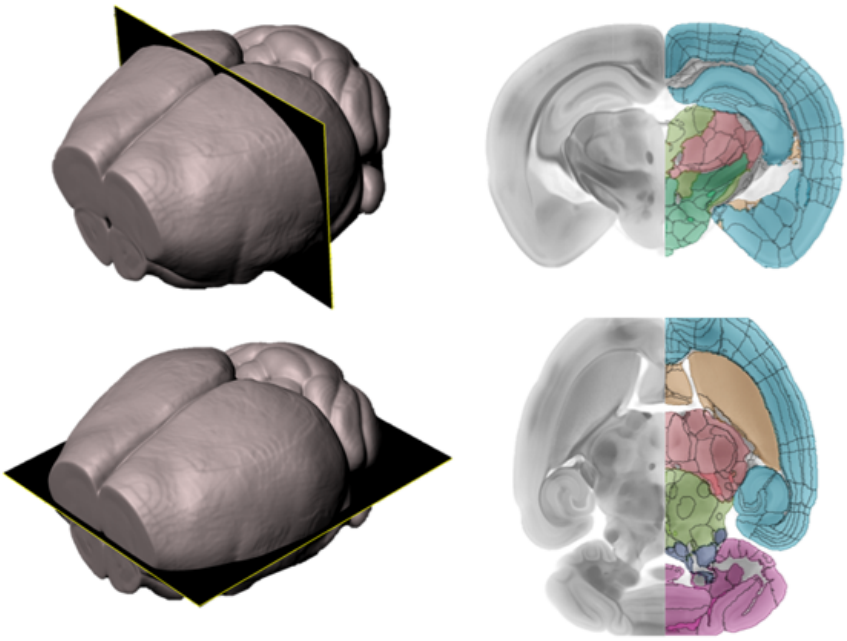

Figure 3.1: LSFM-based mouse brain atlas. Region delineations are shown as an overlay on tissue autofluorescence for a coronal (upper panel) and horizontal (lower panel) section. Left column shows positions of depicted sections in the 3D template volume.

3.2 LSFM-based rat brain atlas

Preclinical research involves also experimental studies in rats. They are often preferred to mice for conducting behavioural studies, stereotaxic surgeries or pharmacological experiments. This is related to their richer behavioural repertoire, higher degree of similarity to humans, and a larger brain compared to mice. For pursuing such experiments in combination with LSFM imaging, the work for creating a LSFM-based rat brain atlas began during the course of this PhD project.

In contrast to mice, relatively few research groups have demonstrated successful immunohistochemical labelling and clearing of intact rat brain hemispheres [Ste+16; Bra+19]. For creating a LSFM-based rat atlas, an iDISCO protocol with prolonged dehydration and clearing steps was used to clear 12-week old Sprague Dawley rat brains. To ensure proper clearing, penetration of labelling agents (few animals were treated with liraglutide to induce c-Fos expression for protocol validation, data not shown), and imaging feasibility, rat brains were halved before sample processing. The cut was made few millimetres from the midline and the bigger hemisphere was used for experiments. One brain was kept intact with the aim to use it as a reference brain, since shrinkage-mediated deformations were expected to occur near the surface where the brain was cut. After processing of brain samples according to the adapted iDISCO protocol, specimen underwent LSFM scanning in sagittal orientation and tile modus. Tissue autofluorescence was collected in red channel (excitation at 560 ± 20 nm, emission at 650 ± 25 nm).

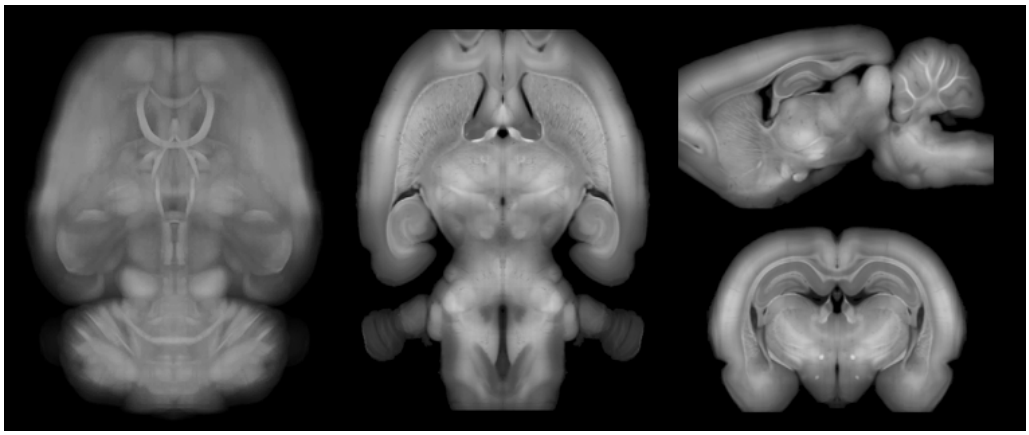

Figure 3.2: LSFM-based rat brain template. Maximum projection of the whole brain template is depicted on the left side in top view. 2D cross-sectional planes of the template are shown in horizontal (middle), sagittal (upper right) and coronal (lower right) views.

The LSFM-based rat brain template was created according to the same concept as the mouse brain template. However, an additional registration step was introduced between pre-processing and iterative averaging algorithms for removing leftover tissue from the removed hemisphere and aligning structures near the brain midline. The step involved two affine registrations of rat brain hemispheres with the reference brain (one hemisphere was discarded before registrations) and trimming of excess tissue in alternating order. The final rat brain template (Figure 3.2) was generated from 7 high-quality rat brain hemispheres with an isotropic voxel size of $(20\ \mu\text{m})^3$ and made symmetric by mirroring the existing hemisphere. Region delineations were transferred to the LSFM-based rat brain template from the WHS rat atlas via whole-brain multi-resolution affine and B-spline registration of the WHS template to the LSFM-template. Due to relatively coarse region delineations provided by the WHS Atlas, five additional brain regions were drawn manually by experts at Gubra and combined with the transferred WHS annotation volume (Figure 3.3). The final annotation volume included 169 brain regions.

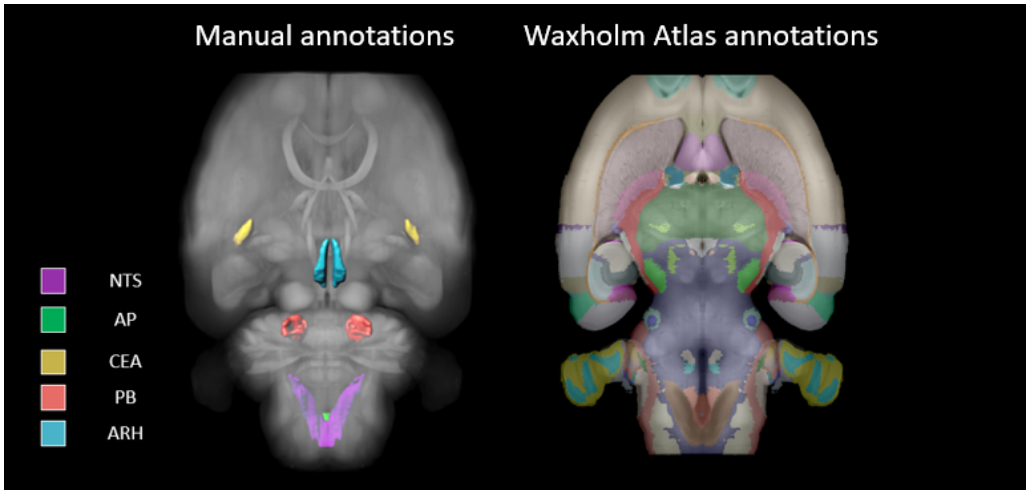

Figure 3.3: LSFM-based rat brain atlas annotations. Manually drawn atlas regions are depicted on the left side in rendered format. Full set of existing regions delineations (WHS and manually drawn region delineations) of the LSFM-based rat atlas is shown in the right image on a 2D cross-sectional plane in horizontal view. Region delineations are visualized in different colors and overlayed on grayscale tissue autofluorescence image. NTS: nucleus of the solitary tract, AP: area postrema, CEA: central amygdalar nucleus, PB: parabrachial nucleus, ARH: arcuate hypothalamic nucleus.

3.3 Discussion and future directions

The mouse and rat brain atlases presented in the previous sections are the first reported LSFM-based rodent atlases for fast and accurate mapping of iDISCO-processed brain samples. Brain templates of both atlases were generated from carefully chosen datasets containing intact samples with no cracks or missing areas and minimum amount of imaging artifacts (e.g. shadows, reflections, bias field). Generation of the brain templates was made possible through high-throughput sample processing and imaging workflow at Gubra providing large amount data with consistent quality. Both brain templates reflect the average morphology of the respective species and are not biased towards one individual brain, as iterative registration and averaging algorithm utilizes average brain volumes as reference images during alignment procedures (the first reference image is only used to establish common orientation of the brain volumes).

Limiting factors of the established atlases are related to the imaging system, characteristics of the animals, sample processing, and existing atlas resources. The size of cleared rodent brains exceeded the working distance of the Ultramicroscope II in all dimensions. This implied that whole brain volumes could not be captured at once and dedicated imaging strategies needed to be introduced to create whole brain templates for rodent brains. Two different strategies were used to create the mouse and rat brain templates. For the mouse brain template, the samples were imaged twice in horizontal view by flipping brains in dorsal-ventral axis. Subsequently, dorsal and ventral volumes were averaged, merged to a whole brain volume and the final template was created by mirroring one of the hemispheres. For the rat brain template, the samples were halved at the midline and one hemisphere of every brain was imaged in sagittal view. Post averaging, the whole brain volume was reconstructed by mirroring the existing hemisphere. Both strategies may introduce image artifacts - strategy used for the mouse brain template results in less distinct structural features in the area of volume overlap, whereas strategy used for the rat brain template may cause slight distortions of structural features near the midline of the brain. These artifacts can be overcome by microscope systems which have a working distance over 1 cm and enable imaging of whole rodent brains at once.

It is also important to note that the LSFM-based mouse and rat atlases are suitable for mapping lean, young adult animals of the same species. However, age, strain, disease (e.g., a neurodegenrative disease), and changes in the tissue processing protocol may affect structural features of the brain as well as intensity distribution of

LSFM-imaged brain volumes. At Gubra, we have observed changes in tissue morphology and intensity in case of old and obese animals, but also when using different fixatives or clearing protocols. Therefore, it is advisable to monitor registration accuracy when experiment involves animals with different characteristics than the ones used to create the brain templates. Poor registration accuracy indicates the need for a separate brain template and a dedicated registration pipeline for obtaining region delineations from established brain atlases.

In September 2021, another LSFM-based mouse brain atlas, named Princeton Mouse Brain Atlas (PMA), was published by Pisano and colleagues [Pis+21]. The atlas template is based on 110 iDISCO-processed, LSFM-imaged mouse brains and has a voxel size of $(20\ \mu\text{m})^3$. The atlas generation process resembles the pipeline used to develop the mouse brain atlas presented here. However, there are two essential differences between the two atlases. First, Pisano and colleagues registered 109 brains to one reference brain using single iteration and computed voxel-wise median of aligned brain samples. Secondly, region delineations from the AIBS CCFv3 were mapped directly into the PMA template space via whole-brain affine and B-spline registrations. These techniques fail to account for variability in mouse brain morphology and do not ensure accurate delineation in hindbrain and interbrain areas. In contrast to mouse brain atlas presented in this thesis, the PMA includes region delineations for cerebellar regions missing in the AIBS CCFv3 annotation volume.

The current LSFM-based brain atlases include region delineations from the AIBS CCFv3 and WHS Atlas. Recently, improved region delineations have been published for mouse and rat brains. Chon and collagues have combined annotations from the AIBS CCFv3 and FP MBSC while the WHS Atlas have been extended to 222 brain regions in 2021 [Hum21; Cho+19]. In order to update region delineations of the developed LSFM-atlases, annotation volumes provided by Chon et al., the PMA, and the WHS Atlas version 4 could be transferred to the LSFM-based brain templates in the future. For achieving a more accurate overlap of region delineations with morphology of the LSFM-based rat brain template, region-wise registration approach as used for the generation of the LSFM-based mouse brain atlas or a Large Deformation Diffeomorphic Metric Mapping approach [Bra+19] should be implemented to transfer region delineations to the LSFM-based rat brain template. Finally, annotation volumes of both LSFM-based rodent brain atlases would greatly benefit from smoothing of regional boundaries in 3D for correcting incorrectly assigned labels at the borders of the annotation volumes [You+21].

Bridging *in vivo* and *ex vivo* neuroimaging modalities

No neuroimaging modality alone is capable of providing all information measured by individual techniques. The gap is especially big between longitudinal *in vivo* and high-resolution *ex vivo* imaging techniques. Brain atlases are not only an excellent strategy for integrating datasets, but also for facilitating inter-modality sharing of information accessible to unique modalities (e.g., such as skull landmarks for CT or individual tract-tracing in 3D histology) and regional divisions based on different contrast mechanisms or conventions. Furthermore, atlases are expandable platforms allowing introduction of new brain templates and can provide access to existing modality-specific databases including but not limited to the AIBS' connectivity atlas and gene expression database [Kua+15; Lei+07; Oh+14]; Blue Brain's cellular, molecular and connectivity atlas [Erö+18; Shi+21; Rei+19]; ViBrism's gene expression database [Mor+19] and The Mouse Connectome Project [Zin+14]. Motivated by the same perspective on integrated atlases, combination of *ex vivo* 2D histology and *in situ* 3D MRI has previously been performed by Johnson, MacKenzie-Graham, Patel and their colleagues [Joh+10; Mac+04; Pat18] while bridging of different 3D imaging modalities has been demonstrated by Goubran, Stolp, Murakami, Salinas and colleagues [Gou+19; Sto+18; Mur+18; Sal+18].

4.1 Multimodal mouse brain atlas framework (Manuscript B)

To date, no standard stereotaxic atlas and pipeline exist for integrating 3D histology and MRI datasets. Although few stereotaxic atlases are available for mouse brains [Agg+09; Don08; FP97], they are either based on 2D histological sections and/or manually identified skull landmarks, making their accuracy suboptimal. To

address this gap in neuroscience research, the PhD project aimed to create a digital mouse brain atlas framework for bridging *in situ* MRI, *ex vivo* LSFM and the AIBS CCFv3. The results of this work were summarized in the manuscript "Multimodal 3D mouse brain atlas framework with skull-derived coordinate system" (Manuscript B, in preparation). The atlas framework connects three modality-specific template spaces and provides users with a stereotaxic coordinate system as well as region delineations from the AIBS CCFv3 in every template space (Figure 4.1). All atlas volumes exhibit a consistent and isotropic voxel size of $(25\ \mu\text{m})^3$. Brain template and diffusion parameter maps available in MRI space are averaged from 12 structural and diffusion MRI datasets and include the following contrasts: T2-weighting, fractional anistropy, axial diffusivity, radial diffusivity, and apparent diffusion coefficient. Two further spaces are defined by the STPT-based and LSFM-based brain templates from the AIBS CCFv3 and LSFM mouse brain atlases, respectively. The brain templates are provided in their modality-specific spaces together with the deformation fields, which can be used for transferring datasets between the spaces. The strategy of modality-specific spaces was adopted due to strong morphological differences between the templates (especially MRI and LSFM). Brain templates should be applicable for fast and accurate whole-brain registration of newly acquired datasets. If all brain templates would have been brought into one common reference space, region-wise registration would be necessary for every newly acquired dataset.

The stereotaxic coordinate system provided with the framework was generated from CT-imaged skulls of the mouse brains included in the MRI-based brain template. For this, CT skull volumes were aligned with their respective MRI brain volumes, bregma and lambda landmarks were extracted from skull sutures in a semi-automatic manner and transferred to the MRI template space. In the MRI template space, landmark coordinates of individual animals were averaged. Average positions for bregma and lambda were used to orient the MRI template to the flat-skull position conventionally used in stereotaxic surgeries. In this orientation, a coordinate system was generated with the origin at average bregma and grid spacing equal to 25 μm. The stereotaxic coordinate system was transferred from the MRI template space to other two template spaces by affine and B-spline transformations followed by reconstruction in 3D. The final orientation of the STPT- and LSFM-based templates was realized by rotating the templates until similar y-coordinates (y-dimension corresponds to anterior-posterior axis) were found at the same coronal section.

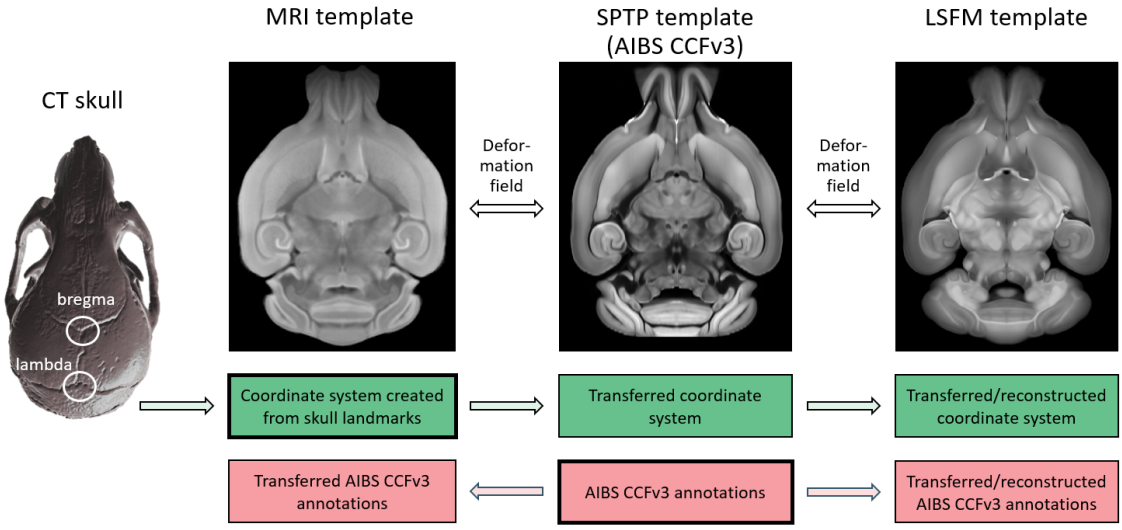

Figure 4.1: Multimodal mouse brain atlas. The top panel visualizes the three main brain templates of the atlas. The second and third panel describe the transfer of the stereotaxic coordinate system and region delineations from the AIBS CCFv3 to other template spaces. The MRI and LSFM templates were generated during this PhD project while the STPT template was adopted from the AIBS CCFv3.

The atlas framework was validated for mapping accuracy and coordinate consistency. For validating mapping between the three template spaces, a random LSFM brain volume was registered to the LSFM template and transferred to the AIBS CCFv3 and MRI template spaces via deformation fields. A similar process was repeated for a random MRI brain volume in opposing direction. Registration accuracy was validated visually using the checkerboard approach. Coordinate consistency was also investigated visually by comparing if the same x-, y- and z-coordinates pinpoint identical anatomical structures in all template spaces. According to visual inspection, cross-modal registrations result in satisfying structural overlap and the stereotaxic coordinates mark identical anatomical structures in all template spaces.

4.2 *In vivo* validation of the stereotaxic coordinate system

For validating, if coordinates of the multimodal atlas framework allow precise targeting of brain structures in stereotaxic surgeries, a mock intracranial injection experiment was performed. The injection accuracy was evaluated using LSFM. The experiment was designed such that the coordinate accuracy of the multimodal atlas could be compared to the coordinate accuracy of the FP MBSC atlas, which is conventionally used to determine coordinates for stereotaxic surgeries. The study

involved one young adult (7-weeks old) C57Bl/6J mouse who was intracranially injected to substantia nigra (SN) of both hemispheres at the same flat-skull position. Injection of the left hemisphere targeted the SN coordinate of the multimodal atlas and injection of the right hemisphere the SN coordinate of the FP MBSC atlas (coordinates are listed in Table 4.1 and visualized in the upper panel of Figure 4.2). Coordinates determined for the SN in both atlas spaces pinpoint the same anatomical site as closely as possible. To be able to see the needle path, 1 μl of fluorescent microbeads (0.02 μm FluoSpheres™, Thermo Fisher Scientific, Massachusetts, United States) was injected into the SN of both hemispheres. Subsequently, the brain was intracardially perfused with NBF, dissected from the skull, and cleared according to the iDISCO protocol. LSFM scans of the cleared brain were acquired in tissue autofluorescence (excitation at 500 ± 20 nm, emission at 545 ± 40 nm) and microbead (excitation at 630 ± 30 nm, emission at 680 ± 30 nm) specific channels.

Atlas	x-coordinate [mm]	y-coordinate [mm]	z-coordinate [mm]
multimodal atlas	2.0	-2.5	4.5
FP MBSC atlas	1.9	-2.8	4.1

Table 4.1: Coordinates of a target site in substantia nigra for performing intracranial stereotaxic injections. Left hemisphere was injected to the coordinate defined by the multimodal atlas and right hemisphere to the coordinate defined by the FP MBSC atlas. x-coordinate determines the position at the lateral-medial axis, y-coordinate the position at the anterior-posterior axis, and the z-coordinate the position at the dorsal-ventral axis.

Brain volumes obtained by LSFM were registered to the LSFM template space of the multimodal atlas. Investigation of the microbead specific channel allowed to determine needle paths in both hemispheres and the final injection sites (lower panel of Figure 4.2). Needle paths revealed that the injection targeting the multimodal atlas coordinate, hit the SN at the correct site, whereas injection targeting the FP MBSC atlas coordinate hit a nucleus dorsal to the SN. Additionally, injection targeting the FP MBSC atlas coordinate was located posterior to the injection targeting the multimodal atlas coordinate. The difference between the injection sites was compared quantitatively by recording the coordinates of the sites hit by the needle tip (Table 4.2) in the multimodal atlas space. Coordinates hit by the needle tip show that the final SN injection site differed 0.1 mm in the anterior-posterior axis from the target site defined by the multimodal atlas. Comparison of the coordinates hit by the needle tip show that the biggest difference in final injection sites was in the dorsal-ventral axis and reached 1.1 mm. A coordinate

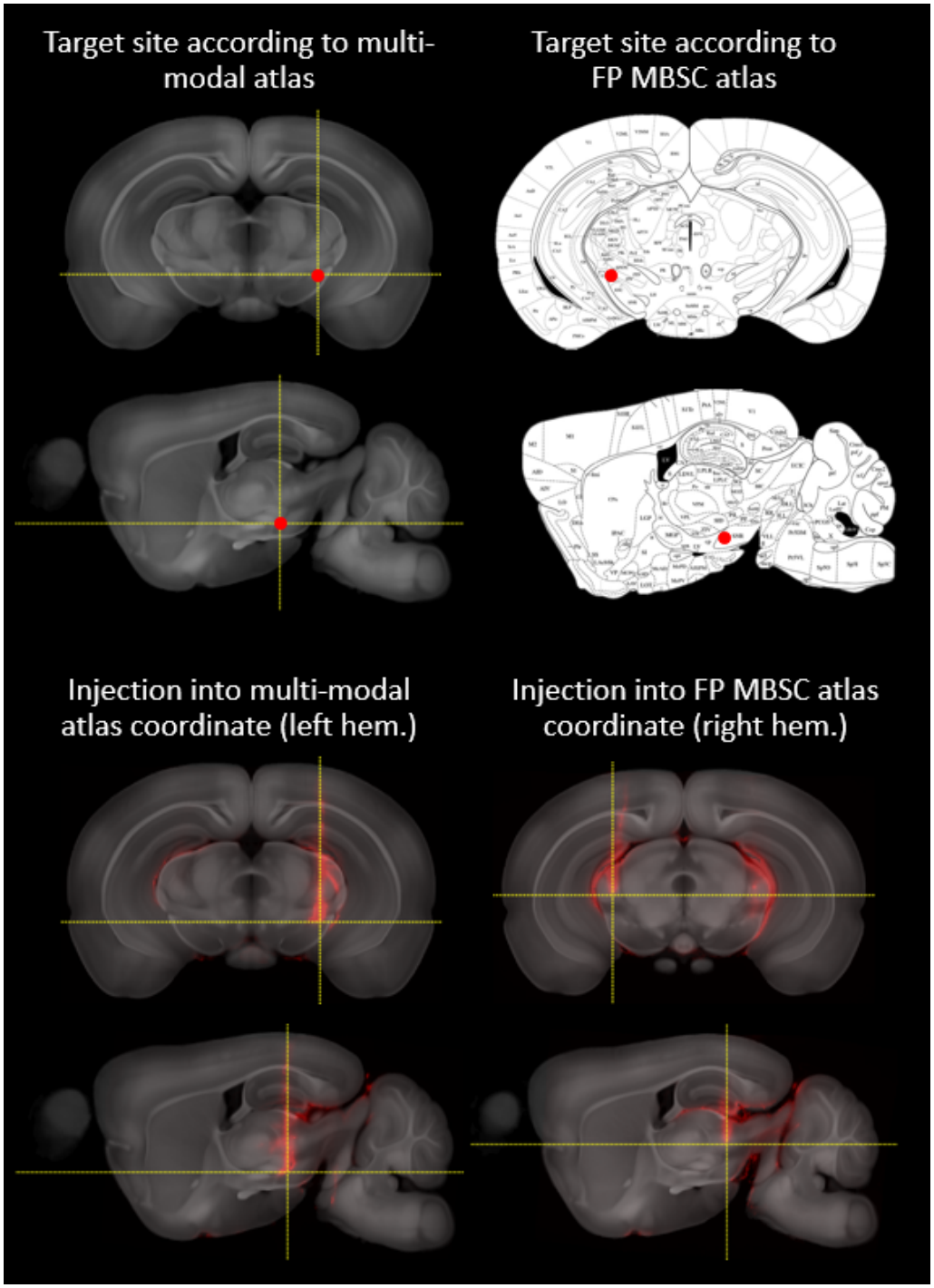

Figure 4.2: Stereotaxic injections into substantia nigra of both hemispheres for comparing coordinate accuracy of the multimodal and FP MBSC atlases. The two upper panels visualize anatomical sites (red dot) which were targeted during stereotaxic injections. The left column shows the target coordinate provided by the multimodal atlas and the right column the target coordinate provided by the FP MBSC atlas (http://labs.gaidi.ca/mouse-brain-atlas) for the same anatomical site in contra-lateral hemispheres. The two lower panels visualize the needle paths resulting from the injections (red) and final coordinates hit by the needle tip (crosshair). The left column provides injection result for the target coordinate from the multimodal atlas and the right column from the FP MBSC atlas in the LSFM template space (grayscale).

difference of 0.3 mm was recorded for the anterior-posterior axis and no coordinate difference was found for the lateral-medial axis.

Injected hemisphere	x-coordinate [mm]	y-coordinate [mm]	z-coordinate [mm]
Left hemisphere	2.0	-2.6	4.5
Right hemisphere	2.0	-2.9	3.4

Table 4.2: Coordinates hit by the needle tip during stereotaxic injections according to the multimodal atlas. Left hemisphere was injected to the coordinate defined by the multimodal atlas and right hemisphere to the coordinate defined by the FP MBSC atlas. x-coordinate determines the position at the lateral-medial axis, y-coordinate the position at the anterior-posterior axis, and the z-coordinate the position at the dorsal-ventral axis

These results may indicate that the multimodal atlas allows more precise targeting of brain structures compared to the FP MBSC atlas. However, the current mock study involved only one animal. As manual errors have a strong impact on the final injection sites, similar study should be performed with multiple animals and for several injection sites to gain statistical power for making a final conclusion on coordinate accuracy.

4.3 Discussion and future directions

The established multimodal atlas framework utilizes multiple annotated template spaces for mapping and integrating MRI and 3D histology datasets. The framework allows to overlay experimental data from *in vivo* and *ex vivo* measurements, or access data in open-access databases collected with MRI, STPT or LSFM imaging systems. Furthermore, integration of datasets in one preferred template space, enables to analyse information from one modality in relation to information provided by another modality. A standardized platform for combination of different neuroimaging techniques is an essential step for facilitating deeper understanding of information provided by modalities, biomarker validation, and synthesis of spatial and temporal data. Furthermore, it supports translation of knowledge gathered via preclinical studies to clinical settings as MRI is one of the standard techniques used to image human brain in disease and therapy. In addition to cross-modal data integration, a stereotaxic coordinate system reflecting precise *in vivo* locations of brain structures is of high value for neuroscience community. An anatomically accurate stereotaxic coordinate system available for templates of multiple modalities enables not only consistent reporting of results from neuroimaging studies, but also stereo-

taxic targeting of brain structures identified in 3D imaging experiments.

Limitations of the current framework are related to its fixed voxel size, animals used to create the templates, and available MRI templates. All brain templates provided with the atlas have a voxel size of (25 μm)^3. This voxel size was chosen due to two reasons. Firstly, a fundamental concept of the multimodal atlas was to connect templates of other imaging modalities with the original, unmodified version of the AIBS CCFv3. The AIBS CCFv3 is available in two versions, with isotropic voxel sizes of (10 μm)^3 and (25 μm)^3. As the coordinate system is defined based on the voxel size, all templates of the framework need to be sampled to equal voxel size to allow transfer of a coordinate system generated in one template space to other template spaces. Therefore, either (10 μm)^3 and (25 μm)^3 were possible voxel sizes for the multimodal atlas framework. Secondly, computer characteristics limit the performance of processing algorithms in terms of available working memory and speed. Images with voxel sizes in range (20-25 μm)^3 have typically file sizes below 1 GB and can be processed relatively fast with mid-range computers, whereas processing of images with (10 μm)^3/voxel exceed 1 GB and consequent processing takes significantly longer time. These reasons lead to the decision to use voxel size of (25 μm)^3 for the brain templates part of multimodal atlas framework.

The stereotaxic coordinate system is a 4D matrix, which assigns x-, y-, and z-coordinates (i.e., a coordinate vector) to every voxel in the template volume. x-, y-, and z- coordinates reflect the distance from the origin, the average bregma landmark, in all three dimensions. This means that a change in voxel size, changes coordinates assigned to every voxel. Although re-sampling of the coordinate system is possible in the MRI template space, re-sampling of the coordinate system in the AIBS CCFv3 and LSFM template spaces is not straight-forward as they are warped to match the anatomical features of the STPT- and LSFM-based brain templates in a non-linear way. Therefore, if re-sampling of the multimodal atlas framework is necessary to reflect a different voxel size than (25 μm)^3, the coordinate system needs to be generated in the re-sampled MRI template space and transferred to other re-sampled templates of the multimodal atlas framework via dedicated registration and reconstruction algorithms.

Brain templates of the multimodal atlas framework reflect an average anatomy of a lean young adult (8-10 weeks old) C57BL/6J mice. However, the number of brain volumes used to generate the templates, are highly variable - T2-weighted MRI template is based on 12, the LSMF template on 139 and AIBS CCFv3 template on

1675 mouse brains. At Gubra, we have previously observed that the quality of the LSFM-based template brain improves significantly when increasing the number of brain volumes included in the template from 10 to 100. The changes are especially apparent for cerebellar areas, e.g., flocculus and paraflocculus. Also, image artifacts, missing areas and edges affect the brain template based on 100 samples less than the template based on 10 samples. However, the quality of the brain templates did not improve visibly when number of brain samples included in the template was increased from 100 to 200. Although brain volumes used to generate the MRI template were acquired from brains in skull minimizing deformations occurring during dissection and processing, morphological differences were observed in cerebellar areas of the MRI-imaged brains. Therefore, the quality of the MRI brain template should be improved by increasing the number of brain samples in the averaged MRI image volumes.

The developed multimodal atlas framework provides users with brain templates generated from image volumes of NBF-fixated brains. It has been previously shown, that certain relaxation values and diffusion parameters are changed in MRI datasets acquired from fixated brains compared to MRI datasets acquired from fresh brains [Dyr+18; Sun+05; Hag+19]. Sun et al., and Haga et al., found that majority of diffusion parameters showed differences between *in vivo* and *ex vivo* measurements of the same brain samples. No differences were found for T2-weighting and fractional anisotropy values in *in vivo* and *ex vivo* brain volumes. The changes were attributed to fixative induced dehydration and temperature reduction. These results indicate that the multimodal atlas framework could be complemented with additional average diffusion parameter maps based on *in vivo* diffusion MRI measurements.

In 2009, Aggarwal and colleagues published a MRI mouse brain atlas with stereotaxic coordinates for six developmental stages [Agg+09]. Although they used bregma and lambda coordinates obtained from CT-imaged skulls to generate a stereotaxic coordinate system, their image proccessing procedure differed from the pipeline used in this PhD project. Aggarwal et al., aligned CT-skulls of individual brains such that their manually defined bregma landmarks overlapped in space, registered *in vivo* T2-weighted MRI image volumes with their respective skulls, and averaged the aligned MRI image volumes. In parallel, a T2-weighted brain template accounting for anatomical variability was produced from the same *in vivo* T2-weighted MRI image volumes using the iterative registration and averaging algorithm. Subsequently, the T2-weighted brain template and diffusion parameter maps from a high-resolution *ex vivo* dataset were registered to the average T2-weighted image volume created in

skull space. In contrast to Aggarwal and colleagues, in this PhD project bregma and lambda points were not pinpointed manually but extracted by an semi-automatic algorithm, aligned to the T2-weighted template space and averaged in the template space. Furthermore, the diffusion parameter maps provided with the multimodal atlas in T2-weighted MRI template space, reflect average diffusion characteristics of multiple animals in contrast to Aggarwal's atlas providing diffusion data for only one animal.

The multimodal brain atlas is an expandable digital resource, which can be connected to other brain templates based on other imaging modalities or tissue clearing protocols. For example, brain templates based on two widely used clearing techniques, CLARITY [Chu+13] and CUBIC [Sus+14], could be added to the framework in the future. Furthermore, users of the multimodal atlas would greatly benefit from a tractographic map which would allow investigations of structural connectivity in a mouse brain. The diffusion MRI dataset, acquired during this PhD project, could be utilized for reconstructing and aligning an average map of white matter tracts to the MRI template space. Future work could potentially also involve a platform for accessing the stereotaxic coordinate system. Currently, the coordinates are provided with the atlas in 4D matrix format which can be accessed either computationally or loaded as an additional channel in an image viewer e.g., ITK-SNAP [Yus+06]. This format is useful for image analysis but not comfortable for planning stereotaxic surgeries. Therefore, a simple application with a user interface, which allows visualization of the atlas templates and extraction of the stereotaxic coordinates for every voxel, could be developed in the future.

Evaluation of brain activity in response to drug therapy

Investigations of neuronal activity offer insight into brain areas affected by a disease or a pharmacological treatment. Traditional 2D histology has been used for decades in preclinical research to map neuronal pathways by labelling and counting c-Fos expressing cells in brain sections [Per+16]. Although 2D histology can be used to identify single c-Fos expressing cells at high magnifications, manual sectioning and cell counting limits the number of regions in which signal can be evaluated. LSFM, however, allows imaging of all c-Fos expressing cells in whole brains offering an opportunity to analyze neuronal activity in an unbiased manner and perform high-throughput screening experiments [Ren+16]. In LSFM datasets, manual counting of c-Fos cells becomes unfeasible and thus, requires automated algorithms for extracting information.

In neuronal activity studies, animals are divided into control and treatment groups for comparing the effect of a stimulus to the baseline activity. Post *in vivo* phase and LSFM imaging, automatic analysis of whole-brain samples is performed in three stages: cell detection, atlas registration and statistical analysis. There are several computational techniques to detect cells in 3D volumes [Sal+18; Ren+16; Tys+21; Kru+21; Für+18]. In this PhD project, improved version of the ClearMap pipeline [Ren+16] was used. Cell segmentation volumes are aligned with a mouse brain atlas for evaluating signals from individual brains in a common reference space, and dividing brain volumes into subvolumes according to region delineations. Here, the LSFM-based mouse brain atlas (Publication A) was used to register cell segmentation volumes without the need for manual intervention to achieve accurate alignment. The last step involving statistical analysis is commonly performed in a region-wise manner. Region-wise statistical analysis involves counting of detected

c-Fos expressing cells in every atlas-defined region and comparing the number of activated cells per region between the treatment and control group. In addition to region-wise statistical testing, this PhD project introduced a voxel-wise statistical analysis approach, which is widely used in MRI and PET image analysis [Kly+18; Whi09], for LSFM-imaged whole brain samples to reveal local treatment effects within atlas-defined regions.

5.1 Voxel-wise statistics for LSFM whole-brain samples (Publication C)

Region-wise statistical analysis of detected c-Fos expressing cells gives a global overview of brain sites where brain activity differences between the control and treatment group animals. However, c-Fos expressing cells are typically forming confined clusters, so called activity hotspots. Region-wise analysis is not able to resolve the distribution of activated cells inside the atlas-defined brain regions. Thus, it may miss simultaneous activation of distinct neuronal populations within the same brain region, or activation hotpots within larger brain areas due to extensive accumulation of baseline activity. In contrast to region-wise statistical analysis, voxel-wise statistics approach would allow to monitor distribution of c-Fos expressing cells throughout the brain and resolve origin, shape, and spread of activated cell clusters.

Until now, voxel-wise analysis has not been part of the standard analysis pipeline for evaluating distributions of activated neurons obtained with LSFM. The reason for this is the sparsity of c-Fos expressing cells at microscopic resolution - c-Fos cells do not overlap at voxel level due to biological variability between the animals. The paper "Comparative study of voxel-based statistical analysis methods for fluorescently labelled and light sheet imaged whole-brain samples" published in 2021 in peer reviewed Proceedings of IEEE 18th International Symposium on Biomedical Imaging (Publication C) identifies the optimal pipeline for voxel-based statistical analysis of 3D histological brain samples. The paper demonstrates implementation of a pre-processing algorithm on LSFM whole-brain datasets of c-Fos expression for enabling voxel-wise group comparisons, and the strength of a probabilistic threshold-free cluster enhancement (pTFCE) technique by comparing six different methods of voxel-wise statistical analysis.

The study was carried out on whole brain samples collected from vehicle and salmon calcitonin (body weight regulating hormone) treated mice. The brain samples were

stained for c-Fos expressing cells and imaged with LSFM. After detection of c-Fos+ cells and registration to the LSFM-based brain atlas, discrete cell segmentations were filtered and converted into continuous signals. Continuous signals reflecting cell densities at a voxel level were obtained by smoothing the volume with a Gaussian kernel determined via bootstrap error minimization algorithm [Van+18]. Thereafter, two-tailed Student's t-test was performed in combination with different correction methods for multiple comparisons: Bonferroni method [Dun61], Benjamini-Hochberg method [BH95], cluster size inference (CSI) [Bul+99], cluster mass inference (CMI) [Bul+99], threshold-free cluster enhancement (TFCE) [SN09] and probabilistic TFCE (pTFCE) [Spi+18]. The resulting voxel-wise p-value maps indicated that the cluster- and TFCE-based methods are able to identify and resolve the shape of drug-induced activity hotspots. It was also found that the CMI, CSI, and TFCE require careful tuning of method-related parameters to detect all activation hotpots. Due to high robustness of the pTFCE to detect activation hotspots without the need for parameter tuning and its ability to reveal signal differences within the same activation hotspots, pTFCE was identified as an optimal approach for voxel-wise analysis of LSFM-volumes labelled for specific cellular populations.

5.2 Effect of anti-obesity drugs on brain activity (Publication D)

Obesity is a major health problem affecting hundreds of millions of people world wide [Wor21] for which relatively few pharmaceutical treatments are available today. It is widely accepted, that the brain is involved in food intake and energy expenditure via complex interplay of hedonic and homeostatic mechanisms [Cle+17]. Extensive efforts in developing effective anti-obesity therapeutics have resulted in pharmaceuticals with various ways of action on central nervous system. Majority of them function by decreasing the food intake [CRG18]. However, only very few existing drug therapies promote significant weight loss while several compounds have been found to cause severe side effects [DH12].

The paper "Whole-brain activation signatures of body weight-lowering drugs" published in 2021 in Molecular Mechanism journal (Publication D) provides insight into common and unique whole-brain activity patterns of different drug classes in a comparative screening study involving six centrally acting anti-obesity drugs. The study utilized a comprehensive image analysis pipeline composed of several processing and atlas tools developed during this PhD project. The screening experiment

involved 80 mice who were divided into 4 vehicle and 6 treatment groups. Animals in treatment groups received an acute dose of one of the following compounds: lorcaserin, rimonabant, bromocriptine, sibutramine, semaglutide and setmelanotide. Mice were terminated 2 hours post dose, and dissected, iDISCO-processed brain samples were LSFM-imaged to capture the c-Fos expression in whole mouse brains. Followingly, the c-Fos expressing cells were segmented according to the improved ClearMap cell detection pipeline and registered with the LSFM-based mouse brain atlas. Comparison of the brain activity between the vehicle and drug treated groups was performed via region- and voxel-wise statistical analysis techniques. Region-wise statistical approach involved fitting of cell count data by GLMs, performing a Dunnet's test for each GLM, and correcting the results for multiple comparisons via Benjamini-Hochberg technique. Voxel-wise statistical analysis utilized the pTFCE method and the Bonferroni correction method at regional level to create voxel-wise p-value maps. Also principal component analysis was carried out on count data for visualizing similarity of brain activity patterns induced by different anti-obesity drugs.

A web-based imaging data viewer (https://g3de.gubra.dk/) based on the LSFM-atlas described in publication A, was set up for making 3D whole-brain activity data available for browsing (Figure 5.1). The results indicated that majority of anti-obesity drugs induce strong activation hotspots across the brain and exhibit distinct activity patterns depending on the drug. Region-wise statistical analysis revealed that four out of six drugs induced significant brain activity in approx. 100 atlas-defined brain areas while two showed significant activity in 55 or less regions. Largest overlap in significant activity patterns were found in subregions of the hindbrain, amygdala, hypothalamus, thalamus, and cerebral cortex. Voxel-wise statistical analysis revealed drug-dependent differences of activation patterns in the parabrachial nucleus (PB). Several distinct activated cell populations were found in the PB for setmelanotide, semaglutide and bromocriptine, whereas rimonabant activated large areas of the nucleus homogeneously. Features of the activity patterns shared between the anti-obesity drugs may pinpoint brain sites playing a key role in appetite regulation and body weight control.

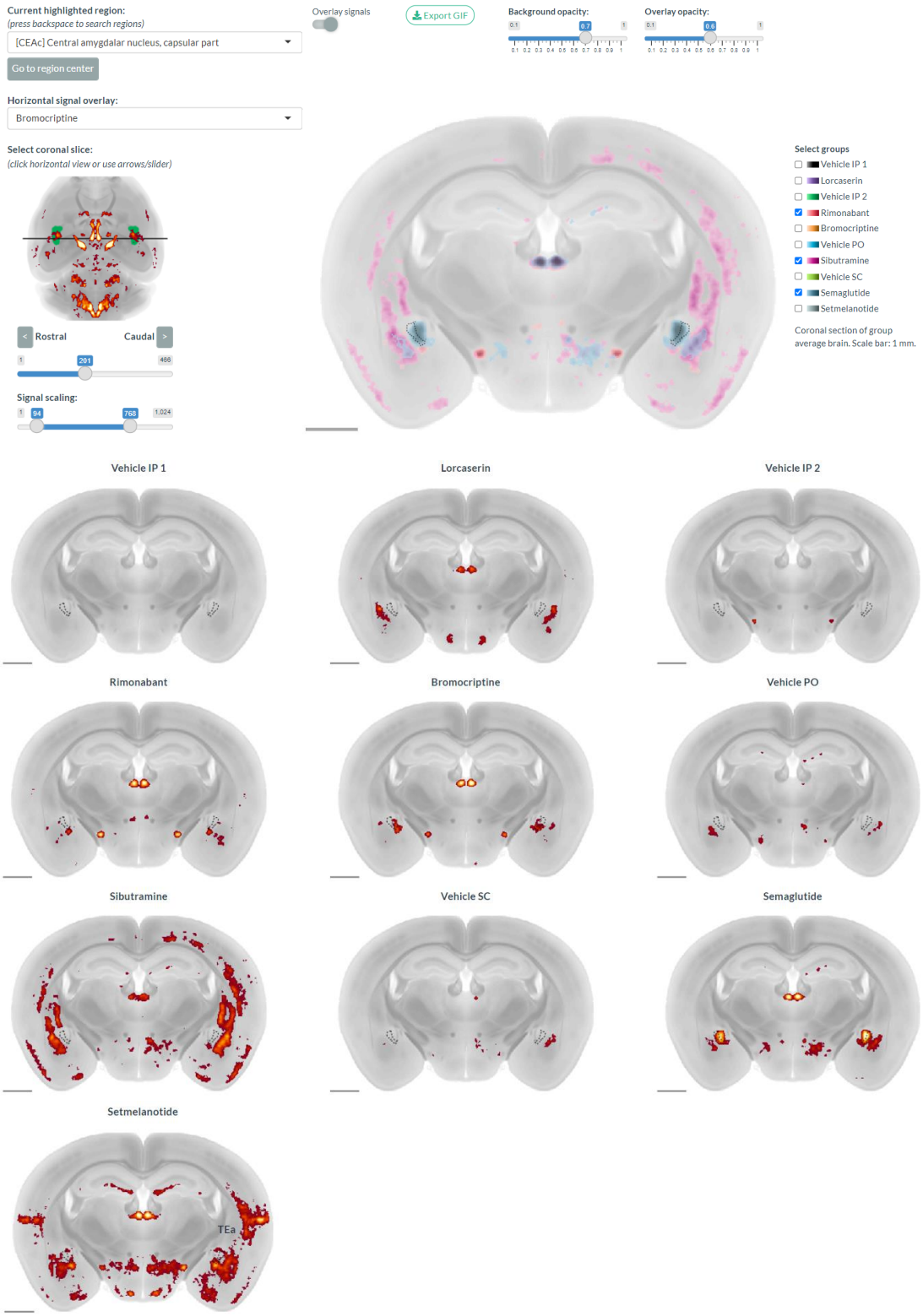

Figure 5.1: Open-access brain viewer for browsing LSFM-based whole brain datasets. The viewer allows exploration of 3D mouse brain datasets in coronal slice view and investigate signals in atlas regions of interest. It is possible to view group-average data side-by-side or as an overlay. Furthermore, the viewer allows to retrieve region-wise cell counts for all study groups and compare the results statistically.

5.3 Discussion and future directions

This PhD project improved and extended the standard ClearMap pipeline for analyzing nuclear markers in whole LSFM-imaged mouse brains. The pipeline was modified by replacing the AIBS CCFv3 atlas with the LSFM-based mouse brain atlas (Publication A), adding pre-processing steps to improve atlas registration as well as cell detection, and including an optional voxel-wise statistical analysis approach (Publication C). The pipeline is almost fully automated, requiring only adjustment of few cell detection parameters. It allows relatively fast sample processing (approx. 2.5 hours per sample) and produces consistent results, unless abnormally high autofluorescence levels complicate the analysis. The improved pipeline enabled to screen the effects of different anti-obesity pharmaceuticals for investigating neuronal network involved in appetite and body weight regulation in an unbiased manner. The improved pipeline is also applicable for studying other nuclear markers in mouse brains.

Combination of the region- and voxel-wise statistical analysis approaches offers an opportunity to obtain an overview of the treatment effect at different levels. The region-wise approach provides information on global signal distribution while the voxel-wise approach describes the exact location and topology of the hotspot. The region-wise approach is dependent on atlas-defined regions. Signals which extend several regions or lay at region boundaries, cannot be quantified accurately by the region-wise approach. Such signal hotspots could be detected by the voxel-wise statistics. The voxel-wise approach is especially useful for locating and identifying distinct cellular subpopulations. Additionally, voxel-wise p-value maps can be used to compare the degree of similarity between signal distributions induced by different treatments. However, the voxel-wise approach is limited by signal density and is highly sensitive to signal variance. Due to these reasons, the voxel-wise approach should not serve as a replacement but complement to the region-wise statistics approach.

In this work, c-Fos expressing cells were detected by monitoring and filtering local intensity maxima of the measured signal. The pipeline identifies cell candidates in ventricular areas and near the tissue surface as false positives, and discards them from statistical analysis. However, the algorithm lacks control over false positive cell candidates within the tissue, for example in blood vessels and capillaries. This problem could be addressed by utilizing deep neuronal networks (DNN) for segmenting vascular compartments and removing cell candidates within vascular segmentations.

Alternatively, DNNs could be applied directly for filtering or detecting fluorescently labelled cells [Tys+21; Kru+21]. Especially promising is the approach taken by Tyson and colleagues, where DNN is trained to identify false positive cells from the set of cell candidates detected by classical image processing techniques. This approach minimizes the number of manual annotations and computational resources required for training.

Another aspect of the pipeline, which could be improved in the future, is registration of broken or incomplete tissue. The current pipeline relies on the Elastix software [Kle+10; Sha+14] for registering samples with the brain atlas. Although, a combination of affine and B-spline registrations works well with Elastix for intact samples, the algorithm fails to map partial or damaged samples to whole brain volumes. This is related to the algorithm trying to match the outlines of fixed and moving image volumes. Branch and colleagues have proposed a solution to tackle this problem [Bra+19]. Their algorithm relies on expectation maximization algorithm for accommodating information on missing data and Large Deformation Diffeomorphic Metric Mapping approach for performing registrations. This approach could be implemented in the presented pipeline to minimize the number of discarded samples and provide an option for partial sample analysis without manual optimization of the atlas.

The setup of the LSFM screening study enabled identification of brain regions potentially involved in appetite and body weight control. The results, however, reflect only one time point in a time course of a pharmacological effect. The time course of brain activity depends on pharmacokinetic and pharmacodynamic properties of the drug but also on down-stream signaling [Jen12]. This implies that the brain activation patterns are dynamic and unique for every drug. For investigating the time course of brain activation triggered by a drug, a combined *in vivo* functional MRI and *ex vivo* LSFM study could be designed. Combination of *in vivo* and *ex vivo* 3D imaging techniques, would allow to monitor brain activation signatures over time and utilize observed dynamics to determine time points at which whole-brain c-Fos expression should be evaluated at high resolution. The established multimodal mouse brain atlas would offer an opportunity to integrate, analyse and compare the collected functional MRI and LSFM datasets.

Studies of brain activation via functional MRI or LSFM-imaging of c-Fos expression are useful for determining potential areas governing appetite and body weight regulation, but lack the information on inter-regional relationships. In order to re-

veal neuronal networks in which the brain regions operate, existence and strength of structural connectivity between the regions should be investigated. This could be done by accessing thousands of viral tract-tracing experiments in AIBS' connectivity atlas [Kua+15; Oh+14] or by reconstructing and accessing white matter tractographic maps in the multimodal mouse brain atlas framework.

Conclusion and outlook

This PhD project focused on the development of brain atlases and computational pipelines for automated analysis of whole rodent brain datasets acquired with 3D imaging modalities. The outcomes of the project include the multimodal mouse brain atlas, the LSFM-based rat brain atlas, and the pipeline for voxel-wise statistical analysis of LSFM-imaged neuronal activity datasets. Applicational value of the atlas resources was demonstrated by comparing LSFM-acquired whole-brain activation profiles of six body-weight lowering drugs in order to reveal a brain-wide network involved in appetite and body weight control.

The multimodal mouse brain atlas framework incorporates and bridges brain templates based on MRI, STPT, and LSFM in their modality-specific spaces. The MRI and LSFM brain templates were created from 12 and 139 samples, respectively, while the STPT brain template was imported from the AIBS CCFv3. The atlas provides access to a skull-derived stereotaxic coordinate system and region delineations of the AIBS CCFv3 in every template space. The atlas has an isotropic voxel size of $(25\ \mu\text{m})^3$ and includes 666 region delineations. Transfer of datasets between the template spaces is realized by deformation fields. The multimodal mouse brain atlas enables accurate co-registration, region delineation, and integration of MRI-, STPT- and LSFM-imaged whole mouse brain samples for computational analysis. Furthermore, the atlas allows users to compare or perform combined analysis of *in vivo*/*ex vivo* MRI and *ex vivo* LSFM measurements, for example to study the overlap of activated brain regions measured by functional MRI and the distribution of a certain protein or a fluorescently labelled drug captured by LSFM. It is also possible to import and overlay data from open-access databases (e.g., databases of AIBS CCFv3 providing gene expression and viral tract-tracing datasets). The stereotaxic coordinate system provided with the multimodal atlas could be used for precise reporting of observed signals or planning of stereotaxic surgeries.

The established LSFM-based rat atlas was generated from seven halved rat brain samples. Region delineation of the LSFM-based rat brain atlas were imported from the WHS rat atlas and five additional regions were drawn in manually by experts at Gubra. The atlas has an isotropic voxel size of $(20\ \mu\text{m})^3$ and includes 169 region delineations. The LSFM-based rat brain atlas allows co-registration and regional delineation of LSFM-imaged rat brain samples for computational analysis.

An optimal approach for voxel-wise statistical evaluation of LSFM-imaged neuronal activity datasets was determined by implementing and comparing six approaches for statistical testing and multiple comparisons corrections. The final pipeline of the voxel-wise statistical analysis includes the bootstrap error minimization algorithm for determining parameters for pre-processing, the pre-processing routine to convert cell segmentation volumes into cell density-like estimates, and the pTFCE approach for statistical analysis. Probabilistic TFCE was found to be a robust method for detecting significantly different signal clusters between study groups without compromising on spatial specificity. The voxel-wise statistical analysis pipeline complements the region-wise statistical analysis for characterizing measured LSFM-imaged brain activity signals at a local level. This could be useful if the experiment aims to identify certain neuronal subpopulations activated by the treatment.

The established mouse brain atlas resources and voxel-wise statistical analysis pipeline were used in a screening study where whole-brain activation signatures of six anti-obesity drugs were investigated using LSFM. The six compounds screened for activity were lorcaserin, rimonabant, bromocriptine, sibutramine, semaglutide and setmelanotide. The results from the region-wise statistical analysis indicate that anti-obesity drugs exhibit highest similarities in activation patterns in the hindbrain, amygdala, hypothalamus, thalamus and cerebral cortex. The voxel-wise statistics revealed distinct activation patterns of anti-obesity drugs in the parabrachial nucleus. These results contribute to the anti-obesity drug discovery efforts by pinpointing a list of brain regions, which could be potential target areas for future body-weight lowering compounds.

Rodent brain atlases and computational tools developed during this PhD project aim to support the neuroscience community in investigating, understanding, and developing effective therapies for CNS disorders. Therefore, atlas resources will be made available via BrainGlobe Atlas API [Cla+20] for allowing researchers to perform computational analysis of 3D rodent brain datasets. The multimodal mouse

brain atlas provides a basis for cross-modality integration and sharing of data. One example for sharing experimental whole-brain LSFM data is the 3D data viewer (https://g3de.gubra.dk/) developed by Gubra to provide access to full data packages presented in publications. Furthermore, the atlas framework can be used to access data in existing databases or to create databases by co-registering and presenting data in the most suitable template space. One such database project, NeuroPedia (https://www.neuropedia.dk/), will be kicked off by Gubra in December 2021. The project aims to catalogue brain-wide maps of anatomical features, protein expression, neuronal activity, and neuronal projections, and make them available in the LSFM template space via brain viewer allowing researchers from all over the world to explore them interactively.

Contributions

Publication A

An Optimized Mouse Brain Atlas for Automated Mapping and Quantification of Neuronal Activity Using iDISCO+ and Light Sheet Fluorescence Microscopy

Johanna Perens, Casper Gravesen Salinas, Jacob Lercke Skytte, Urmas Roostalu, Anders Bjorholm dahl, Tim B. Dyrby, Franziska Wichern, Pernille Barkholt, Niels Vrang, Jacob Jelsing, Jacob Hecksher-Sørensen

Neuroinformatics 19, 433-446, 2021

Neuroinformatics
https://doi.org/10.1007/s12021-020-09490-8

ORIGINAL ARTICLE

An Optimized Mouse Brain Atlas for Automated Mapping and Quantification of Neuronal Activity Using iDISCO+ and Light Sheet Fluorescence Microscopy

Johanna Perens[1,2] · Casper Gravesen Salinas[1] · Jacob Lercke Skytte[1] · Urmas Roostalu[1] · Anders Bjorholm Dahl[2] · Tim B. Dyrby[2,3] · Franziska Wichern[1] · Pernille Barkholt[1] · Niels Vrang[1] · Jacob Jelsing[1] · Jacob Hecksher-Sørensen[1]

Abstract

In recent years, the combination of whole-brain immunolabelling, light sheet fluorescence microscopy (LSFM) and subsequent registration of data with a common reference atlas, has enabled 3D visualization and quantification of fluorescent markers or tracers in the adult mouse brain. Today, the common coordinate framework version 3 developed by the Allen's Institute of Brain Science (AIBS CCFv3), is widely used as the standard brain atlas for registration of LSFM data. However, the AIBS CCFv3 is based on histological processing and imaging modalities different from those used for LSFM imaging and consequently, the data differ in both tissue contrast and morphology. To improve the accuracy and speed by which LSFM-imaged whole-brain data can be registered and quantified, we have created an optimized digital mouse brain atlas based on immunolabelled and solvent-cleared brains. Compared to the AIBS CCFv3 atlas, our atlas resulted in faster and more accurate mapping of neuronal activity as measured by c-Fos expression, especially in the hindbrain. We further demonstrated utility of the LSFM atlas by comparing whole-brain quantitative changes in c-Fos expression following acute administration of semaglutide in lean and diet-induced obese mice. In combination with an improved algorithm for c-Fos detection, the LSFM atlas enables unbiased and computationally efficient characterization of drug effects on whole-brain neuronal activity patterns. In conclusion, we established an optimized reference atlas for more precise mapping of fluorescent markers, including c-Fos, in mouse brains processed for LSFM.

Keywords Light sheet fluorescence microscopy · iDISCO · Tissue clearing · Brain atlas · C-Fos · Whole brain imaging

Introduction

Rodent models are important tools in preclinical drug development for central nervous system (CNS) disorders (Bobela et al. 2014; Esquerda-Canals et al. 2017; Leung and Jia 2016). A common method for characterizing central effects of potential novel therapies is to quantify expression patterns of c-Fos, a proxy for neuronal activation (Dragunow and Faull 1989).

Recent advances in immunohistochemical methods and optical clearing techniques have, together with ex vivo imaging technologies such as light sheet fluorescence microscopy (LSFM), enabled whole-organ imaging (Chung et al. 2013; Ertürk et al. 2012; Jensen et al. 2015; Kjaergaard et al. 2019; Renier et al. 2014; Rocha et al. 2019; Secher et al. 2014). As a result, it is now possible to visualize c-Fos expression at the single cell level in the intact adult mouse brain (Kjaergaard et al. 2019; Nectow et al. 2017; Renier et al. 2016).

In recent years, automated image analysis algorithms have been developed enabling 3D quantification of activated neurons and their signal intensities in the adult mouse brain (Detrez et al. 2019; Jensen et al. 2015; Liebmann et al. 2016; Nectow et al. 2017; Salinas et al. 2018; Schneeberger et al. 2019). The first step of the analysis process is to register LSFM imaging data onto a common reference brain which contains annotated brain regions. Today, the most widely used mouse brain atlas is the common coordinate framework

Electronic supplementary material The online version of this article (https://doi.org/10.1007/s12021-020-09490-8) contains supplementary material, which is available to authorized users.

✉ Jacob Hecksher-Sørensen
jhs@gubra.dk

[1] Gubra ApS, 2970 Hørsholm, Denmark

[2] Department of Applied Mathematics and Computer Science, Technical University Denmark, 2800 Kongens Lyngby, Denmark

[3] Danish Research Centre for Magnetic Resonance, Centre for Functional and Diagnostic Imaging and Research, Copenhagen University Hospital Hvidovre, 2650 Hvidovre, Denmark

Published online: 16 October 2020

version 3 (CCFv3), developed by the Allen Institute for Brain Science (AIBS) (Allen Institute for Brain Science 2011, 2015, 2017; Kuan et al. 2015; Wang et al. 2020). For quantification of fluorescent signals, registration is followed by cell detection, e.g. ClearMap, to segment and count c-Fos positive cells (Nectow et al. 2017; Renier et al. 2016) or extract voxel intensities (Salinas et al. 2018). Finally, the results can be assigned to specific regions using the anatomical reference atlases such as those provided by AIBS.

LSFM image processing pipelines have improved quantitative whole-brain 3D imaging. However, the quality of the LSFM results is highly dependent on sample processing and the imaging methods applied. Whole-organ immunolabelling requires lipid extraction to make the tissue permeable to antibodies (Kim et al. 2018) and enable deep tissue imaging (Vigouroux et al. 2017). In particular, myelin fibers which are lipid-rich (Villares et al. 2015), are more likely to be affected by lipid extraction, leading to non-uniform morphological changes within the brain. Also, various clearing medias have different chemical properties which will result in either shrinkage or expansion of brain structures (Wan et al. 2018). In contrast, the AIBS CCFv3 is based on vibratome-sectioned and two-photon microscopy imaged brains. Consequently, brains imaged with LSFM differ from the AIBS CCFv3 atlas with respect to morphology and signal intensity. This affects the registration accuracy and because the morphological changes introduced by the sample processing are tissue-dependent, some brain regions are more prone to erroneous alignment than others. As result, subsequent data analysis requires time-consuming validation and manual correction to ensure accurate quantification. This is particularly relevant in pre-clinical research where group sizes are often relatively large in order to provide better statistical power.

In our experience, the hindbrain is particularly sensitive to erroneous registration when cleared samples are mapped directly onto the AIBS CCFv3. High quality registration can be achieved using a multi-regional approach where each larger part of the brain, e.g. the hindbrain, is registered separately. However, this procedure reduces analysis speed as initial segmentation of the larger brain structures is required. We aimed to preserve both data flow and quality by generating a reference template based on iDISCO+ processed and LSFM-imaged mouse brains and aligning the AIBS CCFv3 with the template through multi-regional registration.

The LSFM atlas enables fast brain-wide inter-modality registration of other LSFM samples. To confirm accuracy and demonstrate the utility of the LSFM-based reference brain atlas, we determined the c-Fos expression signature of semaglutide, a long-acting glucagon-like peptide-1 (GLP-1) receptor agonist. The LSFM atlas enabled precise mapping of semaglutide-induced c-Fos expression in the mouse whole-brain. In addition to c-Fos imaging, application of the atlas includes also mapping other fluorescent markers imaged by LSFM.

Materials and Methods

Animals

Male C57Bl/6 J mice were obtained from Janvier Labs (Le Genest-Saint-Isle, France), and were maintained in standard housing conditions (12 h light/dark cycle and controlled temperature of 21–23 °C). Mice had ad libitum access to tap water and regular chow (Altromin 1324, Brogaarden, Hørsholm, Denmark) or high fat diet (60% fat, 21% carbohydrates, 19% protein; Ssniff Spezialdiäten GmbH, Soest, Germany). The LSFM atlas was established based on analysis of 139 brains from 8 to 10 weeks old male chow-fed mice. The pharmacology-induced neuronal activity study involved two groups of lean mice and two groups of DIO mice. All groups were aged matched (38 weeks) and consisted of $n = 6$. Lean and DIO control group animals received phosphate buffered saline with BSA, lean and DIO treatment group animals received semaglutide (Ozempic®, Novo Nordisk A/S, Bagsværd, Denmark) dose of 0.04 mg/kg. Both groups were administered subcutaneously 5 ml/kg and the animals were sacrificed 4 h post-dose. All animal procedures were conducted in compliance with internationally accepted principles for the care and use of laboratory animals and were approved by the Danish Animal Experiments Inspectorate (license #2013-15-2934-00784).

Sample Preparation for Immunohistochemistry

Animals were transcardially perfused with heparinized PBS and 40 ml of 10% neutral buffered formalin (CellPath, Newtown, UK) under Hypnorm-Dormicum (fentanyl 788 μg/kg, fluanisone 25 mg/kg and midazolam 12.5 mg/kg, subcutaneous injection) anesthesia. Brains were carefully dissected and immersion-fixed in 10% neutral buffered formalin overnight at room temperature on a horizontal shaker. Whole-brain samples were washed 3 × 30 min in PBS with shaking and dehydrated at room temperature in methanol/H_2O gradient to 100% methanol (20%, 40%, 60%, 80%, 100% methanol, each step 1 h). The brains were stored in 100% methanol (VWR International A/S, Søborg, Denmark) at 4 °C until further processing.

Whole-Brain Immunohistochemistry for Labeling of c-Fos Positive Cells and Clearing

The iDISCO+ (immunolabeling-enabled three-dimensional imaging of solvent-cleared organs) protocol was used for whole brain immunolabelling (Renier et al. 2014, 2016). Samples were washed with 100% methanol for 1 h and incubated overnight in 66% dichloromethane/33% methanol (VWR International A/S, Søborg, Denmark) at room temperature. Then, samples were washed twice in 100% methanol

for 30 min and bleached in chilled fresh 5% H_2O_2 (Acros Organics, Fisher Scientific Biotech Line A/S, Slangerup, Denmark) in methanol overnight at 4 °C. Subsequently, the samples were rehydrated in methanol/PBS series (80%, 60%, 40%, 20% methanol with 0.2% Triton X-100 (Merck, Darmstadt, Germany), each step 1 h) at room temperature, washed in PBS with 0.2% Triton X-100 twice for 1 h at room temperature and in permeabilization solution (PBS with 0.2% Triton X-100, supplemented with 20% volume of DMSO (Merck, Darmstadt, Germany) and 2.3% weight/volume glycine (Merck, Darmstact, Germany)) for 3 days at 37 °C. For c-Fos labeling, unspecific antibody binding was blocked in blocking solution (PBS, 0.2% TritonX-100, 10% DMSO/6% donkey serum (Jackson ImmunoResearch, Cambridgeshire, UK)) for 2 days at 37 °C before incubated in the primary antibody buffer (PTwH, 5% DMSO, 3% donkey serum, 0.2% of 10% NaN_3 (Merck, Darmstadt, Germany)) for 7 days at 37 °C. For visualization of c-Fos expression, rabbit anti-c-Fos antibody (1:5000, Cell Signaling Technology, Massachusetts, US, cat number #2250) was used. Following incubation with primary antibody, the brains were washed in PTwH (PBS, 0.2% Tween 20 (Merck, Darmstadt, Germany), 0.1% of 10 mg/ml heparin solution) for 1 × 10 min, 1 × 20 min, 1 × 30 min, 1 × 1 h, 1× 2 h and 1× 2 days. Subsequently, the brains were incubated in secondary antibody solution (PTwH, 3% donkey serum, 0.2% of 10% NaN_3) for 7 days at 37 °C with donkey anti rabbit Cy-5 antibody (1:1000, Jackson ImmunoResearch, Cambridgeshire, UK, cat no #711–175-152) and washed in PTwH for 1 × 10 min, 1 × 20 min, 1 × 30 min, 1 × 1 h, 1× 2 h and 1× 3 days. For clearing, the brains were dehydrated in a methanol/H2O series (20%, 40%, 60%, 80% and 100% methanol, each step 1 h) at room temperature, incubated in 66% dichloromethane/33% methanol for 3 h at room temperature with shaking and in 100% dichloromethane twice for 15 min with shaking to remove traces of methanol. Finally, the samples were transferred to dibenzyl ether (Merck, Darmstadt, Germany) and stored in closed glass vials until imaged with light sheet fluorescence microscope.

Light Sheet Fluorescence Microscopy of Labeled and Cleared Mouse Brains

All whole-brain samples were imaged in an axial orientation on a LaVision ultramicroscope II setup (Miltenyi Biotec, Bergisch Gladbach, Germany) equipped with a Zyla 4.2P-CL10 sCMOS camera (Andor Technology, Belfast, UK), SuperK EXTREME supercontinuum white-light laser EXR-15 (NKT photonics, Birkerød, Denmark) and MV PLAPO 2XC (Olympus, Tokyo, Japan) objective lens. The samples were attached to the sample holder with neutral silicone and imaged in a chamber filled with dibenzyl ether. Version 7 of the Inspector microscope controller software was used. Images were acquired at 0.63 x magnification (1.2 × total magnification) with an exposure time of 254.47 ms in a z-stack at 10 μm intervals. Acquired volumes (16-bit tiff) had an in-plane resolution of 4.8 μm and z-resolution of 3.78 μm (NA = 0.156). Horizontal focusing was captured in 9 planes with blending mode set to the centre of the image to merge the individual raw images. Data was acquired in two channels, autofluorescence and antibody-specific channel, because the former provides information on tissue structure and the latter on neuronal activity. Autofluorescence volumes were acquired at excitation wavelength of 560 ± 20 nm and emission wavelength of 650 ± 25 nm, laser power was set to 80%. Fluorescently labelled c-Fos positive cells were captured in a specific channel at excitation wavelength of 630 ± 15 nm and emission wavelength of 680 ± 15 nm, laser power was set to 100%.

Image Processing for Creating the Mouse Brain Atlas

An average LSFM mouse brain volume was created from 139 individual mouse brain autofluorescence datasets by an iterative multi-resolution image registration algorithm (Kovačević et al. 2005; Kuan et al. 2015; Umadevi Venkataraju et al. 2019). Pre-processing was initiated by down-sampling to 20 μm isotropic resolution. N3 method (Larsen et al. 2014; Sled et al. 1998; Van Leemput et al. 1999) was applied to correct intensity inhomogeneity. Subsequently, the intensity histograms of the individual volumes were normalized and, contrast adaptive histogram equalization was performed (Fig. 1a, left). For generating an average mouse brain template, a reference volume was randomly selected as a starting point. Six iterative multi-resolution registration steps – one affine and five B-spline transformations were performed for the remaining samples (Fig. 1a, middle). In the first step the brains were registered to the chosen reference brain and in subsequent steps aligned to the average of all brains from the previous step.

Due to the limit in scanning depth in the Z-dimension, which is about 6 mm for our LSFM setup, about half a millimetre of the dorsal cortex was not imaged. To produce a template with full cortex, 15 additional image stacks of cortices were acquired, pre-processed and aligned to the average mouse brain volume. Subsequently, both volumes were merged. Satisfactory axial symmetry was achieved by dividing the template brain volume into three coronal slabs with equal thickness and manually rotating them into correct position. The final template was created by mirroring one hemisphere to the opposite side and merging the hemispheres with a sigmoidal blending function for receiving a symmetric template brain (Fig. 1a, right) Additionally, a tissue mask and a ventricular mask were added to the LSFM template from the AIBS CCFv3 and manually adapted to fit the template.

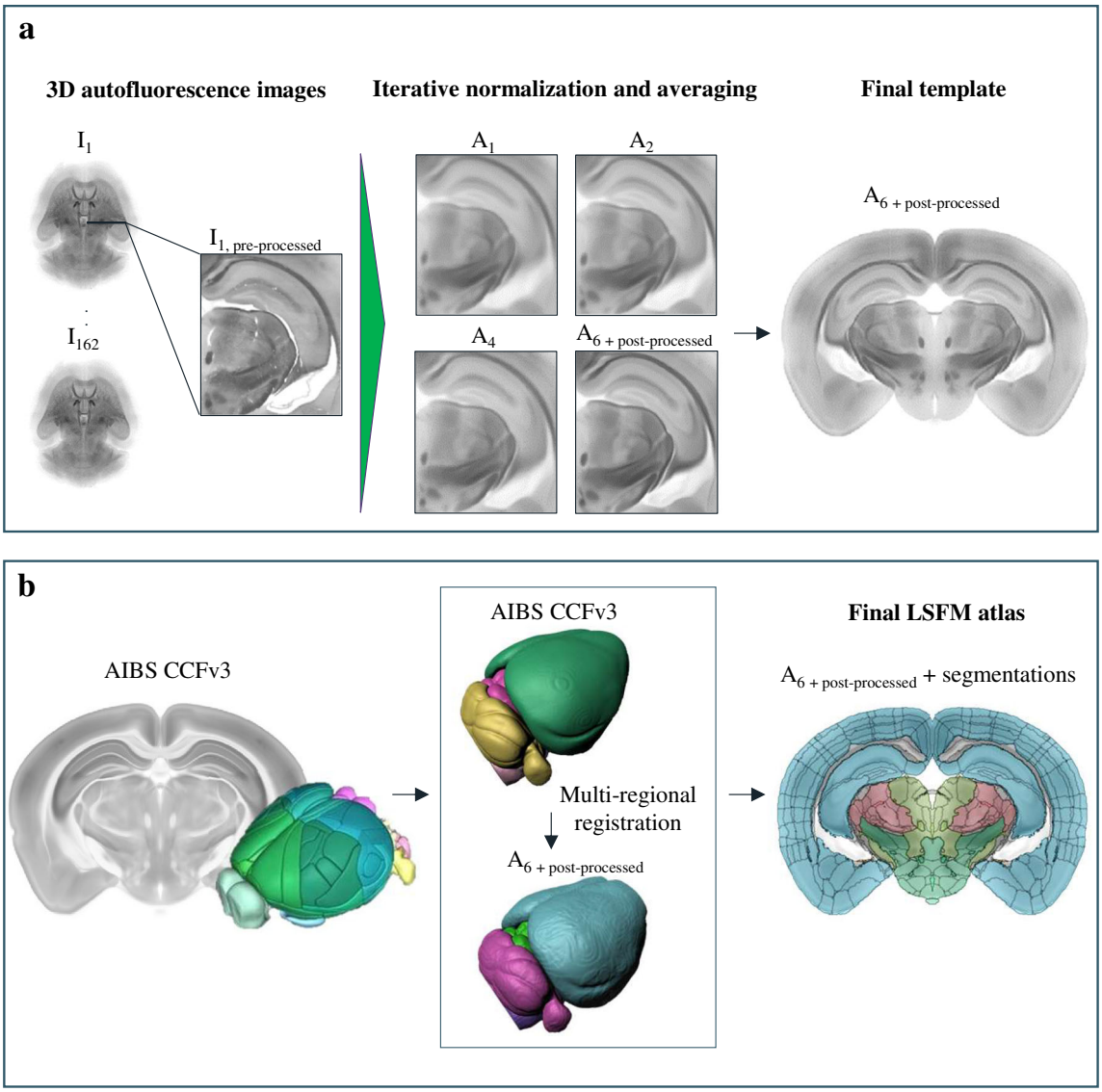

Fig. 1 LSFM-based mouse brain atlas. a) Generation of a brain template based on the LSFM autofluorescence volumes of 139 mice brains using an iterative registration and averaging algorithm. Raw light sheet scans are annotated with I_x where x stands for the animal number, and the intermediate average mouse brain volumes are annotated with A_y where y stands for the iteration step. B) Transfer of brain region segmentations from the AIBS CCFv3 to the LSFM mouse brain template. Brain regions of the AIBS CCFv3 were mapped to the LSFM template in six parts, e.g. cortex to cortex, hindbrain to hindbrain etc.

Brain regional annotations were transferred to the LSFM template from the AIBS CCFv3 (Fig. 1b) (Allen Institute for Brain Science 2011, 2015, 2017; Kuan et al. 2015; Wang et al. 2020). First, the mouse brain template of AIBS was registered onto the LSFM template using multi-resolution affine and B-spline registration. Subsequently, the registered AIBS CCFv3 template and its segmentations were divided into six parental brain regions – cerebral cortex, cerebral nuclei, hindbrain, cerebellum, septal regions and interbrain together with midbrain. The parental regions were then separately registered to the corresponding areas of the LSFM template. Manual corrections were performed for regions near to ventricular system, such as AP and SFO. Segmentation refinements were performed with microscopy image analysis software Imaris™ version 2 (Oxford instruments, Abington, UK). Image processing was performed in Python and Elastix toolbox (Klein et al. 2010; Shamonin et al. 2014) was used to implement the registrations. Detailed description of the atlas creation procedure and full sets of parameters can be found in the Online Resource 1.

Quantification of c-Fos Positive Cells

Neuronal activity was quantified by detecting and counting c-Fos positive cells using an adapted ClearMap routine (Renier

et al. 2016). In brief, the volume pairs collected from the autofluorescence and c-Fos specific channel were aligned slice-by-slice using affine registration in 2D with mattes mutual information as a similarity measure and background subtracted through morphological opening using a disk element. For removing false positive c-Fos signal originating from increased tissue autofluorescence, a signal appearing both in the autofluorescence and the c-Fos specific channel was removed from the specific channel. For identifying c-Fos positive cells, local intensity peaks were monitored by moving a filter cube over the specific channel volume followed by seeded watershed for segmenting the c-Fos positive cells. The initial parameters were taken from the original ClearMap implementation (Renier et al. 2016) but optimized to fit our data, being acquired under different conditions, including image resolution. The size of the filter cube was set to 5x5x3 pixels for effectively detecting all possible c-Fos positive cell candidates. The third dimension of the filter cube was chosen to be smaller than the first and second dimension of the cube since z-resolution of the LSFM volumes was lower than the in-plane resolution. The coordinates of the detected local intensity peaks were used as seeds in watershed segmentation with a background intensity cut-off of 800 and the resulting segmentations were filtered by removing cell segmentation regions smaller than 8 voxels and bigger than 194 voxels. Following c-Fos positive cell detection in the specific channel, the corresponding autofluorescence volumes underwent bias field correction and contrast limited adaptive histogram equalization (similar procedure as for the LSFM mouse brain template creation). For quantifying the number of c-Fos positive cells in individual brain regions, the LSFM atlas was aligned to c-Fos specific channel volumes of individual mice over preprocessed autofluorescence volumes and the number of c-Fos positive was counted in every brain region. Heatmaps visualizing the density of the c-Fos positive cells were created by mapping the specific channel volumes to the LSFM atlas using the inverse transform, generating and summing the spheres of uniform value and 20 μm radius around the centers of the c-Fos positive cells (Renier et al. 2016). Image processing and analysis was performed in Python. 3D visualizations of heatmaps were created with microscopy image analysis software Imaris™ version 2 (Oxford instruments, Abington, UK).

Statistics

For simplicity, 666 individual brain region segmentations of the LSFM atlas were collapsed to their parental regions using the hierarchy tree of the atlas ontology (Online Resource 2) resulting in 284 regions in which the statistical analysis was performed. For determining the difference in the c-Fos positive cell counts, a generalized linear model was fitted to the cell counts observed in each brain region in every animal group. A negative binomial generalized linear model provided a suitable fit to our c-Fos cell count data. For each generalized linear model, a Dunnett's test was performed. Statistical analysis for determining differences in c-Fos expression between semaglutide and vehicle treated mice involved p value adjustment using a multiple comparison method called false discovery rate. Statistical analysis of the data was performed using R statistics library.

Further, all significantly regulated brain regions underwent a two-step manual validation procedure for checking if the used statistical model fits the data points, the significance of the brain regions is not achieved due to outliers and the raw signal is truly originating from the region. First, the fit of cell counts to the generalized linear model was evaluated. This was done by investigating deviance residuals and checking if the residuals aligned with the assumptions of normality and homoscedasticity. Furthermore, Cook's distance was calculated for each cell count data point in the model as a measure of model influence. Regions where the generalized linear model showed severe violations of the assumptions, or the model contained overly influential data points, were discarded. Secondly, the remaining brain regions were visually studied for possible spillover signal from neighboring regions. If the c-Fos response in a region seemed to originate from the neighboring region, e.g. very few c-Fos positive cells were observed only in the border areas of the region while the neighboring areas were exhibiting very high signal, it was declared as not significant.

Results

LSFM Reference Atlas of the Adult Mouse Brains

The standard way of aligning a LSFM scanned mouse brain with the AIBS CCFv3 is to perform a single cross-modality registration of the full brains by computing a global affine and local B-spline transformation in a one-to-one manner (Fig. 2a). However, an alternative strategy is to perform multiple registrations, where each of the major brain structures is aligned individually (Fig. 2b). By comparing the two approaches we observed that multiple registrations yield higher quality registrations in some parts of the brain, e.g. the area postrema (Fig. 2c). However, aligning LSFM-imaged brains using multiple registrations is time-consuming and require both initial segmentation of the larger brain structures and manual validation for each brain which is not compatible with high-throughput analysis. Our solution to this dilemma was to build an LSFM-based reference atlas by aligning the AIBS CCFv3 to the LSFM-based mouse brain template through multi-regional registrations. The present LSFM-based mouse brain reference atlas can be used to analyze individual LSFM-imaged samples directly by fast one-to-one registrations or for improved alignment to the AIBS CCFv3 space if needed (Fig.

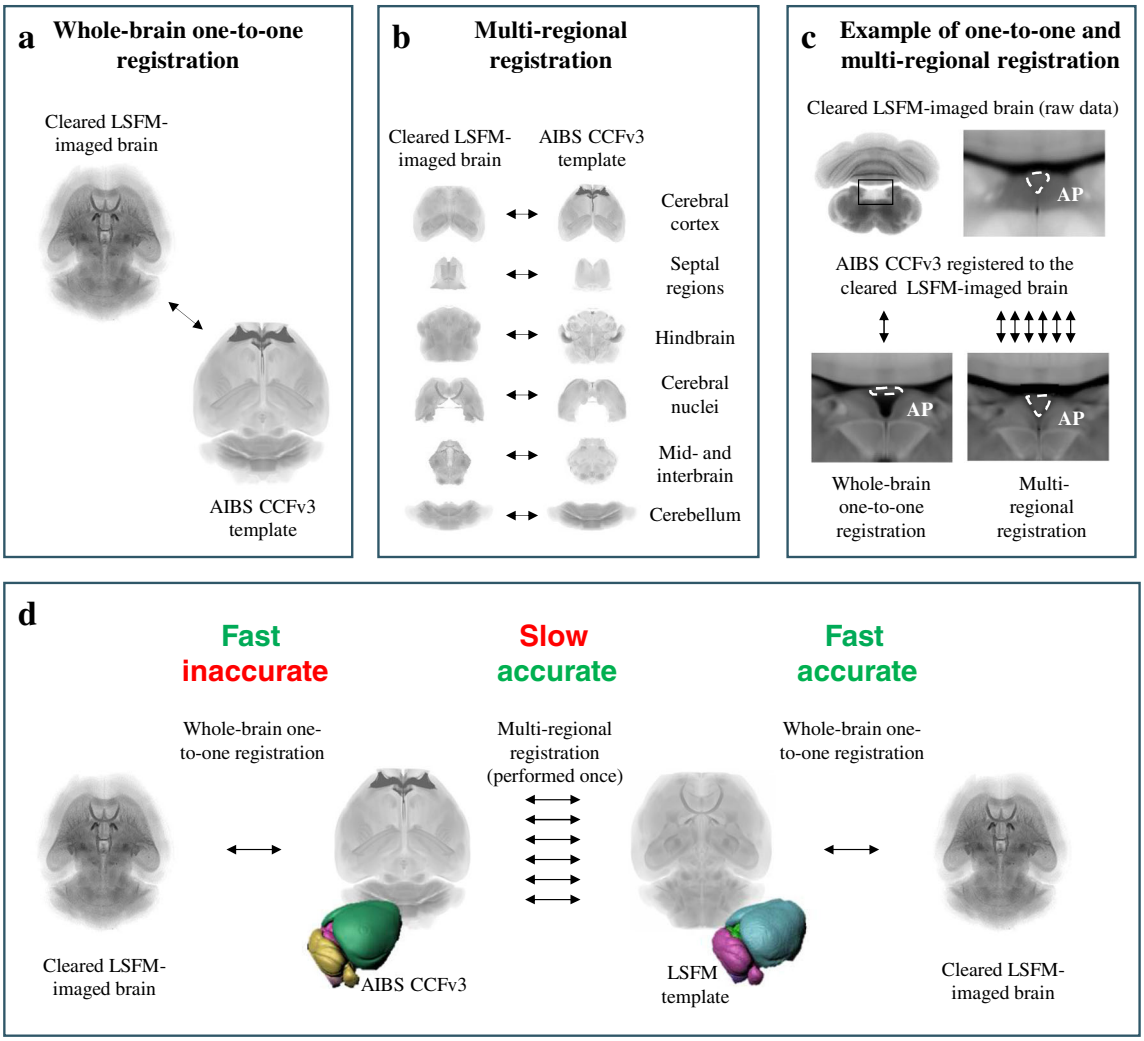

Fig. 2 Techniques for registering LSFM-imaged samples with the AIBS CCFv3. a) Illustration of one-to-one registration between a cleared LSFM-imaged sample and the AIBS CCFv3 template. b) Illustration of multi-regional registration between a cleared LSFM-imaged sample and the AIBS CCFv3 template, where the brain volumes have been divided into six larger brain areas that are mapped individually. c) Example of the registration quality in area postrema (AP) using either one-to-one or multi-regional registration. d) Illustration of the registration flow described in this manuscript. Using one-to-one registration for aligning cleared LSFM-imaged samples with the AIBS CCFv3 is fast but inaccurate in some brain regions like the AP. Multi-regional registration for aligning cleared LSFM-imaged samples with the AIBS CCFv3 template provides better accuracy but is relative slow compared to the one-to-one registration. By generating a template from cleared LSFM-imaged brains and registering the AIBS CCFv3 with it once using multi-regional registration approach we ensure good alignment accuracy between the two templates. Subsequent registrations of cleared LSFM-imaged brains with the LSFM template can then be done directly using fast one-to-one registrations. This way it is possible to achieve both fast as well as accurate registration of cleared LSFM-imaged brains. Regardless of computer performance the speed of analysis improved by a factor of six compared to the multiregional registration

2d). Regardless of computer performance we found that direct alignment to the LSFM atlas improved the registration speed for each brain sample volume by a factor of six.

An LSFM-based mouse brain reference atlas containing an average anatomy template with corresponding brain region annotations was created. The mouse brain template was generated from 139 3D autofluorescence-scanned brain volumes by an iterative multi-resolution image registration algorithm (Fig. 1a). Post-processing of the template involved refinement of the axial symmetry to obtain a midline symmetric atlas viewed from the coronal and horizontal orientation. The axial resolution of the mouse brain template is 20 μm. Brain region annotations for the LSFM template were imported from the AIBS CCFv3 by image registration (Fig. 1b). The annotations were imported as six separate pieces with manual corrections to mitigate the challenge of cross-modality registration. The final atlas contains 666 brain region segmentations with anatomical nomenclature corresponding to the AIBS CCFv3 (hierarchy tree of the atlas ontology in Online Resource 2) (Dong 2008).

Improved Registration of LSFM-Imaged Mouse Brains

To validate that the LSFM reference atlas improved alignment of LSFM-acquired brain volumes, we tested alignment of ten raw LSFM-imaged mouse brain volumes and compared the results to alignment with the AIBS CCFv3 using identical registration procedures. By computing the amount of deformation needed to register each brain into the two atlases, we evaluated the voxel-wise magnitude of displacement necessary to convert the individual brain volumes to either of the atlas template (Fig. 3a). As expected, the LSFM-imaged brain volumes are less deformed when aligned with the generated LSFM atlas compared to alignment with the AIBS CCFv3. We found deformations ranging up to 13 voxels with the AIBS CCFv3 compared to deformations ranging up to 8 voxels with the LSFM atlas. Furthermore, the volume of the area affected by the deformation is smaller for the brains aligned to the LSFM atlas compared to the brains aligned to the AIBS CCFv3. The results show that deformations are most pronounced in the midbrain and hindbrain (Fig. 3a) and most likely the reflect they morphological changes inflicted by tissue processing and clearing.

As the magnitude of the deformation is only an indicative measure by which the registration quality cannot be fully assessed, we further investigated the alignment quality using a standardized metric called intensity variance developed by the Non-Rigid Image Registration Evaluation Project (NIREP) (Christensen et al. 2006). Intensity variance quantifies how much the signal intensity differs per voxel between the set of registered brain volumes and hence, estimates the amount of noise in the data set. We therefore computed the intensity variance for all brain regions using ten LSFM-imaged mouse brains registered to both the LSFM atlas and the AIBS CCFv3 (Fig. 3b). The mean intensity variance determined for the six major brain volumes registered to the AIBS CCFv3 was 17.42 for cerebral cortex, 19.09 for cerebral nuclei, 21.77 for interbrain, 32.38 midbrain, 49.34 for cerebellum and 53.90 for hindbrain. In contrast, the mean intensity variance computed for volumes registered to the LSFM atlas was 19.00 for cerebral cortex, 16.01 for cerebral nuclei, 18.64 for interbrain, 24.13 for midbrain, 44.19 for cerebellum, 30.31 for hindbrain. To analyse these findings in more detail, the intensity variance for all sub-regions within the six major brain regions, were plotted in scatter plots with AIBS CCFv3 values on the y-axis and LSFM atlas values on the x-axis. As for the deformation (Fig. 3a), the most substantial differences in intensity variance were observed in the midbrain and hindbrain. The improvement of the registration accuracy using the LSFM atlas was particularly notable for hindbrain due to significantly lower intensity variance for majority of the sub-regions when LSFM atlas was used for registration.

To further compare the registration quality between the two atlases, 27 landmarks were identified in both the LSFM and the AIBS CCFv3 templates, as well as in the same ten individual brain volumes which were previously used for registration evaluation (Fig. 3c; an atlas template containing the 27 landmarks together with the intensity variance map is available at GitHub and the atlas coordinates for each landmark can be found in the Online Resource 5). For the placement of each landmark several factors were considered. The landmarks should be: 1) easily recognizable in both the AIBS CCFv3 and LSFM templates; 2) distributed brain-wide such that several landmarks were located in cerebral cortex, cerebral nuclei, interbrain, midbrain, hindbrain and cerebellum; 3) distributed along the midline as well as in more lateral parts of the brain; 4) placed in regions with increased local intensity variance, if possible (Fig. 3b). Following the registration of the individual brains to the LSFM atlas and the AIBS CCFv3, the Euclidean distance between the registered and atlas landmarks was calculated. Although this approach also reflects the inherent variation that occurs when placing landmarks, it consistently showed more accurate registration when the LSFM atlas was used as a template.

Accurate c-Fos Quantification in LSFM-Imaged Mouse Brains

For evaluating the performance of the LSFM atlas to assign c-Fos positive cells to anatomical brain regions, we conducted a separate experiment where we mapped the brains from semaglutide-dosed lean mice onto the LSFM and AIBS CCFv3 atlas, respectively, and compared the distribution and number of c-Fos positive cells counted using each atlas (Fig. 4a). The two atlases showed highly overlapping results in the majority of brain regions. However, 11 regions showed significant differences in the number of c-Fos positive cells when comparing data analyzed with the two atlases (Fig. 4b-c). Hence, to determine how registration accuracy impacts the localization of c-Fos positive cells, we compared c-Fos signatures in the hindbrain regions, i.e. the nucleus of the solitary tract (NTS) and the dorsal motor nucleus of the vagus nerve (DMX). According to the LSFM atlas, most c-Fos positive cells were localized to the NTS (234 ± 38 cells) compared to the DMX (144 ± 14 cells) (Fig. 4d). In contrast, the AIBS CCFv3 revealed an opposite pattern (NTS, 95 ± 16 cells; DMX, 205 ± 25 cells) (Fig. 4e). To clarify which atlas is more accurate in the signal localization, we compared the raw microscope images to heatmaps representing c-Fos signal density using either atlas (Fig. 4f). The autofluorescence intensity of NTS is brighter than the intensity of surrounding tissue making it easy to delineate and shows that the raw c-Fos signal is indeed localized in the NTS, thus validating the LSFM atlas mapping. Signal localization accuracy of the LSFM atlas was also assessed for the other nine brain regions with conflicting c-Fos data (data not shown). While improved c-Fos signal localization by the LSFM atlas was confirmed for additional

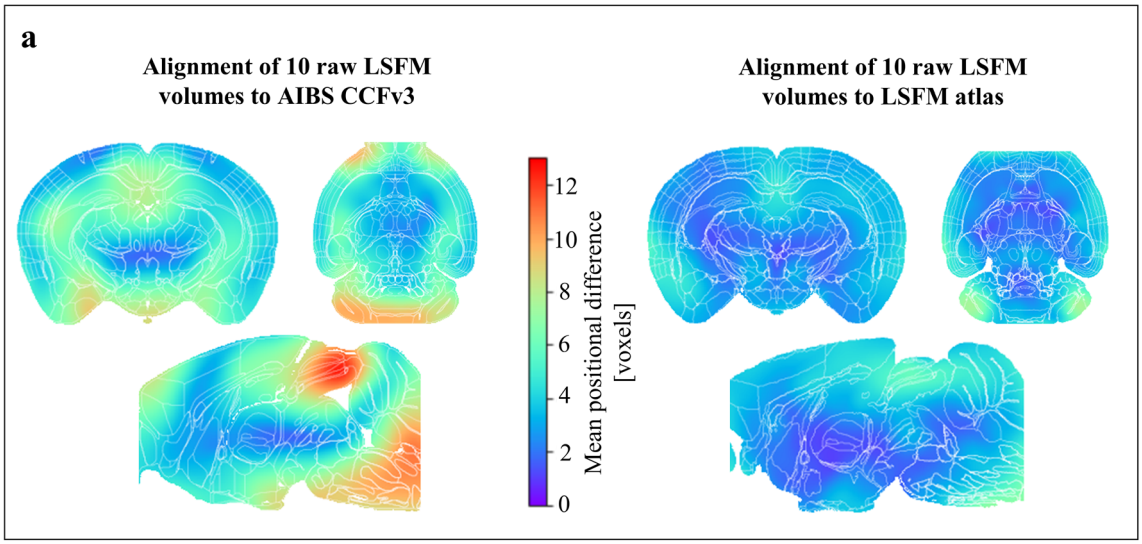
a
Alignment of 10 raw LSFM volumes to AIBS CCFv3
Alignment of 10 raw LSFM volumes to LSFM atlas
Mean positional difference [voxels]
0
2
4
6
8
10
12

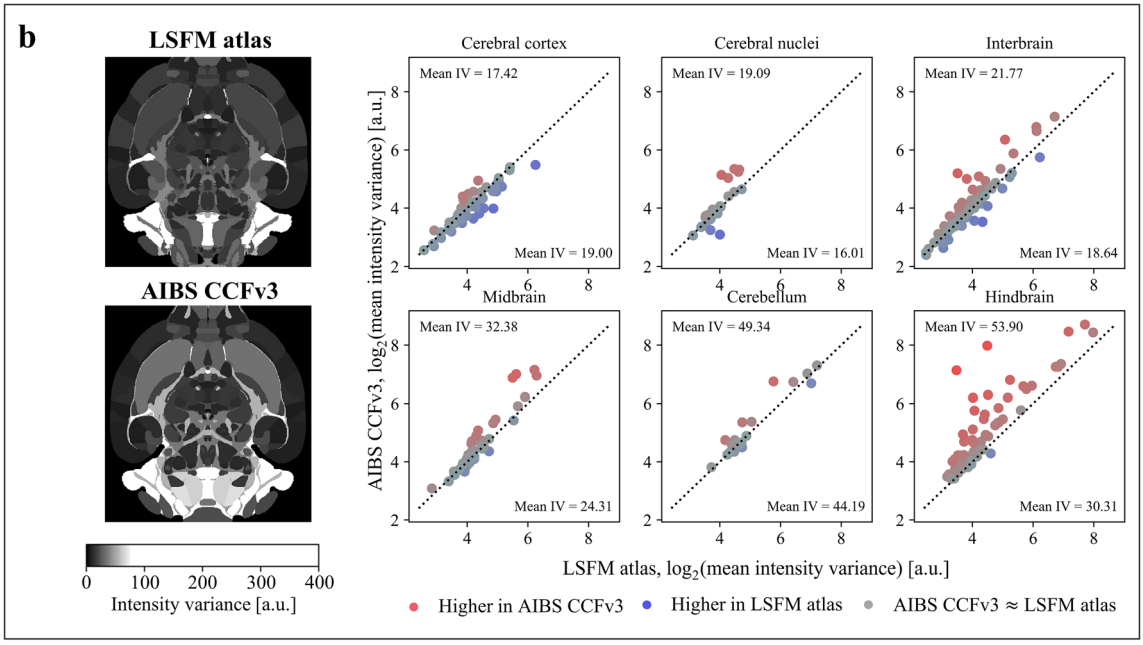
b
LSFM atlas
AIBS CCFv3
0 100 200 300 400
Intensity variance [a.u.]
Cerebral cortex
Cerebral nuclei
Interbrain
Midbrain
Cerebellum
Hindbrain
Mean IV = 17.42
Mean IV = 19.00
Mean IV = 19.09
Mean IV = 16.01
Mean IV = 21.77
Mean IV = 18.64
Mean IV = 32.38
Mean IV = 24.31
Mean IV = 49.34
Mean IV = 44.19
Mean IV = 53.90
Mean IV = 30.31
AIBS CCFv3, log2(mean intensity variance) [a.u.]
LSFM atlas, log2(mean intensity variance) [a.u.]
Higher in AIBS CCFv3
Higher in LSFM atlas
AIBS CCFv3 ≈ LSFM atlas

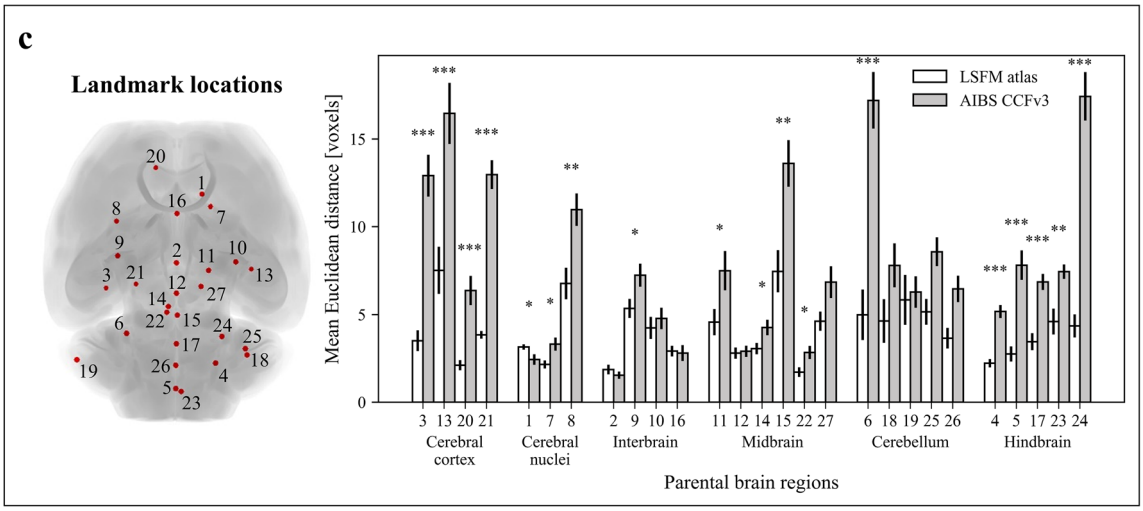
c
Landmark locations
Mean Euclidean distance [voxels]
LSFM atlas
AIBS CCFv3
3 13 20 21
1 7 8
2 9 10 16
11 12 14 15 22 27
6 18 19 25 26
4 5 17 23 24
Cerebral cortex
Cerebral nuclei
Interbrain
Midbrain
Cerebellum
Hindbrain
Parental brain regions

Fig. 3 Improved registration of LSFM-acquired brain volumes using the LSFM atlas. a) Heatmaps illustrate the average magnitude of the deformation resulting from the registration of ten random raw LSFM brain volumes to the AIBS CCFv3 and to the LSFM atlas. b) Registration using the LSFM mouse brain atlas enables improved alignment between individual brains. Intensity variance, a measure for registration performance, was calculated per brain region for the ten random brain volumes aligned to the LSFM atlas and for the same ten brain volumes aligned to the AIBS CCFv3. Highest intensity variance was detected in both cases in ventricular and hindbrain regions (example sections, left). Statistical analysis of the intensity variance was performed using two-tailed Welch's t-test and the resulting significant regions are visualized in the scatter plot (right) along with the mean intensity variance per major brain region for both atlases (denoted as mean IV). The results indicate that the difference in intensity variance values was small for cortical areas. However, majority of brain regions in cerebral nuclei, interbrain, midbrain, cerebellum and hindbrain exhibited higher intensity variance when the AIBS CCFv3 was used for registration compared to when the LSFM atlas was used for registration. c) Registration of the ten brain volumes was further evaluated using 27 landmarks distributed over the whole brain (overview of the landmark positions, left). The landmarks were divided between the six major brain areas in both atlases as well as in the ten brain volumes. Distances between the corresponding landmarks in the individual brains and the atlas templates were calculated after registering the ten brain volumes to the LSFM atlas and the AIBS CCFv3 (bar plot, right). For most landmarks, the calculated distances are lower when the LSFM atlas is used as template. Significant differences in distances between the two atlases was consistently observed in cerebral cortex and hindbrain. Two-tailed Welch's t-test was applied for determining statistical significance in landmark distances between the atlases: $*$ for $0.01 \leq p < 0.05$, $**$ for $0.001 \leq p < 0.01$ and $***$ for $p < 0.001$

five regions (hypoglossal nucleus (XII), presubiculum (PRE), nodulus (NOD), nucleus of the optic tract (NOT) and postsubiculum (POST)). The AIBS CCFv3 performed better in one region, flocculus (FL), while three regions (lateral part of the central amygdalar nucleus (CEAl), parabrachial nucleus (PB) and pedunculopontine nucleus (PPN)), could not be properly evaluated because the ground truth could not be identified due to dispersed c-Fos signal.

C-Fos Detection in a Pharmacological Study

To exemplify the use of the LSFM atlas we performed a study with the aim of quantifying c-Fos expression in mice dosed with the GLP-1 receptor agonist semaglutide. Semaglutide and vehicle was administered peripherally to lean and DIO mice, and the c-Fos expression was evaluated 4 h post-dosing (Fig. 5). When examining the raw LSFM volumes of DIO mice we observed increased autofluorescence in both the specific and the autofluorescence channel, which could potentially lead to false positive c-Fos signals (Supplementary Figs. ESM2 and ESM3). Increased autofluorescence in DIO mice was present throughout the brain, but strongest in the cerebellum (Supplementary Fig. ESM3). Since the increased tissue fluorescence was apparent in both channels, but true positive c-Fos signal was only present in the specific channel, the autofluorescence channel was applied for correction in whole-brain mounts in both lean and DIO mice (Supplementary Figs. ESM2), resulting in significantly improved signal-to-noise ratio specifically in DIO mice (Supplementary Figs. ESM3). To identify the differences between the semaglutide and the vehicle dosed mice, average signal heatmaps in semaglutide-treated lean and obese mice were subtracted voxel-wise from the corresponding vehicle control group (Fig. 5a, c) with statistical analyses on the raw c-Fos positive cell counts (Fig. 5b, d). Compared to vehicle controls, 9 brain regions were significantly regulated by semaglutide treatment in both lean and DIO mice. Semaglutide treated lean and DIO mice showed similar increased c-Fos expression in the bed nuclei of the stria terminalis (BST), paraventricular nucleus of the thalamus (PVT), xiphoid thalamic nucleus (Xi), central amygdalar nucleus (CEA), parabrachial nucleus (PB), nucleus of the solitary tract (NTS) and dorsal motor nucleus of the vagus nerve (DMX) compared to the vehicle treated controls. Additionally, semaglutide treated DIO mice exhibited increased c-Fos expression in the parataenial nucleus (PT) and parasubthalamic nucleus (PSTN), whereas semaglutide treated lean mice showed increased c-Fos expression in the pedunculopontine nucleus (PPN) and mediodorsal nucleus of thalamus (MD) compared to the respective vehicle treated controls.

Discussion

We present here the generation of an LSFM-based mouse brain atlas. Compared to the AIBS CCFv3 (Allen Institute for Brain Science 2011, 2015, 2017; Kuan et al. 2015), the LSFM reference mouse brain atlas provides more accurate anatomical segmentation and quantitative detection of immunolabelled markers in iDISCO+ processed and LSFM-imaged mouse brains, exemplified by characterization of whole-brain c-Fos responses to semaglutide treatment in both lean and DIO mice.

To create an atlas template that is fully representative for average brain anatomy we developed the LSFM atlas based on the variational atlas algorithm previously described (Kovačević et al. 2005; Kuan et al. 2015; Umadevi Venkataraju et al. 2019). This algorithm avoids bias of the template towards the shape of a single chosen reference brain and accounts for morphological differences between the individual brains.

In comparison with the AIBS CCFv3, the created LSFM brain template resulted in registrations with lower amount of deformation, and the intensity variance as well as landmark distances showed improved alignment for LSFM-imaged samples. This is particularly relevant for tissue samples imaged with LSFM since the samples have been cleared and/or

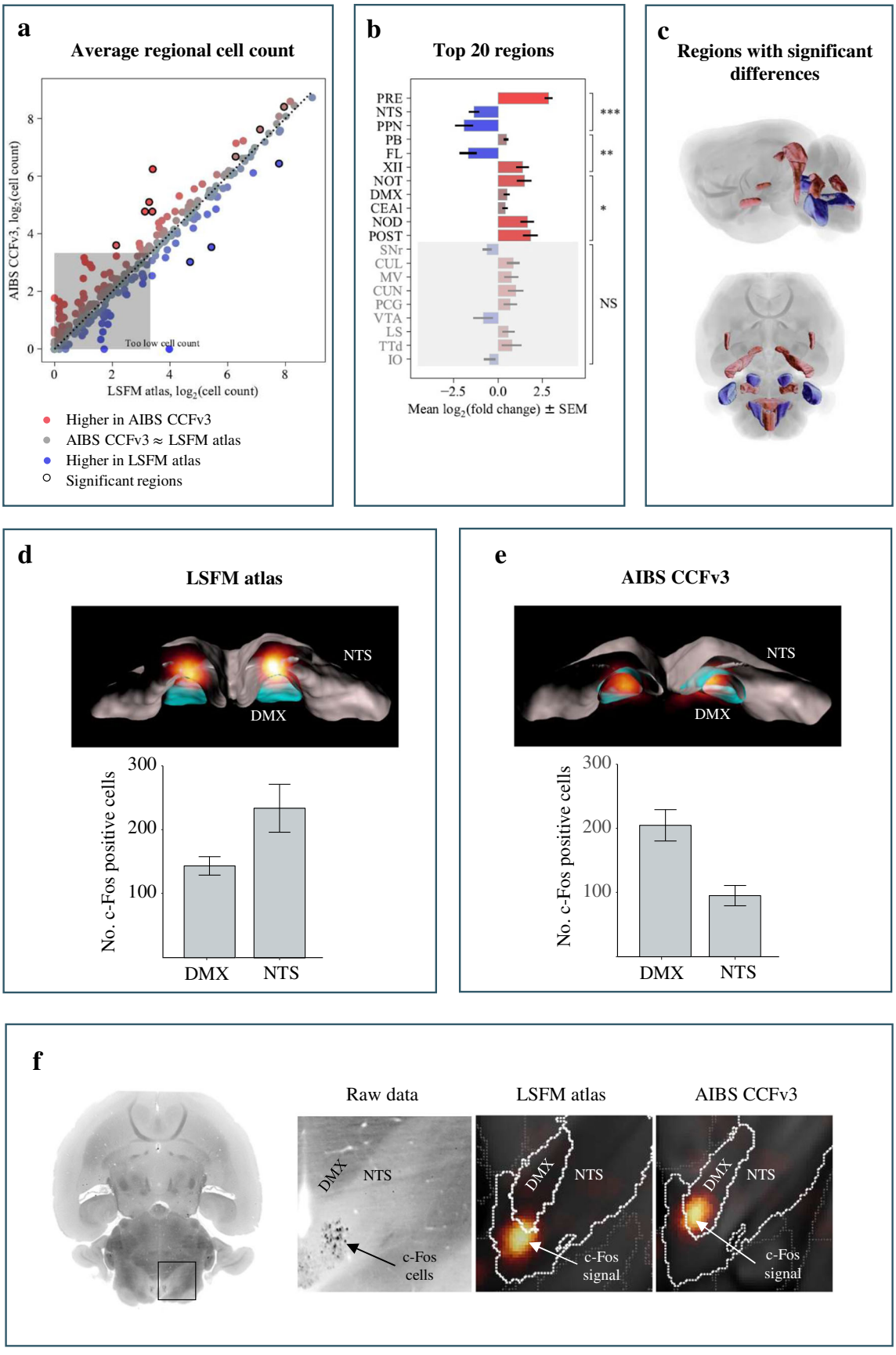
a
Average regional cell count
AIBS CCFv3, log2(cell count)
LSFM atlas, log2(cell count)
Too low cell count
Higher in AIBS CCFv3
AIBS CCFv3 ≈ LSFM atlas
Higher in LSFM atlas
Significant regions
b
Top 20 regions
PRE
NTS
PPN
PB
FL
XII
NOT
DMX
CEAl
NOD
POST
SNr
CUL
MV
CUN
PCG
VTA
LS
TTd
IO
***
**
*
NS
Mean log2(fold change) ± SEM
c
Regions with significant differences
d
LSFM atlas
NTS
DMX
No. c-Fos positive cells
DMX
NTS
e
AIBS CCFv3
NTS
DMX
No. c-Fos positive cells
DMX
NTS
f
Raw data
LSFM atlas
AIBS CCFv3
DMX
NTS
c-Fos cells
c-Fos signal
c-Fos signal

◀ **Fig. 4 Choice of brain atlas influences the number of c-Fos positive cells per brain region.** Comparison of number of c-Fos positive cells in response to semaglutide treatment using the LSFM atlas and the AIBS CCFv3. a) Average number of detected c-Fos expressing cells in every brain region after registration to either the AIBS CCFv3 or the LSFM atlas. Regions in which the c-Fos positive cells are differentially quantified are highlighted by a circle surrounding the data points. An average cell count per group below ten is considered too low to judge. b) The bar chart lists the brain regions and the corresponding mean $\log_2$ fold changes of quantified c-Fos positive cells in these regions according to the *p* value. Blue = higher with LSFM atlas, red = higher with CCFv3. NS stands for not significant, ∗ for $0.01 \leq p < 0.05$, ∗∗ for $0.001 \leq p < 0.01$ and ∗∗∗ for $p < 0.001$. c) Horizontally and sagittally depicted brain volumes highlight the regions in which the c-Fos cells were differentially quantified while using the LSFM atlas and the AIBS CCFv3 for the analysis (same colour code as in b and c). See Online Resource 2 for full names of the brain regions. d-e) Comparison of total number of c-Fos positive cells quantified in 3D-volumes of the nucleus of the solitary tract (NTS) and the dorsal motor nucleus of the vagus nerve (DMX) using the LSFM atlas and the AIBS CCFv3. DMX (blue) and NTS (grey) volumes of both atlases in which the signal (glow colormap) was quantified is visualized in 3D renderings. d) Quantification of c-Fos positive cells following registration of the LSFM atlas to the LSFM-acquired brain volumes showed that in average 234 ± 38 c-Fos positive cells were found in the NTS and 144 ± 14 in the DMX. e) Quantification of c-Fos positive cells following registration of the AIBS CCFv3 to the LSFM-acquired brain volumes. Here the majority of the signal is found in the DMX. Quantification revealed that on average 95 ± 16 c-Fos positive cells are counted in the NTS and 205 ± 25 in the DMX. f) Comparing the raw data to the data in alignment with atlases. DMX has a dense dark appearance compared to NTS

immunolabelled prior to scanning which affect brain morphology by shrinkage/expansion and de-lipidation (Kim et al. 2018; Wan et al. 2018). Furthermore, the contrast within anatomical structures in the brain that are important for subsequent image registration differs between the AIBS CCFv3 template and brain processed for LSFM. These issues have also been recognized by other researchers and a need for a dedicated atlas for cleared LSFM-imaged brains has previously been highlighted (Umadevi Venkataraju et al. 2019).

In this study annotations from the AIBS CCFv3 were mapped to the LSFM atlas template (Wang et al. 2020). However, as annotation volumes are continuously refined (Chon et al. 2019), these can also be aligned to the LSFM template. The process of mapping annotations from an existing atlas to the LSFM-template depends on cross-subject cross-modality registration (i.e. different brain, different microscope) which is difficult and often requires manual corrections. With the respect to mapping annotations from the AIBS CCFv3 to the LSFM-template, the main difficulty was related to morphology differences in the hindbrain and ventricular system. This was solved by stepwise mapping of the annotations for larger parts of the brain such as the hindbrain, together with manual corrections around the ventricular system. Now complete, the LSFM atlas provides the benefit of improved registration of other LSFM-samples together with detailed brain region annotations.

Our results demonstrate that c-Fos signal distribution in hindbrain regions is less accurately mapped using the AIBS CCFv3 compared to delineation of signals using our LSFM reference brain atlas. The large difference may be explained by the high amount of lipid-rich myelin fibers in this part of the brain (Smith 1973). As solvent-based tissue clearing removes lipids, this could explain the difficulty of mapping certain brain volumes to the AIBS CCFv3 which is based on non-cleared tissue samples. In addition to the NTS and DMX, we found improved signal localization using the LSFM atlas in five other brain areas. In four of these areas the improvement could be assigned to the detailed ventricular mask created for the LSFM atlas. Because the AIBS CCFv3 template depicts a narrower ventricular system compared to the LSFM atlas template, this may have resulted in incorrectly assigned c-Fos signal from the choroid plexus to nearby brain regions. In the FL, the AIBS CCFv3 performed better than the LSFM atlas. However, as the FL is often damaged or dislocated during dissection of the brain this may impact the subsequent mapping. In three brain regions we detected a significant difference in the mapping, but we were unable to determine which of the two atlases performed best because the c-Fos signal was too scattered.

In terms of c-Fos detection, DIO mice exhibited relatively high unspecific background signals as compared to lean controls, most likely attributed to lipid-associated autofluorescence. Lipid-containing residues of lysosomal digestion, lipofuscins, have also been reported to increase during aging and oxidative stress (Boellaard et al. 2004) leading to increased autofluorescence (Cho and Hwang 2011; Di Guardo 2015; Schnell et al. 1999). When comparing the c-Fos activity maps between lean and DIO mice we found that the response to semaglutide looked overall similar in both phenotypes with significant c-Fos activation in BST, PVT, Xi, CEA, PB, NTS and DMX. Semaglutide is a glucagon-like peptide-1 (GLP-1) analogue which has been shown to activate GLP-1 receptors in the hypothalamus and brainstem (Secher et al. 2014) and markedly stimulates c-Fos expression in mice (Kjaergaard et al. 2019; Salinas et al. 2018). The observed c-Fos expression pattern observed in this study fits well with these previous reports. Only slight differences were seen between lean and DIO as exemplified by only DIO mice showed significantly upregulated c-Fos expression in the PT and PSTN. It should be noted that lean mice demonstrated a similar c-Fos expression pattern in these regions which, however, did not attain statistical significance.

In this study a c-Fos was detected using a Cy5 labelled secondary antibody. Consequently we used the 560 nm to record the autofluorescence which is different from the mapping reported in the original ClearMap protocol (Renier et al. 2016). However, since the choice of fluorophores might vary from study to study, we tested how the choice of autofluorescence impacts the subsequent mapping (atlas-registered

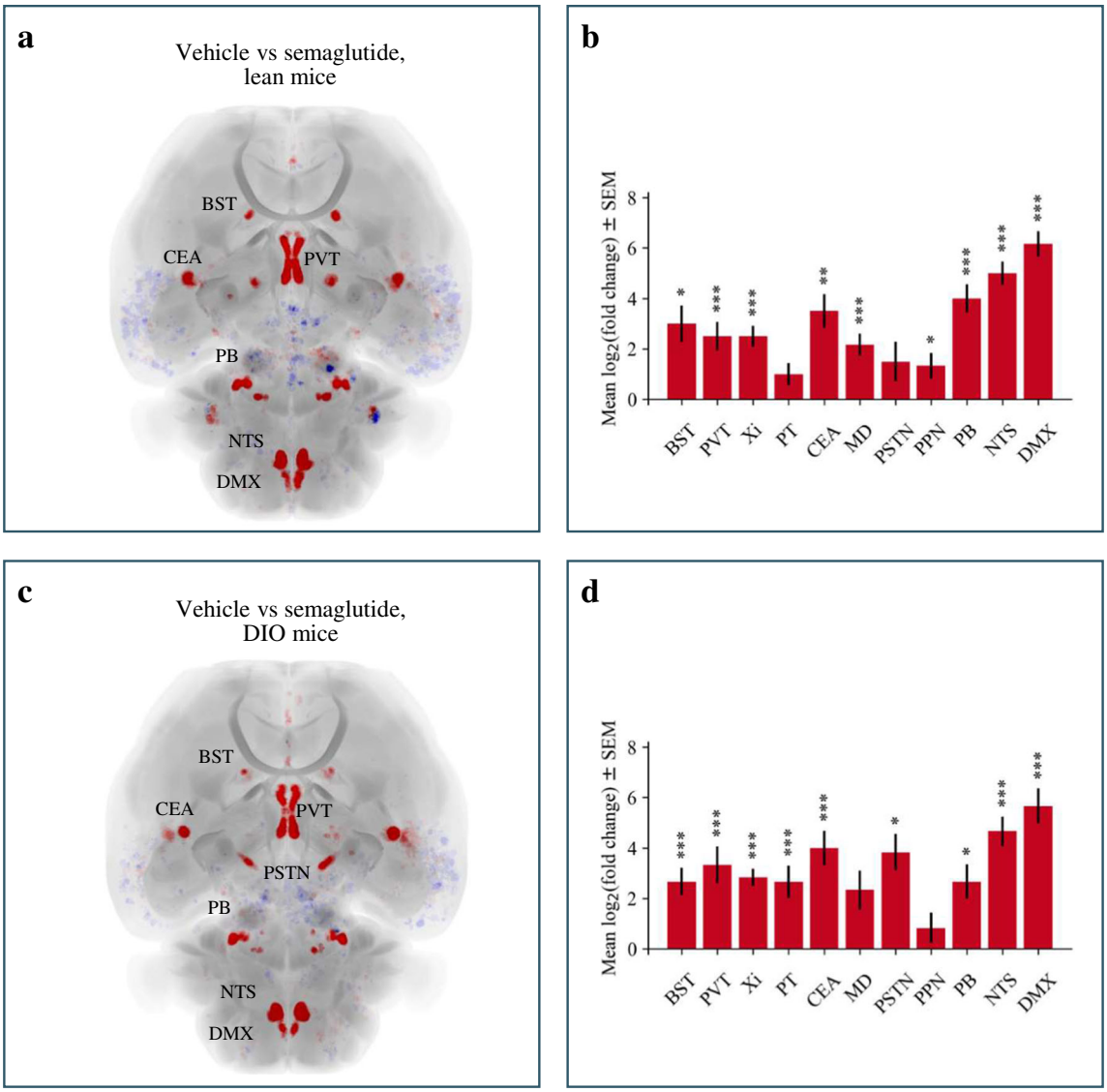

Fig. 5 Differentially regulated c-Fos expression in response to semaglutide administration. Up (red) and down (blue) regulation of c-Fos expression in a) semaglutide treated lean mice in comparison to vehicle treated lean mice and c) in semaglutide treated DIO mice in comparison to vehicle treated DIO mice. Differentially regulated brain regions in response to semaglutide administration in comparison to vehicle treatment and corresponding mean $\log_2$ fold changes of c-Fos positive cells in these regions in b) lean and d) DIO mice. ∗ stands for $0.01 \leq p < 0.05$, ∗ ∗ for $0.001 \leq p < 0.01$ and ∗ ∗ ∗ for $p < 0.001$. *P*-values were adjusted for multiple comparisons using the false discovery rate. See Online Resource 2 for full names of the brain regions

autofluorescence volumes can be found in Github). Although, we obtained the best registration using the 560 nm channel to record the autofluorescence, channels below 700 nm worked as well. When reaching the NIR spectrum the endogenous fluorescence become so weak it can no longer be used for registration.

The average brain generated in this study was created from 8 to 10 week old C57Bl/6 J male mice. Since factors such as age, sex and strain are known to affect brain size and anatomy, it is possible deviations from the average parameters may have a slight impact on the overall quality of registration and quantification. Indeed, we observed that obesity led to an unexpected increase in autofluorescence, presumably due to lipofuscin accumulation. In this case it did not impact on the registration, but it will always be important to consider the possibility that the choice of model may influence registration and quantification.

In conclusion, we developed a dedicated reference atlas allowing faster and more accurate mapping of iDISCO+ processed and LSFM-imaged whole mouse brains. In combination with an improved c-Fos detection algorithm, our pipeline enables for unbiased, automated and computationally efficient quantitative analysis of drug-induced c-Fos expression in the intact mouse brain. The LSFM atlas is highly applicable for fast and precise mapping of fluorescent markers in both the normal mouse brain and mouse models of CNS diseases as

well for improved delineation of compound distribution in the CNS imaged by LSFM (Liebmann et al. 2016; Roostalu et al. 2019; Salinas et al. 2018; Secher et al. 2014).

Information Sharing Statement

LSFM reference atlas files are freely accessible at https://github.com/Gubra-ApS. Quantitative c-Fos data for all brain regions is available as Online Resources 3 and 4. Source code used for generating the LSFM reference atlas along with the code for detecting and quantifying the number of c-Fos positive cells in LSFM mouse brain volumes is accessible at https://github.com/Gubra-ApS.

Acknowledgements The authors would like to acknowledge Lotte Ankjær Frederiksen and Hanne Duus Laustsen for skillful technical assistance.

Funding The work was funded by Gubra ApS and Innovation Fund Denmark grant number (8053-00121B).

Compliance with Ethical Standards

Conflict of Interest Johanna Perens, Casper Gravesen Salinas, Jacob Lercke Skytte, Urmas Roostalu, Franziska Wichern, Pernille Barkholt, and Jacob Hecksher-Sørensen are currently employed by Gubra ApS. Niels Vrang and Jacob Jelsing are the owners of Gubra ApS.

Ethics Approval All animal procedures were conducted in compliance with internationally accepted principles for the care and use of laboratory animals and were approved by the Danish Animal Experiments Inspectorate (license #2013-15-2934-00784).

References

Allen Institute for Brain Science. (2011). Allen Mouse Brain Atlas. *Available from: http://mouse.brain-map.org*.

Allen Institute for Brain Science. (2015). Allen mouse common coordinate framework. *Technical White Paper*.

Allen Institute for Brain Science. (2017). Allen mouse common coordinate framework and reference atlas. *Technical White Paper*.

Bobela, W., Zheng, L., & Schneider, B. L. (2014). Overview of mouse models of Parkinson's disease. *Current protocols in mouse biology, 4*(3), 121–139. https://doi.org/10.1002/9780470942390.mo140092.

Boellaard, J. W., Schlote, W., & Hofer, W. (2004). Ultrastructural pathology species-specific ultrastructure of neuronal Lipofuscin in Hippocampus and Neocortex of subhuman mammals and humans. *Ultrastruct Pathol, 28*(5–6), 341–351. https://doi.org/10.1080/019131290882330.

Cho, S., & Hwang, E. S. (2011). Fluorescence-based detection and quantification of features of cellular senescence. *Methods Cell Biol, 103*, 149–188. https://doi.org/10.1016/B978-0-12-385493-3.00007-3.

Chon, U., Vanselow, D. J., Cheng, K. C., & Kim, Y. (2019). Enhanced and unified anatomical labeling for a common mouse brain atlas. *Nat Commun, 10*, 5067. https://doi.org/10.1038/s41467-019-13057-w.

Christensen, G. E., Geng, X., Kuhl, J. G., Bruss, J., Grabowski, T. J., Pirwani, I. A., et al. (2006). Introduction to the non-rigid image registration evaluation project (NIREP). *Lecture Notes in Computer Science (including subseries Lecture Notes in Artificial Intelligence and Lecture Notes in Bioinformatics), 4057*, 128–135. https://doi.org/10.1007/11784012_16.

Chung, K., Wallace, J., Kim, S.-Y., Kalyanasundaram, S., Andalman, A. S., Davidson, T. J., Mirzabekov, J. J., Zalocusky, K. A., Mattis, J., Denisin, A. K., Pak, S., Bernstein, H., Ramakrishnan, C., Grosenick, L., Gradinaru, V., & Deisseroth, K. (2013). Structural and molecular interrogation of intact biological systems. *Nature, 497*(7449), 332–337. https://doi.org/10.1038/nature12107.

Detrez, J. R., Maurin, H., Van Kolen, K., Willems, R., Colombelli, J., Lechat, B., et al. (2019). Regional vulnerability and spreading of hyperphosphorylated tau in seeded mouse brain. *Neurobiol Dis, 127*, 398–409. https://doi.org/10.1016/j.nbd.2019.03.010.

Di Guardo, G. (2015). Lipofuscin, lipofuscin-like pigments and autofluorescence. *Eur J Histochem, 59*(1), 1–2. https://doi.org/10.4081/ejh.2015.2485.

Dong, H. . (2008). The Allen reference atlas: A digital color brain atlas of the C57BL/6J male mouse. Wiley.

Dragunow, M., & Faull, R. (1989). The use of c-fos as a metabolic marker in neuronal pathway tracing. *J Neurosci Methods, 29*(3), 261–265. https://doi.org/10.1016/0165-0270(89)90150-7.

Ertürk, A., Becker, K., Jährling, N., Mauch, C. P., Hojer, C. D., Egen, J. G., Hellal, F., Bradke, F., Sheng, M., & Dodt, H. U. (2012). Three-dimensional imaging of solvent-cleared organs using 3DISCO. *Nat Protoc, 7*(11), 1983–1995. https://doi.org/10.1038/nprot.2012.119.

Esquerda-Canals, G., Montoliu-Gaya, L., Güell-Bosch, J., & Villegas, S. (2017). Mouse models of Alzheimer's disease. *J Alzheimers Dis, 57*, 1171–1183. https://doi.org/10.3233/JAD-170045.

Jensen, C. B., Secher, A., Hecksher-Sørensen, J., Conradsen, K., & Larsen, R. (2015). Quantification of brain access of exendin-4 in the C57BL mouse model by SPIM fluorescence imaging and the Allen mouse brain reference model. In *Lecture Notes in Computer Science (including subseries Lecture Notes in Artificial Intelligence and Lecture Notes in Bioinformatics)* https://doi.org/10.1007/978-3-319-19665-7_38.

Kim, J. H., Jang, M. J., Choi, J., Lee, E., Song, K. D., Cho, J., et al. (2018). Optimizing tissue-clearing conditions based on analysis of the critical factors affecting tissue-clearing procedures. *Sci Rep, 8*, 12815. https://doi.org/10.1038/s41598-018-31153-7.

Kjaergaard, M., Salinas, C. B. G., Rehfeld, J. F., Secher, A., Raun, K., & Wulff, B. S. (2019). PYY(3-36) and exendin-4 reduce food intake and activate neuronal circuits in a synergistic manner in mice. *Neuropeptides, 73*, 89–95. https://doi.org/10.1016/j.npep.2018.11.004.

Klein, S., Staring, M., Murphy, K., Viergever, M. A., & Pluim, J. P. W. (2010). Elastix: A toolbox for intensity-based medical image registration. *IEEE Trans Med Imaging, 29*(1), 196–205. https://doi.org/10.1109/TMI.2009.2035616.

Kovačević, N., Henderson, J. T., Chan, E., Lifshitz, N., Bishop, J., Evans, A. C., Henkelman, R. M., & Chen, X. J. (2005). A three-dimensional MRI atlas of the mouse brain with estimates of the

average and variability. *Cereb Cortex, 15*(5), 639–645. https://doi.org/10.1093/cercor/bhh165.

Kuan, L., Li, Y., Lau, C., Feng, D., Bernard, A., Sunkin, S. M., Zeng, H., Dang, C., Hawrylycz, M., & Ng, L. (2015). Neuroinformatics of the Allen mouse brain connectivity atlas. *Methods, 73*, 4–17. https://doi.org/10.1016/j.ymeth.2014.12.013.

Larsen, C. T., Iglesias, J. E., & Van Leemput, K. (2014). N3 Bias Field correction explained as a Bayesian modeling method. *Bayesian and grAphical Models for Biomedical Imaging. Lect Notes Comput Sci, 8677*, 1–12. https://doi.org/10.1007/978-3-319-12289-2.

Leung, C., & Jia, Z. (2016). Mouse genetic models of human brain disorders. *Front Genet, 7*, 40. https://doi.org/10.3389/fgene.2016.00040.

Liebmann, T., Renier, N., Bettayeb, K., Greengard, P., Tessier-Lavigne, M., & Flajolet, M. (2016). Three-dimensional study of Alzheimer's disease hallmarks using the iDISCO clearing method. *Cell Rep, 16*(4), 1138–1152. https://doi.org/10.1016/j.celrep.2016.06.060.

Nectow, A. R., Schneeberger, M., Zhang, H., Field, B. C., Renier, N., Azevedo, E., Patel, B., Liang, Y., Mitra, S., Tessier-Lavigne, M., Han, M. H., & Friedman, J. M. (2017). Identification of a brainstem circuit controlling feeding. *Cell., 170*, 429–442.e11. https://doi.org/10.1016/j.cell.2017.06.045.

Renier, N., Adams, E. L., Kirst, C., Dulac, C., Osten, P., & Tessier-Lavigne, M. (2016). Mapping of brain activity by automated volume analysis of immediate early genes. *Cell, 165*(7), 1789–1802. https://doi.org/10.1016/j.cell.2016.05.007.

Renier, N., Wu, Z., Simon, D. J., Yang, J., Ariel, P., & Tessier-Lavigne, M. (2014). iDISCO: A simple, rapid method to immunolabel large tissue samples for volume imaging. *Cell, 159*(4), 896–910. https://doi.org/10.1016/j.cell.2014.10.010.

Rocha, M. D., Düring, D. N., Bethge, P., Voigt, F. F., Hildebrand, S., Helmchen, F., Pfeifer, A., Hahnloser, R. H. R., & Gahr, M. (2019). Tissue clearing and light sheet microscopy: Imaging the Unsectioned adult Zebra finch brain at cellular resolution. *Front Neuroanat, 13*, 1–7. https://doi.org/10.3389/fnana.2019.00013.

Roostalu, U., Salinas, C. B. G., Thorbek, D. D., Skytte, J. L., Fabricius, K., Barkholt, P., John L. M., Jurtz V. I., Knudsen L. B., Jelsing J., Vrang N., Hansen H. H., Hecksher-Sørensen J. (2019). Quantitative whole-brain 3D imaging of tyrosine hydroxylase-labeled neuron architecture in the mouse MPTP model of Parkinson's disease. DMM Disease Models and Mechanisms https://doi.org/10.1242/dmm.042200, 12, dmm042200.

Salinas, C. B. G., Lu, T. T. H., Gabery, S., Marstal, K., Alanentalo, T., Mercer, A. J., Cornea, A., Conradsen, K., Hecksher-Sørensen, J., Dahl, A. B., Knudsen, L. B., & Secher, A. (2018). Integrated brain atlas for unbiased mapping of nervous system effects following Liraglutide treatment. *Sci Rep, 8*(1), 10310. https://doi.org/10.1038/s41598-018-28496-6.

Schneeberger, M., Parolari, L., Das Banerjee, T., Renier, N., Friedman, J. M., & Nectow, A. R. (2019). Regulation of energy expenditure by brainstem GABA neurons in brief. *Cell, 178*(3), 672–685.e12. https://doi.org/10.1016/j.cell.2019.05.048.

Schnell, S. A., Staines, W. A., & Wessendorf, M. W. (1999). Reduction of Lipofuscin-like autofluorescence in fluorescently labeled tissue. *J Histochem Cytochem, 47*(6), 719–730. https://doi.org/10.1177/002215549904700601.

Secher, A., Jelsing, J., Baquero, A. F., Hecksher-Sørensen, J., Cowley, M. A., Dalbøge, L. S., Hansen, G., Grove, K. L., Pyke, C., Raun, K., Schäffer, L., Tang-Christensen, M., Verma, S., Witgen, B. M., Vrang, N., & Bjerre Knudsen, L. (2014). The arcuate nucleus mediates GLP-1 receptor agonist liraglutide-dependent weight loss. *J Clin Investig, 124*, 4473–4488. https://doi.org/10.1172/JCI75276.

Shamonin, D. P., Bron, E. E., Lelieveldt, B. P. F., Smits, M., Klein, S., & Staring, M. (2014). Fast parallel image registration on CPU and GPU for diagnostic classification of Alzheimer's disease. *Frontiers in Neuroinformatics, 7*, 50. https://doi.org/10.3389/fninf.2013.00050.

Sled, J. G., Zijdenbos, A. P., & Evans, A. C. (1998). A nonparametric method for automatic correction of intensity nonuniformity in mri data. *IEEE Trans Med Imaging, 17*(1), 87–97. https://doi.org/10.1109/42.668698.

Smith, M. E. (1973). A regional survey of myelin development: Some compositional and metabolic aspects. *J Lipid Res, 14*(5), 541–551.

Umadevi Venkataraju, K. U., Gornet, J., Murugaiyan, G., Wu, Z., & Osten, P. (2019). Development of brain templates for whole brain atlases. *Progress in Biomedical Optics and Imaging - Proceedings of SPIE, 10865*, 1086511. https://doi.org/10.1117/12.2505295.

Van Leemput, K., Maes, F., Vandermeulen, D., & Suetens, P. (1999). Automated model-based Bias Field correction of MR images of the brain. *IEEE Trans Med Imaging, 18*(10), 885–896. https://doi.org/10.1109/42.811268.

Vigouroux, R. J., Belle, M., & Chédotal, A. (2017). Neuroscience in the third dimension: Shedding new light on the brain with tissue clearing. *Molecular brain, 10*(1), 33. https://doi.org/10.1186/s13041-017-0314-y.

Villares, R., Gutiérrez, J., Fütterer, A., Trachana, V., Del Burgo, F. G., & Martínez-A, C. (2015). Dido mutations trigger perinatal death and generate brain abnormalities and behavioral alterations in surviving adult mice. *Proc Natl Acad Sci U S A, 112*, 4803–4808. https://doi.org/10.1073/pnas.1419300112.

Wan, P., Zhu, J., Xu, J., Li, Y., Yu, T., & Zhu, D. (2018). Evaluation of seven optical clearing methods in mouse brain. *Neurophotonics., 5*. https://doi.org/10.1117/1.nph.5.3.035007.

Wang, Q., Ding, S. L., Li, Y., Royall J., Feng D., Lesnar P., Graddis N., Naeemi M., Facer B., Ho A., Dolbeare T., Blanchard B., Dee N., Wakeman W., Hirokawa K. E., Szafer A., Sunkin S. M., Oh S. W., Bernard A., Phillips J. W., Hawrylycz M., Koch C., Zeng H., Harris J. A., & Ng, L. (2020). The Allen mouse brain common coordinate framework: A 3D reference atlas. *Cell 181*,(4), 936–953.e20. https://doi.org/10.1016/j.cell.2020.04.007.

Online Resource 1 for An Optimized Mouse Brain Atlas for Automated Mapping and Quantification of Neuronal Activity Using iDISCO+ and Light Sheet Fluorescence Microscopy

Johanna Perens, Casper Gravesen Salinas, Jacob Lercke Skytte, Urmas Roostalu, Anders Bjorholm Dahl, Tim B. Dyrby, Pernille Barkholt, Niels Vrang, Jacob Jelsing and Jacob Hecksher-Sørensen (jhs@gubra.dk)

Image processing for creating the LSFM reference atlas: full description and parameters

An average LSFM mouse brain volume was created from 139 individual mouse brain autofluorescence datasets (Kovačević et al., 2005; Kuan et al., 2015; Umadevi Venkataraju et al., 2019). Pre-processing was initiated by down-sampling of the raw autofluorescence volumes to 20 µm isotropic resolution which was performed in axial plane using linear interpolating splines and in z-direction by local averaging of voxels. N3 method (Larsen et al., 2014; Van Leemput et al., 1999) was applied to down-sampled images for correcting the bias field caused by inhomogeneous fixation, clearing or illumination of the sample. Subsequently, contrast limited adaptive histogram equalization (CLAHE) was performed to achieve enhanced local signal contrast and higher visibility of different brain structures. CLAHE was carried out on 2D-images from the bias-field-corrected brain volumes sliced in three orthogonal planes (kernel size 1/3 of image height by 1/6 of 2D-image width, clipping limit 0.01, 255 histogram bins) and its results were then averaged together with the input bias-field-corrected volume. Then, a randomly chosen reference volume was rigidly aligned to the AIBS CCFv3 for realizing its axial symmetry. Pre-processing was finalized by matching the cumulative intensity histograms of the individual volumes with the cumulative intensity histogram of the reference volume.

To generate the average mouse brain template, a reference volume was selected for normalizing the individual brains in orientation, global size, gross shape and intensity. The algorithm was comprised of six iterative registration steps – one affine and five B-spline transformations. In the first step, all pre-processed mouse brain datasets were affinely registered to the pre-processed and CCFv3-oriented reference image according to a multi-resolution strategy and

the resulting datasets were intensity averaged to generate an initial intermediate average brain. In the second step, the linearly aligned images underwent B-spline registration to the first intermediate average brain at the lowest resolution level. Subsequently, an updated intermediate average brain was produced from the non-linearly registered images. The remaining steps were analogous to the second step with the only difference being the resolution level. The highest resolution was reached at the last B-spline registration step.

Due to the limit in scanning depth in Z-dimension, which is about 6 mm for our LSFM setup, the acquired brain volumes missed about half a millimetre of the dorsal cortex. For producing a template with complete cortex, additional 15 autofluorescence volumes of cortices from the same animals were acquired, pre-processed and aligned through multi-resolution affine and B-spline transformations to the cortex reference volume. Then, the normalized cortex volumes were averaged, and the result was aligned through multi-resolution rigid, affine and B-spline transformations to the average mouse brain volume missing the top part of the cortex. Subsequently, the final mouse brain template was produced by matching the intensities of both volumes and combing them by blending the overlapping areas with a sigmoidal function. Satisfying axial symmetry was achieved by dividing the template brain volume into three coronal slabs with equal thickness and manually rotating them into correct position. Subsequently, the three slabs were merged together using the sigmoidal blending function. The final template was created by mirroring one hemisphere to the opposite side and merging the hemispheres with the sigmoidal blending function for receiving a symmetric template brain.

The average LSFM mouse brain template was generated by registration steps which involved maximizing the mattes mutual information for fixed and moving image pairs. Multi-resolution strategy during affine registration was realized by increasing data complexity as well as transformation complexity throughout the 4 resolution levels. Data complexity was modified by smoothing and down-sampling (Gaussian pyramid scheme: σ_{data} = 8/2, 4/2, 2/2, 1/2 voxels) whereas transformation complexity was modified by changing the spacing of the control points on the grid ($\sigma_{transform}$ = 100, 75, 50, 25 voxels). B-spline registrations were performed according to an uni-resolution strategy but by increasing the resolution with every B-spline registration step (σ_{data} = 8/2, 4/2, 2/2, 1.5/2, 1/2 voxels, $\sigma_{transform}$ = 100, 75, 50, 35, 25 voxels. Parameters were optimized for every registration procedure to achieve the best possible spatial alignment for fixed and moving volume pairs.

Brain regions annotations were added to the LSFM template from the AIBS CCFv3. First, the mouse brain template of AIBS was registered to the LSFM template using multi-resolution affine and B-spline registration. Subsequently, the registered AIBS CCFv3 template and its segmentations were divided into six parental brain regions – cerebral cortex, cerebral nuclei, hindbrain, cerebellum, septal regions and interbrain together with midbrain. The parental regions were then separately registered to the corresponding areas of the LSFM template through affine and B-spline transformations and unified by filling in the border gap using distance map computation. This segmentation transfer approach led to misalignments in regions near to ventricular system, such as AP and SFO, which were therefore manually corrected. Further refinement of the segmentations was undertaken using Franklin and Paxinos mouse brain atlas for the ventral tegmental area (VTA) and the compact part of substantia nigra (SNc) as well as for the nucleus accumbens (ACB) which was divided into core and shell part. Segmentation refinements were performed with microscopy image analysis software Imaris™ version 2 (Oxford instruments, Abington, UK). Image processing was performed in Python and Elastix toolbox (Klein et al., 2010; Shamonin et al., 2014) was used to implement the registrations.

REFERENCES

Klein, S., Staring, M., Murphy, K., Viergever, M.A., Pluim, J.P.W., 2010. Elastix: A Toolbox for Intensity-Based Medical Image Registration. IEEE Trans. Med. Imaging 29, 196–205. https://doi.org/10.1109/TMI.2009.2035616

Kovačević, N., Henderson, J.T., Chan, E., Lifshitz, N., Bishop, J., Evans, A.C., Henkelman, R.M., Chen, X.J., 2005. A three-dimensional MRI atlas of the mouse brain with estimates of the average and variability. Cereb. Cortex 15, 639–645. https://doi.org/10.1093/cercor/bhh165

Kuan, L., Li, Y., Lau, C., Feng, D., Bernard, A., Sunkin, S.M., Zeng, H., Dang, C., Hawrylycz, M., Ng, L., 2015. Neuroinformatics of the Allen Mouse Brain Connectivity Atlas. Methods 73, 4–17. https://doi.org/10.1016/j.ymeth.2014.12.013

Larsen, C.T., Iglesias, J.E., Van Leemput, K., 2014. N3 Bias Field Correction Explained as a Bayesian Modeling Method. Bayesian Graph. Model. Biomed. Imaging. Lect. Notes Comput. Sci. 8677, 1–12. https://doi.org/10.1007/978-3-319-12289-2

Shamonin, D.P., Bron, E.E., Lelieveldt, B.P.F., Smits, M., Klein, S., Staring, M., 2014. Fast parallel image registration on CPU and GPU for diagnostic classification of Alzheimer's

disease. Front. Neuroinform. 7, 50. https://doi.org/10.3389/fninf.2013.00050

Umadevi Venkataraju, K.U., Gornet, J., Murugaiyan, G., Wu, Z., Osten, P., 2019. Development of brain templates for whole brain atlases. Prog. Biomed. Opt. Imaging - Proc. SPIE 10865, 1086511. https://doi.org/10.1117/12.2505295

Van Leemput, K., Maes, F., Vandermeulen, D., Suetens, P., 1999. Automated Model-Based Bias Field Correction of MR Images of the Brain. IEEE Trans. Med. Imaging 18, 885–896. https://doi.org/10.1109/42.811268

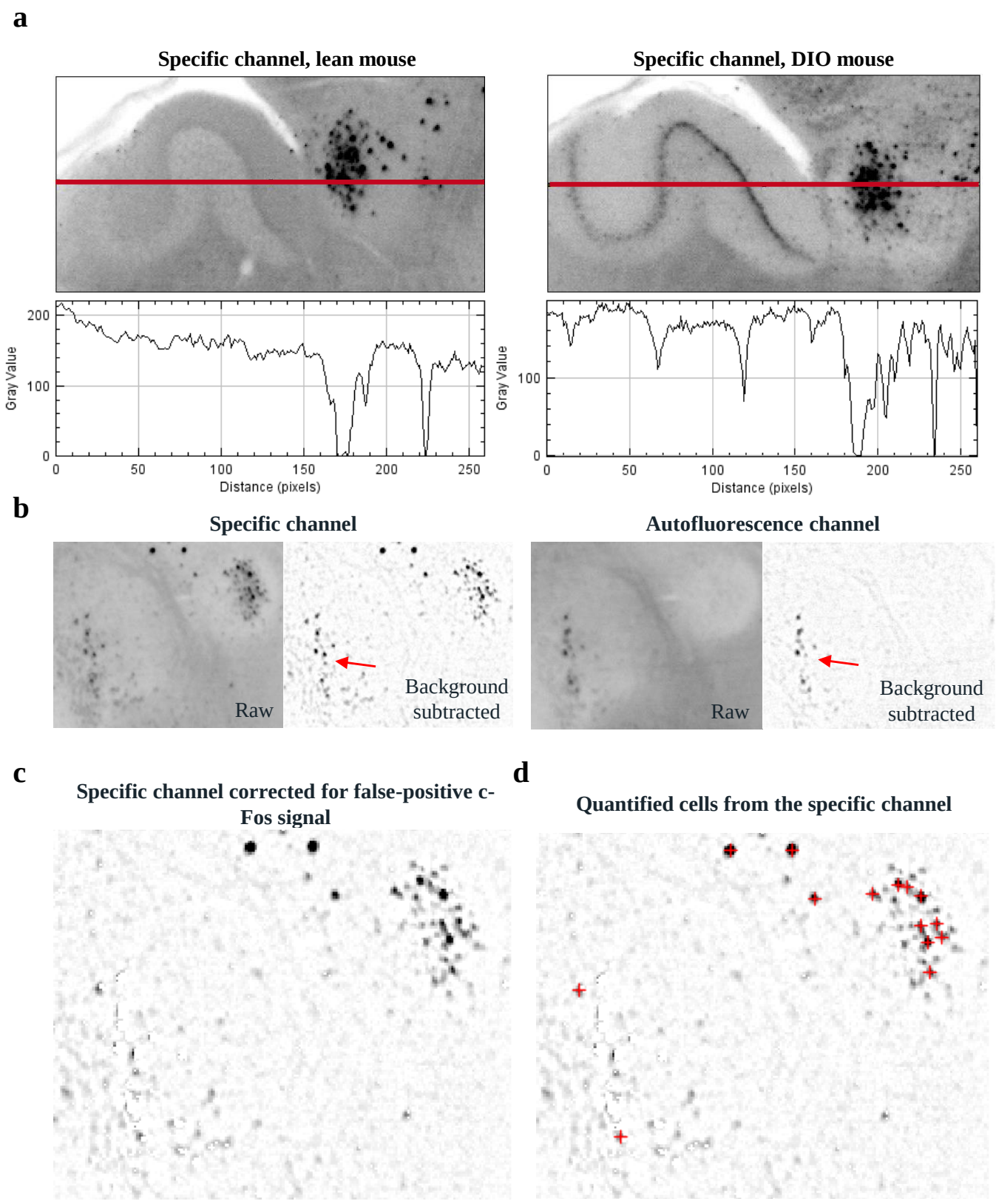

Supplementary figure 1

Improved detection of true c-Fos positive cells after removal of false positive c-Fos signal originating from increased tissue autofluorescence. a) Increased autofluorescence in DIO mice, apparent especially in hindbrain areas such as PB, can be recognized as c-Fos positive cells. b) Increased autofluorescence (red arrow) appear both in autofluorescence as well as in c-Fos specific channel. c) After channel alignment and background subtraction, false positive c-Fos signal is removed from the specific channel and d) true positive c-Fos cells (red cross) are quantified according to the ClearMap algorithm.

a

Raw c-Fos signal in lean animal

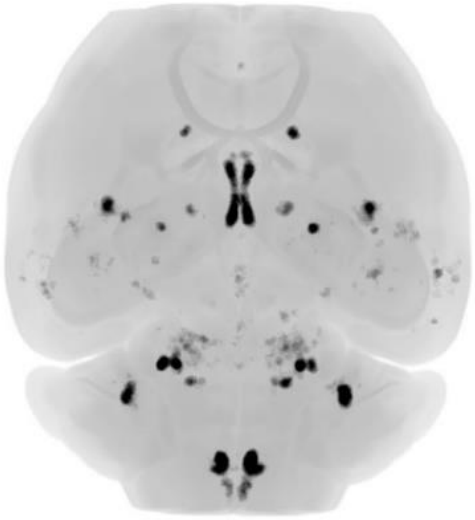

b

Raw c-Fos signal in DIO animal

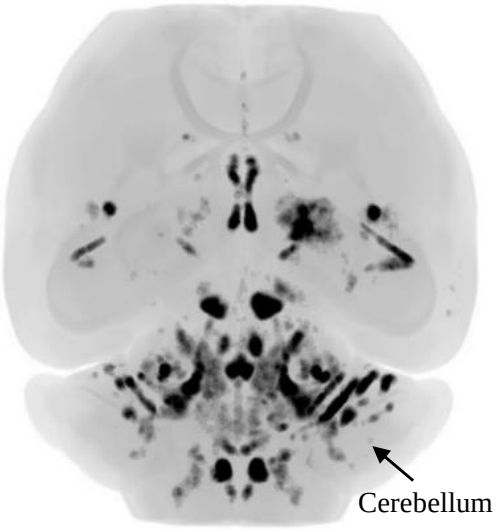

c

Corrected c-Fos signal in lean animal

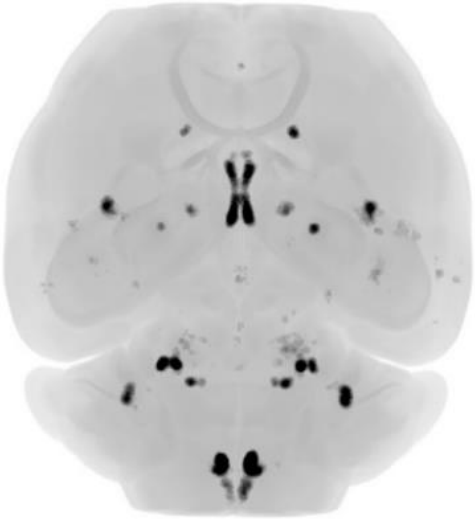

d

Corrected c-Fos signal in DIO animal

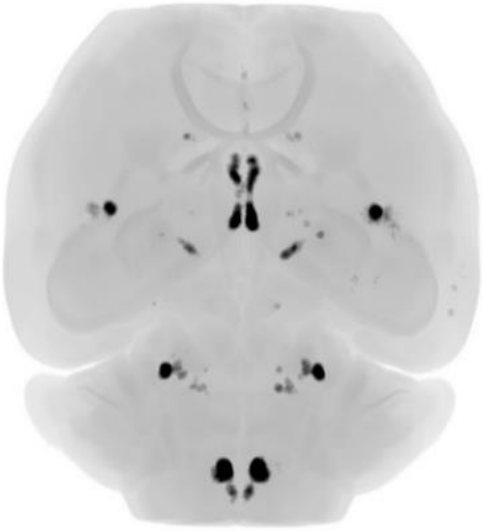

Supplementary figure 2

Removal of the false positive c-Fos signal originating from increased tissue autofluorescence is an essential step for quantifying neuronal activity in DIO mice. This will be demonstrated in an example of heatmaps showing c-Fos response to semaglutide administration. a) ClearMap algorithm without the correction of false positive c-Fos signal performs well in lean mice. b) However, in old and obese mice brains there is an increased autofluorescence that can be detected as false c-Fos positive cells. c) Correction of false positive c-Fos signal does not have a strong impact on the signal fingerprint of young, lean mice, but d) will reduce notably the signal detected in DIO mice.

Manuscript B

Multimodal 3D mouse brain atlas framework with skull-derived coordinate system

Johanna Perens, Casper Gravesen Salinas, Urmas Roostalu, Jacob Lercke Skytte, Carsten Gundlach, Jacob Jelsing, Niels Vrang, Jacob Hecksher-Sørensen, Anders Bjorholm Dahl, Tim B. Dyrby

In preparation, 2021

Multimodal 3D mouse brain atlas framework with skull-derived coordinate system

Johanna Perens[1, 2, 4], Casper Gravesen Salinas[1], Urmas Roostalu[1], Jacob Lercke Skytte[1], Carsten Gundlach[3], Jacob Jelsing[1], Niels Vrang[1], Jacob Hecksher-Sørensen[1, +], Anders Bjorholm Dahl[2, +], Tim B. Dyrby[2, 4, +]

[1] Gubra ApS, Hørsholm, Denmark

[2] Section for Visual Computing, Department of Applied Mathematics and Computer Science, Technical University Denmark, Kongens Lyngby, Denmark

[3] Neutrons and X-rays for Materials Physics, Department of Physics, Technical University Denmark, 2800 Kongens Lyngby, Denmark

[4] Danish Research Centre for Magnetic Resonance, Centre for Functional and Diagnostic Imaging and Research, Copenhagen University Hospital Amager and Hvidovre, Copenhagen, Denmark

[+] Tim B. Dyrby, Anders Bjorholm Dahl and Jacob Hecksher-Sørensen contributed equally to this work.

* Corresponding author: Johanna Perens (mail: jpe@gubra.dk)

Abstract

Magnetic resonance imaging and light-sheet fluorescence microscopy combined with immunohistochemistry and tissue clearing enable researchers to investigate the effect of a disease or a treatment to the brain non-disruptively. These imaging modalities provide complimentary information, especially when performed on the same brain *in vivo* and *ex vivo*, which could reveal yet undiscovered biological mechanisms and support translation to clinical measurements. To enable integration of multimodal image analysis on mouse brains, we have developed a digital atlas framework. The framework includes brain templates based on different imaging modalities, brain region annotations from the Allen's Common Coordinate Framework version 3, and a stereotaxic coordinate system. The two latter are available in all brain template spaces and deformation fields are provided for transferring datasets into preferred template spaces. The stereotaxic coordinate system was generated based on bregma and lambda landmarks acquired by X-ray micro computed tomography, allowing users to extrapolate coordinates from *ex vivo* modalities accurately to spatial positions in a living mouse brain. This new multimodal atlas framework allows for quantitative analysis across *in vivo* and *ex vivo* imaging modalities, consistently reporting of experimental results, and undistorted navigating in the brain during stereotaxic surgeries.

1. Introduction

Uncovering complex functions of the brain for understanding disease mechanisms and developing effective therapies requires a combination of multiple neuroimaging techniques. Integration of *in vivo* and *ex vivo* tissue probing modalities, such as magnetic resonance imaging (MRI) and histology, has therefore been attempted before as it would enable researchers to study both temporal changes in a living brain as well as molecular markers in the same tissue post-mortem (Breckwoldt et al., 2016, 2019; Doerr et al., 2017; Goubran et al., 2019; Johnson et al., 2021; Leuze et al., 2017; MacKenzie-Graham et al., 2004; Morawski et al., 2018; Nie et al., 2019; Purger et al., 2009; Stolp et al., 2018).

MRI is a powerful imaging technique due to its non-invasive nature allowing repetitive scanning of human and animal tissue *in vivo* and *ex vivo*, with a wide range of contrast mechanisms and applications to e.g., visualize cellular structure, neuronal activity, neuronal wiring, blood vessels, blood flow, metabolism, infarction, and malignancy (Dyrby et al., 2018, 2011; Matthews and Jezzard, 2004; Symms et al., 2004; Yousaf et al., 2018). Development of ultra-high field MRI has led to improved resolution enabling high-quality preclinical experiments (Dumoulin et al., 2018; Vaughan et al., 2001). However, detection limit in MRI is still in range of several tens of micrometres (N. Wang et al., 2020; Wei et al., 2016). While MRI provides structural and functional information of the tissue in indirect measures, fluorescence microscopy enables directly visualizing cellular structure and function in the scale of few micrometres. Recent progress in *ex vivo* 3D histology involving tissue clearing and fluorescent tagging of molecular markers, such as 3DISCO (Ertürk et al., 2012), iDISCO (Renier et al., 2014), CUBIC (Susaki et al., 2014), CLARITY (Chung et al., 2013), combined with light sheet fluorescence microscopy (LSFM) enables imaging of intact tissue and whole-organ specimen without disrupting their cytoarchitecture. Although LSFM lacks functionality to resolve longitudinal processes, it has become a widely applied imaging technique in preclinical studies for e.g., investigating gene and protein expression (Hansen et al., 2021; Kjaergaard et al., 2019), cellular architecture (Di Giovanna et al., 2018; Friedmann et al., 2020), neural populations (Roostalu et al., 2019; Silvestri et al., 2015), and distribution of fluorescently labelled molecules (Gabery et al., 2020).

Standard processing of neuroimaging datasets involves co-registration of individual brain volumes with a reference atlas for performing analysis across individuals, comparing study groups, and reporting findings (D. Friedmann et al., 2020; Kirst et al., 2020; Perens et al., 2020; Renier et al., 2016; Salinas et al., 2018; Todorov et al., 2020). Recently, efforts have been made to combine LSFM-imaging with other neuroimaging modalities either for obtaining high-quality region delineations from existing brain atlases (Goubran et al., 2019; Murakami et al., 2018; Perens et al., 2021; Stolp et al., 2018) but also for studying correlations of *in vivo* and *ex vivo* MRI-biomarkers (Breckwoldt et al., 2016, 2019; Doerr et al., 2017; Goubran et al., 2019; Stolp et al., 2018). While Goubran and Stolp demonstrated benefits of LSFM-MRI

integration for validating existing neuroimaging biomarkers (viral tract-tracing in comparison to diffusion MRI-based tractography, associations between cellular microstructure and diffusion characteristics), both Doerr and Breckwoldt showed applicational value of the multimodal approach by investigating innervation of implanted neurons (Doerr et al., 2017) and neoangiogenesis patterns of tumors (Breckwoldt et al., 2019, 2016) in mouse brains.

Rodent brain atlas coordinates are instrumental tools in stereotaxic surgery procedures used for electrode implantation, injections of substances or regional ablations. Today, several brain atlases for adult mice are available, including histology-based mouse brain atlases (Chen et al., 2019; Chon et al., 2019; Dong, 2008; Franklin and Paxinos, 1997; Hof et al., 2000; Jacobowitz and Abbott, 1997; Kaufman, 1992; Rosen et al., 2000; Sidman et al., 1971; Valverde, 2004; Q. Wang et al., 2020), MRI-based atlases (Aggarwal et al., 2009; Badea et al., 2007; Chan et al., 2007; Chuang et al., 2011; Chung et al., 2013; Dorr et al., 2008; Kovačević et al., 2005; Ma et al., 2008, 2005) and combined 2D histology and MRI-based atlases (Johnson et al., 2010; MacKenzie-Graham et al., 2004; Patel, 2018) but only three with skull-derived stereotaxic coordinates (Aggarwal et al., 2009; Dong, 2008; Franklin and Paxinos, 1997). While histology-based atlases exhibit high-resolution structural information and detailed region delineations (Dong, 2008; Franklin and Paxinos, 1997), their structures cannot be translated directly into *in vivo* space. For example, brain collection, processing, and sectioning is likely to introduce deformations leading to inaccuracies compared to *in situ* stereotaxic coordinates (Chan et al., 2007; Li et al., 2013). Another limitation of currently available stereotaxic atlases is the manual approach in identifying skull landmarks for determining the origin of the coordinate system and correct angle of the brain. To circumvent these limitations, objective and consistent detection of skull landmarks may be achieved by applying a standardized computational approach similar to the one developed by Blasiak and colleagues (Blasiak et al., 2010) and using population-averaged landmark locations for generating a coordinate system.

To bridge the gap between microscopic and macroscopic imaging techniques while also enabling translation of findings from *ex vivo* datasets into *in vivo* space, we have developed a multimodal atlas framework. The framework includes MRI and LSFM brain templates, Mouse Brain Common Coordinate Framework (CCFv3) by Allen Institute of Brain Science (AIBS) with serial two-photon microscopy (STPT) brain template (Wang et al., 2020), and a stereotaxic coordinate system based on automatically detected landmarks on computed tomography (CT) -imaged skulls. The AIBS CCFv3 was chosen to bridge the LSFM and MRI templates with the aim to provide access to its comprehensive resources such as region delineations, gene expression database and tract-tracing experiments. Atlas resources will be made freely available via Github (https://github.com/Gubra-ApS/Multi-modal-mouse-brain-atlas) to enable adoption of multimodal approach in standardized computational image analysis pipelines.

2. Results

2.1 Concept of the multimodal atlas framework

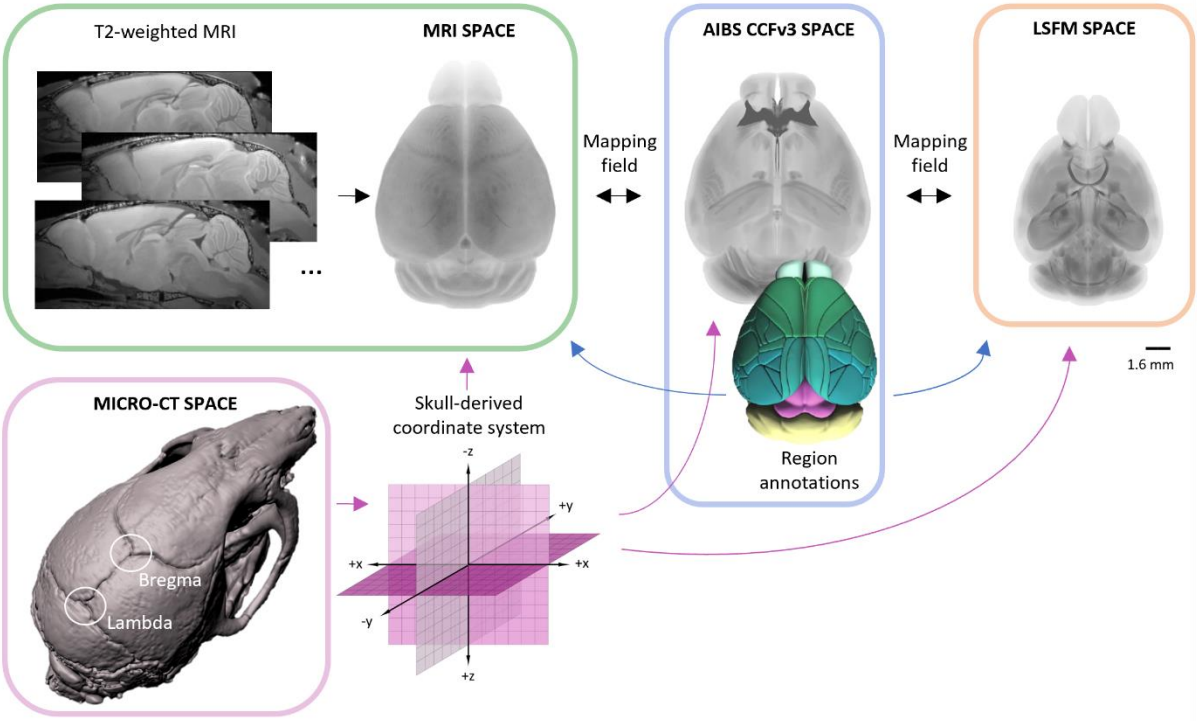

Fig. 1 Framework for a multimodal mouse brain atlas with a stereotaxic coordinate system. CT- and MRI-imaging of 12 mouse head volumes enabled generation of a high-resolution T2-weighted ex vivo-in situ brain template with a coordinate system based on semi-automatically extracted skull landmarks. In order to equip brain templates of different imaging modalities with the same atlas functionalities, a skull-derived coordinate system was transferred from the MRI template to the AIBS CCFv3 and LSFM templates, and region annotations from the AIBS CCFv3 to the MRI and LSFM templates (latter described in (Perens et al., 2021)). Dedicated deformation field volumes were constructed to facilitate mapping of datasets between the three template spaces. All brain templates have an isotropic voxel size of $(25\ \mu m)^3$ and are shown together in the figure with a CT-skull in the same scale.

Multimodal atlases combine brain templates of different imaging modalities in one common space. For the multimodal atlas framework (Fig. 1), we chose another approach as whole-brain samples for LSFM and STPT are extracted from skull, undergo chemical treatment (before LSFM) or sectioning (during STPT), resulting in considerable morphological differences compared to in *vivo*/*in situ* MRI-imaged brains. Therefore, the current atlas framework comprises of MRI-, STPT- and LSFM-based brain templates in their own respective morphological spaces. The MRI brain template was constructed from high-resolution T2-weighted images of brains imaged in skull to mimic *in vivo* setting as closely as possible. The

STPT- and LSFM-based brain templates were adopted from the AIBS CCFv3 (Allen Institute for Brain Science, 2017; Wang et al., 2020) and previously described iDISCO/LSFM-based atlas (Perens et al., 2021). All brain templates were resampled to isotropic voxel size of (25 µm)^3. For enabling transfer of datasets from one template space to another, applicable mapping fields were constructed from deformations introduced when aligning the MRI and AIBS STPT-based templates as well as the AIBS STPT- and LSFM-based templates. Here, the AIBS STPT-based template served as an intermediate between the *in situ* MRI and *ex vivo* LSFM spaces.

In addition to MRI-, STPT- and LSFM-based brain templates, the multimodal atlas framework includes average diffusion MRI parameter maps, detailed region delineations and stereotaxic coordinates in all template spaces. Brain region delineations were adopted from the AIBS CCFv3 and transferred to the other template spaces via mapping fields (the LSFM template already included the AIBS CCFv3 region delineations imported in a similar fashion in a previous work (Perens et al., 2021)). An anatomically accurate stereotaxic coordinate system was generated by computationally identifying standard reference landmarks in CT-imaged skulls and spanning out a coordinate system related to average bregma and lambda positions in the MRI space. Mapping fields were applied here to transfer the coordinate system to the AIBS STPT and LSFM spaces.

2.2. Experimental design

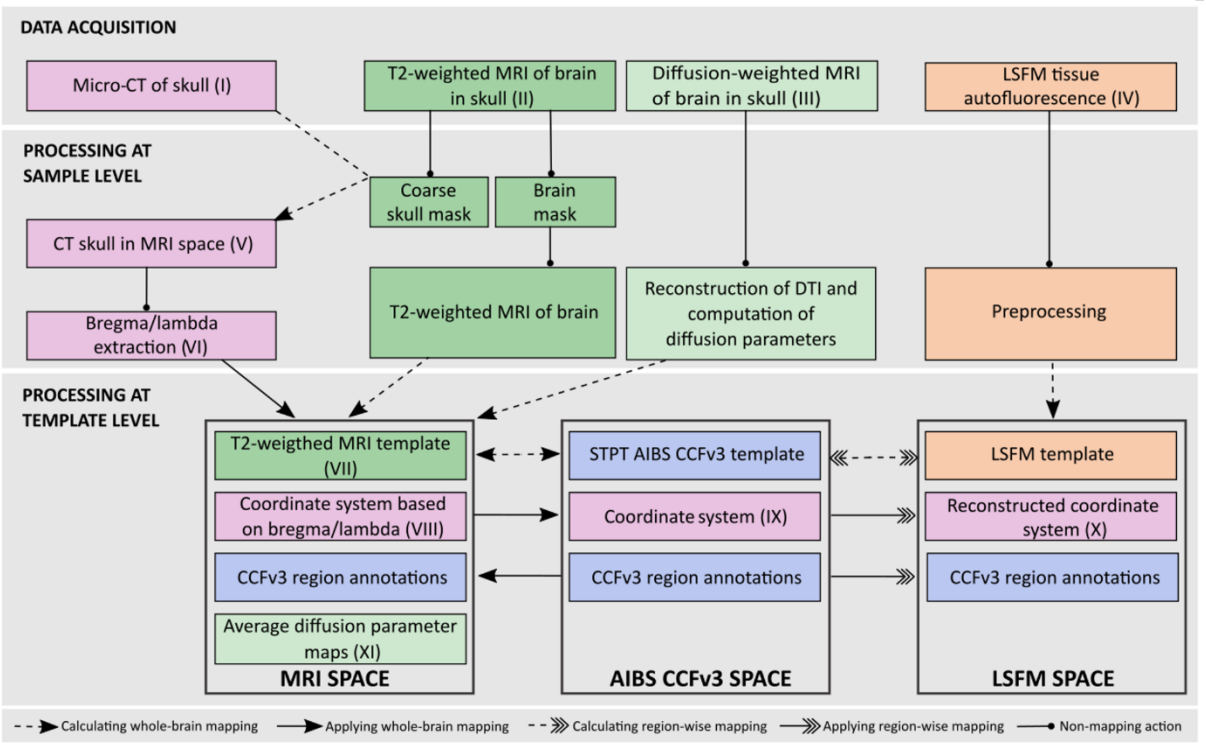

Fig. 2 Computational pipeline for generating a multimodal mouse brain atlas. The computational pipeline describes the architecture and order of the image processing steps for integrating information from CT, MRI, STPT-based AIBS CCFv3, and LSFM. Color-coding of

the steps relates to the modality where information has been extracted from: purple denotes CT, green T2-weighted MRI, light green diffusion MRI, orange LSFM, and blue STPT. Edges connecting the pipeline nodes describe the nature of processing steps: arrow with continuous line indicates computation and application of a transformation matrix while arrow with dashed line stands for application of an already computed transformation matrix, arrow with several arrow-heads indicates region-wise mapping while arrow with single arrow-head stands for whole-brain mapping, and an edge with circular tip connects to the next intermediate result in the computation pipeline achieved by other means than registration. Roman numbers refer to the intermediate results of the processing pipeline shown in Fig. 3 and 4.

The pipeline for setting up multimodal atlas framework (depicted in Fig.2) can be divided into three main stages: data acquisition, sample level image processing and template level image processing. Data acquisition involved collection of image volumes from 12 mouse heads with micro-CT, MRI and LSFM while MRI comprised of T2-weighted structural and diffusion-weighted scans. Initial processing at sample level included segmenting of brain tissue and cranial bone from the T2-weighted MRI scans. Brain tissue segmentations were used as masks to remove skull and superficial non-brain tissue from the T2-weighted images and skull segmentations served as proxies to mediate alignment of CT-imaged skull volumes to T2-weighted MRI brain images of each individual mouse. Subsequently, exact locations of the reference landmarks, bregma and lambda, were identified from MRI-aligned CT skull surfaces. In parallel, diffusion tensors were reconstructed from diffusion-weighted MRI and parameter maps computed from diffusion tensors. Individual LSFM-imaged brain volumes underwent pre-processing similarly to previously published data (Perens et al., 2021).

Processing at template level involved generation of T2-weighted MRI brain template by iterative multi-resolution alignment and averaging algorithm (Kovačević et al., 2005; Kuan et al., 2015; Umadevi Venkataraju et al., 2019). A chain of transformation matrices computed in the template creation process for aligning individual T2-weighted MRI images were applied to bregma and lambda of the same animals for transferring skull landmarks to an average T2-weighted MRI template. Subsequently, an average location was determined for template-aligned bregma and lambda landmarks followed by generation of a 3D coordinate system in the MRI space. Diffusion parameter maps of individual animals were transferred to an oriented T2-weighted MRI template and averaged. Finally, the T2-weighted MRI-, AIBS STPT- and LSFM-based brain templates were linked to each other by 4D deformation fields resulting from bi-directional alignment of the T2-weighted MRI- and AIBS STPT-based templates as well as the AIBS STPT- and LSFM-based templates. Region delineation from the AIBS CCFv3 and stereotaxic coordinates from the T2-weighted MRI templates were transferred to the other templates by applying deformation fields generated in the previous step.

2.3 Multimodal imaging of a mouse brain sample

In the current work, we demonstrate the feasibility of sequential imaging the same mouse specimen with three very different modalities while preserving tissue integrity, tissue contrast and achieving high-quality datasets. Raw micro-CT, MRI and LSFM image volumes of the same specimen are shown in Fig. 3a. The micro-CT-imaged skull volume was acquired with an isotropic voxel size of $(22.6\ \mu m)^3$, the T2-weighted MRI with $(78\ \mu m)^3$, the diffusion-weighted MRI with $(125\ \mu m)^3$ and the LSFM tissue autofluorescence with $(4.8\ \mu m)^2$ in plane and 10 µm axial voxel size. Coronal, sagittal and lambdoidal sutures were clearly visible on the micro-CT-imaged skull surface. The T2-weighted MRI brain image showed strong contrast between the white and grey matter, no signal in the skull area, and high signal for the superficial tissues. Diffusion-weighted MRI exhibited high signal in areas with restricted diffusion perpendicular to the applied gradient direction (in total 60 gradient directions were applied) and no signal for skull and superficial tissue. LSFM volumes of tissue autofluorescence show high contrast between different tissue types, despite keeping the perfusion fixed brain sample in phosphate buffered saline for 2-4 weeks while performing micro-CT and MRI scanning. Transferring the micro-CT skull dataset to one of the T2-weighted MRI brains shows that a mouse brain fills tightly the inner volume of the skull (Fig. 3b).

2.4 Establishing precise origin and orientation for a stereotaxic atlas

Stereotaxic coordinate systems rely on anatomical landmarks on the skull surface which have a fixed geometric relation to underlying brain structures and have uniform locations across individuals. Standard cranial landmarks are bregma and lambda, located at the intersection of the coronal suture with the cranial midline and at the intersection of lambdoidal suture with the cranial midline, respectively (Blasiak et al., 2010; Franklin and Paxinos, 1997). Both reference points are necessary to navigate accurately in the brain as they define the origin of the coordinate system and orientation of the head used in stereotaxic surgery. Fig. 3c-d visualizes the procedure for semi-automatically extracting bregma and lambda landmarks from CT-imaged skulls.

Skull sutures made of connective tissue appear as few millimeter deep grooves between cranial plates. Due to their different depth compared to the skull surface, the sutures can be identified by generating a depth image in the dorsal-ventral axis. Then, the skull is extracted from the depth image and the top part of the skull surface is projected onto 2D plane by saving the voxels with highest intensity in dorsal-ventral axis. In the projected image, skull sutures appear as void structures and can be manually segmented (Fig. 3c, left). Individual skull sutures were then fitted (Fig. 3c, middle) and coronal and lambdoidal suture junctions at the sagittal suture were computed to obtain xy-coordinates of the landmarks (Fig. 3c, right). z-coordinates were determined by locating the outer edge of skull surface at the xy-coordinate in the dorsal direction (Fig. 3d).

To generate a stereotaxic coordinate system, skull landmarks were aligned with an anatomical brain template. For this purpose, the T2-weighted MRI brain template created from 12 mouse

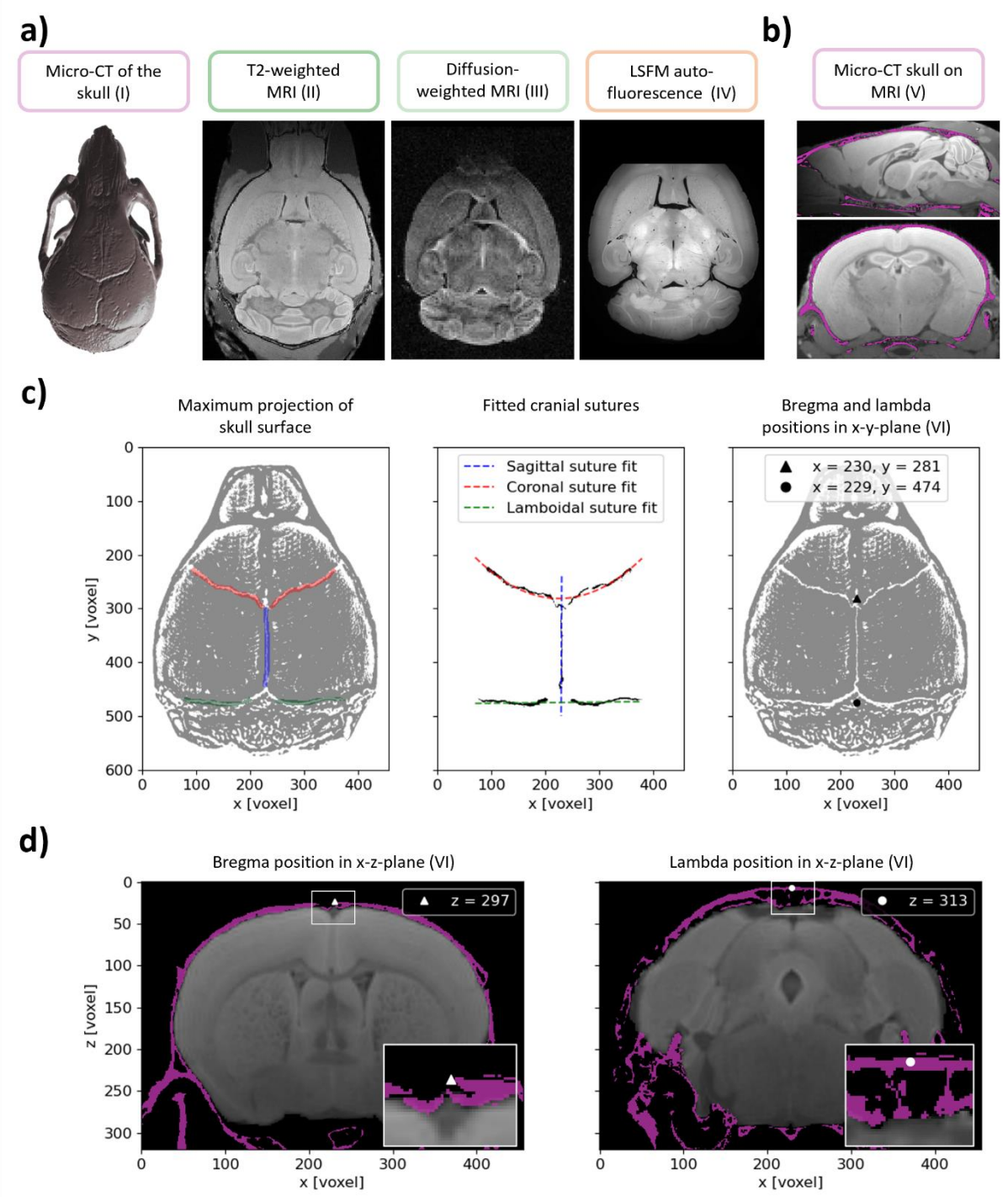

Fig. 3 Automatic extraction of bregma and lambda from CT skull volumes. a) Raw images of the skull and brain from the same mouse acquired sequentially via CT with efficient isotropic voxel size of $(22.6\ \mu m)^3$, T2-weighted MRI with isotropic voxel size of $(78\ \mu m)^3$, diffusion MRI with isotropic voxel size of $(125\ \mu m)^3$ (shown for one gradient direction from 60) and LSFM with $(4.8\ \mu m)^2$ in plane and 10 µm axial voxel size. Both T2-weighted and diffusion MRI were acquired from a brain in the skull. Brains were dissected from skulls for iDISCO+ treatment and clearing before performing LSFM. b) A rigidly aligned CT-imaged skull (purple) to the T2-weighted MRI brain image (grayscale) of the same mouse. c) Extraction and fitting of coronal

(red), sagittal (blue) and lamboidal (green) sutures for determining x-y-coordinates for bregma (Δ) and lambda (o). Sutures were extracted from maximum projection images of skull surfaces by manually drawn suture masks while bregma and lambda were found by identifying intersection points of the individual suture fits. d) Determination of the z-coordinate for bregma (Δ) and lambda (o) on top of the skull. Roman numbers indicate steps in the processing pipeline shown in Fig. 2 for which the result is shown.

brain images was used (Fig. 4a). Before transferring individual bregma and lambda coordinates into the template space, the T2-weighted MRI template was refined by contrast-enhancement and mirroring a hemisphere with highest quality, resulting in a symmetric atlas when viewed from coronal and horizontal orientations. Individual bregma and lambda coordinates where then averaged in the template space, followed by rotation of the T2-weighted MRI template for aligning the average bregma and lambda landmarks to the same horizontal level (Fig. 4b). The final template-space coordinates for the average bregma were x = 227.00 $\pm$ 4.73 voxels, y = 270.00 $\pm$ 5.80 voxels, z = 16.00 $\pm$ 1.85 voxels and for the average lambda were x = 227.00 $\pm$ 3.32 voxels, y = 462.00 $\pm$ 1.87 voxels, z = 16.00 $\pm$ 1.00 voxels (Fig. 4b-c). The average distance measured between bregma and lambda landmarks of individual animals was found to be Δ(bregma, lambda) = 192 $\pm$ 5.94 voxels corresponding to Δ(bregma, lambda) = 4.80 $\pm$ 0.15 mm.

2.5 Skull-derived stereotaxic coordinate system for MRI, AIBS CCFv3 and LSFM atlases

A stereotaxic coordinate system was generated in the oriented T2-weighted MRI template space originating from the average bregma position according to the coordinate-convention followed by Paxinos and Franklin (Franklin and Paxinos, 1997) with isotropic step size of 0.025 mm (Fig. 4e, left column). The coordinate-convention defines that the x-axis corresponds to medial-lateral axis, the y-axis to anterior-posterior axis, and the z-axis to dorsal-ventral axis. Additionally, the convention implicates the x-coordinates are positive for both hemispheres, y-coordinates are positive anterior to the origin and negative posterior to the origin, and z-coordinates are positive ventral to the origin and negative dorsal to the origin. The resulting coordinate system was transferred to the AIBS STPT- and LSFM-based templates via pre-computed deformation fields (Fig. 4e, middle and right columns). Both the AIBS STPT- and LSFM-based templates were reoriented to show comparable y-coordinate values for structures in the same coronal planes. Also, a volume with the original orientation of the AIBS CCFv3 with skull-derived coordinates was kept in the atlas framework. Conversion of the coordinate system to the AIBS STPT- and LSFM-based templates caused the coordinate system to deform when following the same anatomical structures as in the T2-weighted MRI template. Since this deformation of the coordinate system reflects the changes incurred during tissue processing it is barely visible in the AIBS space while the coordinates in the LSFM space exhibited non-equidistant spacing and extensive deformation (Fig. 4e).

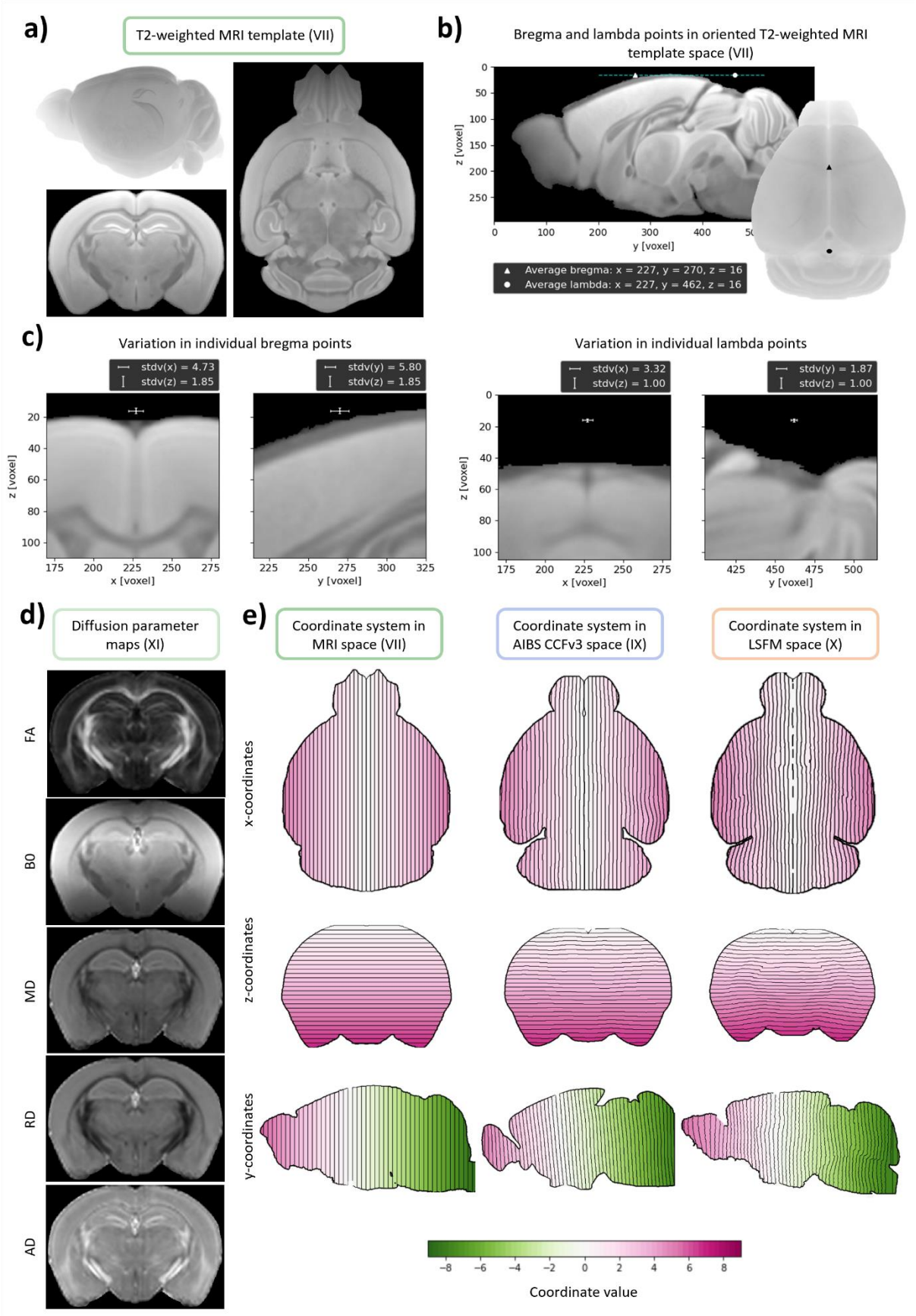

Fig. 4 Skull-derived coordinate system in MRI, AIBS CCFv3 and LSFM spaces. a) The MRI

template created from 12 in-skull-imaged T2-weighted MRI images using an iterative registration and averaging algorithm. b) Position of the average bregma (Δ) and lambda (o) points in the MRI template space visualized in sagittal and 3D top view. The MRI template was oriented such that the average bregma and lambda points are on the same z-level (shown by the cyan dashed line). c) Variation in bregma and lambda positions of individual skulls shown as a standard deviation from the average bregma and lambda in x-, y-, and z-dimensions. d) Coronal slices of averaged diffusion tensor derived parameters created from 7 in-skull-imaged diffusion-weighted MRI images: fractional anisotropy (FA), B0, mean diffusivity (MD), radial diffusivity (RD) and axial diffusivity (AD). Intensity in FA maps was scaled to range $[0,1]$ and intensity of MD, AD and RD to range $[0,0.0006]$. e) A coordinate system was created in the bregma-lambda oriented MRI template space with isotropic coordinate spacing of (25 µm)^3 and transferred to the AIBS CCFv3 and bregma-lambda oriented LSFM template spaces by applying transformation matrices from the whole-brain mapping between the MRI template and AIBS CCFv3 and region-wise mapping between the AIBS CCFv3 and LSFM template. The coordinate system is visualized in horizontal view for x-coordinates, coronal view for z-coordinates, and sagittal view for y-coordinates. Color scale indicates coordinate values for every voxel and equidistant (step size 250 µm from origin) contour lines (black) indicate levels at which coordinate values are constant. Roman numbers indicate steps in the processing pipeline shown in Fig. 2 for which the result is shown.

2.6 Integrating information between atlas spaces

Conversion of data volumes between the MRI, AIBS CCFv3 and LSFM spaces is enabled via deformation fields provided together with the multimodal atlas. Deformation fields are 4D matrices describing the 3-dimensional movement of every voxel in a transferable data volume which can be applied to image volumes using a software for biomedical image registration (e.g., Elastix). Conversion of the skull-derived stereotaxic coordinate system to the AIBS CCFv3 and LSFM spaces was performed using constructed deformation fields. Identical anatomical structures were found in the close proximity of the landmarks in the MRI-, AIBS STPT- and LSFM-based templates indicating correspondence of the skull-derived stereotaxic coordinate system in all three template spaces (Fig. 5a). For demonstrating mapping accuracy between the MRI-, AIBS STPT-, and LSFM-based templates, a random LSFM and T2-weighted MRI image was aligned to all three brain templates via deformation fields (Fig. 5b). Matching structures of every brain template with the overlayed sample volume suggest that the transfer between brain templates of the multimodal atlas is accurate.

3. Discussion

Recent progress in non-destructive neuroimaging methods and registration software has enabled sophisticated alignment strategies for establishing a multimodal mouse brain atlas framework with stereotaxic coordinates. In contrast to previously reported multimodal atlases, which combine brain templates from different types of imaging modalities and region delineation overlay in one reference space (MacKenzie-Graham et al., 2004; Nie et al., 2019;

Purger et al., 2009), the multimodal atlas framework preserves the templates in their modality-specific space together with region delineations and stereotaxic coordinates. Deformation fields make it possible to move newly acquired datasets between the template spaces. The approach adopted in previously published research works for creating multimodal atlases, suits well for integrating modalities relying on similar sample processing protocols and thus, results in brain templates with comparable morphology, which do not require extensive deforming upon alignment. Alignment of such brain templates with newly acquired sample volumes, would not affect registration quality due to rather small morphological differences between the template and sample. However, processing of LSFM-imaged samples introduce morphological changes due to tissue shrinkage caused by clearing media (Qi et al., 2019; Renier et al., 2016). Given the different morphologies, combination of MRI and LSFM brain templates would result in error-prone whole-brain mapping requiring laborious region-wise registration procedures for aligning newly acquired samples with respective templates. This is avoided here, when using modality-specific spaces in the multimodal atlas.

Angle and origin of the stereotaxic coordinate system generated for the multimodal atlas framework rely on standard skull landmarks bregma and lambda. In the past, few alternative landmarks have been proposed for navigating in murine brains. Chan and colleagues (Chan et al., 2007) suggested a new landmark pair consisting of the lambda suture junction and the rostal confluence of the venous sinus (RCS) anterior to bregma, as they showed not only less variability between specimen, but also between mouse strains compared to using paired bregma and lambda. Intersection point of the posterior edges of the cerebral hemispheres as an origin of a stereotaxic coordinate system for murine brains has also been proposed (Xiao, 2007). As both landmark systems are not visually detectable from the dorsal skull surface and can only be visualized in an intersectional view of the imaged skull or brain, they require exposure of the brain or image-guidance during surgery. Stereotaxic surgeries of rodent brains are rarely performed with CT- or MRI-guidance, but emerging camera-guided robotic systems for intra-cranial surgeries (Ly et al., 2021) combined with neural networks (Zhou et al., 2020) could help to identify less variable cranial landmarks to potentially adopt additional anatomical reference points.

In the current work, bregma and lambda landmarks were detected from CT-imaged skull surfaces by identifying intersection points of fitted cranial sutures. Similar to Chan and colleagues (Chan et al., 2007), we observed higher variance when identifying bregma coordinates compared to lambda coordinates in all three dimensions, which is in agreement with more variable shape and sharper angle between coronal sutures compared to lambdoidal sutures. Highest standard deviation from the mean coordinates was found in y-dimension for both landmarks and reached maximally 145 µm. This could be attributed to the initial manual orientation of individual skulls into a flat-surface position for landmark detection, resulting in slightly different perspective to suture lines in the maximum-projection image of the skull surface. Identification of bregma and lambda coordinates from individual animals allowed to determine the mean distance between reference landmarks. Consistently

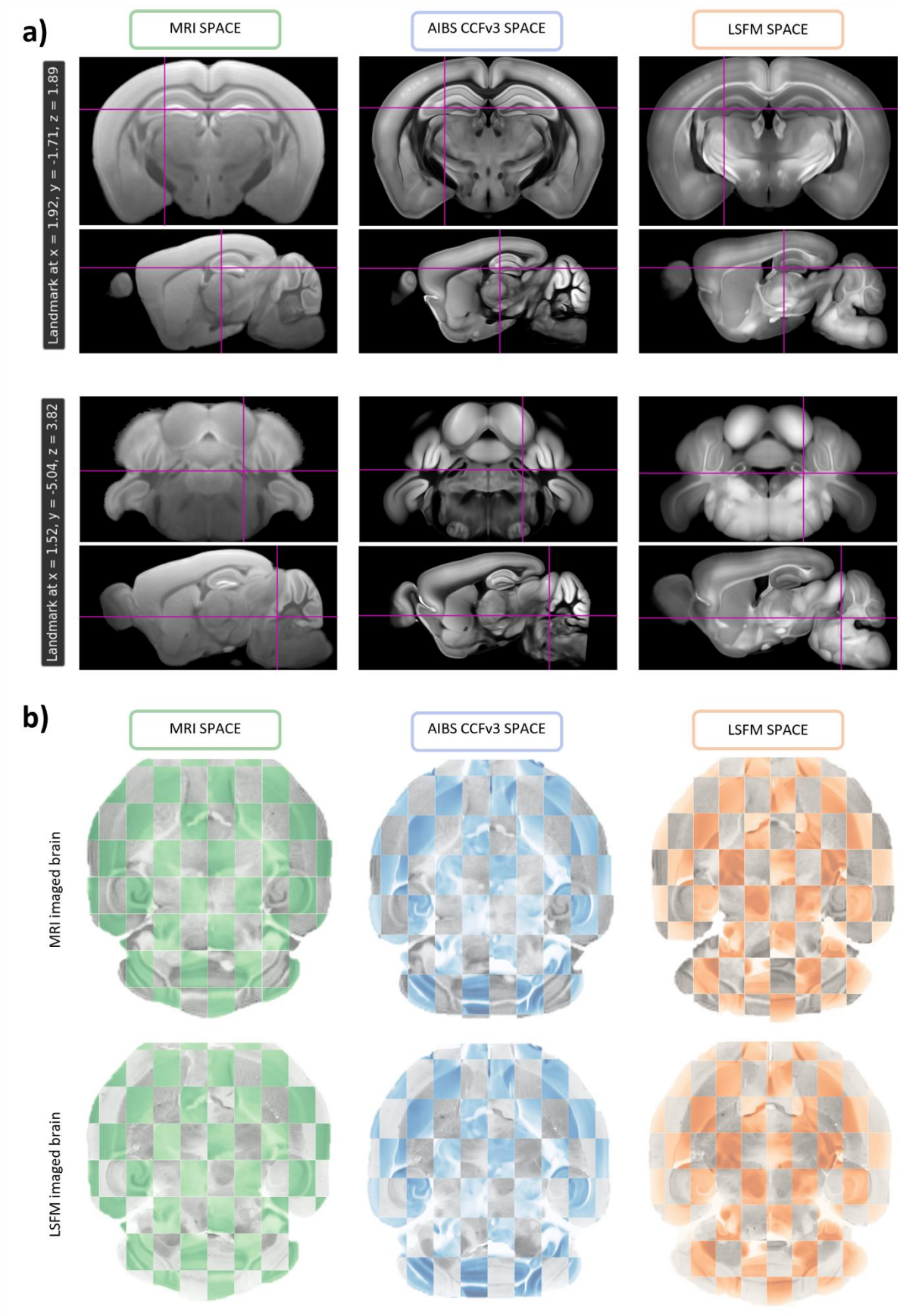

Fig. 5 Correspondence of the coordinate system and accuracy of deformation field mapping

between the MRI, AIBS CCFv3 and LSFM spaces. a) Two anatomical landmarks, one in the dentate gyrus (two upper panels) and one in the parabrachial nucleus (two lower panels), shown in the MRI, AIBS CCFv3, and LSFM template spaces in coronal and sagittal view. Purple crosshair indicates the spatial location of the exact same x-, y-, and z-coordinate in all three template spaces. b) Checkerboard representation of a randomly picked MRI- (upper panel) and LSFM-imaged (lower panel) brain sample registered to the MRI, AIBS CCFv3, and LSFM template spaces via constructed deformation fields. The mapped MRI- and LSFM-imaged samples are visualised in grayscale while the MRI, AIBS CCFv3 and LSFM templates are depicted in green, blue and orange color scales, respectively.

approx. 0.6mm higher values for bregma-lambda distance were observed compared to reported values (Aggarwal et al., 2009; Franklin and Paxinos, 1997; Zhou et al., 2020). This is probably related to the parabolic fitting of coronal sutures in this work, causing bregma to move slightly anterior from the true intersection point of the coronal and sagittal sutures.

The multimodal atlas framework has a fixed 25 µm isotropic voxel size. Re-sampling of the atlas to other voxel sizes can be accomplished by creating all templates with the new voxel size, calculating mapping fields between the templates, and aligning a newly generated coordinate system with updated grid-spacing with other templates. Assigning coordinate values at ventricle borders posed a challenge in bridging the different imaging modalities due to observed enlargement of ventricles in cleared brains. To overcome this, we used interpolation of coordinates from neighbouring regions. This can potentially result in minor inaccuracies, as one voxel in the MRI space can be mapped to several in LSFM space.

	Multimodal atlas	Franklin and Paxinos	AIBS CCFv1	Aggarwal et. Al., 2009
Age [weeks]	10	8-14	8	9
Skull extraction	no	yes	yes	no
Modality	MRI	2D histology	2D histology	MRI
Sample treatment	perfusion fixation	perfusion fixation, frozen	fresh-frozen	perfusion fixation
Width in x [mm]	10.2	9.2	10.6	10
Length in y [mm]	14.3	15.0	15.0	14.3
Depth in z [mm]	7.3	5.9	7.3	6.3

Table 1. Dimensions of brain templates in existing stereotaxic brain atlases for C57Bl/6J mice. Dimensions describe the size of the brain template in 3-dimensions and are derived from stereotaxic grids overlayed with the template. x-, y- and z-axis correspond to medial-lateral, anterior-posterior and crania-caudal axes, respectively. Length of the brain in y-axis was defined as the distance between the tip of the olfactory bulb and the end of cerebellum.

Measurements of the width, length and depth of the brain templates have an uncertainty of 0.1-0.2 mm depending on the atlas.

The skull-derived coordinate system allows for comparing the dimensions of the *ex vivo-in situ*-imaged T2-weighted MRI template to dimensions of other existing stereotaxic atlas templates (Table 1). Comparison of brain templates from different standard atlases reveals that width and depth of the Franklin and Paxinos atlas template is at least 1 mm smaller than that of the multimodal atlas MRI template. Furthermore, length of the AIBS CCFv1 and Franklin and Paxinos atlas template is 0.7 mm larger while depth of Aggarwal's template was found to be 1 mm smaller compared to the respective dimensions of the multimodal atlas MRI template. Size discrepancies to the multimodal atlas MRI template can be related to age and biological variance between individual brains, since the T2-weighted template is based on population-averaged brain volume, whereas templates of the other stereotaxic atlases rely on single specimen. The possible reason for considerably smaller width and depth of the Franklin and Paxinos atlas template is due to fixation-related shrinkage of skull-extracted tissue (Lee et al., 2021). Increased length of the Franklin and Paxinos atlas and the AIBS CCFv1 template could be caused by variations in microtome section thickness of a few-µm range accumulating for hundreds of collected sections.

We and others have previously mapped brain-wide response to CNS drug treatment at high resolution using light sheet microscopy (Gabery et al., 2020; Hansen et al., 2021; Kjaergaard et al., 2019; Skovbjerg et al., 2021). These studies have revealed important insights into brain circuits influenced by drug treatment. Further analysis of these identified neuronal populations using e.g., brain site-specific drug application, viral tract-tracing for connectome studies or electrode implantation has been hampered by difficulties in transferring the coordinates from the LSFM space *in vivo* settings. First, the presented atlas framework allows identifying the exact spatial location of neuronal populations *in vivo* for performing accurate stereotaxic targeting. Secondly, compatibility of the LSFM space with the MRI and AIBS CCFv3 space permits large-scale integration of LSFM-imaged neuronal populations with AIBS' gene expression and connectivity atlases. The applicability extends also to other open-source MRI, STPT and LSFM datasets available at Neuroimaging Tools & Resources Collaboratory (NITRC) repository, OpenNeuro platform by Stanford Center for Reproducible Neuroscience, EBRAINS data repository.

In summary, we have established a multimodal mouse brain atlas framework with a skull-derived coordinate system, including *ex vivo-in situ* MRI-based, the AIBS *ex vivo* STPT-based, as well as *ex vivo* LSFM-based templates in modality-specific spaces, and deformation fields bridging the 3D whole-brain templates. The purpose of the atlas is to facilitate integrating and performing combined analysis of *in vivo* and *ex vivo* whole-brain datasets via co-registration. Also, the atlas provides stereotaxic coordinates more closely reflecting *in situ* coordinates for enabling anatomically more accurate data reporting and improve stereotaxic surgery procedures. The multimodal atlas framework is extendable with other brain templates (e.g., based on various MRI contrasts, clearing methods, imaging modalities), region delineation

volumes (e.g., (Chon et al., 2019)), coordinate systems based on different origin (e.g., (Chan et al., 2007; Xiao, 2007)), anatomical maps (e.g., vascular trees (Di Giovanna et al., 2018; Todorov et al., 2020), and structural connectivity (Friedmann et al., 2020).

4. Materials and methods

4.1 Animals and sample preparation

Animal experiments were conducted in compliance with internationally accepted principles for the use of laboratory animals and approved by Danish Animal Experiments Inspectorate (license #2013-15-2934-00784). Male C57Bl/6J mice (n=12) were obtained from Janvier Labs (Le Genest-Saint-Isle, France) and housed in controlled environment (12h light/dark cycle, 21±2˚C humidity 50±10%) with ad libitum access to tap water and chow (Altromin 1324, Hørsholm, Denmark). 10-week old mice were sacrificed via transcardial perfusion of heparinized phosphate buffered saline (PBS) and 40 ml of 10% neutral buffered formalin (CellPath, Newtown, UK) while under 2-4% isoflurane/O_2 (Attane Vet., ScanVet Animal Health, Fredensborg, Denmark) anaesthesia. Mouse skulls were removed and cleaned from superficial tissue, then post-fixed in 10% neutral buffered formalin for four days at 4˚C and washed to remove excess fixative in PBS/NaN_3 for 2-4 weeks until CT and MRI. After CT and MRI imaging, brains were carefully dissected from skulls and processed according to iDISCO+ (immunolabeling-enabled three-dimensional imaging of solvent-cleared organs) protocol (Renier et al., 2014) as described in (Perens et al., 2021) using reagents from the same vendors. In contrast to the original iDISCO+ protocol, no antibodies were included in the staining buffers.

4.2 Data acquisition

4.2.1 Micro-computed tomography (micro-CT)

For obtaining bregma and lambda locations from skull surface, 3D mouse skull volumes were imaged using high-resolution micro-CT. Bregma and lambda are visually detectable landmarks on the skull, which are conventionally used to navigate in the brain of a living mouse, for example during stereotaxic surgeries. Image volumes were acquired with ZEISS XRadia Versa XRM-410 scanner at the 3D Imaging Centre, at Technical University of Denmark, by collecting 1601 projections of the skull with exposure time of 2s per projection and tube voltage set to 50 kVp. Resulting skull volumes exhibited isotropic voxel size of $(22.6\ \mu m)^3$.

4.2.2 Magnetic resonance imaging (MRI)

Ex vivo-in situ MRI mouse brain scanning was done at the Danish Research Centre for Magnetic Resonance using a 7.0 T Bruker Biospec preclinical MRI system equipped with a maximum strength of 660 mT/m. Transmit/receive used a dual cryogenic radiofrequency surface coils optimised for mouse brain MRI (CryoProbe, Bruker Biospin MRI GmbH, Ettlingen, Germany). The imaging protocol included a 3h-long high-resolution structural T2-weighted MRI and a subsequent 13h-long diffusion-weighted scan. For acquiring the T2-weighted MRI, a True 3D FISP sequence (i.e., gradient balanced steady-state coherent sequence along three

axes) was used with the following settings: flip angle = 30˚, TE = 2.5 ms, TR = 5.1 ms, number of repetitions = 1, number of averages = 60, bandwidth = 12 5kHz, image size = 256 × 256 × 128 pixels, field of view = 20 mm × 20 mm × 10 mm, and isotropic voxel size of $(78\ \mu m)^3$. For acquiring the diffusion-weighted MRI, a spin echo sequence with single line read-out was used with the following settings: flip angle = 90˚, TE = 26 ms, TR = 5700 ms, number of repetitions = 1, number of averages = 1, bandwidth = 20 kHz, matrix size = 128 × 128, field of view = 16 mm × 16 mm, number of slices = 55, slice thickness = 0.125 µm, isotropic voxel size of $(125\ \mu m)^3$, gradient strength = 456 mT/m, gradient duration = 5 ms, gradient separation = 13 ms, encoding duration =0.8 ms, and number of directions = 60. A b-value of 4000 s/mm^2 adjusted to *ex vivo* tissue with decreased diffusivity was used.

4.2.3 Light sheet fluorescence microscopy (LSFM)

Skull-dissected and cleared brain samples were imaged in dibenzyl ether in axial orientation on a LaVision ultramicroscope II (Miltenyi Biotec, Bergisch Gladbach, Germany) equipped with a Zyla 4.2P-CL10 sCMOS camera (Andor Technology, Belfast, UK), SuperK EXTREME supercontinuum white-light laser EXR-15 (NKT Photonics, Birkerød, Denmark), and MV PLAPO 2XC (Olympus, Tokyo, Japan) objective lens. Version 7 of the Imspector microscope controller software was used. Images from tissue the structure were acquired at an excitation wavelength 560 nm $\pm$ 20 nm and emission wavelength of 620 nm $\pm$ 30 nm with 80% laser power, 1.2X total magnification, 257 ms exposure time, 9 horizontal focusing steps, and blend-blend mode in a z-stack at 10 µm intervals. Resulting brain volumes (16 bit-tiff) had a $(4.8\ \mu m)^2$ in-plane and 3.8 µm axial voxel size (NA = 0.156).

4.3 Brain atlases bridged in the current work

4.3.1 Mouse common coordinate framework by Allen Institute of Brain Science (AIBS CCF)

Latest version of the AIBS CCF, CCF version 3 (CCFv3) released in 2017 includes a 3D template brain based on tissue autofluorescence volumes and an annotation volume with 662 region delineations (Allen Institute for Brain Science, 2017; Q. Wang et al., 2020). Raw data of the template stems from 1675 specimens collected with a serial two-photon tomography (STPT) in the red channel (excitation at 925 nm) in coronal 2D sections with an in-plane voxel size of $(0.35\ \mu m)^2$ at every 100 µm through the anterior-posterior axis. The CCFv3 is accessible with isotropic voxel sizes of $(10\ \mu m)^3$ and $(25\ \mu m)^3$ which could be realized in anterior-posterior dimension due to slight offsets in positions of vibrotome-cut sections for each brain. Region annotations provided by the CCFv3 are manually drawn delineations in 3D space based on features from structural, transgenic, tracing, cytoarchitectonic, chemoarchitectonic, and in situ hybridization datasets.

4.3.2 Light sheet fluorescence microscopy (LSFM) based mouse brain atlas

The LSFM based atlas was made publicly available in 2020 and includes a 3D template brain based on tissue autofluorescence volumes of iDISCO+ processed brains and an annotation volume transferred region-wise from the AIBS CCFv3 (Perens et al., 2021). An anatomical

template of the LSFM atlas was created from 139 brain volumes acquired in the red channel (excitation at 560 nm $\pm$ 20 nm, emission at 650 nm $\pm$ 25 nm) by optically sectioning samples in the axial orientation with $(4.8\ \mu m)^2$ in-plane voxel size, 3.8 µm axial voxel size, and a 10 µm distance between the sections. The final voxel size of the LSFM atlas is $(20\ \mu m)^3$ in all three dimensions. The atlas is fully dedicated for mapping cleared and LSFM-imaged brain samples as the chemicals used in the iDISCO+ protocol causes brain samples to deform resulting in a different morphology than the AIBS CCFv3 template.

4.4 Image processing

4.4.1 General

The majority of data processing was performed in Python 3.7 except the extraction of brain tissue from T2-weighted MRI scans which was performed in MATLAB R2020a. All the scripts used for data processing were custom-made and based on publicly available packages such as, Numpy (Harris et al., 2020), Scikit-image (van der Walt et al., 2014), SciPy (Virtanen et al., 2020), and SimpleITK (Beare et al., 2018; Lowekamp et al., 2013; Yaniv et al., 2018) for Python, and NIfTI (Shen, 2021) for MATLAB. Diffusion parameter maps were calculated with MRtrix toolbox 3.0 (Tournier et al., 2019). ITK-SNAP 3.8 (Yushkevich et al., 2006) was used for visualizing processing results as well as performing manual corrections to tissue masks. The Elastix toolbox 4.9 (Klein et al., 2010; Shamonin et al., 2014) was deployed to implement registrations.

4.4.2 Generation of brain and skull masks

As the MRI-volumes were acquired from mouse brains in the skull, skull stripping was performed before co-registration and averaging of the brain samples for generating a T2-weighted template brain. For extracting the brain from the surrounding tissue, a T2-weighted structural image was binarized such that all voxels belonging to the brain tissue were given the value 1 and all voxels belonging to the background the value 0. As several voxels in the tissue around the skull showed intensity values in the same range as the voxels in the brain tissue, the binarized image underwent morphological opening and erosion with a disk-formed structuring element (radius = 2). Subsequently, the biggest connected component was found from the image and dilated with the same structuring element as used in previous morphological operations. Finally, left-over holes in the brain mask were filled and manual corrections were made in the hindbrain area where the signal intensity of the original image was the lowest.

For mitigating co-registration of CT-imaged skull volumes to MRI-images of the same individuals, a coarse skull mask was generated for individual T2-weighted image. First, the T2-weighted image was binarized at the threshold found by Otsu's method. Then, the brain mask of the same T2-weighted image was dilated using a cubic structuring element until the mask reached the outer edge of skull. Finally, voxels of the binarized T2-weighted image which have

positive intensity values outside of the skull surface are set to zero using the dilated brain mask.

4.4.3 Registration at sample level

The registration procedures at sample level were initialised by up-sampling of CT, MRI, and tissue mask volumes to $(25\ \mu m)^3$ voxel size followed by multi-resolution rigid alignment of MRI images to the AIBS CCFv3 template for orienting every sample volume to the standard orientation. Subsequently, CT-imaged skulls were registered to the corresponding MRI images by multi-resolution rigid registration via skull masks extracted from T2-weighted images. A multi-resolution registration strategy for mapping of CT-skulls was realized by blurring fixed and moving image volumes with smoothing kernels of decreasing size before performing registration at every resolution level. Both rigid registration procedures were performed by maximizing normalized correlation for fixed and moving image pairs and using stochastic gradient descent as an optimization method.

The T2-weighted MRI mouse brain template was generated by applying the same registration procedure used for creating the LSFM mouse brain template (Perens et al., 2021) inspired by (Chan et al., 2007; Kuan et al., 2015; Umadevi Venkataraju et al., 2019). In brief, the algorithm involved one multi-resolution affine and five uni-resolution B-spline transformation steps at increasing resolutions. Increase in resolution was realized by decreasing the size of the smoothing kernel, down-sampling, and spacing of control points of the deformation grid. After every registration step, resulting datasets were intensity averaged to generate an intermediate average brain which served as a reference brain volume in the following registration step. All registration steps used to create the T2-weighted MRI mouse brain template deployed mattes mutual information as a similarity metric and gradient descent as an optimization method. For B-Spline registrations, the following optimization parameters were specified: gain factor a = 10000, $\alpha = 0.6$, A = 100. For realizing symmetry between the hemispheres of the resulting average T2-weighted MRI brain, a final very coarse multi-resolution B-spline registration to the AIBS CCFv3 was performed using same similarity metric, optimization method, and parameters as for the previous registrations except that registration was only performed at 2 lower resolutions with a = 5000.

4.4.4 Registration at template level

Registration procedures at the template level involved computing transformation matrices to enable mapping between the T2-weighted MRI and AIBS CCFv3 templates and between the AIBS CCFv3 and LSFM templates (all templates with isotropic voxel size of $(25\ \mu m)^3$). While mapping between the T2-weighted MRI and AIBS CCFv3 templates was performed in a whole-brain manner, alignment of the AIBS CCFv3 and LSFM templates required region-wise approach as shown in (Perens et al., 2021). The previous work focused only on registration of the AIBS CCFv3 template to the LSFM template, in the current work registration was also conducted in the opposing direction. All between-template registrations included multi-resolution affine and B-spline transformations with the mattes mutual information similarity

metric and a gradient descent optimization method. For B-spline registrations, the following optimization parameters were specified: a = 10000 (in case of hindbrain a = 40000 and septum a = 50000), $\alpha = 0.6$, A = 100. Multi-resolution strategy was realized by decreasing the size of the smoothing kernel, down-sampling, and spacing of the control points of the deformation grid.

4.4.5 Detection of skull landmarks

Skull landmarks bregma and lambda were determined from every CT-imaged skull sample by a semi-automatic computational algorithm. First, a subvolume constituting only the dorsal half of the skull with sutures was sampled from a CT-skull volume aligned to the corresponding T2-weighted MRI image (described in 4.4.3). Then an intensity threshold ($I_{global} = 1$) was found for distinguishing the skull from the background, a depth image was computed by summing up all voxels belonging to the background along the z-axis (dorsal-ventral axis), and the depth image was smoothed with a Gaussian kernel ($\sigma_{depth} = 3$). Subsequently, maximum projection of the extracted skull surface along z-axis was calculated, slightly smoothed with a Gaussian kernel ($\sigma_{projection} = 0.5$), and thresholded ($I_{suture} = 2.5$) for visualizing the sutures clearly. Suture curves were extracted from the final maximum projection image by applying manually drawn masks for coronal, sagittal, and lambdoidal sutures. The mask for the lambdoidal suture only included straight horizontally oriented sutures and excluded the triangular part of the suture. While the coronal suture was fitted by quadratic least squares regression, both sagittal and lambdoidal sutures were fitted by linear least squares regression. In-plane (x and y) coordinates for bregma were identified by calculating the intersection of coronal and sagittal suture fits and for lambda by calculating the intersection of sagittal and lambdoidal suture fits. For determining the z-coordinate of bregma and lambda, which is by definition located on top of the skull, a small subvolume (5-10 pixels x 10 pixels x number of pixels in z-axis) was extracted from the whole CT-skull volume. Subsequently, intensity values in x- and y-axis were averaged resulting in intensity profile of the skull in the z-axis at a close vicinity to the xy-locations of bregma and lambda. z-coordinate was finally found by identifying the outer boundary between the skull surface and background from the intensity profile.

4.4.6 Generating and mapping of a stereotaxic coordinate system

The chain of transformation matrices computed for the individual T2-weighted MRI images as described in 4.4.3 were applied to bregma and lambda landmarks extracted from MRI-aligned CT-skulls of the corresponding animals for transforming landmarks to the T2-weighted MRI template space. Positions of the landmarks for the individual animals were averaged and the final T2-weighted MRI template together with the average landmarks was rotated such that bregma and lambda were aligned horizontally (i.e., positioned at the same z-level). A coordinate system could then be generated by using the average bregma position as an origin for all three dimensions and a step size equal to voxel size (step size = 0.025 mm). A coordinate volume was generated with the exact same matrix shape as the horizontally aligned T2-

weighted MRI template and every element in the coordinate volume was assigned a vector containing x-, y- and z-coordinate. The coordinate values assigned to the elements in the coordinate volume describe the distance of the voxel edge nearest to the origin from the origin in millimetres (e.g. when the x-coordinate of the voxel overlapping with bregma is 0, then the x-coordinate of the neigbouring voxel in lateral direction is 0.0125 (mm) and the next neighbouring voxel is 0.0125 (mm) + 0.0250 (mm) = 0.0375 (mm)).

The transformation matrix resulting from mapping of the T2-weighted MRI template to the AIBS CCFv3 (described in 4.4.4) was applied to transfer the average bregma- and lambda-derived coordinate system from the MRI template space to the AIBS CCFv3 space. Followingly, six transformation matrices resulting from mapping the AIBS CCFv3 region-wise to the LSFM template (described in 4.4.4) were applied to the coordinate system parcellated into cortical, cerebral nuclei, interbrain + midbrain, hindbrain, cerebellar, and septal subvolumes to transfer the coordinate system from the AIBS CCFv3 space to the LSFM template space. For reconstructing the whole coordinate system in the LSFM template space, subvolumes were merged into one volume. While original coordinates were kept in the non-overlapping areas, coordinates in the overlapping and gap areas needed to be interpolated. Interpolation was performed in 2D on planes showing gradient in coordinate values (x- and z-coordinates in coronal planes, y-coordinates in the axial planes). Post-processing of the coordinate system involved assigning reasonable coordinate values to left-over voxels based on coordinate values of neighbouring voxels.

4.4.7 Generation of deformation fields

Deformation fields were generated for providing a possibility to transform datasets fast and accurately between the T2-weighted MRI, AIBS CCFv3, and LSFM template spaces in all directions. The Transformix program (Klein et al., 2010; Shamonin et al., 2014) which comes as part of the Elastix toolbox 4.9 was used to generate the deformation fields and can also be utilized for applying them. As mapping between the T2-weighted MRI template and the AIBS CCFv3 was performed in whole-brain manner (described in 4.4.4), deformation fields provided by Transformix did not require further processing. However, as mapping between the AIBS CCFv3 and LSFM templates was performed in region-wise manner (described in 4.4.4), Transformix created six deformation field volumes, one for mapping every region. These six region-specific deformation fields needed to be combined into one volume for facilitating transfer of whole-brain datasets between the AIBS CCFv3 and LSFM templates. For reconstructing the deformation field, vector-fields of every region were extracted from the corresponding deformation field volumes via masking and then merged into one volume. While the original vector-elements were kept in the non-overlapping areas, vector-elements in the overlapping and gap areas were interpolated in 2D-planes (x and z vector elements in the coronal planes, y vector elements in axial planes). Post-processing of the deformation field involved setting y and z vector elements outside the brain tissue to a very high value for avoiding ghost images in the mapped volumes.

4.4.8 Processing of diffusion MRI images

Diffusion datasets were successfully acquired for 7 animals. Pre-processing of diffusion-weighted MRI involved coarse rotation of the volumes and gradient directions to the orientation of the T2-weighted MRI template, denoising (Veraart et al., 2016), and removal of Gibbs ringing (Kellner et al., 2016). Diffusion tensors were estimated from pre-processed diffusion-weighted MRI images for every voxel in the brain according to the standard Mrtrix toolbox 3.0 methodology and settings. Diffusion characteristics, such as fractional anisotropy (FA), mean apparent diffusion coefficient (ADC), axial diffusivity (AD), and radial diffusivity (RD), were derived from diffusion tensors (Basser et al., 1994). Additionally, B0-volumes (n=5) collected without diffusion-sensitizing gradients were averaged. Diffusion tensor datasets upsampled to voxel size of $(25\ \mu m)^3$ were registered to T2-weighted MRI template by mapping individual B0-volumes to the template using multi-resolution affine and B-spline registration and applying computed transformation matrices to the other diffusion parameter maps. Finally, the maps were averaged in the T2-weighted MRI template.

Acknowledgements:

We would like to thank Hanne Duus Lautsen and Mette Musfelth Nebbelunde for their skillful assistance in the lab.

Funding:

The work was funded by Gubra ApS and Innovation Fund Denmark, grant number 8053-00121B.

References

Aggarwal M, Zhang J, Miller MI, Sidman RL, Mori S. 2009. Magnetic resonance imaging and micro-computed tomography combined atlas of developing and adult mouse brains for stereotaxic surgery. *Neuroscience* **162**:1339–1350. doi:10.1016/j.neuroscience.2009.05.070

Allen Institute for Brain Science. 2017. Allen Mouse Common Coordinate Framework and Reference Atlas, Technical White Paper.

Badea A, Ali-Sharief AA, Johnson GA. 2007. Morphometric analysis of the C57BL/6J mouse brain. *Neuroimage* **37**:683–693. doi:10.1016/j.neuroimage.2007.05.046

Basser PJ, Mattiello J, Lebihan D. 1994. Estimation of the Effective Self-Diffusion Tensor from the NMR Spin Echo. *J Magn Reson Ser B* **103**:247–254. doi:10.1006/JMRB.1994.1037

Beare R, Lowekamp B, Yaniv Z. 2018. Image Segmentation, Registration and Characterization in R with SimpleITK. *J Stat Softw* **86**. doi:10.18637/JSS.V086.I08

Blasiak T, Czubak W, Ignaciak A, Lewandowski MH. 2010. A new approach to detection of the bregma point on the rat skull. *J Neurosci Methods* **185**:199–203. doi:10.1016/j.jneumeth.2009.09.022

Breckwoldt MO, Bode J, Kurz FT, Hoffmann A, Ochs K, Ott M, Deumelandt K, Krüwel T, Schwarz D, Fischer M, Helluy X, Milford D, Kirschbaum K, Solecki G, Chiblak S, Abdollahi A, Winkler F, Wick W, Platten M, Heiland S, Bendszus M, Tews B. 2016. Correlated magnetic resonance imaging and ultramicroscopy (MR-UM) is a tool kit to assess the dynamics of glioma angiogenesis. *Elife* **5**:1–17. doi:10.7554/eLife.11712

Breckwoldt MO, Bode J, Sahm F, Krüwel T, Solecki G, Hahn A, Wirthschaft P, Berghoff AS, Haas M, Venkataramani V, Von Deimling A, Wick W, Herold-Mende C, Heiland S, Platten M, Bendszus M, Kurz FT, Winkler F, Tews B. 2019. Correlated MRI and ultramicroscopy (MR-UM) of brain tumors reveals vast heterogeneity of tumor infiltration and neoangiogenesis in preclinical models and human disease. *Front Neurosci* **13**:1–10. doi:10.3389/fnins.2018.01004

Chan E, Kovacevíc N, Ho SKY, Henkelman RM, Henderson JT. 2007. Development of a high resolution three-dimensional surgical atlas of the murine head for strains 129S1/SvImJ and C57Bl/6J using magnetic resonance imaging and micro-computed tomography. *Neuroscience* **144**:604–615. doi:10.1016/j.neuroscience.2006.08.080

Chen Y, McElvain LE, Tolpygo AS, Ferrante D, Friedman B, Mitra PP, Karten HJ, Freund Y, Kleinfeld D. 2019. An active texture-based digital atlas enables automated mapping of structures and markers across brains. *Nat Methods* **16**:341–350. doi:10.1038/s41592-019-0328-8

Chon U, Vanselow DJ, Cheng KC, Kim Y. 2019. Enhanced and unified anatomical labeling for a common mouse brain atlas. *Nat Commun* **10**:5067. doi:10.1038/s41467-019-13057-w

Chuang N, Mori S, Yamamoto A, Jiang H, Ye X, Xu X, Richards LJ, Nathans J, Miller MI, Toga AW, Sidman RL, Zhang J. 2011. An MRI-based atlas and database of the developing mouse brain. *Neuroimage* **54**:80–89. doi:10.1016/j.neuroimage.2010.07.043

Chung K, Wallace J, Kim S-Y, Kalyanasundaram S, Andalman AS, Davidson TJ, Mirzabekov JJ, Zalocusky KA, Mattis J, Denisin AK, Pak S, Bernstein H, Ramakrishnan C, Grosenick L, Gradinaru V, Deisseroth K. 2013. Structural and molecular interrogation of intact biological systems. *Nature* **497**:332–337. doi:10.1038/nature12107

Di Giovanna AP, Tibo A, Silvestri L, Müllenbroich MC, Costantini I, Allegra Mascaro AL, Sacconi L, Frasconi P, Pavone FS. 2018. Whole-Brain Vasculature Reconstruction at the Single Capillary Level. *Sci Rep* **8**:12573. doi:10.1038/s41598-018-30533-3

Doerr J, Schwarz MK, Wiedermann D, Leinhaas A, Jakobs A, Schloen F, Schwarz I, Diedenhofen M, Braun NC, Koch P, Peterson DA, Kubitscheck U, Hoehn M, Brüstle O. 2017. Whole-brain 3D mapping of human neural transplant innervation. *Nat Commun* **8**:1–7. doi:10.1038/ncomms14162

Dong H. 2008. The Allen Reference Atlas: a Digital Color Brain Atlas of the C57BL/6J Male Mouse. Wiley.

Dorr AE, Lerch JP, Spring S, Kabani N, Henkelman RM. 2008. High resolution three-

dimensional brain atlas using an average magnetic resonance image of 40 adult C57Bl/6J mice. *Neuroimage* **42**:60–69. doi:10.1016/J.NEUROIMAGE.2008.03.037

Dumoulin SO, Fracasso A, van der Zwaag W, Siero JCW, Petridou N. 2018. Ultra-high field MRI: Advancing systems neuroscience towards mesoscopic human brain function. *Neuroimage* **168**:345–357. doi:10.1016/J.NEUROIMAGE.2017.01.028

Dyrby TB, Baaré WFC, Alexander DC, Jelsing J, Garde E, Søgaard L V. 2011. An ex vivo imaging pipeline for producing high-quality and high-resolution diffusion-weighted imaging datasets. *Hum Brain Mapp* **32**:544–563. doi:10.1002/HBM.21043

Dyrby TB, Innocenti GM, Bech M, Lundell H. 2018. Validation strategies for the interpretation of microstructure imaging using diffusion MRI. *Neuroimage* **182**:62–79. doi:10.1016/J.NEUROIMAGE.2018.06.049

Ertürk A, Becker K, Jährling N, Mauch CP, Hojer CD, Egen JG, Hellal F, Bradke F, Sheng M, Dodt HU. 2012. Three-dimensional imaging of solvent-cleared organs using 3DISCO. *Nat Protoc* **7**:1983–1995. doi:10.1038/nprot.2012.119

Franklin KBJ, Paxinos G. 1997. The Mouse Brain in Stereotaxic Coordinates, 1st ed. San Diego: Academic Press.

Friedmann D, Pun A, Adams EL, Lui JH, Kebschull JM, Grutzner SM, Castagnola C, Tessier-Lavigne M, Luo L. 2020. Mapping mesoscale axonal projections in the mouse brain using a 3D convolutional network. *Proc Natl Acad Sci* **117**:11068–11075. doi:10.1073/PNAS.1918465117

Gabery S, Salinas CG, Paulsen SJ, Ahnfelt-Rønne J, Alanentalo T, Baquero AF, Buckley ST, Farkas E, Fekete C, Frederiksen KS, Helms HCC, Jeppesen JF, John LM, Pyke C, Nøhr J, Lu TT, Polex-Wolf J, Prevot V, Raun K, Simonsen L, Sun G, Szilvásy-Szabó A, Willenbrock H, Secher A, Knudsen LB. 2020. Semaglutide lowers body weight in rodents via distributed neural pathways. *JCI Insight* **5**. doi:10.1172/jci.insight.133429

Goubran M, Leuze C, Hsueh B, Aswendt M, Ye L, Tian Q, Cheng MY, Crow A, Steinberg GK, McNab JA, Deisseroth K, Zeineh M. 2019. Multimodal image registration and connectivity analysis for integration of connectomic data from microscopy to MRI. *Nat Commun* **10**:1–17. doi:10.1038/s41467-019-13374-0

Hansen HH, Perens J, Roostalu U, Skytte JL, Salinas CG, Barkholt P, Thorbek DD, Rigbolt KTG, Vrang N, Jelsing J, Hecksher-Sørensen J. 2021. Whole-brain activation signatures of weight-lowering drugs. *Mol Metab* **47**:101171. doi:10.1016/j.molmet.2021.101171

Harris CR, Millman KJ, van der Walt SJ, Gommers R, Virtanen P, Cournapeau D, Wieser E, Taylor J, Berg S, Smith NJ, Kern R, Picus M, Hoyer S, van Kerkwijk MH, Brett M, Haldane A, del Río JF, Wiebe M, Peterson P, Gérard-Marchant P, Sheppard K, Reddy T, Weckesser W, Abbasi H, Gohlke C, Oliphant TE. 2020. Array programming with NumPy. *Nat 2020 5857825* **585**:357–362. doi:10.1038/s41586-020-2649-2

Hof PR, Young WG, Bloom FE, Belichenko P V., Celio MR. 2000. Comparative cytoarchitectonic atlas of the C57BL/6 and 129/Sv mouse brains, 1st ed. Amsterdam: Elsevier.

Jacobowitz DM, Abbott LC. 1997. Chemoarchitectonic atlas of the developing mouse brain,

1st ed. Boca Raton: CRC Press.

Johnson GA, Badea A, Brandenburg J, Cofer G, Fubara B, Liu S, Nissanov J. 2010. Waxholm Space: An image-based reference for coordinating mouse brain research. *Neuroimage* **53**:365–372. doi:10.1016/J.NEUROIMAGE.2010.06.067

Johnson GA, Laoprasert R, Anderson RJ, Cofer G, Cook J, Pratson F, White LE. 2021. A multicontrast MR atlas of the Wistar rat brain. *Neuroimage* **242**:118470. doi:10.1016/j.neuroimage.2021.118470

Kaufman M. 1992. Atlas of Mouse Development, 1st ed. London: Academic Press.

Kellner E, Dhital B, Kiselev VG, Reisert M. 2016. Gibbs-ringing artifact removal based on local subvoxel-shifts. *Magn Reson Med* **76**:1574–1581. doi:10.1002/MRM.26054

Kirst C, Skriabine S, Vieites-Prado A, Topilko T, Bertin P, Gerschenfeld G, Verny F, Topilko P, Michalski N, Tessier-Lavigne M, Renier N. 2020. Mapping the Fine-Scale Organization and Plasticity of the Brain Vasculature. *Cell* **180**:780-795.e25. doi:10.1016/j.cell.2020.01.028

Kjaergaard M, Salinas CBG, Rehfeld JF, Secher A, Raun K, Wulff BS. 2019. PYY(3-36) and exendin-4 reduce food intake and activate neuronal circuits in a synergistic manner in mice. *Neuropeptides* **73**:89–95. doi:10.1016/j.npep.2018.11.004

Klein S, Staring M, Murphy K, Viergever MA, Pluim JPW. 2010. Elastix: A Toolbox for Intensity-Based Medical Image Registration. *IEEE Trans Med Imaging* **29**:196–205. doi:10.1109/TMI.2009.2035616

Kovačević N, Henderson JT, Chan E, Lifshitz N, Bishop J, Evans AC, Henkelman RM, Chen XJ. 2005. A three-dimensional MRI atlas of the mouse brain with estimates of the average and variability. *Cereb Cortex* **15**:639–645. doi:10.1093/cercor/bhh165

Kuan L, Li Y, Lau C, Feng D, Bernard A, Sunkin SM, Zeng H, Dang C, Hawrylycz M, Ng L. 2015. Neuroinformatics of the Allen Mouse Brain Connectivity Atlas. *Methods* **73**:4–17. doi:10.1016/j.ymeth.2014.12.013

Lee BC, Lin MK, Fu Y, Hata J, Miller MI, Mitra PP. 2021. Multimodal cross-registration and quantification of metric distortions in marmoset whole brain histology using diffeomorphic mappings. *J Comp Neurol* **529**:281–295. doi:10.1002/CNE.24946

Leuze C, Aswendt M, Ferenczi E, Liu CW, Hsueh B, Goubran M, Tian Q, Steinberg G, Zeineh MM, Deisseroth K, McNab JA. 2017. The separate effects of lipids and proteins on brain MRI contrast revealed through tissue clearing. *Neuroimage* **156**:412–422. doi:10.1016/j.neuroimage.2017.04.021

Li X, Aggarwal M, Hsu J, Jiang H, Mori S. 2013. AtlasGuide: Software for stereotaxic guidance using 3D CT/MRI hybrid atlases of developing mouse brains. *J Neurosci Methods* **220**:75–84. doi:10.1016/j.jneumeth.2013.08.017

Lowekamp BC, Chen DT, Ibanez L, Blezek D. 2013. The Design of SimpleITK. *Front Neuroinform* **7**:45. doi:10.3389/FNINF.2013.00045

Ly PT, Lucas A, Pun SH, Dondzillo A, Liu C, Klug A, Lei TC. 2021. Robotic stereotaxic system

based on 3D skull reconstruction to improve surgical accuracy and speed. *J Neurosci Methods* **347**:108955. doi:10.1016/J.JNEUMETH.2020.108955

Ma Y, Hof PR, Grant SC, Blackband SJ, Bennett R, Slatest L, Mcguigan MD, Benveniste H. 2005. A three-dimensional digital atlas database of the adult C57BL/6J mouse brain by magnetic resonance microscopy. *Neuroscience* **135**:1203–1215. doi:10.1016/j.neuroscience.2005.07.014

Ma Y, Smith D, Hof PR, Foerster B, Hamilton S, Blackband SJ, Yu M, Benveniste H. 2008. In vivo 3D digital atlas database of the adult C57BL/6J mouse brain by magnetic resonance microscopy. *Front Neuroanat* **2**:1–10. doi:10.3389/neuro.05.001.2008

MacKenzie-Graham A, Lee E-F, Dinov ID, Bota M, Shattuck DW, Ruffins S, Yuan H, Konstantinidis F, Pitiot A, Ding Y, Hu G, Jacobs RE, Toga AW. 2004. A multimodal, multidimensional atlas of the C57BL/6J mouse brain. *J Anat* **204**:93–102. doi:10.1111/J.1469-7580.2004.00264.X

Matthews PM, Jezzard P. 2004. Functional magnetic resonance imaging. *J Neurol Neurosurg Psychiatry* **75**:6–12.

Morawski M, Kirilina E, Scherf N, Jäger C, Reimann K, Trampel R, Gavriilidis F, Geyer S, Biedermann B, Arendt T, Weiskopf N. 2018. Developing 3D microscopy with CLARITY on human brain tissue: Towards a tool for informing and validating MRI-based histology. *Neuroimage* **182**:417–428. doi:10.1016/j.neuroimage.2017.11.060

Murakami TC, Mano T, Saikawa S, Horiguchi SA, Shigeta D, Baba K, Sekiya H, Shimizu Y, Tanaka KF, Kiyonari H, Iino M, Mochizuki H, Tainaka K, Ueda HR. 2018. A three-dimensional single-cell-resolution whole-brain atlas using CUBIC-X expansion microscopy and tissue clearing. *Nat Neurosci* **21**:625–637. doi:10.1038/s41593-018-0109-1

Nie B, Wu D, Liang S, Liu H, Sun X, Li P, Huang Q, Zhang T, Feng T, Ye S, Zhang Z, Shan B. 2019. A stereotaxic MRI template set of mouse brain with fine sub-anatomical delineations: Application to MEMRI studies of 5XFAD mice. *Magn Reson Imaging* **57**:83–94. doi:10.1016/j.mri.2018.10.014

Patel J. 2018. The mouse brain: A 3D atlas registering MRI, CT, and histological sections in three cardinal planes. John Hopkins University.

Perens J, Salinas CG, Skytte JL, Roostalu U, Dahl AB, Dyrby TB, Wichern F, Barkholt P, Vrang N, Jelsing J, Hecksher-Sørensen J. 2021. An Optimized Mouse Brain Atlas for Automated Mapping and Quantification of Neuronal Activity Using iDISCO+ and Light Sheet Fluorescence Microscopy. *Neuroinformatics* **19**:433–446. doi:10.1007/S12021-020-09490-8/FIGURES/5

Purger D, McNutt T, Achanta P, Quĩones-Hinojosa A, Wong J, Ford E. 2009. A histology-based atlas of the C57BL/6J mouse brain deformably registered to in vivo MRI for localized radiation and surgical targeting. *Phys Med Biol* **54**:7315–7327. doi:10.1088/0031-9155/54/24/005

Qi Y, Yu T, Xu J, Wan P, Ma Y, Zhu J, Li Y, Gong H, Luo Q, Zhu D. 2019. FDISCO: Advanced solvent-based clearing method for imaging whole organs. *Sci Adv* **5**:eaau8355.

doi:10.1126/sciadv.aau8355

Renier N, Adams EL, Kirst C, Dulac C, Osten P, Tessier-Lavigne M. 2016. Mapping of Brain Activity by Automated Volume Analysis of Immediate Early Genes. *Cell* **165**:1789–1802. doi:10.1016/j.cell.2016.05.007

Renier N, Wu Z, Simon DJ, Yang J, Ariel P, Tessier-Lavigne M. 2014. iDISCO: A Simple, Rapid Method to Immunolabel Large Tissue Samples for Volume Imaging. *Cell* **159**:896–910. doi:10.1016/j.cell.2014.10.010

Roostalu U, Salinas CBG, Thorbek DD, Skytte JL, Fabricius K, Barkholt P, John LM, Jurtz VI, Knudsen LB, Jelsing J, Vrang N, Hansen HH, Hecksher-Sørensen J. 2019. Quantitative whole-brain 3D imaging of tyrosine hydroxylase-labeled neuron architecture in the mouse MPTP model of Parkinson's disease. *Dis Model Mech* **12**. doi:10.1242/dmm.042200

Rosen GD, Williams AG, Capra JA, Connolly MT, Cruz B, Lu L, Airey DC, Kulkarni K, Williams RW. 2000. The Mouse Brain Library. *Int Mouse Genome Conf 14*.

Salinas CBG, Lu TTH, Gabery S, Marstal K, Alanentalo T, Mercer AJ, Cornea A, Conradsen K, Hecksher-Sørensen J, Dahl AB, Knudsen LB, Secher A. 2018. Integrated Brain Atlas for Unbiased Mapping of Nervous System Effects Following Liraglutide Treatment. *Sci Rep* **8**:10310. doi:10.1038/s41598-018-28496-6

Shamonin DP, Bron EE, Lelieveldt BP, Smits M, Klein S, Staring M. 2014. Fast parallel image registration on CPU and GPU for diagnostic classification of Alzheimer's disease. *Front Neuroinform* **7**. doi:10.3389/FNINF.2013.00050

Shen J. 2021. Tools for NIfTI and ANALYZE.

Sidman RL, Angevine JB, Taber-Pierce E. 1971. Atlas of the mouse brain and spinal cord (Commonwealth Fund Publications). Cambridge: Harvard University Press.

Silvestri L, Paciscopi M, Soda P, Biamonte F, Iannello G, Frasconi P, Pavone FS. 2015. Quantitative neuroanatomy of all Purkinje cells with light sheet microscopy and high-throughput image analysis. *Front Neuroanat* **9**:1–11. doi:10.3389/fnana.2015.00068

Skovbjerg G, Roostalu U, Hansen HH, Lutz TA, Le Foll C, Salinas CG, Skytte JL, Jelsing J, Vrang N, Hecksher-Sørensen J. 2021. Whole-brain mapping of amylin-induced neuronal activity in receptor activity–modifying protein 1/3 knockout mice. *Eur J Neurosci* **54**:4154–4166. doi:10.1111/EJN.15254

Stolp HB, Ball G, So PW, Tournier JD, Jones M, Thornton C, Edwards AD. 2018. Voxel-wise comparisons of cellular microstructure and diffusion-MRI in mouse hippocampus using 3D Bridging of Optically-clear histology with Neuroimaging Data (3D-BOND). *Sci Rep* **8**:1–12. doi:10.1038/s41598-018-22295-9

Susaki EA, Tainaka K, Perrin D, Kishino F, Tawara T, Watanabe TM, Yokoyama C, Onoe H, Eguchi M, Yamaguchi S, Abe T, Kiyonari H, Shimizu Y, Miyawaki A, Yokota H, Ueda HR. 2014. Whole-Brain Imaging with Single-Cell Resolution Using Chemical Cocktails and Computational Analysis. *Cell* **157**:726–739. doi:10.1016/j.cell.2014.03.042

Symms M, Jäger HR, Schmierer K, Yousry TA. 2004. A review of structural magnetic

resonance neuroimaging. *J Neurol Neurosurg Psychiatry* **75**:1235–1244. doi:10.1136/jnnp.2003.032714

Todorov MI, Paetzold JC, Schoppe O, Tetteh G, Shit S, Efremov V, Todorov-Völgyi K, Düring M, Dichgans M, Piraud M, Menze B, Ertürk A. 2020. Machine learning analysis of whole mouse brain vasculature. *Nat Methods* **17**:442–449. doi:10.1038/s41592-020-0792-1

Tournier JD, Smith R, Raffelt D, Tabbara R, Dhollander T, Pietsch M, Christiaens D, Jeurissen B, Yeh CH, Connelly A. 2019. MRtrix3: A fast, flexible and open software framework for medical image processing and visualisation. *Neuroimage* **202**:116137. doi:10.1016/J.NEUROIMAGE.2019.116137

Tyson AL, Margrie TW. 2021. Mesoscale microscopy and image analysis tools for understanding the brain. *Prog Biophys Mol Biol*. doi:10.1016/j.pbiomolbio.2021.06.013

Umadevi Venkataraju KU, Gornet J, Murugaiyan G, Wu Z, Osten P. 2019. Development of brain templates for whole brain atlases. *Prog Biomed Opt Imaging - Proc SPIE* **10865**:1086511. doi:10.1117/12.2505295

Valverde F. 2004. Golgi atlas of the postnatal mouse brain. New York: Springer-Verlag.

van der Walt S, Schönberger JL, Nunez-Iglesias J, Boulogne F, Warner JD, Yager N, Gouillart E, Yu T. 2014. scikit-image: image processing in Python. *PeerJ* **2**. doi:10.7717/PEERJ.453

Vaughan JT, Garwood M, Collins CM, Liu W, DelaBarre L, Adriany G, Andersen P, Merkle H, R. G, Smith MB, Ugurbil K. 2001. 7T vs. 4T: RF power, homogeneity, and signal-to-noise comparison in head images. *Magn Reson Med* **46**:24–30. doi:10.1002/MRM.1156

Veraart J, Novikov DS, Christiaens D, Ades-aron B, Sijbers J, Fieremans E. 2016. Denoising of diffusion MRI using random matrix theory. *Neuroimage* **142**:394–406. doi:10.1016/J.NEUROIMAGE.2016.08.016

Virtanen P, Gommers R, Oliphant TE, Haberland M, Reddy T, Cournapeau D, Burovski E, Peterson P, Weckesser W, Bright J, van der Walt SJ, Brett M, Wilson J, Millman KJ, Mayorov N, Nelson ARJ, Jones E, Kern R, Larson E, Carey CJ, Polat İ, Feng Y, Moore EW, VanderPlas J, Laxalde D, Perktold J, Cimrman R, Henriksen I, Quintero EA, Harris CR, Archibald AM, Ribeiro AH, Pedregosa F, van Mulbregt P. 2020. SciPy 1.0: fundamental algorithms for scientific computing in Python. *Nat Methods 2020 173* **17**:261–272. doi:10.1038/s41592-019-0686-2

Wang N, White LE, Qi Y, Cofer G, Johnson GA. 2020. Cytoarchitecture of the mouse brain by high resolution diffusion magnetic resonance imaging. *Neuroimage* **216**. doi:10.1016/j.neuroimage.2020.116876

Wang Q, Ding SL, Li Y, Royall J, Feng D, Lesnar P, Graddis N, Naeemi M, Facer B, Ho A, Dolbeare T, Blanchard B, Dee N, Wakeman W, Hirokawa KE, Szafer A, Sunkin SM, Oh SW, Bernard A, Phillips JW, Hawrylycz M, Koch C, Zeng H, Harris JA, Ng L. 2020. The Allen Mouse Brain Common Coordinate Framework: A 3D Reference Atlas. *Cell* **181**:936-953.e20. doi:10.1016/J.CELL.2020.04.007

Wei H, Xie L, Dibb R, Li W, Decker K, Zhang Y, Johnson GA, Liu C. 2016. Imaging whole-brain cytoarchitecture of mouse with MRI-based quantitative susceptibility mapping. *Neuroimage* **137**:107–115. doi:10.1016/j.neuroimage.2016.05.033

Xiao J. 2007. A new coordinate system for rodent brain and variability in the brain weights and dimensions of different ages in the naked mole-rat. *J Neurosci Methods* **162**:162–170. doi:10.1016/j.jneumeth.2007.01.007

Yaniv Z, Lowekamp BC, Johnson HJ, Beare R. 2018. SimpleITK Image-Analysis Notebooks: a Collaborative Environment for Education and Reproducible Research. *J Digit Imaging* **31**:290–303. doi:10.1007/S10278-017-0037-8

Yousaf T, Dervenoulas G, Politis M. 2018. Advances in MRI MethodologyInternational Review of Neurobiology. Elsevier Inc. pp. 31–76. doi:10.1016/bs.irn.2018.08.008

Yushkevich PA, Piven J, Hazlett HC, Smith RG, Ho S, Gee JC, Gerig G. 2006. User-guided 3D active contour segmentation of anatomical structures: significantly improved efficiency and reliability. *Neuroimage* **31**:1116–1128. doi:10.1016/J.NEUROIMAGE.2006.01.015

Zhou P, Liu Z, Wu H, Wang Y, Lei Y, Abbaszadeh S. 2020. Automatically detecting bregma and lambda points in rodent skull anatomy images. *PLoS One* **15**:1–11. doi:10.1371/journal.pone.0244378

Publication C

Comparative study of voxel-based statistical analysis methods for fluorescently labelled and light-sheet imaged whole-brain samples

Johanna Perens, Jacob Lercke Skytte, Casper Gravesen Salinas, Jacob Hecksher-Sørensen, Tim B. Dyrby, Anders Bjorholm Dahl

2021 IEEE 18th International Symposium on Biomedical Imaging (ISBI), 1433-1437, 2021

2021 IEEE 18th International Symposium on Biomedical Imaging (ISBI)
April 13-16, 2021, Nice, France

2021 IEEE 18th International Symposium on Biomedical Imaging (ISBI) | 978-1-6654-1246-9/20/$31.00 ©2021 IEEE | DOI: 10.1109/ISBI48211.2021.9434015

COMPARATIVE STUDY OF VOXEL-BASED STATISTICAL ANALYSIS METHODS FOR FLUORESCENTLY LABELLED AND LIGHT SHEET IMAGED WHOLE-BRAIN SAMPLES

Johanna Perens[1,2,], Jacob Lercke Skytte[1], Casper Gravesen Salinas[1], Jacob Hecksher-Sørensen[1], Tim B. Dyrby[2,3], Anders Bjorholm Dahl[2]*

1 - Gubra ApS, 2970 Hørsholm, Denmark

2 - Department of Applied Mathematics and Computer Science, Technical University Denmark, 2800 Kongens Lyngby, Denmark

3 - Danish Research Centre for Magnetic Resonance, Centre for Functional and Diagnostic Imaging and Research, Copenhagen University Hospital Hvidovre, 2650 Hvidovre, Denmark

∗Corresponding author: Johanna Perens (mail: jpe@gubra.dk)

ABSTRACT

Light sheet microscopy of fluorescently labelled and optically cleared intact organs is a novel approach which enables to visualize structure and function of the brain in 3D. The methodology is gaining popularity in the neuroscience community and dedicated algorithms are being developed for segmenting and quantifying different neurological markers. However, comparisons of marker characteristics between the study groups are conventionally performed by conducting statistical testing for every atlas-defined brain region. While this statistical approach yields viable results, it is biased by the region delineations and does not provide information on the signal properties at a voxel level. In this work, we convert the 3D histological signal from segmented c-Fos+ cells into a format suitable for conducting voxel-wise group comparisons and demonstrate the potential of a recent technique, probabilistic threshold-free cluster enhancement method, in a brief comparative study of six different approaches to voxel-based statistical analysis.

Index Terms — threshold free cluster enhancement, voxel-based, statistics, light sheet fluorescence microscopy, iDISCO

1. INTRODUCTION

Recent advances in whole-organ immunohistochemical treatments and optical clearing [1]–[4] in combination with light sheet fluorescence microscopy (LSFM) have enabled investigating anatomy, normal physiology, and disease pathology in 3-dimensional space [5]–[8]. The advantage of volumetric imaging is especially apparent when it comes to studying the complexity of the brain since it enables to capture different markers of interest in all brain areas at once while preserving the cytoarchitectonic structure of tissue. Moreover, image volumes of brains can be accurately mapped into a common reference space for comparing the signal across individual samples. Such methodology has successfully been applied to explore gene expression [9], cell populations [7], vasculature [10], neuronal projections [11], drug and other tracer distributions in the brain [12].

Widely used conventional analysis of the 3D-imaged sample volumes involves segmentation of a marker of interest followed by region-wise quantification and statistical testing [13] utilizing digital 3D atlases [14], [15]. While the region-based statistical analysis pinpoints brain areas which are affected by the treatment, it is highly dependent on the definition of region delineations. Consequently, the approach is not suitable for providing information on exact spatial origin, shape and spread of the signal, as well as distinguishing between multiple effects occurring within the same delineated region. Such characteristics could, however, be revealed by applying voxel-wise statistical analysis techniques which are already established in the functional MRI-field [16], [17].

Pre-processing of the histological data is required prior to voxel-wise statistics due to biological inter-subject variability of the signal observed with microscopic resolution. This implies that the same signal does not necessarily appear in the exact same voxel in individual registered brain samples. Additionally, existing spatial statistics methods tend to assume continuous signals while histological datasets exhibit discrete signals. Vandenberghe and colleagues [18] have pioneered in adapting 3D histological datasets into a format suitable for conducting voxel-wise statistical analysis. Their approach relies on smoothing of marker segmentation volumes with a Gaussian kernel while the optimal standard deviation of the kernel is determined by a bootstrap error minimization algorithm.

The goal of this work was to identify and implement the optimal voxel-wise statistical analysis approach for LSFM-imaged brain samples. Analysis of compound induced brain activation signatures seen by iDISCO+ c-Fos staining in salmon calcitonin (hormone regulating body weight) treated mice is provided as an example case and used to compare six different voxel-based statistical analysis methods.

2. MATERIALS AND METHODS

2.1. Animals and drug treatment

Male 10-week-old C57Bl/6J mice obtained from Janvier Labs (Le Genest-Saint-Isle, France) were fasted for 12 hours before dosing with vehicle (n = 8, i.p., 50 mM sodium acetate with 5% mannitol,

5 ml/kg) and salmon calcitonin trifluoroacetic acid (n = 8, i.p., 12 nmol/kg, 5 ml/kg; Bachem AG, Bubendorf, Switzerland). The mice were sacrificed two hours post-dose.

2.2 Sample preparation and 3D imaging

The mice were anesthetized by Hypnorm-Dormicum (s.c.), the brain samples were dissected from the skulls and processed according to the iDISCO+ protocol [2] as described in [15] using reagents and antibodies from the same vendors. The brain samples were scanned with Lavision ultramicroscope II (Miltenyi Biotec GmbH, Bergisch Gladbach, Germany). Respecive z-stacks were acquired in axial view at 10 µm intervals (1.2× magnification, NA=0.156, exposure time 254 ms) and the resulting volumes had an in-plane resolution of 4.8 µm and a z-resolution of 3.78 µm. Imaging was performed in two channels, autofluorescence at 560 ± 20 nm (excitation) and 650 ± 25 nm (emission) wavelength and c-Fos staining at 630 ± 15 nm (excitation) and 680 ± 15 nm (emission) wavelength.

2.3. Feature segmentation

Acquired image volumes were examined for c-Fos+ cells using an adapted ClearMap cell detection routine [19] described in [15]. A binary segmentation labelling of the c-Fos+ cell centre coordinates was produced. One animal from each group was excluded from further analysis due to either unproportionally high or low total number of c-Fos+ in the brain.

2.4 Pre-processing of segmentation volumes

2.4.1 Registration

The segmentation volumes were registered to the LSFM-based mouse brain atlas space (with a 20 µm isotropic resolution) via corresponding autofluorescence volumes through affine and b-spline transformations [15] using the Elastix toolbox [20]. Mattes mutual information was utilized as a similarity measure for the registrations.

2.4.2 Parameter optimization for pre-processing

To facilitate a group-wise statistical comparison of the histological signal at voxel level, the detected cells in the segmentation volumes were converted into Gaussian random fields (format often assumed for voxel-based statistics methods). Vandenberghe and colleagues [18] showed that a suitable approach is to apply Gaussian smoothing to the cell segmentation volume, which results in a volume where voxel values correspond to cell density-like estimates. An optimal standard deviation of the smoothing kernel can be found via a bootstrap error minimization routine which is performed for every study group using a range of standard deviations for the smoothing kernel. The method requires generation of bootstrap sample sets in the size of the study groups while the sets contain randomly sampled combinations of individual segmentation volumes with replacement. Equation for computing the bootstrap error is

$$E_{bootstrap} = \frac{1}{N_{ID}} \sum_{k=1}^{N_{ID}} \frac{1}{N_{B\backslash k}} \sum_{s \epsilon B\backslash k} \frac{1}{n} \sum_{i=1}^{n} (\mu_i^s - S_i^k)^2 \quad (1)$$

where N_{ID} stands for number of individuals k in the study group, $B\backslash k$ for the bootstrap set containing all sample sets s excluding k, $N_{B\backslash k}$ for number of sample sets in the $B\backslash k$, n for number of voxels in the brain volume, μ^s for the mean smoothed segmentation volume of samples in set s and S^k for the segmentation volume of individual k. An optimal smoothing kernel broadens the support of each detected cell centre in the individual segmentation volumes, such that they best represent the average signal of the group.

In this study 100 bootstrap sample sets were generated from un-processed segmentation volumes, and the bootstrap error was calculated for smoothing kernel standard deviations ranging from 1 to 4.5 voxels.

2.4.3 Creating density maps for voxel-based statistics

For the pre-processing of the registered cell segmentation volumes, signal appearing in sparsely populated areas (maximum 1 cell per 100 μm^3 in average for the treatment and the corresponding vehicle group volumes) was masked out from the segmentation images to avoid merging of diffuse cell clusters in the statistical analysis. Secondly, a Gaussian background noise ($\mu = 0$, $\sigma = 0.1$) was added to the cell segmentation volumes to avoid high statistical values due to zero background signal [21]. Finally, the segmentation volumes were smoothed with the optimal kernel and the signal from the right and left hemisphere was averaged to improve statistical power.

2.5. Voxel-based statistical analysis

Voxel-based statistical analysis was performed by investigating several statistical testing and correction techniques for multiple comparisons. A two-tailed student t-test (assuming unequal variance) and a subsequent conversion from t-values to z-values (which was required by some techniques) was carried out across the voxels in one hemisphere. Hereafter, six different approaches to correct for multiple comparisons were carried out: 1) family-wise error rate (FWER) via the Bonferroni method [22], 2) false discovery rate (FDR) via the Benjamini Hochberg method [23], 3) cluster size inference (CSI) [24], 4) cluster mass inference (CMI) [24], 5) threshold-free cluster enhancement (TFCE) [25] and 6) probabilistic TFCE (pTFCE) [26]. FDR and FWER were included in the comparison because they are widely applied in the 3D-imaging field as default procedures. CMI, CSI, TFCE and pTFCE considered in the comparison have been proposed as alternative solutions for the multiple testing problem since unlike FDR and FWER they do not rely on problematic assumptions associated with signal smoothness and noise.

For CSI and CMI, a user-defined cluster forming threshold was applied to the pre-processed segmentation volumes and the resulting clusters were quantified. In CSI, the cluster size was defined as the number of voxels belonging to a signal cluster and in CMI, the cluster mass was calculated by the sum of z-values of the voxels inside a cluster. The applied cluster forming thresholds were $z = 1.96$ (same as in [18]) and $z = 3.3$, which corresponded to $p = 0.05$ and $p = 0.001$ respectively. Hypothesis testing for CSI and CMI was performed using permutation testing where a distribution under the null hypothesis was created by storing the maximum cluster size/mass at each permutation (number of permutations = 1000). Clusters with a size/mass greater than the threshold found at $p < 0.05$ in the null hypothesis distributions were considered significant.

TFCE and pTFCE are both described as topology-based belief boosting methods, referring to the z-value of single voxels being enhanced by all voxels with a lower z-value if they are spatially connected. TFCE has two parameters that control how much emphasis should be put on cluster extent (E) and height (H). In this study, standard parameters $E = 0.5$ and $H = 2.0$ were used when performing TFCE [25]. TFCE relies on permutation testing, where the maximum enhanced z-value was stored for each

permutation (number of permutations = 1000). While pTFCE is similar to TFCE, it has been implemented in a probabilistic framework that relies on the aggregation of Bayes-rule derived conditional probabilities of threshold heights for certain cluster sizes.

3. RESULTS AND DISCUSSION

3.1. Optimal processing of cell segmentation volumes

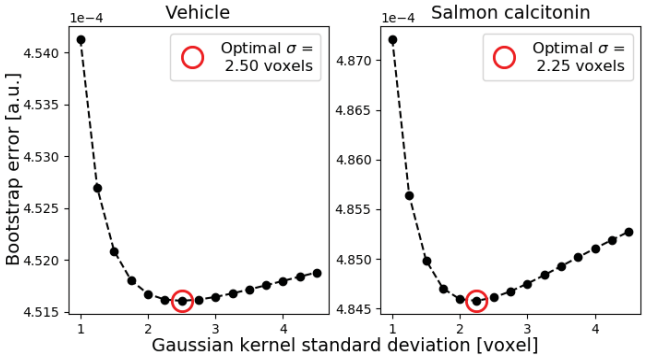

Fig. 1. Bootstrap error minimization for determining the optimal standard deviation of the Gaussian kernel for smoothing the cell segmentation volumes. The bootstrap error was computed separately for vehicle and salmon calcitonin treated animals.

A central assumption of voxel-wise group comparisons is an overlapping signal region in registered tissue samples which can be achieved by smoothing the segmentation volumes with a Gaussian kernel of suitable size. The bootstrap error minimization scheme used for determining the smoothing kernel size [18] produced curves with convex shape for both vehicle and salmon calcitonin group (Fig. 1). Optimal standard deviation of the smoothing kernel was found to be 2.25 voxels for the salmon calcitonin group and 2.5 voxels for the vehicle group. The bootstrap error curve for salmon calcitonin group exhibited a pronounced minimum whereas the bootstrap error curve for the vehicle was flatter in the vicinity of the minimum.

The curvature of the bootstrap error is related to the spread of the segmented objects. The c-Fos signal for vehicle animals was diffuse and random whereas drug treatment evoked activity localized in certain brain areas. This also implies that the amount of smoothing has less effect on the baseline than on the drug induced signal in creating the signal overlap. Therefore, it is reasonable to use the optimal standard deviation of the Gaussian kernel found for the group with the smallest radius for bootstrap error function curvature to smooth the segmentation volumes of all study groups. Naturally, the optimal smoothing kernel size may vary depending on the treatment compound and the fluorescent marker studied due to different imaging parameters and signal characteristics (e.g. density, shape, size).

3.2. Comparison of voxel-based statistics methods

To determine a statistical method suitable for reliably recognizing and evaluating the origin, spread and significance of 3D histological signals, spatial p-value maps from six different statistical approaches were compared (Fig. 2). A heatmap for the average up- and downregulation of c-Fos expression (Fig. 2a) visualizes locations and shapes of signal clusters which are potential candidates for the effect of salmon calcitonin - bed nuclei of stria terminalis (BST), central amygdalar nucleus (CEA), paraventricular nucleus of the thalamus (PVT), parabrachial nucleus (PB), nucleus of the solitary tract (NTS) and dorsal motor nucleus of the vagus nerve (DMX). A statistical approach was considered to perform well if a significant activation was found in the candidate brain areas while maintaining low rate of false positives.

The large number of voxels in the 3D imaged brain volumes, is a well-known issue of voxel-wise t-tests which manifests in a large amount of false positive voxels when left uncorrected (Fig. 2b) and only few significant voxels when corrected using the standard FDR (Fig. 2c) and FWER (Fig. 2d) methods [27], [28]. It is also important to mention, that FDR as well as FWER assume all performed tests are independent which is not the case for spatial data. Contrary to the FDR and FWER corrections, CSI and CMI demonstrate noticeable improvement in resolving signal location and shape (Fig. 2e-h). The number of signal clusters, their shape and significance level determined by the cluster-based methods are highly dependent on the user-defined parameters, which could facilitate confirmation bias in conducted studies. The results for the cluster-based methods also designate that the CMI approach is more reliable in detecting signal clusters than CSI (Fig. 2e-f). This results from the fact that CMI takes both the spatial extent of the signal as well as the signal magnitude into account while CSI is only dependent on the former. A major drawback for CSI and CMI, when detecting signals, is that a single p-value is assigned to all voxels inside a cluster. This means that if multiple signal sources are located within the same significant cluster, these will be obfuscated by CSI and CMI, unless the cluster-forming threshold is carefully chosen.

On the other hand, TFCE and pTFCE (Fig. 2i-j) detect significant clusters while retaining high spatial specificity, which can reveal signal differences between individual cluster voxels (Fig. 2k). TFCE and pTFCE are conceptually similar approaches and will deliver comparable results when appropriate parameters are found for TFCE. However, standard parameters proposed by Smith and Nichols [25] do not achieve identical results to pTFCE as seen in voxel-wise significance values and identification of the NTS-cluster (Fig.2i-j). Different standard parameters found for functional MRI [25] and EEG [29] indicate that the TFCE parameters are not universal but depend on the characteristics of the measured signal. To circumvent the laborious identification process of optimal TFCE parameters for various kinds of immunohistochemical stains and fluorescent markers, pTFCE could be applied for evaluating histological signals. An additional advantage of pTFCE over TFCE is its computational efficiency since pTFCE does not rely on permutation testing.

Despite the clear benefits of pTFCE being parameter-free, faster, and providing voxel level inference, we experienced a few practical limitations regarding diffuse signals and sample variance. According to our experience, if pTFCE and TFCE are performed on histological data which exhibits large areas with diffuse signal, the detected signal clusters can be merged into one, with reduced spatial specificity. This issue could be avoided by applying density filtering during the pre-processing procedure. Furthermore, TFCE and pTFCE seem to be extremely sensitive to signal differences between the individual animals belonging to the same study group which could be both related to either biological or experimental (e.g. laser strength, tissue damage, registration quality) origins. The issue of sensitivity could be overcome by including a sufficient number of animals in each study group (circa

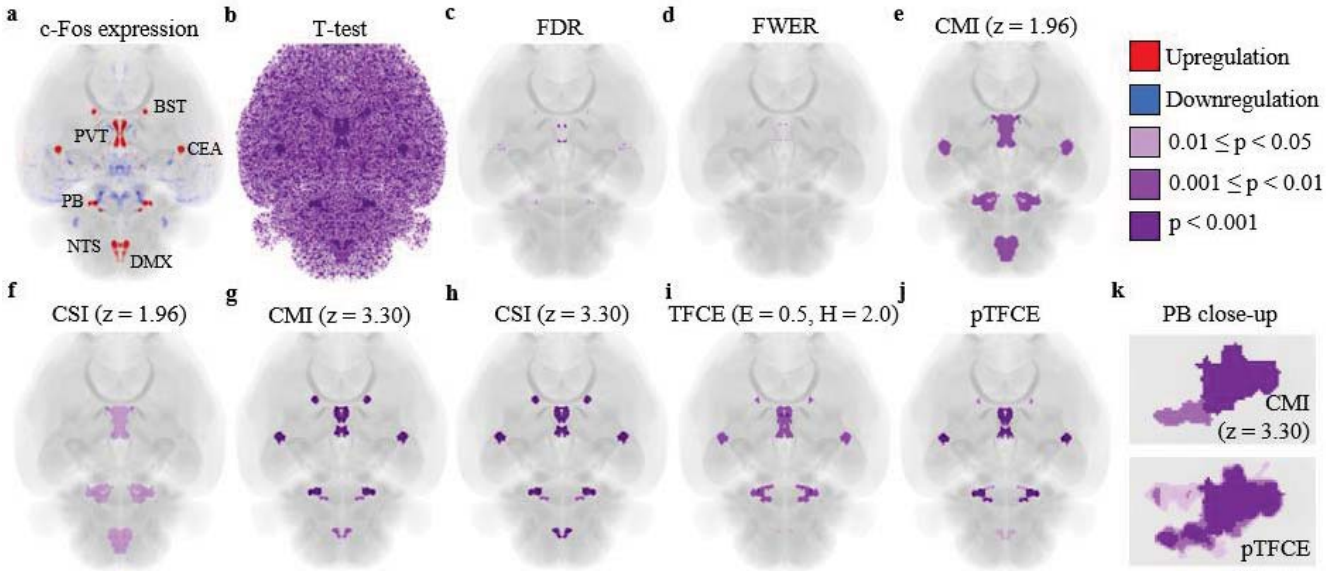

Fig. 2. Comparison of spatial p-value distributions resulting from different voxel-based statistical analysis techniques and multiple comparison corrections. Brain areas exhibiting statistically significant ($p < 0.05$) regulation of c-Fos expression are highlighted and the levels of significance are divided into three discrete levels indicated by graded purple colors. Up- and downregulation heatmap of c-Fos expression is created by subtraction of the average vehicle heatmaps from the average treatment group heatmaps (individual heatmaps are generated by smoothing the segmentation volumes with a Gaussian kernel of $\sigma = 2.25$ voxels). Visualizations are horizontal maximum intensity projections of the 3D dataset and were created with Imaris™ software (version 2, Oxford instruments, Abington, UK).

10 or more). For characterizing the effect of a diffuse signal and sample variance on the TFCE and pTFCE outcomes, future studies should be undertaken using simulated datasets as they enable quantitative comparison of statistical maps to ground truth information.

4. CONCLUSION

Voxel-based statistics is a promising analysis approach which enables to investigate 3D histological data from a perspective complimentary to the conventional, region-based statistical analysis. Comparative analysis of the voxel-based techniques conducted in the current study revealed that the pTFCE method is superior to FDR, FWER, TFCE, and cluster-based techniques. The potential of the pTFCE approach lies in the ability to detect signal clusters unbiased by the atlas-defined regions, resolve the 3-dimensional shape of the area where an effect takes place, and identify neuronal subpopulations affected by a treatment both in the same atlas-defined region as well as in the same signal cluster.

5. REFERENCES

[1] A. Ertürk *et al.*, "Three-dimensional imaging of solvent-cleared organs using 3DISCO," *Nat. Protoc.*, vol. 7, no. 11, pp. 1983–1995, 2012.

[2] N. Renier, Z. Wu, D. J. Simon, J. Yang, P. Ariel, and M. Tessier-Lavigne, "iDISCO: A Simple, Rapid Method to Immunolabel Large Tissue Samples for Volume Imaging," *Cell*, vol. 159, no. 4, pp. 896–910, 2014.

[3] K. Chung *et al.*, "Structural and molecular interrogation of intact biological systems," *Nature*, vol. 497, no. 7449, pp. 332–337, 2013.

[4] E. A. Susaki, K. Tainaka, D. Perrin, H. Yukinaga, A. Kuno, and H. R. Ueda, "Advanced CUBIC protocols for whole-brain and whole-body clearing and imaging," *Nat. Protoc.*, vol. 10, no. 11, pp. 1709–1727, Nov. 2015.

[5] T. Liebmann, N. Renier, K. Bettayeb, P. Greengard, M. Tessier-Lavigne, and M. Flajolet, "Three-Dimensional Study of Alzheimer's Disease Hallmarks Using the iDISCO Clearing Method," *Cell Rep.*, vol. 16, no. 4, pp. 1138–1152, Jul. 2016.

[6] A. Hahn *et al.*, "Large-scale characterization of the microvascular geometry in development and disease by tissue clearing and quantitative ultramicroscopy," *J. Cereb. Blood Flow Metab.*, 2020.

[7] U. Roostalu *et al.*, "Quantitative whole-brain 3D imaging of tyrosine hydroxylase-labeled neuron architecture in the mouse MPTP model of Parkinson's disease," *Dis. Model. Mech.*, vol. 12, no. 11, pp. dmm042200–dmm042200, 2019.

[8] C. Pan *et al.*, "Deep Learning Reveals Cancer Metastasis and Therapeutic Antibody Targeting in the Entire Body," *Cell*, vol. 179, no. 7, pp. 1661-1676.e19, 2019.

[9] M. Kjaergaard, C. B. G. Salinas, J. F. Rehfeld, A. Secher, K. Raun, and B. S. Wulff, "PYY(3-36) and exendin-4 reduce food intake and activate neuronal circuits in a synergistic manner in mice," *Neuropeptides*, vol. 73, pp. 89–95, Feb. 2019.

[10] A. P. Di Giovanna *et al.*, "Whole-Brain Vasculature Reconstruction at the Single Capillary Level," *Sci. Rep.*, vol. 8, no. 1, p. 12573, 2018.

[11] C. Pan *et al.*, "Shrinkage-mediated imaging of entire organs and organisms using uDISCO," *Nat. Methods*, vol. 13, no. 10, pp. 859–867, 2016.

[12] S. Gabery *et al.*, "Semaglutide lowers body weight in rodents via distributed neural pathways," *JCI Insight*, vol. 5, no. 6, Mar. 2020.
[13] N. Renier, E. L. Adams, C. Kirst, C. Dulac, P. Osten, and M. Tessier-Lavigne, "Mapping of Brain Activity by Automated Volume Analysis of Immediate Early Genes," *Cell*, vol. 165, no. 7, pp. 1789–1802, 2016.
[14] L. Kuan *et al.*, "Neuroinformatics of the Allen Mouse Brain Connectivity Atlas," *Methods*, vol. 73, pp. 4–17, 2015.
[15] J. Perens *et al.*, "An Optimized Mouse Brain Atlas for Automated Mapping and Quantification of Neuronal Activity Using iDISCO+ and Light Sheet Fluorescence Microscopy," *Neuroinformatics*, pp. 1–14, 2020.
[16] A. Caria, "Mesocorticolimbic interactions mediate fMRI-guided regulation of self-generated affective states," *Brain Sci.*, vol. 10, no. 4, p. 223, Apr. 2020.
[17] A. Gaillard *et al.*, "Greater activation of the response inhibition network in females compared to males during stop signal task performance," *Behav. Brain Res.*, vol. 386, p. 112586, 2020.
[18] M. E. Vandenberghe *et al.*, "Voxel-Based Statistical Analysis of 3D Immunostained Tissue Imaging," *Front. Neurosci.*, vol. 12, no. 754, 2018.
[19] N. Renier *et al.*, "Mapping of Brain Activity by Automated Volume Analysis of Immediate Early Genes.," *Cell*, vol. 165, no. 7, pp. 1789–1802, Jun. 2016.
[20] S. Klein, M. Staring, K. Murphy, M. A. Viergever, and J. P. W. Pluim, "Elastix: A Toolbox for Intensity-Based Medical Image Registration," *IEEE Trans. Med. Imaging*, vol. 29, no. 1, pp. 196–205, 2010.
[21] G. R. Ridgway, V. Litvak, G. Flandin, K. J. Friston, and W. D. Penny, "The problem of low variance voxels in statistical parametric mapping; a new hat avoids a 'haircut,'" *Neuroimage*, vol. 59, no. 3, pp. 2131–2141, 2021.
[22] O. J. Dunn, "Multiple Comparisons Among Means," *J. Am. Stat. Assoc.*, vol. 56, no. 293, pp. 52–64, 1961.
[23] Y. Benjamini and Y. Hochberg, "Controlling the False Discovery Rate: A Practical and Powerful Approach to Multiple Testing," 1995.
[24] E. T. Bullmore, J. Suckling, S. Overmeyer, S. Rabe-Hesketh, E. Taylor, and M. J. Brammer, "Global, voxel, and cluster tests, by theory and permutation, for a difference between two groups of structural mr images of the brain," *IEEE Trans. Med. Imaging*, vol. 18, no. 1, pp. 32–42, 1999.
[25] S. M. Smith and T. E. Nichols, "Threshold-free cluster enhancement: Addressing problems of smoothing, threshold dependence and localisation in cluster inference," *Neuroimage*, vol. 44, pp. 83–98, 2009.
[26] T. Spisák *et al.*, "Probabilistic TFCE: A generalized combination of cluster size and voxel intensity to increase statistical power," *Neuroimage*, vol. 185, pp. 12–26, 2018.
[27] T. Nichols and S. Hayasaka, "Controlling the familywise error rate in functional neuroimaging: A comparative review," *Statistical Methods in Medical Research*, vol. 12, no. 5. pp. 419–446, Oct-2003.
[28] G. Lohmann *et al.*, "Inflated false negative rates undermine reproducibility in task-based fMRI," *bioRxiv*, Mar. 2017.
[29] A. Mensen and R. Khatami, "Advanced EEG analysis using threshold-free cluster-enhancement and non-parametric statistics," *Neuroimage*, vol. 67, pp. 111–118, 2013.

6. COMPLIANCE WITH ETHICAL STANDARDS

The Danish Animal Experiments Inspectorate approved all animal procedures which were conducted according to internationally accepted principles for the use of laboratory animals (license #2013-15-2934-00784).

7. ACKNOWLEDGMENTS

The work was funded by Gubra ApS and Innovation Fund Denmark grant number (8053-00121B). The authors declare that they have no conflict of interest.

Publication D

Whole-brain activation signatures of weight-lowering drugs

Henrik H. Hansen, Johanna Perens, Urmas Roostalu, Jacob Lercke Skytte, Casper Gravesen Salinas, Pernille Barkholt, Ditte Dencker Thorbek, Kristoffer T. G. Rigbolt, Niels Vrang, Jacob Jelsing

Molecular Metabolism 47, 101171, 2021

Original Article

MOLECULAR METABOLISM

Whole-brain activation signatures of weight-lowering drugs

Henrik H. Hansen[*,1], **Johanna Perens**[1], **Urmas Roostalu, Jacob Lercke Skytte, Casper Gravesen Salinas, Pernille Barkholt, Ditte Dencker Thorbek, Kristoffer T.G. Rigbolt, Niels Vrang, Jacob Jelsing, Jacob Hecksher-Sørensen**[**]

ABSTRACT

Objective: The development of effective anti-obesity therapeutics relies heavily on the ability to target specific brain homeostatic and hedonic mechanisms controlling body weight. To obtain further insight into neurocircuits recruited by anti-obesity drug treatment, the present study aimed to determine whole-brain activation signatures of six different weight-lowering drug classes.

Methods: Chow-fed C57BL/6J mice (n = 8 per group) received acute treatment with lorcaserin (7 mg/kg; i.p.), rimonabant (10 mg/kg; i.p.), bromocriptine (10 mg/kg; i.p.), sibutramine (10 mg/kg; p.o.), semaglutide (0.04 mg/kg; s.c.) or setmelanotide (4 mg/kg; s.c.). Brains were sampled two hours post-dosing and whole-brain neuronal activation patterns were analysed at single-cell resolution using c-Fos immunohistochemistry and automated quantitative three-dimensional (3D) imaging.

Results: The whole-brain analysis comprised 308 atlas-defined mouse brain areas. To enable fast and efficient data mining, a web-based 3D imaging data viewer was developed. All weight-lowering drugs demonstrated brain-wide responses with notable similarities in c-Fos expression signatures. Overlapping c-Fos responses were detected in discrete homeostatic and non-homeostatic feeding centres located in the dorsal vagal complex and hypothalamus with concurrent activation of several limbic structures as well as the dopaminergic system.

Conclusions: Whole-brain c-Fos expression signatures of various weight-lowering drug classes point to a discrete set of brain regions and neurocircuits which could represent key neuroanatomical targets for future anti-obesity therapeutics.

Keywords Imaging; iDISCO; Light sheet fluorescence microscopy; c-Fos; Obesity; Anti-Obesity drugs

1. INTRODUCTION

Obesity represents a complex medical and behavioural problem which is insufficiently managed by current treatment interventions. Over the past decades, it has become increasing clear that the brain plays a fundamental role in regulating energy balance and body weight homeostasis. Central control of eating and energy balance is determined by a rich interplay of humoral, neuronal and molecular mechanisms. Peripheral signals of metabolic status, such as circulating factors (macronutrients, endocrine hormones) and neural innervation (vagal sensory nerves), activate distinct brain areas in a highly organised, hierarchical fashion. The involved central nervous system (CNS) circuits are regulated by both central and peripheral neurotransmitters, including hormones, neuropeptides, catecholamines and other endogenous ligands acting on specific receptor systems that regulate homeostatic and hedonic pathways [1]. The hypothalamus is considered one of the most important target structures for blood-borne hormonal and metabolic factors [2]. Also, there is ample evidence to support a key role for circumventricular organs, specialised brain structures with extensive vascularisation and fenestration, in sensing and relaying interoceptive signals of the nutritional state from the gut and viscera. Among these sensory areas, the brainstem dorsal vagal complex (DVC) is ideally positioned to transduce peripheral metabolic signals [3]. The executive control of food intake involves the cortico-limbic system receiving homeostatic signals relayed from the hypothalamus, amygdala and brainstem [4]. Many of the neurocircuits and hormones known to underlie the sensations of hunger and satiety also alter the activity in neural pathways controlling cue-potentiated feeding, pleasure and reward. In particular, the dopaminergic system has been implicated in the motivational and hedonic aspects of eating [5,6]. Excess caloric intake leading to obesity may therefore be conceptualised as the integral effects of deficient appetite regulation and eating-related impulse control [7]. Accordingly, neuroimaging studies in obese patients have linked efficient weight loss to altered activity in key brain sites for control of autonomic, executive and hedonic signalling [8].

The search for effective weight-lowering therapies has resulted in the development of obesity therapeutics with various modes and sites of

Gubra, Hørsholm, Denmark

[1] Henrik H. Hansen and Johanna Perens contributed equally to this work.

*Corresponding author. Gubra, Hørsholm Kongevej 11B, DK-2970 Hørsholm, Denmark. Tel. +45 31 52 26 50. E-mail: hbh@gubra.dk (H.H. Hansen).

**Corresponding author. Gubra, Hørsholm Kongevej 11B, DK-2970 Hørsholm, Denmark. Tel. +45 29 86 94 07. E-mail: jhs@gubra.dk (J. Hecksher-Sørensen).

Received November 20, 2020 • Revision received January 21, 2021 • Accepted January 21, 2021 • Available online 30 January 2021

https://doi.org/10.1016/j.molmet.2021.101171

Abbreviations

AAA	anterior amygdalar area
ACB	nucleus accumbens
APN	anterior pretectal nucleus
ARH	arcuate hypothalamic nucleus
AP	area postrema
BLA	basolateral amygdalar nucleus
BST	bed nuclei of the stria terminalis
CA3	field CA3 of the Ammon's horn
CEA	central amygdalar nucleus
CLA	claustrum
DG	dentate gyrus
DMH	dorsomedial nucleus of the hypothalamus
DMX	dorsal motor nucleus of the vagus nerve
DVC	dorsal vagal complex
iDISCO	immunolabelling-enabled imaging of solvent-cleared organs
EP	endopiriform nucleus
FDR	false discovery rate
FWER	family-wise error rate
G3DE	Gubra 3D Experience data viewer
HIP	hippocampal region
IMD	intermediodorsal nucleus of the thalamus
IP	intraperitoneal
IRN	intermediate reticular nucleus
IMD	intermediodorsal nucleus of the thalamus
LA	lateral amygdalar nucleus
LGv	ventral part of the lateral geniculate complex
LHA	lateral hypothalamic area
LP	lateral posterior nucleus of the thalamus
LPO	the lateral preoptic nucleus
LSFM	light sheet fluorescence microscopy
MD	mediodorsal nucleus of the thalamus
MDRNd	dorsal medullary reticular nucleus
MPO	medial preoptic nucleus
MY-mot	motor related part of medulla
NTS	nucleus of the solitary tract
PARN	parvicellular reticular nucleus
PB	parabrachial nucleus
PH	posterior hypothalamic nucleus
PO	peroral
PPT	posterior pretectal nucleus
PS	parastriatal nucleus
PSTN	parasubthalamic nucleus
pTFCE	probabilistic threshold-free cluster enhancement
PVH	paraventricular hypothalamic nucleus
PVT	paraventricular nucleus of the thalamus
SC	subcutaneous
SCm	motor related superior colliculus
SGN	thalamic suprageniculate nucleus
SNc	substantia nigra pars compacta
SUM	supramammillary nucleus
TU	tuberomammillary nucleus
VMH	ventromedial hypothalamic nucleus
VPLpc	parvicellular part of the ventroposteromedial thalamic nucleus
VTA	ventral tegmental area
ZI	zona incerta

CNS action. Most, if not all, centrally acting anti-obesity therapeutics act as appetite suppressants or curb food reward sensitivity [9,10]. Existing medicines to combat the obesity epidemic are, however, disappointingly few in number as drug development for obesity has been notoriously difficult due to insufficient clinical efficacy or safety concerns [11]. The few compounds that promote significant weight loss are associated with adverse side effects that cause treatment discontinuation or prevent long-term therapy in obese patients [12]. Understanding of peptide receptor function in regulating energy balance has evolved considerably in the past few years, which has resulted in an increased focus on developing modified gut peptides and neuropeptides as anti-obesity drugs [13].

The increasing number of weight-lowering drugs characterised in obese patients provides unique insights into shared and specific CNS responses to the various drug classes. Given the highly different molecular mechanisms targeted by centrally acting anti-obesity therapeutics, a scrutinised comparative analysis would optimally require imaging of the CNS pharmacological effects on a brain-wide scale. Methods for imaging deep within transparent organs has proven instrumental for unbiased mouse whole-brain mapping and quantitation of brain activation patterns at single-cell resolution using c-Fos expression as a proxy for neuronal stimulation [14]. Here, we mapped and compared mouse whole-brain c-Fos expression signatures of six centrally acting weight-lowering drugs with documented clinical effect, including lorcaserin (Belviq, 5-HT_{2C} receptor agonist), rimonabant (Acomplia, cannabinoid CB_1 receptor antagonist), bromocriptine (Parlodel, dopamine D_2 receptor agonist), sibutramine (Meridia, dual noradrenaline-serotonin reuptake inhibitor), semaglutide (Ozempic, glucagon-like peptide-1 (GLP-1) receptor agonist) and setmelanotide (RM-493, melanocortin-4 receptor (MC4R) agonist) [9,13,15]. Our study pinpoints brain regions and nuclei which could represent critical targets for future anti-obesity therapeutics.

2. MATERIALS AND METHODS

2.1. Animals

The Danish Animal Experiments Inspectorate approved all experiments which were conducted according to internationally accepted principles for the use of laboratory animals (license #2013-15-2934-00784). Male C57Bl/6J mice (9 weeks old, n = 80) were from Janvier Labs (Le Genest Saint Isle, France) and housed in a controlled environment (12-h light/dark cycle, lights on at 3 AM, 21 ± 2 °C, humidity 50 ± 10%). Each animal was identified by an implantable subcutaneous microchip (PetID Microchip, E-vet, Haderslev, Denmark). Mice had ad libitum access to tap water and regular chow (Altromin 1324, Brogaarden, Hørsholm, Denmark) throughout the study and were acclimatised for one week before study start.

2.2. Drug treatment

The study was conducted in the light phase. Mice were single-housed and randomized to treatment based on body weight recorded one day before treatment start. Compounds included lorcaserin hydrochloride hemihydrate (Adooq Bioscience, Irvine, CA); rimonabant hydrochloride (Chemos GmbH, Regenstauf, Germany); bromocriptine mesylate (Toronto Research Chemicals, Toronto, ON, Canada); sibutramine (AH Diagnostics, Aarhus, Denmark); semaglutide (Hoersholm Pharmacy, Hoersholm, Denmark) and setmelanotide hydrochloride (MetChemExpress, Monmouth Junction, NJ). Vehicles were as follows: 0.1% Tween-80 in saline (vehicle IP1, for lorcaserin); 5% dimethylsulfoxide + 5% chremophor in saline

(vehicle IP2, for rimonabant and bromocriptine), 0.5% hydroxypropyl methylcellulose (vehicle PO, for sibutramine), phosphate-buffered saline + 0.1% bovine serum albumin (vehicle SC, for semaglutide and setmelanotide). Mice (n = 8 per group) were dosed with lorcaserin (7 mg/kg, 36 μmol/kg, i.p.), rimonabant (10 mg/kg, 22 μmol/kg, i.p.), bromocriptine (10 mg/kg, 15 μmol/kg, i.p.), sibutramine (10 mg/kg, 36 mmol/kg, p.o.), semaglutide (0.04 mg/kg, 9.7 nmol/kg, s.c.) or setmelanotide (4 mg/kg, 3.5 μmol/kg, s.c.). Doses were corrected for individual salt weight. Corresponding control groups were administered vehicle (5 ml/kg, i.p., s.c. or p.o.). All compounds were prepared fresh and administered during the light phase.

2.3. Tissue processing

Mice were sedated with 2–4% isoflurane/O_2 (Attane Vet., ScanVet Animal Health, Fredensborg, Denmark) inhalation, anaesthetised by Hypnorm-Dormicum (fentanyl 788 μg/kg, fluanisone 25 mg/kg and midazolam 12.5 mg/kg, s.c.) and transcardially perfused with heparinized PBS and 10% neutral-buffered formalin. Brain samples were collected, prepared, immunolabelled and cleared according to the iDISCO+ protocol [16,17] as described in [18] using identical reagents and antibodies.

2.4. Light sheet microscopy

Brains were imaged in axial orientation using a Lavision ultramicroscope II (Miltenyi Biotec GmbH, Bergisch Gladbach, Germany) with Zyla 4.2P-CL10 sCMOS camera (Andor Technology, Belfast, United Kingdom), SuperK EXTREME supercontinuum white-light laser EXR-15 (NKT photonics, Birkerød, Denmark) and MV PLAPO 2XC (Olympus, Tokyo, Japan) objective lens. Horizontal images were acquired at 0.63× magnification (1.2 × total magnification) with an exposure time of 254 ms in a z-stack at 10 μm intervals. Acquired volumes (16-bit tiff) had an in-plane resolution of 4.8 μm and a z-resolution of 3.78 μm (NA = 0.156). Data were acquired in two channels, autofluorescence at 560 ± 20 nm (excitation) and 650 ± 25 nm (emission) wavelength (80% laser power) and c-Fos staining at 630 ± 15 nm (excitation) wavelength and 680 ± 15 nm (emission).

2.5. Image analysis

Image processing, registration and cell detection was performed according to the method by Perens et al. [18]. Identification of c-Fos+ cells involved detection of local intensity peaks within a moving filter cube of 5 × 5 × 3 pixels and seeded watershed segmentation (background intensity cut-off of 400 for specific channel, size of watershed segmentation volumes between 8 and 194 voxels), whereas detected intensity peaks were used as seeds. For cell quantification per brain region, light sheet fluorescence microscopy (LSFM) atlas was aligned to the individual cell segmentation volumes via pre-processed autofluorescence volumes through affine and b-spline transformations. Heatmaps depicting the up- and downregulation of c-Fos expression were created by aligning the cell-segmentation volumes to the LSFM-based mouse brain atlas using the inverse transform, generating and summing Gaussian spheres ($\sigma = 2$ voxels) around the centres of the c-Fos positive cells followed by subtraction of the average vehicle heatmaps from the group average heatmaps and removing the signal from non-significant brain regions based on the results of region-based statistical analysis. Image processing was performed in Python, and the Elastix software was applied to implement the registrations [19,20]. All registrations utilised mutual information as a similarity measure. 3D visualizations of heatmaps were created with the microscopy image analysis software Imaris™ version 2 (Oxford instruments, Abington, UK).

2.6. Region-based statistics

Statistical analysis of the c-Fos cell counts was performed in 308 atlas-defined brain regions, which were created by merging the 666 region segmentations of the LSFM mouse brain atlas according to a hierarchy tree of the atlas ontology [18,21]. A generalised linear model (GLM) was fitted to the number of detected c-Fos positive cells in each brain region in every animal group using a negative binomial for modelling the distribution of the datapoints. For each GLM, a Dunnett's test was performed. Due to the large number of regions in which the statistical test was performed, Benjamin-Hochberg false discovery rate (FDR) correction (cut-off of 0.05) was performed on the p-values. Statistical analysis was performed using R packages MASS, multcomp, lmtest and car [22–26]. Subsequently, a two-step manual validation was conducted to verify that the datapoints follow the negative binomial distribution, significance of the regions is not achieved due to outliers and the signal is not resulting from a spillover from neighbouring regions. The former was done by investigating deviance residuals and discarding significant regions if the residuals are violating the assumptions of normality and homoscedasticity. To quantify the influence of individual data points, Cook's distance was calculated, and significant regions with overly influential data points were discarded. Finally, origins of the signals were visually studied in the remaining significant regions and if spillover was identified, the region was declared as not significant. Two animals (vehicle SC, setmelanotide treatment) were excluded from the region-based statistical analysis due to suboptimal tissue quality.

2.7. Voxel-based statistics

Voxel-based statistical analysis was performed on the cell segmentation volumes. The pre-processing followed the approach by Vandenberghe et al. [27] for converting binary segmentation volumes of immunostained markers into Gaussian random fields which enable signal comparisons on a voxel level. First, the segmentation volumes were converted to the LSFM-based mouse brain atlas space. Subsequently, signal occurring in low-density areas (1 cell per 100 μm^3 in average per group comparison for the hindbrain and cerebellum, and 1–5 cells per 100 μm^3 for the cerebrum, midbrain and interbrain) was excluded from the analysis. Gaussian background noise ($\mu = 0$, $\sigma = 0.1$) was added to the binary cell segmentation volumes, and the volumes underwent smoothing with a Gaussian kernel with an optimal standard deviation ($\sigma = 2.25$) determined via bootstrap error minimization [27]. The last step of the pre-processing involved averaging the smoothed cell segmentations of the right and left hemisphere to improve statistical power. Voxel-wise statistical analysis was performed according to the probabilistic threshold-free cluster enhancement (pTFCE) method [28], while the hindbrain and cerebellum were analysed separately from the cerebrum, interbrain and midbrain. Standard values were used for the parameters Nh (number of thresholds), Zest (cluster-forming threshold) and C (connectivity) when performing pTFCE analysis. Family-wise error rate (FWER) was applied for multiple comparisons adjustments. Four animals were excluded from the voxel-based statistical analysis: the same two animals which were removed from the region-based statistical analysis and two additional mice from the bromocriptine-dosed group due to extremely low total cell counts.

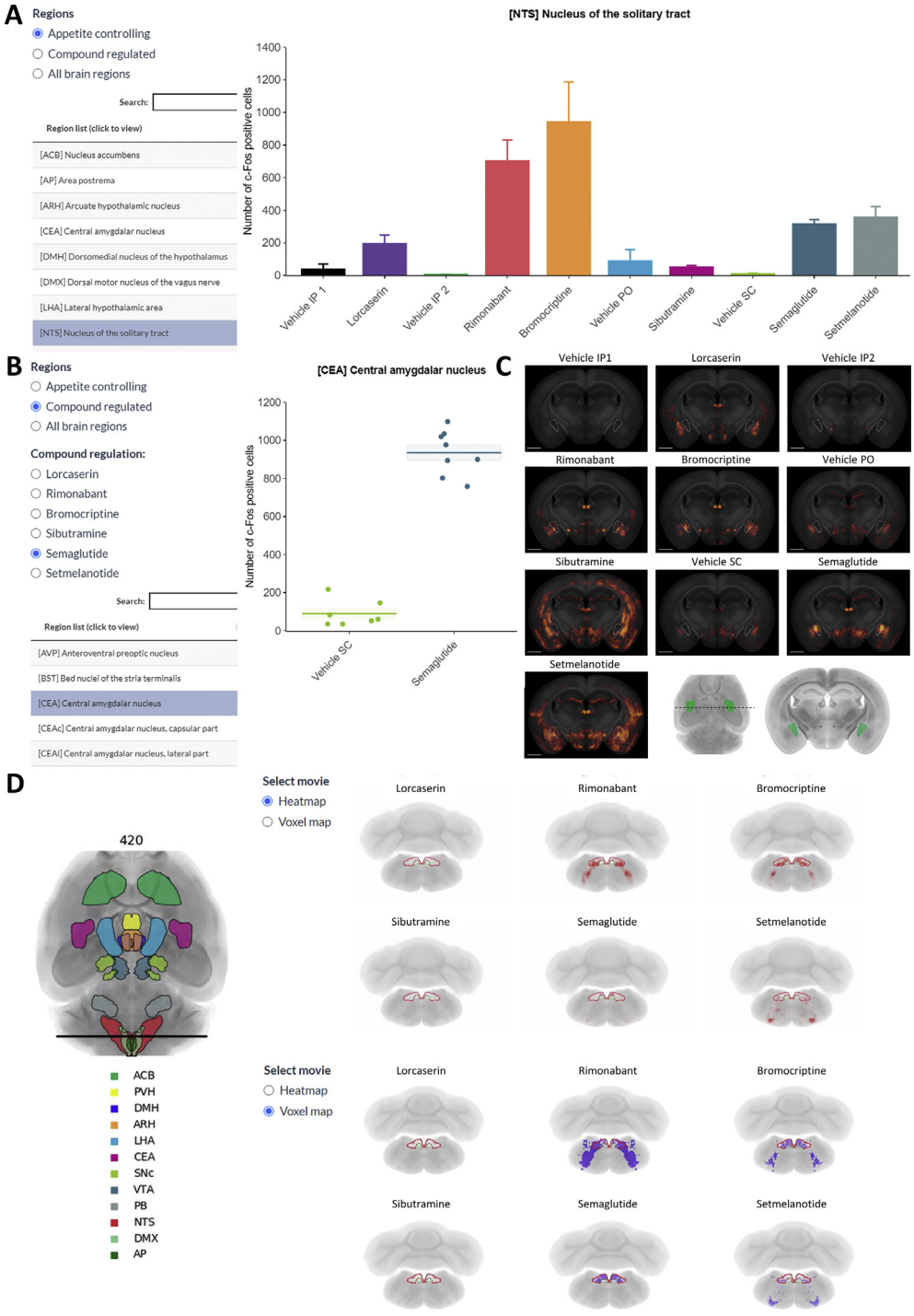

Figure 1: Web-based whole-brain imaging data viewer (Gubra 3D Experience/G3DE, https://g3de.gubra.dk/). **(A)** User interface of the online data browsing system showing the quantitative data for all treatment groups in selected appetite-regulating brain region (nucleus of the solitary tract, NTS). **(B)** Brain regions with compound-induced statistically significantly regulation of c-Fos+ cell numbers ($p < 0.05$ vs. corresponding vehicle control group). Example of data filtered to show only semaglutide-induced regulation of c-Fos expression (c-Fos + cell counts) in the central amygdalar nucleus (CEA) in each individual mouse (dot plot with indication of average number of c-Fos+ cells ± S.E.M.). **(C)** Representative group-average c-Fos expression heatmaps for each individual drug tested. *Lower panel*: Corresponding dorsal and coronal view of selected brain region. **(D)** Online movies showing whole-brain c-Fos responses to weight-lowering drugs (selected coronal plane at the level of the nucleus of the solitary tract, NTS). The 12 appetite-regulating regions are delineated in the coronal slice-by-slice fly-through movies. *Upper panel*: Heatmaps showing vehicle-subtracted average whole-brain c-Fos expression in response to weight-lowering compounds. Statistically significant changes ($p < 0.05$; Dunnett's test negative binomial generalized linear model, FDR < 0.05 for p-value adjustment) in c-Fos expression in response to treatment with weight-lowering compounds compared to corresponding vehicle controls are depicted in red (upregulation) and blue (downregulation). *Lower panel*: P-value maps from voxel-based statistical analysis visualising whole-brain c-Fos responses to individual weight-lowering drugs. Statistically significant changes between the treatment and vehicle group ($p < 0.05$) are indicated by graded purple colour.

3. RESULTS

3.1. Web-based imaging data viewer

All data are accessible using a web-based 3D imaging data viewer (Gubra 3D Experience/G3DE, https://g3de.gubra.dk/) allowing fast and efficient data mining as well as 3D visualisation of individual whole-brain c-Fos expression signatures of the drugs tested. The viewer provides users the opportunity to look up individual regions and display the quantitative data for all the treatment groups (Figure 1A) and filter for regions with statistically significant response to drug treatment (Figure 1B). For selected regions, the anatomical location and representative heatmaps of group-average c-Fos expression are displayed for each treatment in common reference space (coronal view, Figure 1C). The viewer also includes fly-through movies with indication of significant up- and downregulation of c-Fos expression in response to compound administration according to region-based statistical analysis and p-value maps, respectively (Figure 1D).

3.2. Brain-wide c-Fos expression profiles of weight-lowering drugs

Six weight-lowering drugs were profiled for acute effects on c-Fos expression patterns evaluated two hours after peripheral administration. Stimulated c-Fos expression, signifying neuronal activation, was a characteristic profile of all drugs tested. The drugs exhibited distinct whole-brain c-Fos expression signatures (Figure 2A–F). Accordingly, global c-Fos expression signatures of each individual drug were clearly separated (Figure 2G). The top 15 most influential brain regions driving the clustering of individual drug responses are indicated in Figure 2H. Out of 308 atlas-defined mouse brain areas analysed, the number of activated areas was most extensive for rimonabant (136 areas), setmelanotide (133 areas), lorcasarin (123 areas) and bromocriptine (96 areas). In comparison, brain activation patterns were more anatomically restricted for sibutramine (55 areas) and semaglutide (21 areas). Drug-induced c-Fos expression profiles also differed at the subregional level (see the G3DE data viewer).

3.3. Activation of key brain areas involved in energy homeostasis and hedonic eating

The weight-lowering drugs showed differential effects in key brain areas regulating energy homeostasis and hedonic eating (Figure 3, G3DE data viewer). These 12 areas included cardinal hypothalamic feeding centres [paraventricular (PVH), dorsomedial (DMH) and arcuate (ARH) hypothalamic nucleus; lateral hypothalamic area, (LHA)]; central amygdalar nucleus (CEA); major dopaminergic pathways [nucleus accumbens (ACB), substantia nigra pars compacta (SNC), ventral tegmental area (VTA)] as well as components of the brainstem [parabrachial nucleus (PB), nucleus of the solitary tract (NTS), dorsal motor nucleus of the vagus nerve (DMX), area postrema (AP)]. A further detailed analysis included all significantly regulated brain areas (Figure 4, G3DE data viewer). The most notable c-Fos signals are summarised below, with special emphasis on overlapping features of the six weight-lowering drugs.

3.3.1. Hypothalamus

Only setmelanotide induced c-Fos expression in all four designated subdivisions of the hypothalamus (PVH, DMH, ARH, LHA), see Figure 3. Lorcaserin, rimonabant, bromocriptine and setmelanotide significantly increased c-Fos + cell counts in the ARH and DMH, albeit to a different degree. Lorcaserin and setmelanotide also increased c-Fos + cell counts in the PVH. Rimonabant stimulated c-Fos expression in the LHA. Sibutramine and semaglutide showed no effect on c-Fos expression in the PVH, DMH, ARH and LHA. With the exception of sibutramine, all drugs activated the parastriatal nucleus (PS), parasubthalamic nucleus (PSTN) and supramammillary nucleus (SUM). Overlapping drug effects were detected in several other hypothalamic areas controlling energy balance, such as the lateral/medial preoptic nucleus (LPO, MPO), posterior hypothalamic nucleus (PH), tuberomammillary nucleus (TU), ventromedial hypothalamic nucleus (VMH) and zona incerta (ZI), see Figure 4.

3.3.2. Thalamus and cerebral cortex

Several areas of the thalamus and cerebral cortex were influenced by treatments. Notably, all drugs increased c-Fos expression in the paraventricular (PVT), intermediodorsal (IMD) and mediodorsal (MD) nuclei of the thalamus (Figure 4). Only rimonabant and setmelanotide showed additional effects in the 'gustatory thalamus' (parvicellular part of the ventroposteromedial thalamic nucleus (VPLpc, G3DE data viewer)). Lorcaserin, rimonabant, bromocriptine, sibutramine and setmelanotide stimulated c-Fos expression in visceral, limbic and primary gustatory cortical layers (Figures 2 and 4). Semaglutide did not influence c-Fos expression in any cortical areas examined.

3.3.3. Amygdala

All drugs robustly stimulated c-Fos expression in the amygdala, however, with drug-dependent subanatomical differences. Lorcaserin, rimonabant, bromocriptine, semaglutide and setmelanotide showed effects in the CEA. Whereas lorcasarin, rimonabant, bromocriptine and setmelanotide affected all parts of the CEA (central, medial, lateral), semaglutide only stimulated the medial part of the CEA (G3DE data viewer). With the exception of semaglutide, all drugs increased c-Fos expression in other amygdalar areas, such as the basolateral amygdalar nucleus (BLA), lateral amygdalar nucleus (LA) and anterior amygdalar area (AAA) (Figure 4). In the BLA, the effect of lorcaserin and sibutramine was located in the posterior/anterior part, while rimonabant, bromocriptine and setmelanotide affected all subdivisions (anterior, posterior, ventral; G3DE data viewer).

3.3.4. Striatum and midbrain

With the exception of semaglutide, all drugs stimulated c-Fos expression in the ACB (Figure 3). Differences in drug responses were observed within distinct anatomical divisions of the ACB, *i.e.*, the shell and core (G3DE data viewer). The c-Fos signal was restricted to the shell (for lorcasarin, rimonabant, bromocriptine) or included both the shell and core (for sibutramine and setmelanotide). For other striatal areas affected, see Figure 4. With the exception of semaglutide, all other drugs stimulated c-Fos expression in the midbrain (Figure 4). While lorcaserin, rimonabant, bromocriptine and setmelanotide promoted c-Fos induction in the VTA, the SNc was refractory to all drugs tested (Figure 3). A subset of midbrain sensorimotor areas, including reticular nuclei, were also stimulated by lorcaserin, rimonabant, bromocriptine and setmelanotide.

3.3.5. Brainstem

Semaglutide increased c-Fos expression in all four designated brainstem areas (AP, NTS, DMX, PB), see Figure 3. Notably, only semaglutide stimulated the AP. Semaglutide also induced c-Fos expression in Barrington's nucleus, but showed no further effects in the brainstem (Figure 4). Both bromocriptine and setmelanotide increased c-Fos expression in PB, NTS and DMX. While rimonabant induced c-Fos in the PB and NTS, only the NTS responded to lorcaserin administration. Sibutramine did not influence c-Fos expression in the PB, NTS, DMX and AP (Figure 3). Other brainstem areas were activated by lorcaserin,

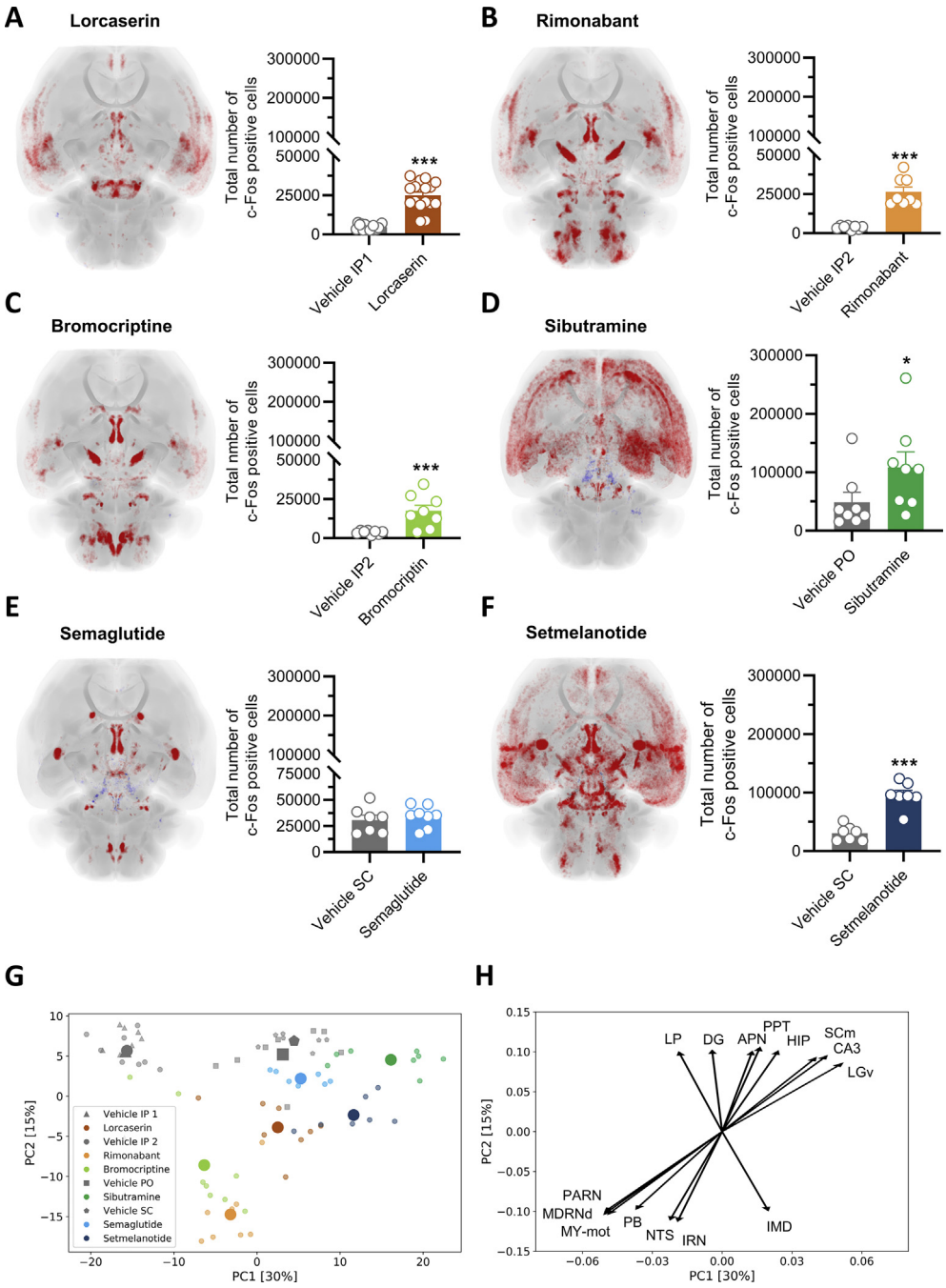

Figure 2: 3D mapping and quantification of whole-brain c-Fos responses to acute treatment with various weight-loss promoting compounds. Quantification and statistical analysis of c-Fos expression was performed in 308 brain regions. **(A)** Lorcaserin (7 mg/kg, i.p.), **(B)** rimonabant (10 mg/kg, i.p.), **(C)** bromocriptine (10 mg/kg, i.p.), **(D)** sibutramine (10 mg/kg, p.o.), **(E)** semaglutide (0.04 mg/kg, s.c.) and **(F)** setmelanotide (4 mg/kg, s.c.). All samples were registered into an LSFM-based mouse brain atlas. Heatmaps (dorsal view) depict vehicle-subtracted average whole-brain c-Fos expression ($n = 7$-8 mice per group) responses to the individual drug. Brain areas with statistically significant changes in c-Fos expression ($p < 0.05$; Dunnett's test negative binomial generalised linear model, FDR < 0.05 for p-value adjustment) are delineated in red (upregulation) or blue (downregulation) compared to corresponding vehicle controls. Coronal slice-by-slice fly-through of the heatmaps can be found in the G3DE imaging viewer. Bar plots show the differences in total numbers of c-Fos+ cells detected in compound and corresponding vehicle-dosed mice (*$p < 0.05$, ***$p < 0.001$; Dunnett's test negative binomial generalised linear model). **(G)** Principal component analysis (PCA) of whole-brain c-Fos expression. The PCA plot illustrates the degree of separation between individual drug effects on global c-Fos expression patterns (large markers indicate group average). **(H)** PCA loading plot depicting the coefficients of the top 15 most influential brain regions driving the clustering of data points in PCA plot. *Abbreviations*: Vehicle IP1, 0.1% Tween-80 in saline (intraperitoneal); Vehicle IP2, 5% DMSO + 5% chremophor in saline (intraperitoneal); Vehicle PO, 0.5% hydroxypropyl methylcellulose (peroral); Vehicle SC, 0.1% bovine serum albumin in phosphate-buffered saline (PBS, subcutaneous); *PARN*, parvicellular reticular nucleus; *MDRNd*, dorsal medullary reticular nucleus; *MY-mot*, motor-related part of medulla; *PB*, parabrachial nucleus; *NTS*, nucleus of the solitary tract; *IRN*, intermediate reticular nucleus; *IMD*, intermediodorsal nucleus of the thalamus, *LP*, lateral posterior nucleus of the thalamus; *DG*, dentate gyrus; *LGv*, ventral part of the lateral geniculate complex; *APN*, anterior pretectal nucleus; *PPT*, posterior pretectal nucleus; *HIP*, hippocampal region; *SCm*, motor-related superior colliculus; *CA3*, field CA3 of the Ammon's horn.

rimonabant, bromocriptine, sibutramine and setmelanotide (Figure 4). For these drugs, most frequent overlapping effects were associated with activation of pontine and medullary reticular nuclei. Although the majority of drugs activated AP, NTS, DMX and PB, c-Fos responses were heterogenous within these nuclei (Figure 1D, G3DE data viewer). To consider discrete changes in c-Fos + cell patterns not tracked by the atlas-guided analysis, we mapped changes in c-Fos+ cell clusters using label-free voxel-based statistical analysis. The p-value maps revealed different subanatomical responses to weight-lowering drugs (G3DE data viewer). For example, rimonabant, bromocriptine, semaglutide and setmelanotide activated large clusters of neurons in different segments of the PB (Figure 5). In contrast, c-Fos+ cell density did not change following administration of lorcaserin and sibutramine, signifying highly scattered c-Fos responses to these drugs.

3.3.6. Other areas

Overlapping drug effects were observed in subdivisions of the pallidum [bed nuclei of the stria terminalis (BST), substantia innominata] and subcortical plate [claustrum (CLA), endopiriform nucleus (EP)] (Figure 4). Drug effects were also detected within components of the hippocampal formation (Figure 4, G3DE data viewer).

4. DISCUSSION

Using c-Fos immunoreactivity as an indirect marker for neuronal activity, we mapped mouse whole-brain activation signatures of six individual weight-lowering drugs with different central mechanisms of action. A highly shared feature was activation of several nuclei and neurocircuits involved in the regulation of homeostatic feeding and food reward sensitivity. To facilitate the accessibility of the data presented here, a dedicated online interactive data browsing system was established. This resource will provide the community a platform for exploring the data in further detail and hopefully serve as the basis for future studies.

The largest overlap in c-Fos expression patterns was observed in the brainstem, amygdala, hypothalamus, thalamus and cortex. It is noteworthy that five out of six weight-lowering drugs stimulated components of the DVC, albeit showing anatomically distinct effects in the individual components (AP, NTS, DMX). Notably, weight-lowering drugs activating the DVC also activated the CEA and BST. Satiation signals arriving at the level of the dorsal vagal complex are distributed widely in the hypothalamus, amygdala and cortex [29]. Activation of the DVC triggers powerful satiation signals, which are conveyed by downstream feeding control circuitries, involving the PB, CEA and BST, to promote meal termination [30–32]. Large clusters of neurons in the medial/lateral NTS and lateral PB were activated by rimonabant, bromocriptine, semaglutide and setmelanotide. The NTS is a highly heterogenous structure with several molecularly undefined neuron populations being recruited by anorexigenic drugs; however, NTS neurons communicate viscerosensory information to the PB as one important neural pathway in feeding control. Accordingly, recent experimental evidence indicates that activation of mid-caudal NTS neurons projecting to the lateral PB is sufficient to elicit satiety responses [30]. Because lorcaserin promoted highly dispersed c-Fos expression in the NTS without concurrent activation of the PB, it may be speculated that this induction pattern did not lead to coordinated NTS responses.

The hypothalamus is characterised by numerous connections with essentially every major part of the brain, including the brainstem, amygdala, thalamus, and hippocampus [33]. Hypothalamic mechanisms have been implicated in the weight-lowering properties of the weight-lowering drug classes characterized in the present study [9,11]. Accordingly, five out of six weight-lowering drugs stimulated c-Fos expression in the hypothalamus, ranging from activation of few discrete nuclei (for semaglutide) to numerous nuclei across the entire hypothalamus (for setmelanotide). The PSTN, PS and SUM were activated by all drugs tested. The PSTN is rapidly activated by ingestion of palatable foods and has been proposed to suppress hedonic feeding behaviour via connections to the CEA and the insular cortex (AI) [34]. Also, the PS is an integral part of a satiety network involving the PB, CEA and AI [32]. The SUM has recently been identified as a neural substrate involved in relaying ghrelin-associated hunger signalling [35]. Cardinal hypothalamic areas engaged in feeding control and energy expenditure (ARH, DMH, LPO, MPO) were activated by most of the drugs tested. These areas are intimately connected and receive multiple humoral and neuronal inputs involved in energy homeostasis [33,36]. Less overlapping c-Fos profiles were observed for other prominent nutrient-sensing and feeding regulatory areas, such as the VMH, PVH and LHA [33]. Considering the melanocortin system plays an essential role in energy homeostasis [37], it is noteworthy that several of the weight-lowering drugs directly or indirectly stimulate melanocortin signalling pathways in specific areas of the hypothalamus (ARH) and brainstem (NTS) [38–40].

The weight-lowering drugs also activated medial/midline nuclei of thalamus (MD, PVT), which are principally connected to reciprocally activated corticolimbic (*e.g.*, ORB, ILA) and limbic subcortical structures (*e.g.*, BLA, ACB, BST). While the MD is closely involved in cognitive processes, PVT activation may encode palatable food reward associated with dopamine release in the ACB [41]. A subset of drugs showed combined stimulatory effects in the VPLpc ('gustatory thalamus') and GU, which forms a thalamocortical neurocircuit involved in taste processing [42].

CNS pathways regulating energy homeostasis are closely coupled with neurocircuits regulating food motivation and reward. Because the dopaminergic system is critically involved in hedonic feeding [5,6], we assessed whether drug-induced c-Fos signals also included dopaminergic areas in the striatum and midbrain. Four out of six drugs stimulated c-Fos expression in both the VTA and ACB. The VTA-ACB dopamine pathway is considered a key substrate for the incentive, reinforcing and motivational aspects of food intake [7]. The LHA-VTA-ACB loop has also been implicated in feeding and reward signalling [43]; however, LHA stimulation was not a common characteristic of the weight-lowering drugs tested. Almost all drugs stimulated the CLA, which receives dopamine inputs and transduces reward-associated signals to the ORB [44].

Brainstem and hypothalamic nuclei have classically been implicated in the appetite regulatory effects of GLP-1 receptor agonists [45], CB_1 receptor antagonists [46] and MC4R agonists [47]. The highly discrete c-Fos response to semaglutide is consistent with the peptide only accessing circumventricular/paraventricular areas [40]. Lack of blood–brain barrier penetrability of semaglutide suggests that c-Fos signals in deeper feeding centres, such as the ACB, BST, CEA and VTA, are secondary to direct effects in the hindbrain and hypothalamus. In the ARH, GLP-1 receptor agonist induced inhibition of food intake is mediated by direct activation of proopiomelanocortin/cocaine-and amphetamine-regulated transcript (POMC/CART) neurons and indirect inhibition of neuropeptide Y/agouti-related peptide (NPY/AgRP) neurons [48,49]. Despite ARH targeting of semaglutide, we and others have been unable to demonstrate enhanced arcuate c-Fos expression following treatment with semaglutide and liraglutide, a closely related analogue [40,50]. From these studies, it is unclear whether the lack of c-Fos response reflects opposing effects on POMC and NPY neuronal

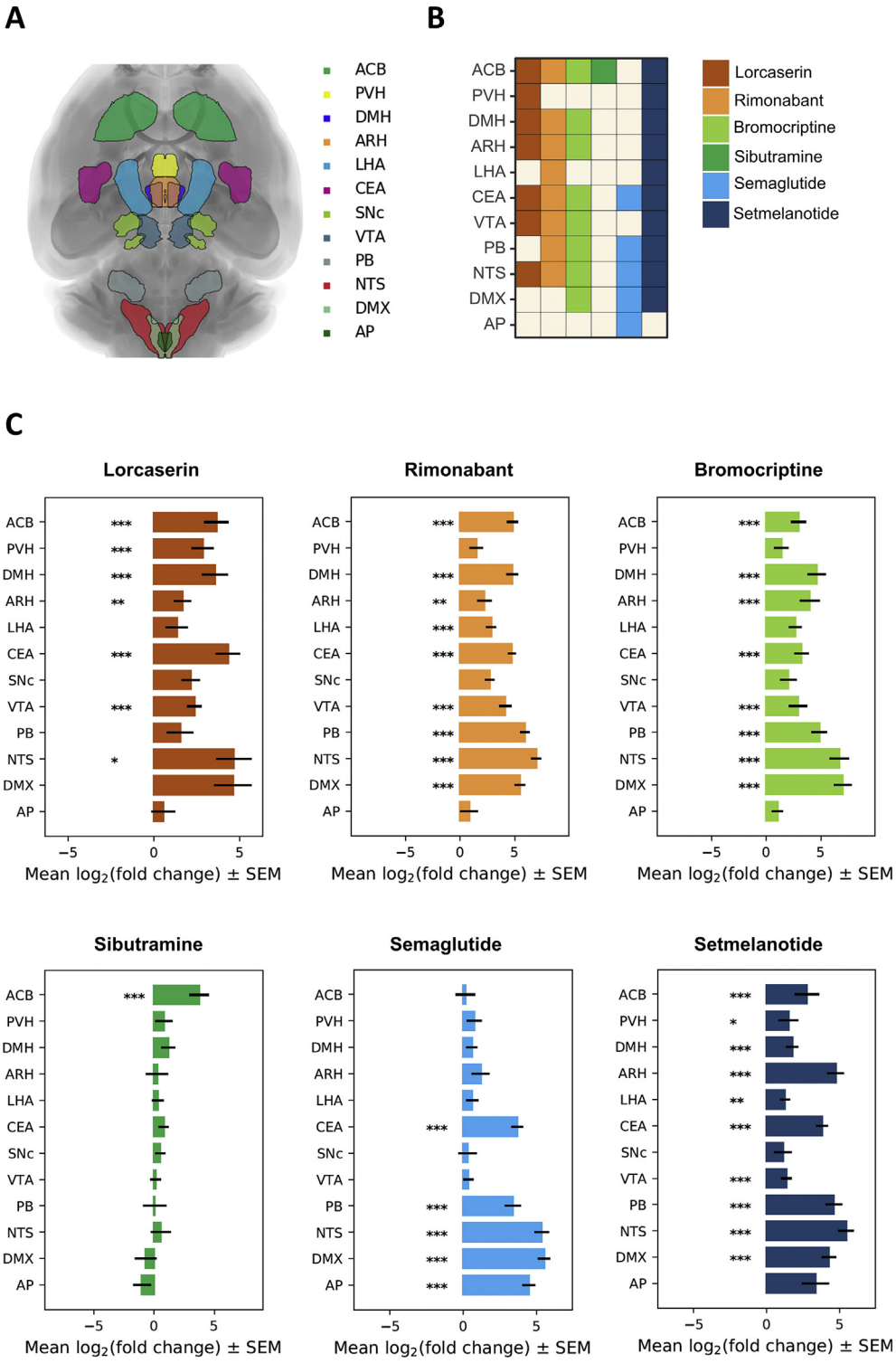

Figure 3: Overlapping and specific c-Fos expression signatures of weight-lowering drugs in major appetite-regulating brain regions. (A) Anatomical map (dorsal view) depicting 12 selected brain regions involved in appetite regulation. **(B)** Summary of drug-induced c-Fos induction across the 12 individual brain regions ($p < 0.05$; Dunnett's test negative binomial generalised linear model, FDR < 0.05 for p-value adjustment). **(C)** Fold-change (log2 scale, mean $\pm$ S.E.M.) in c-Fos positive cell counts in the 12 selected brain regions (rostro-caudal order) compared to corresponding vehicle controls. Dunnett's test negative binomial generalised linear model with p-value adjustment for multiple comparisons using FDR < 0.05 was applied for statistical analysis (*$p < 0.05$; **$p < 0.01$, ***$p < 0.001$). Abbreviations: *ACB*, nucleus accumbens; *ARH*, arcuate hypothalamic nucleus; *AP*, area postrema; *CEA*, central amygdalar nucleus; *DMH*, dorsomedial nucleus of the hypothalamus; *DMX*, dorsal motor nucleus of the vagus nerve; *LHA*, lateral hypothalamic area; *NTS*, nucleus of the solitary tract; *PB*, parabrachial nucleus; *PVH*, paraventricular hypothalamic nucleus; *SNc*, substantia nigra pars compacta; *VTA*, ventral tegmental area.

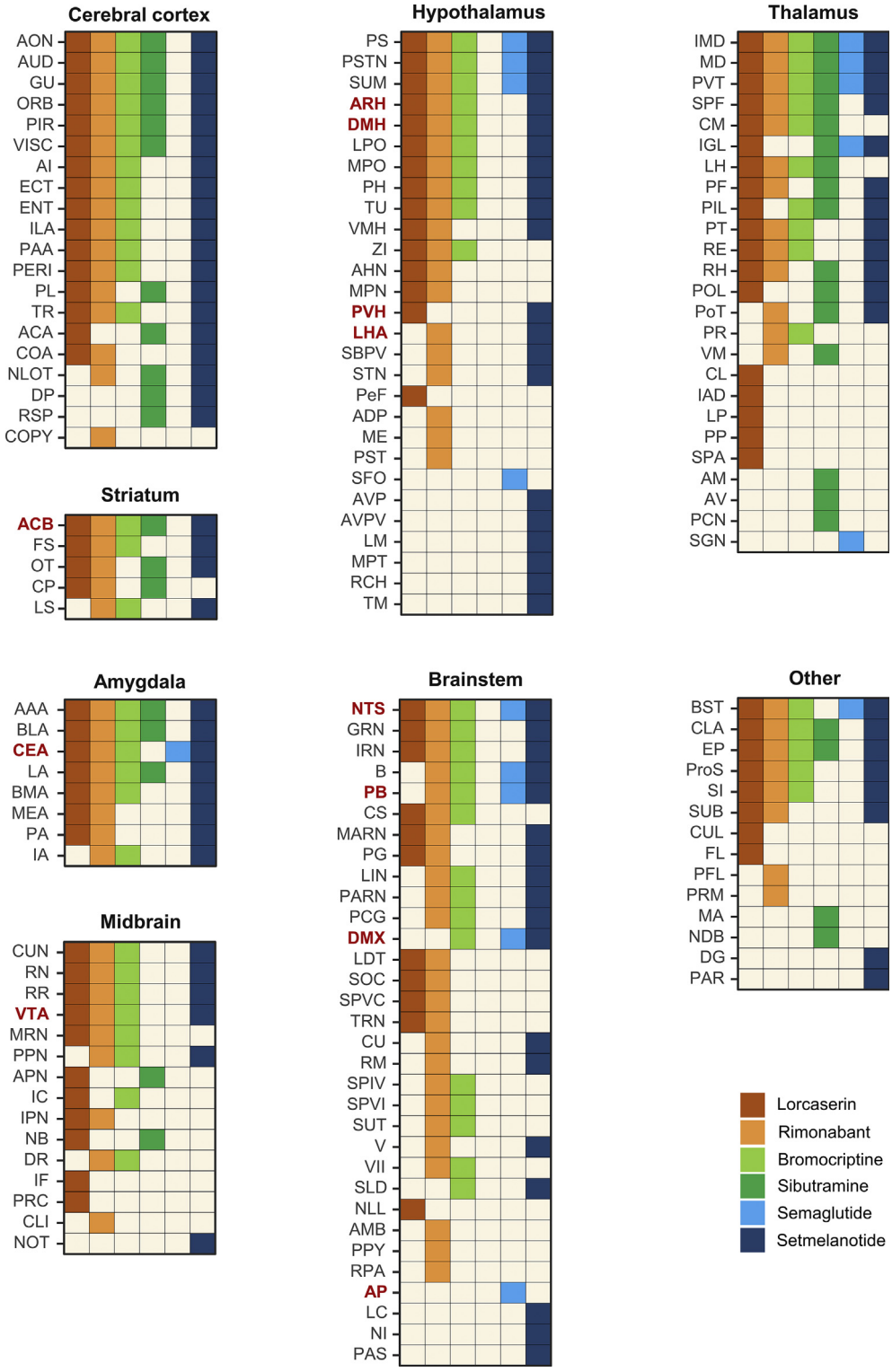

Figure 4: Whole-brain c-Fos expression signatures in response to weight-lowering compounds. Significant changes in c-Fos+ cell counts ($p < 0.05$) following administration of each individual weight-lowering compound. Dunnett's test negative binomial generalised linear model with p-value adjustment for multiple comparisons using FDR (cut-off of 0.05) was applied for statistical analysis. Regulated brain regions are categorised anatomically and ranked according to the number of drugs demonstrating a similar effect. With the exception of reduced c-Fos+ cell counts in the thalamic supragenicular nucleus (SGN, significantly down-regulated by liraglutide only), all significantly regulated areas exhibited increased c-Fos+ cell counts following drug treatment as compared to corresponding vehicle controls. Major appetite-regulating regions are indicated in red (*ACB*, nucleus accumbens; *ARH*, arcuate hypothalamic nucleus; *AP*, area postrema; *CEA*, central amygdalar nucleus; *DMH*, dorsomedial nucleus of the hypothalamus; *DMX*, dorsal motor nucleus of the vagus nerve; *LHA*, lateral hypothalamic area; *NTS*, nucleus of the solitary tract; *PB*, parabrachial nucleus; *PVH*, paraventricular hypothalamic nucleus; *VTA*, ventral tegmental area). For other abbreviated brain regions, see the web-based imaging data viewer.

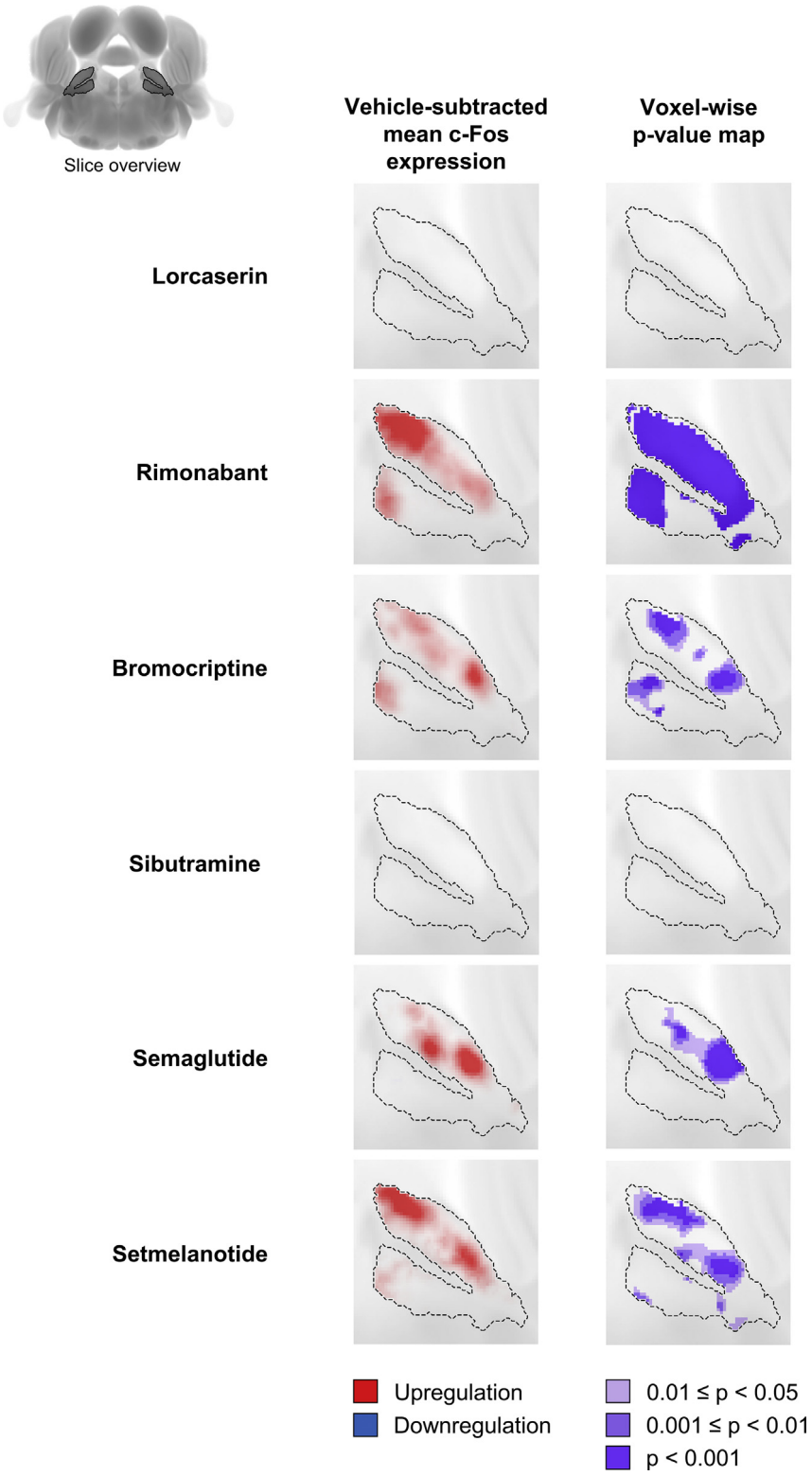

Figure 5: Subregional differentiation of c-Fos responses in the parabrachial nucleus in response to weight-lowering compounds. Voxel-wise statistical analysis of c-Fos expression was performed on pre-processed segmentation images of c-Fos+ cells using the pTFCE method and FWER approach for p-value adjustments. Resulting spatial p-value distributions ($p < 0.05$) are shown for the parabrachial nucleus in a representative coronal cross-section for different compound treatments (right column). Levels of statistical significance are indicated by graded purple colours. Vehicle-subtracted group means of c-Fos expression are depicted in the left column (red, upregulation; blue downregulation as compared to corresponding vehicle controls). The signal appearing in the neighbouring regions of parabrachial nucleus has been marked on both p-value distribution and c-Fos expression visualizations for clarity. Coronal slice-by-slice fly-through of whole brain p-value distribution resulting from voxel-based statistical analysis is exemplified in Figure 1D and can be seen in the web-based imaging data viewer.

activity or whether peripherally administered GLP-1 receptor agonists may predominantly have indirect effects on ARH neurotransmission. Studies have also suggested role for GLP-1 receptors in the regulation of reward-associated circuits involving the ACB, VTA, LS and PVT [51]. Only the PVT, which projects to ACB and receives excitatory input from NTS [52], was activated by semaglutide.

In contrast to semaglutide, lorcasarin, bromocriptine, rimonabant and setmelanotide promoted extensive and brain-wide c-Fos responses, which could imply that these drugs have improved CNS accessibility and/or evoke amplified excitatory responses in targeted neurocircuits. Lorcaserin, rimonabant and setmelanotide promoted broad stimulatory effects in the hypothalamus, including the ARH, which is strongly linked to the appetite regulatory action of these compounds [38,39,46]. Also NTS neurons are important targets for achieving the full anorectic effect of 5-HT_{2C} receptor stimulation [38]. In keeping with ARH-PVH connectivity being critical for the anorectic effects of MC4R agonists [39], setmelanotide also activated the PVH. The exact molecular mechanisms linking D_2 receptor activation to body weight regulation are unclear, but bromocriptine has been reported to promote satiation and thermogenesis via modulation of mesolimbic (ACB, VTA) and hypothalamic (LHA, ZI) dopaminergic signalling [53,54]. Lorcaserin, rimonabant and setmelanotide also stimulated c-Fos expression in ACB and VTA. Accumulating experimental evidence suggests that these compounds can reduce palatable food reward by indirect or direct action on ACB-VTA dopaminergic neurotransmission [55–57]. Although sibutramine did not evoke significant c-Fos stimulatory responses in the hypothalamus, available preclinical data suggest that sibutramine confers appetite suppression by enhancing adrenoceptor activity in ARC and LH [58]. In our study, sibutramine-induced c-Fos signals were largely confined to the cortex, amygdala and thalamus, which is consistent with the antidepressant, anxiolytic and analgesic action of dual serotonin-noradrenaline reuptake inhibitors [59–61].

Several weight-lowering compounds have glucoregulatory effects, which may involve central mechanisms of action independent of weight loss. Accordingly, rodent studies have suggested a role for the hypothalamus in the glucoregulatory effects of lorcaserin, rimonabant, bromocriptine and setmelanotide [9,62–65]. Furthermore, brain stem melanocortin neurocircuitries have been implicated in the anti-diabetic action of 5-HT_{2C} receptor and MC4R agonists [38,62,66]. Further studies are needed to determine whether glucoregulatory mechanisms contribute to the individual drug-induced c-Fos signatures.

It should be considered that drug-induced changes in whole-brain c-Fos architecture may represent composite signatures of both therapeutic and adverse effects. Components of the brainstem reticular formation, which integrates somatic and visceral inputs and subserve important autonomic, motor and cardiovascular functions [67], were activated by rimonabant, bromocriptine, sibutramine and setmelanotide. AP, NTS and CEA signalling have been implicated in visceral malaise, and enhanced NTS-CEA connectivity may be an important mechanism for GLP-1 receptor agonist-induced nausea responses [68]. Adverse central effects are not common with lorcaserin and bromocriptine treatment [69,70]. In contrast, rimonabant was withdrawn from the market in 2008 due to increased risk of neuropsychiatric adverse effects, notably depression and anxiety, which is consistent with prominent CB_1 receptor expression in brain areas associated with regulation of emotion such as the prefrontal cortex, hippocampus and amygdala [71]. In the current study, major components of the prefrontal cortex and amygdala were activated by rimonabant. Sibutramine was withdrawn from the market in 2010 because of cardiovascular safety concerns. Sibutramine was devoid of c-Fos effects in the brainstem, supporting that haemodynamic responses to sibutramine are mediated by stimulation of peripheral adrenoceptor function [72]. Setmelanotide increases heart rate and blood pressure in rodents [73], but not in non-human primates and humans [74,75]. MC4R-induced cardiovascular effects in rodents have been linked to increased sympathetic activity in spinal pre-ganglionic neurons [66]. CNS accessibility may also be a critical factor for adverse cardiovascular effects of MC4R agonists [73].

Centrally acting weight-lowering drugs show very similar c-Fos signatures in lean and obese mice, making it useful to profile c-Fos expression signatures of weight-lowering compounds in lean mice. Accordingly, acute administration of semaglutide induces overall similar whole-brain c-Fos signature in lean and diet-induced obese (DIO) mice [18]. Although comparative c-Fos expression studies in lean and obese mice have not been reported for all compounds tested in the present study, conventional histological studies have demonstrated comparable c-Fos responses in lean and obese mice treated with 5-HT_{2C} receptor agonists [76,77], CB_1 receptor antagonists [78,79] and MC4R agonists [80,81], respectively.

Drug doses were within ranges applied in mouse in vivo efficacy studies reported previously [38,40,82–86]. It should be emphasised that the drugs tested have different weight loss efficacy in both preclinical and clinical settings, which is determined by several factors, such as mode of action, pharmacokinetics, CNS drug and target distribution, as well as therapeutic index. The current study was not specifically designed to compare individual drug doses which would ultimately elicit similar weight loss. Temporal dynamics c-Fos expression should also be considered, as whole-brain c-Fos expression patterns were only determined two hours after dosing. For example, recent LSFM studies have demonstrated further anatomically restricted c-Fos signals four hours after semaglutide administration in lean mice [18,40]. A detailed profiling of time- and dose–response relationships on c-Fos expression could therefore further enable interpretation of the individual drug-induced brain activation signatures. Due to technical limitations, the current study cannot identify areas of inhibition. Other methods should be therefore employed to specifically delineate the various signalling pathways and neurocircuits recruited by centrally acting weight-lowering drugs.

5. CONCLUSION

In conclusion, we pinpoint several overlapping whole-brain activation signatures of various weight-lowering drugs. This shared feature suggests that weight-lowering drugs stimulate distinct homeostatic and non-homeostatic feeding centres. Future centrally acting anti-obesity compounds may be specifically designed to target key components of this neurocircuitry framework to provide more effective and sustained weight loss in obese patients.

FUNDING

The work was funded by Innovation Fund Denmark (JP, grant number 8053-00121B)..

AUTHOR CONTRIBUTIONS

PB, NV, JJ and JHS conceived and designed the experiments. JHS, JP, UR, JLS, CGS, PB and DDT carried out the experiments. HHH, JP, UR, JLS, CGS, PB, KTGR, NV, JJ and JHS analysed and interpreted the data. HHH, JP, JLS, KTGR, JJ and JHS wrote the paper. All authors reviewed and approved the final paper.

DATA AVAILABILITY

All data are accessible using the web-based imaging data viewer (G3DE, https://g3de.gubra.dk).

ACKNOWLEDGEMENTS

N/A

CONFLICT OF INTEREST

All authors are employed by Gubra; NV and JJ are owners of Gubra.

REFERENCES

[1] Clemmensen, C., Müller, T.D., Woods, S.C., Berthoud, H.-R., Seeley, R.J., Tschöp, M.H., 2017. Gut-brain cross-talk in metabolic control. Cell 168(5): 758–774. https://doi.org/10.1016/j.cell.2017.01.025.

[2] Berthoud, H.R., Münzberg, H., Morrison, C.D., 2017. Blaming the brain for obesity: integration of hedonic and homeostatic mechanisms. Gastroenterology 152(7):1728–1738. https://doi.org/10.1053/j.gastro.2016.12.050.

[3] Hoyda, T.D., Smith, P.M., Ferguson, A.V., 2009. Gastrointestinal hormone actions in the central regulation of energy metabolism: potential sensory roles for the circumventricular organs. International Journal of Obesity 33:S16–S21. https://doi.org/10.1038/ijo.2009.11.

[4] Caron, A., Richard, D., 2017. Neuronal systems and circuits involved in the control of food intake and adaptive thermogenesis. Annals of the New York Academy of Sciences, 35–53. https://doi.org/10.1111/nyas.13263.

[5] Tulloch, A.J., Murray, S., Vaicekonyte, R., Avena, N.M., 2015. Neural responses to macronutrients: hedonic and homeostatic mechanisms. Gastroenterology 148(6):1205–1218. https://doi.org/10.1053/j.gastro.2014.12.058.

[6] Berthoud, H.-R., Lenard, N.R., Shin, A.C., 2011. Food reward, hyperphagia, and obesity. American Journal of Physiology - Regulatory, Integrative and Comparative Physiology 300(6):R1266–R1277.

[7] Ferrario, C.R., Labouèbe, G., Liu, S., Nieh, E.H., Routh, V.H., Xu, S., et al., 2016. Homeostasis meets motivation in the battle to control food intake. Journal of Neuroscience 36:11469–11481. Society for Neuroscience.

[8] Farr, O.M., Li, C.S.R., Mantzoros, C.S., 2016. Central nervous system regulation of eating: insights from human brain imaging. Metabolism: Clinical and Experimental, 699–713. https://doi.org/10.1016/j.metabol.2016.02.002.

[9] Gautron, L., Elmquist, J.K., Williams, K.W., 2015. Neural control of energy balance: translating circuits to therapies. Cell, 133–145. https://doi.org/10.1016/j.cell.2015.02.023.

[10] Coulter, A.A., Rebello, C.J., Greenway, F.L., 2018. Centrally acting agents for obesity: past, present, and future. Drugs, 1113–1132. https://doi.org/10.1007/s40265-018-0946-y.

[11] Dietrich, M.O., Horvath, T.L., 2012. Limitations in anti-obesity drug development: the critical role of hunger-promoting neurons. Nature Reviews Drug Discovery 11(9):675–691. https://doi.org/10.1038/nrd3739.

[12] Khera, R., Murad, M.H., Chandar, A.K., Dulai, P.S., Wang, Z., Prokop, L.J., et al., 2016. Association of pharmacological treatments for obesity withweight loss and adverse events a systematic review and meta-analysis. JAMA - Journal of the American Medical Association 315(22):2424–2434. https://doi.org/10.1001/jama.2016.7602.

[13] Srivastava, G., Apovian, C., 2018. Future pharmacotherapy for obesity: new anti-obesity drugs on the horizon. Current Obesity Reports, 147–161. https://doi.org/10.1007/s13679-018-0300-4.

[14] Farivar, R., Zangenehpour, S., Chaudhuri, A., 2004. Cellular-resolution activity mapping of the brain using immediate-early gene expression. Frontiers in Bioscience, 104–109. https://doi.org/10.2741/1198.

[15] Cincotta, A.H., Meier, A.H., 1996. Bromocriptine (Ergoset) reduces body weight and improves glucose tolerance in obese subjects. Diabetes Care 19(6):667–670. https://doi.org/10.2337/diacare.19.6.667.

[16] Renier, N., Wu, Z., Simon, D.J., Yang, J., Ariel, P., Tessier-Lavigne, M., 2014. iDISCO: a simple, rapid method to immunolabel large tissue samples for volume imaging. Cell 159(4):896–910. https://doi.org/10.1016/j.cell.2014.10.010.

[17] Renier, N., Adams, E.L., Kirst, C., Dulac, C., Osten, P., Tessier-Lavigne, M., 2016. Mapping of brain activity by automated volume Analysis of immediate early genes. Cell 165(7):1789–1802. https://doi.org/10.1016/j.cell.2016.05.007.

[18] Perens, J., Salinas, C.G., Skytte, J.L., Roostalu, U., Dahl, A.B., Dyrby, T.B., et al., 2020. An optimized mouse brain atlas for automated mapping and quantification of neuronal activity using iDISCO+ and light sheet fluorescence microscopy. Neuroinformatics. https://doi.org/10.1007/s12021-020-09490-8.

[19] Klein, S., Staring, M., Murphy, K., Viergever, M.A., Pluim, J.P.W., 2010. elastix: a toolbox for intensity-based medical image registration. IEEE Transactions on Medical Imaging 29(1):196–205. https://doi.org/10.1109/TMI.2009.2035616.

[20] Shamonin, D.P., Bron, E.E., Lelieveldt, B.P.F., Smits, M., Klein, S., Staring, M., 2014. Fast parallel image registration on CPU and GPU for diagnostic classification of Alzheimer's disease. Frontiers in Neuroinformatics 7:50. https://doi.org/10.3389/fninf.2013.00050.

[21] Wang, Q., Ding, S.L., Li, Y., Royall, J., Feng, D., Lesnar, P., et al., 2020. The allen mouse brain common coordinate framework: a 3D reference atlas. Cell 181(4):936–953. https://doi.org/10.1016/j.cell.2020.04.007 e20.

[22] R Core Team, 2018. R: a language and environment for statistical computing. Vienna, Austria.

[23] Venables, W., Ripley, B., 2002. Modern applied statistics with S. New York, USA: Springer. Fourth.

[24] Hothorn, T., Bretz, F., Westfall, P., 2008. Simultaneous inference in general parametric models. Biometrical Journal 50(3):346–363.

[25] Zeileis, A., Hothorn, T., 2002. Diagnostic checking in regression relationships. R News 2(3):7–10.

[26] Fox, J., Weisberg, S., 2019. An R companion to applied regression. Thousand Oaks, CA, USA: Sage. Third.

[27] Vandenberghe, M.E., Souedet, N., Hérard, A.S., Ayral, A.M., Letronne, F., Balbastre, Y., et al., 2018. Voxel-based statistical analysis of 3D immunostained tissue imaging. Frontiers in Neuroscience 12(754). https://doi.org/10.3389/fnins.2018.00754.

[28] Spisák, T., Spisák, Z., Zunhammer, M., Bingel, U., Smith, S., Nichols, T., et al., 2018. Probabilistic TFCE: a generalized combination of cluster size and voxel intensity to increase statistical power. NeuroImage 185:12–26. https://doi.org/10.1016/j.neuroimage.2018.09.078.

[29] Berthoud, H.R., 2008. The vagus nerve, food intake and obesity. Regulatory Peptides, 15–25. https://doi.org/10.1016/j.regpep.2007.08.024.

[30] Roman, C.W., Derkach, V.A., Palmiter, R.D., 2016. Genetically and functionally defined NTS to PBN brain circuits mediating anorexia. Nature Communications 7. https://doi.org/10.1038/ncomms11905.

[31] Carter, M.E., Soden, M.E., Zweifel, L.S., Palmiter, R.D., 2013. Genetic identification of a neural circuit that suppresses appetite. Nature 503(7474):111–114. https://doi.org/10.1038/nature12596.

[32] Zséli, G., Vida, B., Martinez, A., Lechan, R.M., Khan, A.M., Fekete, C., 2016. Elucidation of the anatomy of a satiety network: focus on connectivity of the parabrachial nucleus in the adult rat. Journal of Comparative Neurology 524(14):2803–2827. https://doi.org/10.1002/cne.23992.

[33] Simpson, K.A., Martin, N.M., Bloom, S.R., 2008. Hypothalamic regulation of appetite. Expert Review of Endocrinology and Metabolism, 577–592. https://doi.org/10.1586/17446651.3.5.577.

[34] Barbier, M., Chometton, S., Pautrat, A., Miguet-Alfonsi, C., Datiche, F., Gascuel, J., et al., 2020. A basal ganglia-like corticala-amygdalara-hypothalamic network mediates feeding behavior. Proceedings of the National

Academy of Sciences of the United States of America 117(27):15967–15976. https://doi.org/10.1073/pnas.2004914117.

[35] Le May, M.V., Hume, C., Sabatier, N., Schéle, E., Bake, T., Bergström, U., et al., 2019. Activation of the rat hypothalamic supramammillary nucleus by food anticipation, food restriction or ghrelin administration. Journal of Neuroendocrinology 31(7). https://doi.org/10.1111/jne.12676.

[36] Blouet, C., Schwartz, G.J., 2010. Hypothalamic nutrient sensing in the control of energy homeostasis. Behavioural Brain Research, 1–12. https://doi.org/10.1016/j.bbr.2009.12.024.

[37] Garfield, A.S., Lam, D.D., Marston, O.J., Przydzial, M.J., Heisler, L.K., 2009. Role of central melanocortin pathways in energy homeostasis. Trends in Endocrinology and Metabolism, 203–215. https://doi.org/10.1016/j.tem.2009.02.002.

[38] D'Agostino, G., Lyons, D., Cristiano, C., Lettieri, M., Olarte-Sanchez, C., Burke, L.K., et al., 2018. Nucleus of the solitary tract serotonin 5-HT2C receptors modulate food intake. Cell Metabolism 28(4):619–630. https://doi.org/10.1016/j.cmet.2018.07.017 e5.

[39] Baldini, G., Phelan, K.D., 2019. The melanocortin pathway and control of appetite-progress and therapeutic implications. Journal of Endocrinology, R1–R33. https://doi.org/10.1530/JOE-18-0596.

[40] Gabery, S., Salinas, C.G., Paulsen, S.J., Ahnfelt-Rønne, J., Alanentalo, T., Baquero, A.F., et al., 2020. Semaglutide lowers body weight in rodents via distributed neural pathways. JCI Insight 5(6). https://doi.org/10.1172/jci.insight.133429.

[41] Vertes, R.P., Linley, S.B., Hoover, W.B., 2015. Limbic circuitry of the midline thalamus. Neuroscience & Biobehavioral Reviews, 89–107. https://doi.org/10.1016/j.neubiorev.2015.01.014.

[42] Samuelsen, C.L., Gardner, M.P.H., Fontanini, A., 2013. Thalamic contribution to cortical processing of taste and expectation. Journal of Neuroscience 33(5): 1815–1827. https://doi.org/10.1523/JNEUROSCI.4026-12.2013.

[43] Stuber, G.D., Wise, R.A., 2016. Lateral hypothalamic circuits for feeding and reward. Nature Neuroscience, 198–205. https://doi.org/10.1038/nn.4220.

[44] Terem, A., Gonzales, B.J., Peretz-Rivlin, N., Ashwal-Fluss, R., Bleistein, N., del Mar Reus-Garcia, M., et al., 2020. Claustral neurons projecting to frontal cortex mediate contextual association of reward. Current Biology. https://doi.org/10.1016/j.cub.2020.06.064.

[45] Kanoski, S.E., Hayes, M.R., Skibicka, K.P., 2016. GLP-1 and weight loss: unraveling the diverse neural circuitry 310(10):R885–R895. https://doi.org/10.1152/ajpregu.00520.2015.

[46] Koch, M., 2017. Cannabinoid receptor signaling in central regulation of feeding behavior: a mini-review. Frontiers in Neuroscience. https://doi.org/10.3389/fnins.2017.00293.

[47] Ellacott, K.L.J., Cone, R.D., 2004. The central melanocortin system and the integration of short- and long-term regulators of energy homeostasis. Recent Progress in Hormone Research, 395–408. https://doi.org/10.1210/rp.59.1.395.

[48] Secher, A., Jelsing, J., Baquero, A.F., Hecksher-Sørensen, J., Cowley, M.A., Dalbøge, L.S., et al., 2014. The arcuate nucleus mediates GLP-1 receptor agonist liraglutide-dependent weight loss. Journal of Clinical Investigation 124(10):4473–4488. https://doi.org/10.1172/JCI75276.

[49] Sisley, S., Gutierrez-Aguilar, R., Scott, M., D'Alessio, D.A., Sandoval, D.A., Seeley, R.J., 2014. Neuronal GLP1R mediates liraglutide's anorectic but not glucose-lowering effect. Journal of Clinical Investigation 124(6): 2456–2463.

[50] Adams, J.M., Pei, H., Sandoval, D.A., Seeley, R.J., Chang, R.B., Liberles, S.D., et al., 2018. Liraglutide modulates appetite and body weight through glucagon-like peptide 1 receptor-expressing glutamatergic neurons. Diabetes 67:1538–1548. American Diabetes Association Inc.

[51] Müller, T.D., Finan, B., Bloom, S.R., D'Alessio, D., Drucker, D.J., Flatt, P.R., et al., 2019. Glucagon-like peptide 1 (GLP-1). Molecular Metabolism, 72–130. https://doi.org/10.1016/j.molmet.2019.09.010.

[52] Ong, Z.Y., Liu, J.J., Pang, Z.P., Grill, H.J., 2017. Paraventricular thalamic control of food intake and reward: role of glucagon-like peptide-1 receptor signaling. Neuropsychopharmacology 42(12):2387–2397. https://doi.org/10.1038/npp.2017.150.

[53] Davis, L.M., Michaelides, M., Cheskin, L.J., Moran, T.H., Aja, S., Watkins, P.A., et al., 2009. Bromocriptine administration reduces hyperphagia and adiposity and differentially affects dopamine D2 receptor and transporter binding in leptin-receptor-deficient Zucker rats and rats with diet-induced obesity. Neuroendocrinology 89(2):152–162.

[54] Folgueira, C., Beiroa, D., Porteiro, B., Duquenne, M., Puighermanal, E., Fondevila, M.F., et al., 2019. Hypothalamic dopamine signalling regulates brown fat thermogenesis. Nature Metabolism 1(8):811–829. https://doi.org/10.1038/s42255-019-0099-7.

[55] Higgins, G.A., Zeeb, F.D., Fletcher, P.J., 2017. Role of impulsivity and reward in the anti-obesity actions of 5-HT2C receptor agonists. Journal of Psychopharmacology, 1403–1418. https://doi.org/10.1177/0269881117735797.

[56] Melis, T., Succu, S., Sanna, F., Boi, A., Argiolas, A., Melis, M.R., 2007. The cannabinoid antagonist SR 141716A (Rimonabant) reduces the increase of extra-cellular dopamine release in the rat nucleus accumbens induced by a novel high palatable food. Neuroscience Letters 419(3):231–235. https://doi.org/10.1016/j.neulet.2007.04.012.

[57] Pandit, R., Omrani, A., Luijendijk, M.C.M., De Vrind, V.A.J., Van Rozen, A.J., Ophuis, R.J.A.O., et al., 2016. Melanocortin 3 receptor signaling in midbrain dopamine neurons increases the motivation for food reward. Neuropsychopharmacology 41(9):2241–2251. https://doi.org/10.1038/npp.2016.19.

[58] Jackson, H.C., Bearham, M.C., Hutchins, L.J., Mazurkiewicz, S.E., Needham, A.M., Heal, D.J., 1997. Investigation of the mechanisms underlying the hypophagic effects of the 5-HT and noradrenaline reuptake inhibitor, sibutramine, in the rat. British Journal of Pharmacology 121(8):1613–1618. https://doi.org/10.1038/sj.bjp.0701311.

[59] Bravo, L., Llorca-Torralba, M., Berrocoso, E., Micó, J.A., 2019. Monoamines as drug targets in chronic pain: focusing on neuropathic pain. Frontiers in Neuroscience. https://doi.org/10.3389/fnins.2019.01268.

[60] Papakostas, G.I., Thase, M.E., Fava, M., Nelson, J.C., Shelton, R.C., 2007. Are antidepressant drugs that combine serotonergic and noradrenergic mechanisms of action more effective than the selective serotonin reuptake inhibitors in treating major depressive disorder? A meta-analysis of studies of newer agents. Biological Psychiatry 62(11):1217–1227. https://doi.org/10.1016/j.biopsych.2007.03.027.

[61] Kornstein, S.G., Russell, J.M., Spann, M.E., Crits-Christoph, P., Ball, S.G., 2009. Duloxetine in the treatment of generalized anxiety disorder. Expert Review of Neurotherapeutics, 155–165. https://doi.org/10.1586/14737175.9.2.155.

[62] Burke, L.K., Ogunnowo-Bada, E., Georgescu, T., Cristiano, C., de Morentin, P.B.M., Valencia Torres, L., et al., 2017. Lorcaserin improves glycemic control via a melanocortin neurocircuit. Molecular Metabolism 6(10): 1092–1102. https://doi.org/10.1016/j.molmet.2017.07.004.

[63] Kumar, K.G., Sutton, G.M., Dong, J.Z., Roubert, P., Plas, P., Halem, H.A., et al., 2009. Analysis of the therapeutic functions of novel melanocortin receptor agonists in MC3R- and MC4R-deficient C57BL/6J mice. Peptides 30(10): 1892–1900. https://doi.org/10.1016/j.peptides.2009.07.012.

[64] O'Hare, J.D., Zieliński, E., Cheng, B., Scherer, T., Buettner, C., 2011. Central endocannabinoid signaling regulates hepatic glucose production and systemic lipolysis. Diabetes 60(4):1055–1062. https://doi.org/10.2337/db10-0962.

[65] Furigo, I.C., Suzuki, M.F., Oliveira, J.E., Ramos-Lobo, A.M., Teixeira, P.D.S., Pedroso, J.A., et al., 2019. Suppression of prolactin secretion partially explains the antidiabetic effect of bromocriptine in ob/ob Mice. Endocrinology 160(1): 193–204. https://doi.org/10.1210/en.2018-00629.

[66] Sohn, J.W., Harris, L.E., Berglund, E.D., Liu, T., Vong, L., Lowell, B.B., et al., 2013. Melanocortin 4 receptors reciprocally regulate sympathetic and parasympathetic preganglionic neurons. Cell 152(3):612–619. https://doi.org/10.1016/j.cell.2012.12.022.

[67] Yates, B.J., Stocker, S.D., 1998. Integration of somatic and visceral inputs by the brainstem. Functional considerations. Experimental Brain Research, 269–275. https://doi.org/10.1007/s002210050342.

[68] Kanoski, S.E., Rupprecht, L.E., Fortin, S.M., De Jonghe, B.C., Hayes, M.R., 2012. The role of nausea in food intake and body weight suppression by peripheral GLP-1 receptor agonists, exendin-4 and liraglutide. Neuropharmacology 62(5–6):1916–1927.

[69] Tchang, B.G., Abel, B., Zecca, C., Saunders, K.H., Shukla, A.P., 2020. An up-to-date evaluation of lorcaserin hydrochloride for the treatment of obesity. Expert Opinion on Pharmacotherapy 21(1):21–28. https://doi.org/10.1080/14656566.2019.1685496.

[70] Lamos, E.M., Levitt, D.L., Munir, K.M., 2016. A review of dopamine agonist therapy in type 2 diabetes and effects on cardio-metabolic parameters. Primary Care Diabetes, 60–65. https://doi.org/10.1016/j.pcd.2015.10.008.

[71] Mackie, K., 2005. Distribution of cannabinoid receptors in the central and peripheral nervous system. Cannabinoids. Springer-Verlag. p. 299–325.

[72] Birkenfeld, A.L., Schroeder, C., Boschmann, M., Tank, J., Franke, G., Luft, F.C., et al., 2002. Paradoxical effect of sibutramine on autonomic cardiovascular regulation. Circulation 106(19):2459–2465. https://doi.org/10.1161/01.CIR.0000036370.31856.73.

[73] Sharma, S., Garfield, A.S., Shah, B., Kleyn, P., Ichetovkin, I., Moeller, I.H., et al., 2019. Current mechanistic and pharmacodynamic understanding of melanocortin-4 receptor activation. Molecules. https://doi.org/10.3390/molecules24101892.

[74] Collet, T.H., Dubern, B., Mokrosinski, J., Connors, H., Keogh, J.M., Mendes de Oliveira, E., et al., 2017. Evaluation of a melanocortin-4 receptor (MC4R) agonist (Setmelanotide) in MC4R deficiency. Molecular Metabolism 6(10):1321–1329. https://doi.org/10.1016/j.molmet.2017.06.015.

[75] Kievit, P., Halem, H., Marks, D.L., Dong, J.Z., Glavas, M.M., Sinnayah, P., et al., 2013. Chronic treatment with a melanocortin-4 receptor agonist causes weight loss, reduces insulin resistance, and improves cardiovascular function in diet-induced obese rhesus macaques. Diabetes 62(2):490–497. https://doi.org/10.2337/db12-0598.

[76] Doslikova, B., Garfield, A.S., Shaw, J., Evans, M.L., Burdakov, D., Billups, B., et al., 2013. 5-HT2C receptor agonist anorectic efficacy potentiated by 5-HT1B receptor agonist coapplication: an effect mediated via increased proportion of pro-opiomelanocortin neurons activated. Journal of Neuroscience 33(23):9800–9804. https://doi.org/10.1523/JNEUROSCI.4326-12.2013.

[77] Zhou, L., Sutton, G.M., Rochford, J.J., Semple, R.K., Lam, D.D., Oksanen, L.J.J., et al., 2007. Serotonin 2C receptor agonists improve type 2 diabetes via melanocortin-4 receptor signaling pathways. Cell Metabolism 6(5):398–405. https://doi.org/10.1016/j.cmet.2007.10.008.

[78] Tam, J., Szanda, G., Drori, A., Liu, Z., Cinar, R., Kashiwaya, Y., et al., 2017. Peripheral cannabinoid-1 receptor blockade restores hypothalamic leptin signaling. Molecular Metabolism 6(10):1113–1125. https://doi.org/10.1016/j.molmet.2017.06.010.

[79] Sinnayah, P., Jobst, E.E., Rathner, J.A., Caldera-Siu, A.D., Tonelli-Lemos, L., Eusterbrock, A.J., et al., 2008. Feeding induced by cannabinoids is mediated independently of the melanocortin system. PloS One 3(5). https://doi.org/10.1371/journal.pone.0002202.

[80] Rowland, N.E., Schaub, J.W., Robertson, K.L., Andreasen, A., Haskell-Luevano, C., 2010. Effect of MTII on food intake and brain c-Fos in melanocortin-3, melanocortin-4, and double MC3 and MC4 receptor knockout mice. Peptides 31(12):2314–2317. https://doi.org/10.1016/j.peptides.2010.08.016.

[81] Benoit, S.C., Schwartz, M.W., Lachey, J.L., Hagan, M.M., Rushing, P.A., Blake, K.A., et al., 2000. A novel selective melanocortin-4 receptor agonist reduces food intake in rats and mice without producing aversive consequences. Journal of Neuroscience 20(9):3442–3448. https://doi.org/10.1523/jneurosci.20-09-03442.2000.

[82] Lau, J., Bloch, P., Schäffer, L., Pettersson, I., Spetzler, J., Kofoed, J., et al., 2015. Discovery of the once-weekly glucagon-like peptide-1 (GLP-1) analogue semaglutide. Journal of Medicinal Chemistry 58(18):7370–7380. https://doi.org/10.1021/acs.jmedchem.5b00726.

[83] Clemmensen, C., Finan, B., Fischer, K., Tom, R.Z., Legutko, B., Sehrer, L., et al., 2015. Dual melanocortin-4 receptor and GLP -1 receptor agonism amplifies metabolic benefits in diet-induced obese mice. EMBO Molecular Medicine 7(3):288–298. https://doi.org/10.15252/emmm.201404508.

[84] Trillou, C.R., Arnone, M., Delgorge, C., Gonalons, N., Keane, P., Maffrand, J.P., et al., 2003. Anti-obesity effect of SR141716, a CB1 receptor antagonist, in diet-induced obese mice. American Journal of Physiology - Regulatory, Integrative and Comparative Physiology 284(2 53–2). https://doi.org/10.1152/ajpregu.00545.2002.

[85] Cincotta, A.H., Tozzo, E., Scislowski, P.W.D., 1997. Bromocriptine/SKF38393 treatment ameliorates obesity and associated metabolic dysfunctions in obese (ob/ob) mice. Life Sciences 61(10):951–956. https://doi.org/10.1016/S0024-3205(97)00599-7.

[86] Mashiko, S., Ishihara, A., Iwaasa, H., Moriya, R., Kitazawa, H., Mitobe, Y., et al., 2008. Effects of a novel Y5 antagonist in obese mice: combination with food restriction or sibutramine. Obesity 16(7):1510–1515. https://doi.org/10.1038/oby.2008.223.

Bibliography

[Agg+09] M. Aggarwal et al. “Magnetic resonance imaging and micro-computed tomography combined atlas of developing and adult mouse brains for stereotaxic surgery”. In: *Neuroscience* 162.4 (2009), pp. 1339–1350.

[All17] Allen Institute for Brain Science. *Allen Mouse Common Coordinate Framework and Reference Atlas*. Tech. rep. 2017.

[AO20] Melissa J. Armstrong and Michael S. Okun. “Diagnosis and Treatment of Parkinson Disease: A Review”. In: *JAMA - Journal of the American Medical Association* 323.6 (2020), pp. 548–560.

[AWB15] Jeffrey R. Ashton, Jennifer L. West, and Cristian T. Badea. “In vivo small animal micro-CT using nanoparticle contrast agents”. In: *Frontiers in Pharmacology* 6 (2015), p. 256.

[Asi+95] K. E. Asin et al. “Rotation and striatal c-fos expression after repeated, daily treatment with selective dopamine receptor agonists and levodopa”. In: *Journal of Pharmacology and Experimental Therapeutics* 273.3 (1995), pp. 1483–1490.

[BAJ07] A. Badea, A. A. Ali-Sharief, and G. A. Johnson. “Morphometric analysis of the C57BL/6J mouse brain”. In: *NeuroImage* 37.3 (2007), pp. 683–693.

[Bai17] Sylvain Baillet. “Magnetoencephalography for brain electrophysiology and imaging”. In: *Nature Neuroscience* 20.3 (2017), pp. 327–339.

[BB19] Ian J. Bamford and Nigel S. Bamford. “The Striatum’s Role in Executing Rational and Irrational Economic Behaviors”. In: *Neuroscientist* 25.5 (2019), pp. 475–490.

[BC12] Mark G. Baxter and Paula L. Croxson. “Facing the role of the amygdala in emotional information processing”. In: *Proceedings of the National Academy of Sciences* 109.52 (2012), pp. 21180–21181.

[Bec+12] Klaus Becker et al. "Chemical Clearing and Dehydration of GFP Expressing Mouse Brains". In: *PLOS ONE* 7.3 (2012), e33916.

[BH95] Yoav Benjamini and Yosef Hochberg. *Controlling the False Discovery Rate: A Practical and Powerful Approach to Multiple Testing*. Tech. rep. 1. 1995, pp. 289–300.

[BR16] G. B. Bissonette and M. R. Roesch. "Development and function of the midbrain dopamine system: what we know and what we need to". In: *Genes, Brain and Behavior* 15.1 (2016), pp. 62–73.

[Blo46] F. Bloch. "Nuclear Induction". In: *Physical Review* 70.7-8 (1946), p. 460.

[Bra+19] Audrey Branch et al. "An optimized tissue clearing protocol for rat brain labeling, imaging, and high throughput analysis". In: *bioRxiv* (2019), p. 639674.

[Bre+16] Michael O. Breckwoldt et al. "Correlated magnetic resonance imaging and ultramicroscopy (MR-UM) is a tool kit to assess the dynamics of glioma angiogenesis". In: *eLife* 5 (2016), pp. 1–17.

[Bri+10] Dana I. Briggs et al. "Diet-induced obesity causes ghrelin resistance in arcuate NPY/AgRP neurons". In: *Endocrinology* 151.10 (2010), pp. 4745–4755.

[Bul+99] Edward T. Bullmore et al. "Global, voxel, and cluster tests, by theory and permutation, for a difference between two groups of structural mr images of the brain". In: *IEEE Transactions on Medical Imaging* 18.1 (1999), pp. 32–42.

[CP19] Jennifer Shane Williamson Campbell and Gilbert Bruce Pike. "Diffusion Magnetic Resonance Imaging". In: *Encyclopedia of Biomedical Engineering*. Elsevier, 2019, pp. 505–518.

[Cha+07] E. Chan et al. "Development of a high resolution three-dimensional surgical atlas of the murine head for strains 129S1/SvImJ and C57Bl/6J using magnetic resonance imaging and micro-computed tomography". In: *Neuroscience* 144.2 (2007), pp. 604–615.

[Cha+11] Pei Ting Chao et al. "Knockdown of NPY expression in the dorsomedial hypothalamus promotes development of brown adipocytes and prevents diet-induced obesity". In: *Cell metabolism* 13.5 (2011), pp. 573–583.

[Cho+19] Uree Chon et al. "Enhanced and unified anatomical labeling for a common mouse brain atlas". In: *Nature communications* 10.1 (2019), p. 5067.

[Chu+11] Nelson Chuang et al. "An MRI-based atlas and database of the developing mouse brain". In: *NeuroImage* 54.1 (2011), pp. 80–89.

[Chu+13] Kwanghun Chung et al. "Structural and molecular interrogation of intact biological systems". In: *Nature* 497.7449 (2013), pp. 332–337.

[Cie11a] R. Cierniak. "Some Words About the History of Computed Tomography". In: *X-Ray Computed Tomography in Biomedical Engineering* (2011), pp. 7–19.

[Cie11b] Robert Cierniak. "The Physics of Data Acquisition". In: *X-Ray Computed Tomography in Biomedical Engineering*. 1st ed. Springer, London, 2011. Chap. 4, pp. 63–81.

[Cla+20] Federico Claudi et al. "BrainGlobe Atlas API: a common interface for neuroanatomical atlases". In: *Journal of Open Source Software* 5.54 (2020), p. 2668.

[Cle+17] Christoffer Clemmensen et al. "Gut-Brain Cross-Talk in Metabolic Control". In: *Cell* 168.5 (2017), pp. 758–774.

[CGD19] Stella Corsetti, Frank Gunn-Moore, and Kishan Dholakia. "Light sheet fluorescence microscopy for neuroscience". In: *Journal of Neuroscience Methods* 319 (2019), pp. 16–27.

[CRG18] Ann A. Coulter, Candida J. Rebello, and Frank L. Greenway. *Centrally Acting Agents for Obesity: Past, Present, and Future*. 2018.

[Cre+08] Alex de Crespigny et al. "3D micro-CT imaging of the postmortem brain". In: *Journal of Neuroscience Methods* 171.2 (2008), pp. 207–213.

[DAn18] Egidio D'Angelo. "Physiology of the cerebellum". In: *Handbook of Clinical Neurology*. Vol. 154. Elsevier, 2018, pp. 85–108.

[Dav+20] Korbin M. Davis et al. "PET and SPECT Imaging of the Brain: History, Technical Considerations, Applications, and Radiotracers". In: *Seminars in Ultrasound, CT and MRI* 41.6 (2020), pp. 521–529.

[Di 15] Giovanni Di Guardo. "Lipofuscin, lipofuscin-like pigments and autofluorescence". In: *European Journal of Histochemistry* 59.1 (2015), p. 2485.

[DH12] Marcelo O Dietrich and Tamas L Horvath. "Limitations in anti-obesity drug development: the critical role of hunger-promoting neurons." In: *Nature reviews. Drug discovery* 11.9 (2012), pp. 675–91.

[Don08] H.W Dong. *The Allen Reference Atlas: a Digital Color Brain Atlas of the C57BL/6J Male Mouse*. Wiley, 2008.

[Dor+08] A. E. Dorr et al. "High resolution three-dimensional brain atlas using an average magnetic resonance image of 40 adult C57Bl/6J mice". In: *NeuroImage* 42.1 (2008), pp. 60–69.

[Dra57] L. E. Drain. "Principles and applications of nuclear magnetic resonance". In: *British Journal of Applied Physics* 8 (1957), pp. 27–33.

[Dum+18] Serge O. Dumoulin et al. "Ultra-high field MRI: Advancing systems neuroscience towards mesoscopic human brain function". In: *NeuroImage* 168 (2018), pp. 345–357.

[Dun61] Olive Jean Dunn. "Multiple Comparisons Among Means". In: *Journal of the American Statistical Association* 56.293 (1961), pp. 52–64.

[Dun55] Charles W. Dunnett. "A Multiple Comparison Procedure for Comparing Several Treatments with a Control". In: *Journal of the American Statistical Association* 50.272 (1955), pp. 1096–1121.

[Dyr+11] Tim B. Dyrby et al. "An ex vivo imaging pipeline for producing high-quality and high-resolution diffusion-weighted imaging datasets". In: *Human Brain Mapping* 32.4 (2011), pp. 544–563.

[Dyr+18] Tim B. Dyrby et al. "Validation strategies for the interpretation of microstructure imaging using diffusion MRI". In: *NeuroImage* 182 (2018), pp. 62–79.

[Ern+09] Marianne B. Ernst et al. "Enhanced Stat3 activation in POMC neurons provokes negative feedback inhibition of leptin and insulin signaling in obesity". In: *The Journal of neuroscience : the official journal of the Society for Neuroscience* 29.37 (2009), pp. 11582–11593.

[Erö+18] Csaba Erö et al. "A cell atlas for the mouse brain". In: *Frontiers in Neuroinformatics* 12 (2018), p. 84.

[Ert+12] Ali Ertürk et al. "Three-dimensional imaging of solvent-cleared organs using 3DISCO". In: *Nature Protocols* 7.11 (2012), pp. 1983–1995.

[Fan+21] Chunyu Fang et al. "Minutes-timescale 3D isotropic imaging of entire organs at subcellular resolution by content-aware compressed-sensing light-sheet microscopy". In: *Nature Communications 2021 12:1* 12.1 (2021), pp. 1–13.

[FT19] Anteneh M. Feyissa and William O. Tatum. "Adult EEG". In: *Handbook of Clinical Neurology*. Vol. 160. Elsevier B.V., 2019. Chap. 7, pp. 103–124.

[FP97] K. B. J. Franklin and G. Paxinos. *The Mouse Brain in Stereotaxic Coordinates*. 1st ed. San Diego: Academic Press, 1997.

[Für+18] Daniel Fürth et al. "An interactive framework for whole-brain maps at cellular resolution". In: *Nature Neuroscience* 21.6 (2018), p. 895.

[Gab+20] Sanaz Gabery et al. "Semaglutide lowers body weight in rodents via distributed neural pathways". In: *JCI Insight* 5.6 (2020).

[GBD19] GBD 2016 Neurology Collaborators. "Global, regional, and national burden of neurological disorders, 1990-2016: a systematic analysis for the Global Burden of Disease Study 2016". In: *The Lancet. Neurology* 18.5 (2019), pp. 459–80.

[Gou+19] Maged Goubran et al. "Multimodal image registration and connectivity analysis for integration of connectomic data from microscopy to MRI". In: *Nature Communications* 10.1 (2019), pp. 1–17.

[GR17] Roger N. Gunn and Eugenii A. Rabiner. "Imaging in Central Nervous System Drug Discovery". In: *Seminars in Nuclear Medicine* 47.1 (2017), pp. 89–98.

[Guo+19] Wenyan Guo et al. "Whole-mount in situ hybridization of mouse brain to precisely locate mRNAs via fluorescence tomography". In: *Journal of Biophotonics* 12.4 (2019), e201800249.

[Hag+19] Yawara Haga et al. "MR Imaging Properties of ex vivo Common Marmoset Brain after Formaldehyde Fixation". In: *Magnetic Resonance in Medical Sciences* 18.4 (2019), pp. 253–259.

[HK17] Michael M. Halassa and Sabine Kastner. "Thalamic functions in distributed cognitive control". In: *Nature Neuroscience* 20 (2017), pp. 1669–1679.

[Han+21] Henrik H. Hansen et al. "Whole-brain activation signatures of weight-lowering drugs". In: *Molecular Metabolism* 47.January (2021), p. 101171.

[Her09] Suzana Herculano-Houzel. "The human brain in numbers: A linearly scaled-up primate brain". In: *Frontiers in Human Neuroscience* 3 (2009), p. 31.

[HML06] Suzana Herculano-Houzel, Bruno Mota, and Roberto Lent. "Cellular scaling rules for rodent brains". In: *Proceedings of the National Academy of Sciences of the United States of America* 103.32 (2006), pp. 12138–12143.

[Hob+20] Deirdre B. Hoban et al. "Impact of α-synuclein pathology on transplanted hESC-derived dopaminergic neurons in a humanized α-synuclein rat model of PD". In: *Proceedings of the National Academy of Sciences of the United States of America* 117.26 (2020), pp. 15209–15220.

[Hum21] Human Brain Project. *Volumetric rat brain atlas on EBRAINS now covers entire brain.* 2021.

[JMP18] Stanley Jacobson, Elliott M. Marcus, and Stanley Pugsley. "Cerebral Cortex Functional Localization". In: *Neuroanatomy for the Neuroscientist* (2018), pp. 297–328.

[JT05] Steven J Janke and Frederick C Tinsley. "Statistical Inference". In: *Introduction to Linear Models and Statistical Inference.* Hoboken, NJ, USA: John Wiley & Sons, Ltd, 2005. Chap. 5, pp. 155–216.

[Jen12] Bruce G. Jenkins. "Pharmacologic magnetic resonance imaging (phMRI): Imaging drug action in the brain". In: *NeuroImage* 62.2 (2012), pp. 1072–1085.

[Joh+10] G. Allan Johnson et al. "Waxholm Space: An image-based reference for coordinating mouse brain research". In: *NeuroImage* 53.2 (2010), pp. 365–372.

[Jol+12] Aurélie Joly-Amado et al. "Hypothalamic AgRP-neurons control peripheral substrate utilization and nutrient partitioning". In: *The EMBO journal* 31.22 (2012), pp. 4276–4288.

[KLG16] Shervin Kamalian, Michael H. Lev, and Rajiv Gupta. "Computed tomography imaging and angiography – principles". In: *Handbook of Clinical Neurology.* 1st ed. Vol. 135. Elsevier B.V., 2016. Chap. 1, pp. 3–20.

[Kja+19] Marina Kjaergaard et al. "PYY(3-36) and exendin-4 reduce food intake and activate neuronal circuits in a synergistic manner in mice". In: *Neuropeptides* 73 (2019), pp. 89–95.

[Kjo+15] Lisa J. Kjonigsen et al. "Waxholm Space atlas of the rat brain hippocampal region: Three-dimensional delineations based on magnetic resonance and diffusion tensor imaging". In: *NeuroImage* 108 (2015), pp. 441–449.

[Kle+10] Stefan Klein et al. "Elastix: A Toolbox for Intensity-Based Medical Image Registration". In: *IEEE Transactions on Medical Imaging* 29.1 (2010), pp. 196–205.

[Kly+18] Ivan S. Klyuzhin et al. "Data-driven, voxel-based analysis of brain PET images: Application of PCA and LASSO methods to visualize and quantify patterns of neurodegeneration". In: *PLOS ONE* 13.11 (2018), e0206607.

[KMG12] Witold Kosiński, Paweł Michalak, and Piotr Gut. "Robust Image Registration Based on Mutual Information Measure". In: *Journal of Signal and Information Processing* 03.02 (2012), pp. 175–178.

[Kov+05] N. Kovačević et al. "A three-dimensional MRI atlas of the mouse brain with estimates of the average and variability". In: *Cerebral Cortex* 15.5 (2005), pp. 639–645.

[Kru+21] Oleh Krupa et al. "NuMorph: Tools for cortical cellular phenotyping in tissue-cleared whole-brain images". In: *Cell Reports* 37.2 (2021), p. 109802.

[Kua+15] Leonard Kuan et al. "Neuroinformatics of the Allen Mouse Brain Connectivity Atlas". In: *Methods* 73 (2015), pp. 4–17.

[Lau73] P. C. Lauterbur. "Image Formation by Induced Local Interactions: Examples Employing Nuclear Magnetic Resonance". In: *Nature* 242 (1973), pp. 190–191.

[Lei+07] Ed S. Lein et al. "Genome-wide atlas of gene expression in the adult mouse brain". In: *Nature* 445.7124 (2007), pp. 168–176.

[LJ00] Ronald A. Leslie and Michael F. James. "Pharmacological magnetic resonance imaging: a new application for functional MRI". In: *Trends in Pharmacological Sciences* 21.8 (2000), pp. 314–318.

[Lie+16] Thomas Liebmann et al. "Three-Dimensional Study of Alzheimer's Disease Hallmarks Using the iDISCO Clearing Method". In: *Cell Reports* 16.4 (2016), pp. 1138–1152.

[LL11] Michael A Long and Albert K Lee. "Intracellular recording in behaving animals". In: (2011).

[Ma+05] Y. Ma et al. "A three-dimensional digital atlas database of the adult C57BL/6J mouse brain by magnetic resonance microscopy". In: *Neuroscience* 135.4 (2005), pp. 1203–1215.

[Ma+08] Yu Ma et al. "In vivo 3D digital atlas database of the adult C57BL/6J mouse brain by magnetic resonance microscopy". In: *Frontiers in Neuroanatomy* 2.APR (2008), pp. 1–10.

[Mac+04] Allan MacKenzie-Graham et al. "A multimodal, multidimensional atlas of the C57BL/6J mouse brain". In: *Journal of Anatomy* 204.2 (2004), pp. 93–102.

[MT10] Henrik Madsen and Poul Thyregod. "Generalized linear models". In: *Introduction to general and generalized linear models*. 1st ed. Bosa Roca: Taylor & Francis Group, 2010. Chap. 4, pp. 87–156.

[Man+20] Matteo Mancini et al. "A multimodal computational pipeline for 3D histology of the human brain". In: *Scientific Reports* 10.1 (2020), pp. 1–21.

[MJ04] P.M. Matthews and P. Jezzard. "Functional magnetic resonance imaging". In: *Journal of Neurology, Neurosurgery & Psychiatry* 75 (2004), pp. 6–12.

[McL64] Dan McLachlan. "Extreme Focal Depth in Microscopy". In: *Applied Optics* 3.9 (1964), p. 1009.

[MT91] J. W. Mink and W. T. Thach. "Basal Ganglia Motor Control. I. Nonexclusive Relation of Pallidal Discharge to Five Movement Modes". In: *Journal of Neurophysiology* 65.2 (1991), pp. 273–300.

[Mon05] Monica Monici. "Cell and tissue autofluorescence research and diagnostic applications". In: *Biotechnology Annual Review* 11 (2005), pp. 227–256.

[Mor+19] Masahiko Morita et al. "ViBrism DB: an interactive search and viewer platform for 2D/3D anatomical images of gene expression and co-expression networks". In: *Nucleic Acids Research* 47.D1 (2019), pp. D859–D866.

[Mur+18] Tatsuya C. Murakami et al. "A three-dimensional single-cell-resolution whole-brain atlas using CUBIC-X expansion microscopy and tissue clearing". In: *Nature Neuroscience* 21.4 (2018), pp. 625–637.

[NR99] W. R. Nitz and P. Reimer. "Contrast mechanisms in MR imaging". In: *European Radiology* 9 (1999), pp. 1032–1046.

[NGS20] Teresa Nolte, Nicolas Gross-Weege, and Volkmar Schulz. "(Hybrid) SPECT and PET Technologies". In: *Molecular Imaging in Oncology.* 2nd ed. Springer, Cham, 2020. Chap. 3, pp. 111–133.

[Oh+14] Seung Wook Oh et al. "A mesoscale connectome of the mouse brain". In: *Nature* 508.7495 (2014), pp. 207–214.

[Ose+19] Kirsten K. Osen et al. "Waxholm Space atlas of the rat brain auditory system: Three-dimensional delineations based on structural and diffusion tensor magnetic resonance imaging". In: *NeuroImage* 199 (2019), pp. 38–56.

[Pap+14] Eszter A. Papp et al. "Waxholm Space atlas of the Sprague Dawley rat brain". In: *NeuroImage* 97 (2014), pp. 374–386.

[Pat18] Jaymin Patel. "The mouse brain: A 3D atlas registering MRI, CT, and histological sections in three cardinal planes". PhD thesis. John Hopkins University, 2018.

[PC21] Surojit Paul and Eduardo Candelario-Jalil. "Emerging neuroprotective strategies for the treatment of ischemic stroke: An overview of clinical and preclinical studies". In: *Experimental Neurology* 335.August 2020 (2021), p. 113518.

[Per+21a] Johanna Perens et al. "An Optimized Mouse Brain Atlas for Automated Mapping and Quantification of Neuronal Activity Using iDISCO+ and Light Sheet Fluorescence Microscopy". In: *Neuroinformatics* 19 (2021), pp. 433–446.

[Per+21b] Johanna Perens et al. "Comparative study of voxel-based statistical analysis methods for fluorescently labelled and light sheet imaged whole-brain samples". In: *2021 IEEE 18th International Symposium on Biomedical Imaging (ISBI)* (2021), pp. 1433–1437.

[Per+16] Anne Sophie Perrin-Terrin et al. "The c-FOS Protein Immunohistological Detection: A Useful Tool As a Marker of Central Pathways Involved in Specific Physiological Responses In Vivo and Ex Vivo". In: *Journal of Visualized Experiments : JoVE* 110 (2016), p. 53613.

[Pis+21] Thomas J. Pisano et al. "Homologous organization of cerebellar pathways to sensory, motor, and associative forebrain". In: *Cell Reports* 36.12 (2021), p. 109721.

[PTP46] E. M. Purcell, H. C. Torrey, and R. V. Pound. "Resonance absorption by nuclear magnetic moments in a solid". In: *Physical Review* 69.1-2 (1946), p. 37.

[Rab+38] I. I. Rabi et al. "A New Method of Measuring Nuclear Magnetic Moment". In: *Physical Review* 53.4 (1938), p. 318.

[Rei+19] Michael W. Reimann et al. "A null model of the mouse whole-neocortex micro-connectome". In: *Nature Communications* 10.3903 (2019), p. 11630.

[Ren+14] Nicolas Renier et al. "iDISCO: A Simple, Rapid Method to Immunolabel Large Tissue Samples for Volume Imaging". In: *Cell* 159.4 (2014), pp. 896–910.

[Ren+16] Nicolas Renier et al. "Mapping of Brain Activity by Automated Volume Analysis of Immediate Early Genes". In: *Cell* 165.7 (2016), pp. 1789–1802.

[Rit04] Erik L. Ritman. "Micro-computed tomography - Current status and developments". In: *Annual Review of Biomedical Engineering* 6 (2004), pp. 185–208.

[Roo+19] Urmas Roostalu et al. "Quantitative whole-brain 3D imaging of tyrosine hydroxylase-labeled neuron architecture in the mouse MPTP model of Parkinson's disease". In: *Disease Models and Mechanisms* 12.11 (2019).

[Sal+18] Casper Bo Gravesen Salinas et al. "Integrated Brain Atlas for Unbiased Mapping of Nervous System Effects Following Liraglutide Treatment". In: *Scientific Reports* 8.1 (2018), p. 10310.

[Sec+14] Anna Secher et al. "The arcuate nucleus mediates GLP-1 receptor agonist liraglutide-dependent weight loss". In: *The Journal of Clinical Investigation* 124.10 (2014), pp. 4473–4488.

[Sha+14] D. P. Shamonin et al. "Fast parallel image registration on CPU and GPU for diagnostic classification of Alzheimer's disease". In: *Frontiers in Neuroinformatics* 7 (2014).

[SMS13] Gabi Shefer, Yonit Marcus, and Naftali Stern. "Is obesity a brain disease?" In: *Neuroscience & Biobehavioral Reviews* 37.10 (2013), pp. 2489–2503.

[Shi+21] Polina Shichkova et al. "A Standardized Brain Molecular Atlas: A Resource for Systems Modeling and Simulation". In: *Frontiers in Molecular Neuroscience* 14 (2021), p. 251.

[SZ02] H. Siedentopf and R. Zsigmondy. "Über Sichtbarmachung und Größenbestimmung ultramikroskopischer Teilchen, mit besonderer Anwendung auf Goldrubingläser". In: *Annalen der Physik* 315.1 (1902), pp. 1–39.

[SG09] Karolina P. Skibicka and Harvey J. Grill. "Hypothalamic and hindbrain melanocortin receptors contribute to the feeding, thermogenic, and cardiovascular action of melanocortins". In: *Endocrinology* 150.12 (2009), pp. 5351–5361.

[Sko+21] Grethe Skovbjerg et al. "Whole-brain mapping of amylin-induced neuronal activity in receptor activity–modifying protein 1/3 knockout mice". In: *European Journal of Neuroscience* 54.1 (2021), pp. 4154–4166.

[Smi+09] Kyle S. Smith et al. "Ventral Pallidum Roles in Reward and Motivation". In: *Behavioural brain research* 196.2 (2009), pp. 155–167.

[SN09] Stephen M. Smith and Thomas E. Nichols. "Threshold-free cluster enhancement: Addressing problems of smoothing, threshold dependence and localisation in cluster inference". In: *NeuroImage* 44 (2009), pp. 83–98.

[Sor+07] E. Soria-Gómez et al. "Pharmacological enhancement of the endocannabinoid system in the nucleus accumbens shell stimulates food intake and increases c-Fos expression in the hypothalamus". In: *British Journal of Pharmacology* 151.7 (2007), pp. 1109–1116.

[Spi+18] Tamás Spisák et al. "Probabilistic TFCE: A generalized combination of cluster size and voxel intensity to increase statistical power". In: *NeuroImage* 185 (2018), pp. 12–26.

[Ste+16] Marzena Stefaniuk et al. "Light-sheet microscopy imaging of a whole cleared rat brain with Thy1-GFP transgene". In: *Scientific Reports* 6 (2016), p. 28209.

[Sto+18] H. B. Stolp et al. "Voxel-wise comparisons of cellular microstructure and diffusion-MRI in mouse hippocampus using 3D Bridging of Optically-clear histology with Neuroimaging Data (3D-BOND)". In: *Scientific Reports* 8.1 (2018), pp. 1–12.

[Sun+05] Shu Wei Sun et al. "Formalin fixation alters water diffusion coefficient magnitude but not anisotropy in infarcted brain". In: *Magnetic resonance in medicine* 53.6 (2005), pp. 1447–1451.

[Sus+14] Etsuo A Susaki et al. "Whole-Brain Imaging with Single-Cell Resolution Using Chemical Cocktails and Computational Analysis". In: *Cell* 157.3 (2014), pp. 726–739.

[Sym+04] M. Symms et al. "A review of structural magnetic resonance neuroimaging". In: *Journal of Neurology, Neurosurgery and Psychiatry* 75.9 (2004), pp. 1235–1244.

[TYL21] Ting Tian, Zhaoyang Yang, and Xiaoguang Li. "Tissue clearing technique: Recent progress and biomedical applications". In: *Journal of Anatomy* 238.2 (2021), pp. 489–507.

[Tót+18] Zoltán Tóth et al. "Non-competitive antagonists of NMDA and AMPA receptors decrease seizure-induced c-fos protein expression in the cerebellum and protect against seizure symptoms in adult rats". In: *Acta Histochemica* 120.3 (2018), pp. 236–241.

[Tys+21] Adam L. Tyson et al. "A deep learning algorithm for 3D cell detection in whole mouse brain image datasets". In: *PLoS Computational Biology* 17.5 (2021), pp. 1–17.

[Ued+20] Hiroki R. Ueda et al. "Whole-Brain Profiling of Cells and Circuits in Mammals by Tissue Clearing and Light-Sheet Microscopy". In: *Neuron* 106.3 (2020), pp. 369–387.

[Uma+19] Kannan U. Umadevi Venkataraju et al. "Development of brain templates for whole brain atlases". In: *Progress in Biomedical Optics and Imaging - Proceedings of SPIE* 10865 (2019), p. 1086511.

[Van+18] Michel E. Vandenberghe et al. "Voxel-Based Statistical Analysis of 3D Immunostained Tissue Imaging". In: *Frontiers in Neuroscience* 12.754 (2018).

[VS20] Miguel Vaz and Samuel Silvestre. "Alzheimer's disease: Recent treatment strategies". In: *European Journal of Pharmacology* 887.May (2020), p. 173554.

[VBS93] A. H. Voie, D. H. Burns, and F. A. Spelman. "Orthogonal-plane fluorescence optical sectioning: Three-dimensional imaging of macroscopic biological specimens". In: *Journal of Microscopy* 170.3 (1993), pp. 229–236.

[Wan+18] Peng Wan et al. "Evaluation of seven optical clearing methods in mouse brain". In: *Neurophotonics* 5.3 (2018), p. 035007.

[Wan+20a] Nian Wang et al. "Cytoarchitecture of the mouse brain by high resolution diffusion magnetic resonance imaging". In: *NeuroImage* 216.November 2019 (2020).

[Wan+20b] Quanxin Wang et al. "The Allen Mouse Brain Common Coordinate Framework: A 3D Reference Atlas". In: *Cell* 181.4 (2020), pp. 936–953.

[WKP10a] Charles Watson, Matthew Kirkcaldie, and George Paxinos. "Nerve cells and synapses". In: *The Brain*. Academic Press, 2010, pp. 1–10.

[WKP10b] Charles Watson, Matthew Kirkcaldie, and George Paxinos. "Techniques for studying the brain". In: *The Brain*. Academic Press, 2010. Chap. 11, pp. 153–165.

[Wei+16] Hongjiang Wei et al. "Imaging whole-brain cytoarchitecture of mouse with MRI-based quantitative susceptibility mapping". In: *NeuroImage* 137 (2016), pp. 107–115.

[WC05] Quan Wen and Dmitri B Chklovskii. "Segregation of the Brain into Gray and White Matter: A Design Minimizing Conduction Delays". In: *PLOS Computational Biology* 1.7 (2005), e78.

[Whi09] Jennifer L. Whitwell. "Voxel-Based Morphometry: An Automated Technique for Assessing Structural Changes in the Brain". In: *Journal of Neuroscience* 29.31 (2009), pp. 9661–9664.

[Wor21] World Health Organization. *Obesity*. 2021.

[Wu+16] Zufeng Wu et al. "Medical Image Registration Using B-Spline Transform". In: *International Journal of Simulation - Systems, Science and Technology* 17.48 (2016), pp. 1–1.

[Xia07] Jun Xiao. "A new coordinate system for rodent brain and variability in the brain weights and dimensions of different ages in the naked mole-rat". In: *Journal of Neuroscience Methods* 162.1-2 (2007), pp. 162–170.

[XD17] Yuanyuan Xie and Richard I. Dorsky. "Development of the hypothalamus: conservation, modification and innovation". In: *Development* 144.9 (2017), pp. 1588–1599.

[You+21] David M. Young et al. "Constructing and optimizing 3d atlases from 2d data with application to the developing mouse brain". In: *eLife* 10 (2021), pp. 1–92.

[YDP18] Tayyabah Yousaf, George Dervenoulas, and Marios Politis. "Advances in MRI Methodology". In: *International Review of Neurobiology*. 1st ed. Vol. 141. Elsevier Inc., 2018. Chap. 2, pp. 31–76.

[Yus+06] P.A. Yushkevich et al. "User-guided 3D active contour segmentation of anatomical structures: significantly improved efficiency and reliability". In: *NeuroImage* 31.3 (2006), pp. 1116–1128.

[Zha+18] Pengfei Zhang et al. "High-resolution deep functional imaging of the whole mouse brain by photoacoustic computed tomography in vivo". In: *Journal of Biophotonics* 11.1 (2018), e201700024.

[Zin+14] Brian Zingg et al. "Neural networks of the mouse neocortex". In: *Cell* 156.5 (2014), pp. 1096–1111.